This work is protected by copyright and other intellectual property rights and duplication or sale of all or part is not permitted, except that material may be duplicated by you for research, private study, criticism/review or educational purposes. Electronic or print copies are for your own personal, non-commercial use and shall not be passed to any other individual. No quotation may be published without proper acknowledgement. For any other use, or to quote extensively from the work, permission must be obtained from the copyright holder/s.

ELECTRON-INDUCED SECONDARY ELECTRON EMISSION SPECTROSCOPY OF SURFACES

A thesis presented for the degree of Doctor of Philosophy at the University of Keele by

P. R. Harris B.A.

EMI-Varian Limited
Hayes, Middlesex.

November 1972

BRITISH LIBRARY

IMAGING SERVICES NORTH

Boston Spa, Wetherby
West Yorkshire, LS23 7BQ
www.bl.uk

BEST COPY AVAILABLE.

VARIABLE PRINT QUALITY

BRITISH LIBRARY

IMAGING SERVICES NORTH
Boston Spa, Wetherby
West Yorkshire, LS23 7BQ
www.bl.uk

ORIGINAL COPY TIGHTLY BOUND

TO SIMON AND ADRIAN

CONTENTS

ACKNOWLEDGEMENTS

The author wishes to acknowledge with grateful thanks:

Professor D.J.E. Ingram for the use of his laboratory facilities.

Dr. E.B. Pattinson for constructive guidance and excellent supervision throughout this work.

Dr. S. Thomas for much advice and assistance during the early stages.

Dr. M. Suleman, Mr. B. Wright and other colleagues and friends in the Physics Department for many helpful discussions and suggestions.

Mr. F. Rowerth and his technical staff for invaluable assistance throughout this work; in particular, Mr. G. Dudley and the staff of the Workshop for their skill in fabricating the experimental chamber and Mr. M.G. Davies and the staff of the Electronic Workshop for much help with the design and construction of the circuitry and the maintenance of commercial equipment.

Dr. K.H. Kreuchen, Mr. M.J. Smith and colleagues at EMI-Varian Ltd., for the continued interest they have shown in this work.

Mr. M.T. Cheney for all the photographic work

Miss K.B. Davies for the most efficient way she has undertaken the task of the presentation, typing and duplication of this thesis, and for photocopying the diagrams.

The States of Guernsey Education Council and EMI-Varian Ltd., for the generous provision of an industrial studentship for the period 1969-71.

My wife for her constant encouragement.

ABSTRACT

An introduction to the subject of secondary electron emission, characteristic energy loss and Auger electron spectroscopy is given, together with a brief survey of some relevant published work. An apparatus consisting of a 360° retarding field spectrometer is described, together with the associated circuitry for the measurement of total yield, backscattering coefficient, the energy distribution, and its differential, of electron induced secondary electrons. Careful design of the analyser has enabled an energy resolution of better than 0.3% to be obtained and made possible the use of a wide range of incident electron angles and energies.

Results are presented for the secondary electron yield and Auger electron spectra of a Zr/Al bulk getter. These show that the material has a low yield which may well make it suitable for gettering applications in electron beam tubes.

High resolution Auger spectra of Pd, Ag, Su, Sb, Cu and Al are given showing fine structure previously seen only by workers using a cylindrical mirror analyser. In the case of Al, satellite peaks around the main peak can be interpreted by a plasmon gain and loss mechanism. Characteristic energy losses using a range of primary energies from 100eV to 1keV and incident angles from 0° to 60° have also been measured for the same metals, leading to the identification of surface, bulk and multiple plasma losses, and

inter and intra-band transition losses.

Extensive fine structure discovered in the low energy region of 0-25eV for Pd, Ag, Cu and Al is associated with the preferential emission of conduction band electrons from states of high symmetry, rather than with plasmon gains.

CHAPTER I

INTRODUCTION AND REVIEW

1.1 Introduction

It has been known since near the beginning of the century that when a solid is bombarded with radiation it may emit electrons. If the incident radiation is in the form of photons, the emitted electrons are termed photoelectrons, and where it consists of electrons or other particles the resulting electrons are called secondary electrons. Basically what happens is that the incident radiation can dissipate its energy by interaction with the electrons in the solid, exciting them into various states. These electrons may, together with the reflected portion of the radiation, escape from the solid if they have sufficient kinetic energy.

We are concerned in this thesis with various aspects of the secondary electron emission of surfaces bombarded with electrons of incident energy between 100 and 3000 electron volts (eV). This subject has proved to be of some technological significance since materials with a high yield of secondary electrons are tremendously important in the design of such instruments as electron multipliers, image intensifiers etc., and substances of low secondary yield find application in, for example, reducing the 'multipactor' effect in high power electron beam tubes (Kreuchen and Diserens 1958). Much theoretical effort has also been expended in the study of the various processes determining the yield of surfaces, but the mechanisms involved are not fully understood, despite the volume of experimental work which has been done.

The energy distribution of secondary electrons has also been extensively studied, both in reflection, first investigated by Farnsworth (1925) and Rudberg (1930), and transmission through thin films (Ruthemann 1941). Small discrete energy losses of the reflected (or transmitted) electrons have been observed and can be largely explained in terms of single electron and many electron excitations. More recently, renewed interest has developed in the study of the energy distribution of secondary electrons, since it can provide an extremely sensitive method of surface analysis; i.e. Auger electron spectroscopy (Lander 1953, Harris 1968). It is also possible that high resolution studies of the secondary electrons of very low energy may give some information on the conduction band structure above the vacuum level (Willis et al. 1971 and this thesis Chapter 6).

In this chapter we give a brief introduction to the subject of secondary electron emission, together with a mention of some related fields, and a survey of relevant published work. In Chapter 2, the design and performance of an instrument for measuring the total yield and energy distribution of secondary electrons is described, and the remainder of the dissertation is concerned with a discussion of some results obtained with this equipment, and suggestions for further studies.

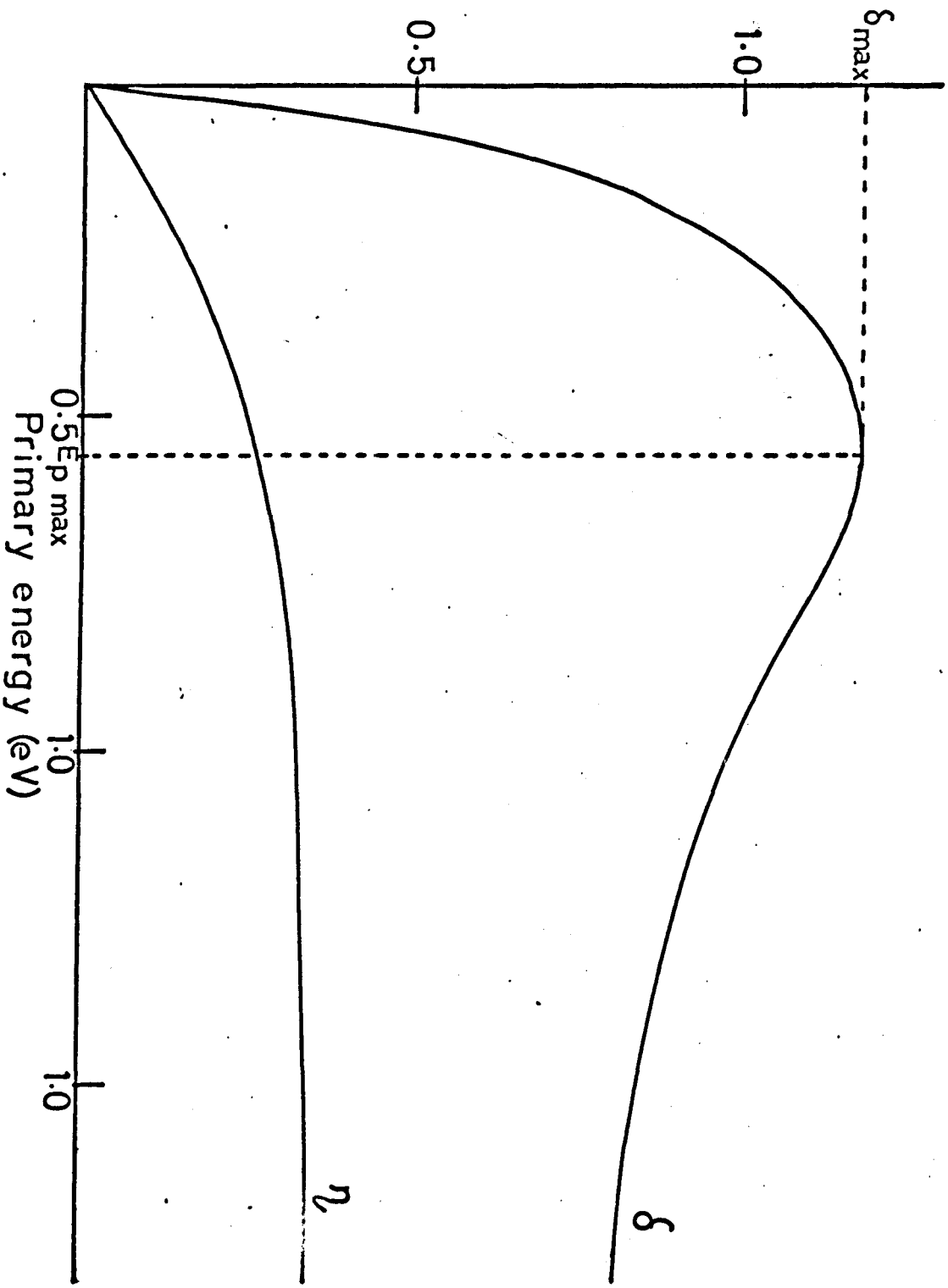

Figure 1.1 A typical yield curve

1.2 Secondary electron yield

The secondary electron yield of a material is dependent on a number of factors, and many investigations have been made of the effect of these parameters on the yield. The total secondary yield, or secondary emission coefficient, δ, is the number of electrons emitted per incident electron. If i_p be the primary current and i_s the secondary current, then

$$\delta = i_s/i_p$$

It is customary to divide the secondary electrons arbitrarily into two groups of electrons: the backscattered electrons with energies of more than 50eV, and the so-called true secondaries of less than 50eV energy. The backscattering coefficient, η, is then

$$\eta = i_{bs}/i_p$$

where i_{bs} is the current due to the backscattered electrons.

An important property of a material is the variation of δ and η with primary energy, E_p, known as the yield curve. The general shape of this curve is similar for most materials and is shown in Figure 1.1. δ rises from zero at primary energy zero to a maximum value, δ_{max}, at $E_{p_{max}}$; thereafter falling gradually with increased primary energy. On the other hand, η rises fairly steeply up to $E_{p_{max}}$ but thereafter only very gradually with increased energy.

A qualitative explanation of this behaviour is fairly simple. At low primary energies, the penetration of the incident beam is low so that most of the secondaries are produced near the surface region, where their escape probability is high. As the primary energy increases, the number of collisions producing secondaries also increases; however, the penetration depth of the primaries also increases so that a smaller proportion of secondaries finds its way to the surface region with sufficient energy to escape. Since a large proportion of secondaries produced is of low energy, the effect of the increased depth of origin of the secondaries tends to predominate after a critical energy, $E_{p_{max}}$, at which the penetration depth of the primaries is roughly equal to the average escape depth of the secondaries.

The higher energy secondaries comprising i_{bs} have, of course, a greater average escape depth, which increases together with the penetration depth of the primaries with increase in energy. As a consequence, the δ, E_p curve usually continues to rise very slowly after $E_{p_{max}}$, whereas the η, E_p curve tends to fall.

It follows from the dependence of yield on the penetration depth of the primaries that the yield for a fixed primary energy increases with the angle of the incident beam from normal. There will also be an enhancement of the yield from the velocity component parallel to the surface, since the required scattering angle for the emission of secondaries has been reduced. From the variation of yield with incident angle, Bruining (1936, 1938) was able to calculate the mean depth of origin of secondaries for nickel to be about 30Å.

The variation of yield with incident angle is less for a rough surface than a smooth surface, because the angle of incidence is less well defined. The total yield of a rough surface is also lower than for a smooth one; this is believed to be because of the formation of miniature 'Faraday cages' preventing the escape of the secondaries that are produced (Bruining 1954).

It has also been found (Thomas and Pattinson 1970) that back-scattered primary electrons are far more efficient in producing secondary electrons than incoming primaries. The method used involved the controlled deposition of thin films of a low yield material (aluminium) on to 'high yield' substrates (gold and platinum), and measuring the 'break points' in the δ, E_p and η, E_p curves at various thicknesses of the aluminium overlayer (Holiday and Sternglass 1959). They found that the efficiency of the backscattered electrons in producing secondaries in aluminium varied from about 3 at 2keV to 6 at 1keV primary energy, and that the escape depth of the secondaries was about 50 - 80Å.

The mean depth of origin of secondaries is generally about 50Å as the above examples have shown; consequently secondary emission is predominantly a surface effect. In addition, any surface impurities, while not necessarily directly contributing to the secondary yield of the material, may result in variations in the surfaee work function, drastically affecting the number of secondaries able to escape. It is essential, therefore, for secondary emission studies of surfaces to be

carried out in ultra high vacuum conditions, if results characteristic of clean surfaces are to be obtained.

Quantitative theories of secondary electron yield have not yet been very successful, and there exists a large number of theories, each using a somewhat different working model. The most successful 'theories' such as those of Bruining (1954) and Baroody (1950) are largely phenomenological in nature, but more fundamental theories have not yet provided good agreement with experimental results. Consequently, at present, measurements of yield and backscattering coefficients of materials do not provide much insight into the electronic structure of surfaces, but are of more technological importance.

Far more information is obtained from studies of the energy distribution of secondary electrons, though even in this case the theoretical position is somewhat confused. In view of the brief nature of this discussion of the phenomenon of secondary electron emission particular mention should be made of the comprehensive reviews of Gibbons (1966), Bruining (1954), Kollath (1937) and Hachenberg and Brauer (1959).

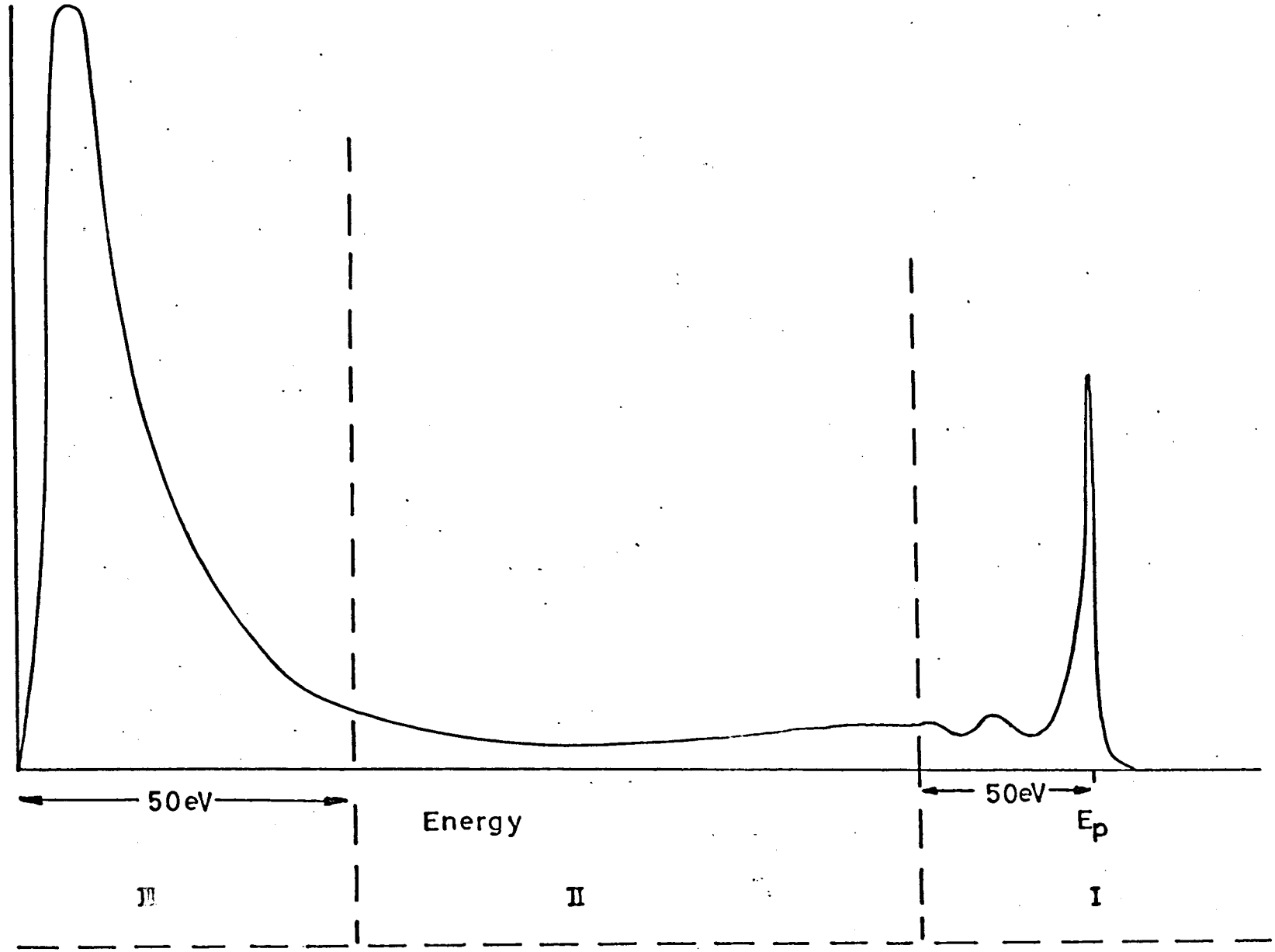

Figure 1.2 Energy distribution of secondaries

1.3 Energy Distribution of Secondaries

1.3.1 Introduction

The general shape of the energy distribution of secondaries reflected from a surface is shown in Figure 1.2. It is evident that there are three areas of interest, which have been labelled I, II and III on the diagram. The large peak in region I contains electrons which have been elastically reflected from the surface; below this in energy are found small peaks, corresponding to reflected electrons which have lost discrete quantities of energy in the excitation of plasmons (Pines 1956) or inter- and intra-band transitions of the lattice electrons. Region II contains comparatively few electrons, and is chosen arbitrarily to extend from an energy of about 50eV to an energy loss of about 50eV from the elastic peak. It is in this section that under high sensitivity, it is possible to locate Auger electrons and also, occasionally, reflected electrons which have suffered an energy loss due to the ionisation of core levels.

The bulk of the secondaries appears in region III, the so-called 'slow' peak. Some Auger electron peaks also occur here, but their identification is complicated by the large background slope. More recently a number of other peaks have also been discovered, whose origins cannot be explained with regard to Auger transitions (Jenkins and Chung 1971, Willis et al. 1971, and this thesis Chapter 6). It would appear that they could possibly result either from plasmon gains

(Jenkins and Chung) or from transitions involving the band structure above the vacuum level (Willis et al.).

To summarise, there are two types of peak observed in the energy distribution of secondaries. The energy loss peaks, most of which are found in region I, occur at fixed energies relative to the primary energy, E_p, and are measured relative to this peak. The second type of peak (such as an Auger electron or "characteristic gain" peak) occurs at a discrete energy independent of primary energy and its energy is measured relative to zero energy.

In the following sections we discuss the energy distribution of secondaries in more detail with particular regard to energy losses, Auger electrons, and energy gains, corresponding approximately to regions I, II and III.

1.3.2 Characteristic energy losses

a) Introduction

Most investigations of the characteristic energy losses of materials have been made by transmission through thin foils, relying on a dispersive electron lens for energy selection. The energy losses observed with this method are usually very strong and narrow, but problems of surface contamination can give rise to ambiguous results. The advantage of this method is that dispersive electron lenses of the Mollenstedt (1949) type may be readily attached to electron microscopes. The targets used for transmission work have to be prepared in the form

of thin self-supporting foils and the primary energies required are many tens of keV.

For measurements with lower primary energies, reflection techniques from solid targets are employed, and it is this method that has been used in the present investigation.

b) Plasmons

Where the valence electrons of the material under investigation from a free electron gas, the observed energy losses for clean surfaces can be readily understood in terms of the plasma oscillation theory of Pines (1956). The predicted plasmon energy is given by the expression $h\omega_p = \hbar(\frac{4\pi ne^2}{m})^{\frac{1}{2}}$ (in c.g.s. units); $n = \frac{V\rho}{A}$ is the density of free electrons, e and m are the electronic charge and (effective) mass, V is the valency, ρ the density and A the atomic weight. Consequently, for free electron metals, the plasmon frequency depends primarily upon the density of electrons in the solid. The effect of the boundary between the vacuum and the solid has been investigated through the dielectric theory by Ritchie (1957) who predicted the occurrence of a surface or lowered plasma loss in the surface region occurring with a frequency $\omega_p/\sqrt{2}$. Further generalisation by Stern and Ferrell (1960) revealed that a thin oxide layer on a metal surface could lower the surface plasma loss to a value $\omega_p/\sqrt{1+\varepsilon}$ where ε is the dielectric constant of the absorbed layer.

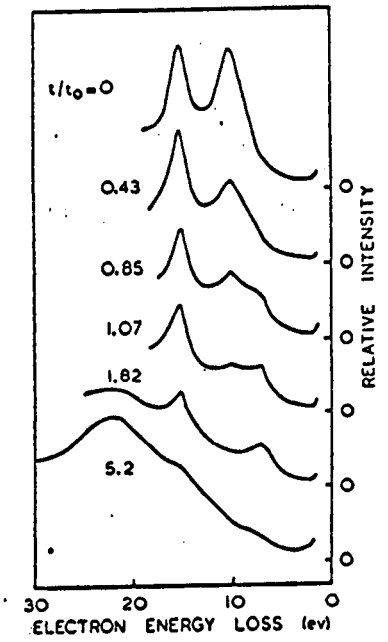

FIG.(a) Portions of the characteristic loss spectra of aluminum in progressive stages of oxidation. The number against each curve is the average value of t/t_0, where t was the elapsed time after evaporation of aluminum and t_0 was the time in which the measured intensity of the plasma loss decreased to half its initial value. All curves are drawn to the same arbitrary linear intensity scale, the zero of which is shown in each case.

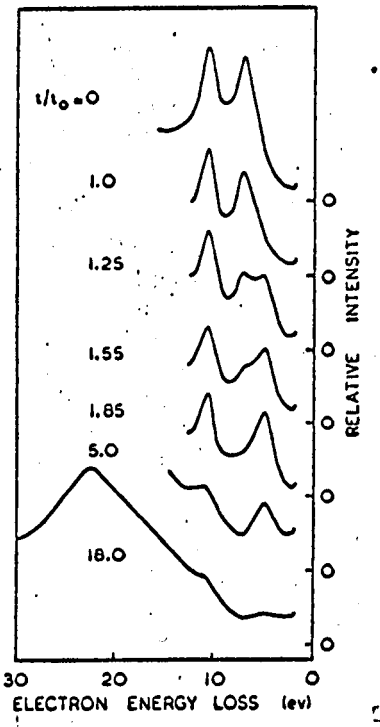

FIG.(b) Portions of the characteristic loss spectra of magnesium in progressive stages of oxidation corresponding to the values of t/t_0 indicated.

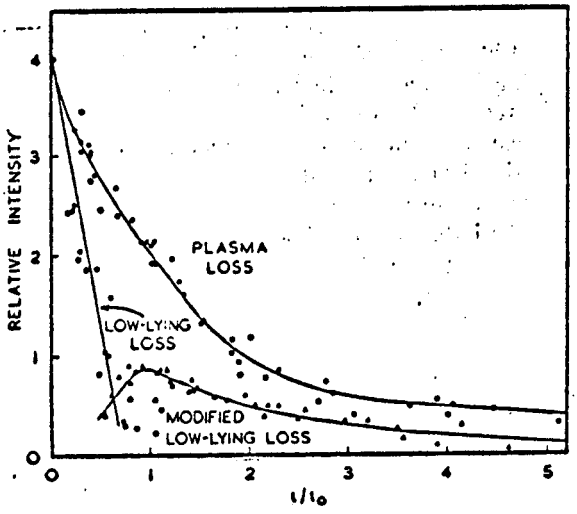

FIG.(c) Intensities of the plasma loss (○), the low-lying loss (●), and the modified low-lying loss (▲) in aluminum as a function of t/t_0. Each intensity measurement was made by subtracting an appropriate background from the observed height of the loss peak.

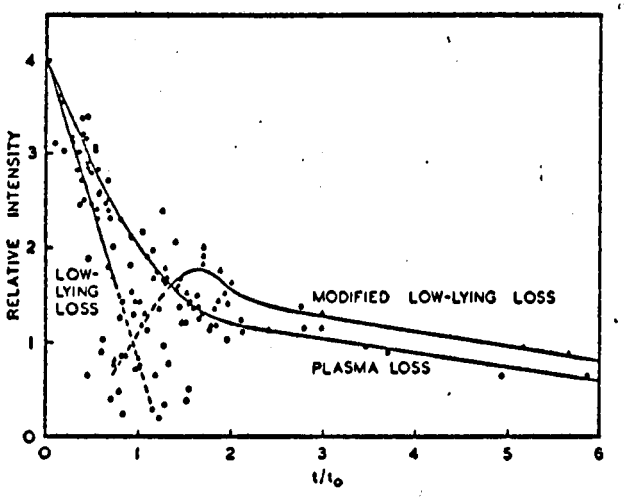

FIG.(d) Intensities of the plasma loss (○), the low-lying loss (●), and the modified low-lying loss (▲) in magnesium as a function of t/t_0. The large scatter in the measurements of the low-lying and modified low-lying loss intensities in the vicinity of $t/t_0=1$ results from each peak appearing on a steep background due to the other peak.

FIGURE 1-3 CHARACTERISTIC LOSS SPECTRA OF Al AND Mg

These theories have provided quite satisfactory explanations of the observed energy losses in the "free electron gas" metals such as aluminium, magnesium and beryllium, both on clean and oxidised surfaces. The characteristic energy losses of aluminium and magnesium were extensively studied by Powell and Swan (1959), using a reflection method and primary energies of from 750 - 2000eV. They were found to consist of multiples and combinations of two fundamental energies, 10.3eV and 15.3eV in the case of aluminium and 7.1eV and 10.6eV in the case of magnesium. Agreement between the observed and calculated values of $\hbar\omega_p/\sqrt{2}$ and $\hbar\omega_p$ for each metal was within 10%.

The dramatic effect of surface oxidation on the energy loss spectra as observed by Powell and Swan (1960) is shown in Figure 1.3. The general behaviour is the same in each case. The first noticeable effect is the attenuation of the surface plasmon loss, followed by the appearance of a modified surface plasmon loss at 7.1eV for aluminium and 4.9eV in magnesium. This behaviour is consistent with the prediction of Stern and Ferrell (1960) on the effects of the formation of a dielectric surface layer of oxide. Powell and Swan were only able to infer that the chemisorbed layer was an oxide layer, but Suleman (1972), using in addition Auger spectroscopy, was able to correlate the changes in the energy loss spectra of aluminium, beryllium and iron with the appearance and disappearance of surface oxide.

The final oxide spectra for both metals can be seen to be very similar with a prominent loss at 22.2eV. This was not identified by

Powell and Swan, but it is probably an ionisation loss of the oxygen 2s level at 24eV. The absence of any plasmon losses for the oxidised metals can be understood by the valence electrons having been "mopped up" by the oxygen, and therefore not being free.

c) Inter- and intra-band transitions

The interpretation of the energy loss spectra for the transition and noble metals is more complex. In the first place, it is not reasonable to consider the valence electrons as a free electron gas, and secondly, since the valency of the transition metals is variable it is not obvious what value to take for V, the number of electrons per atom. It is possible that because of these factors plasmon loss may not always be the predominant energy loss mechanism and that processes involving ionisations of, or transitions between, the outer energy levels of the metal atoms may be more important. These processes of inter- and intra-band transitions are termed single electron excitations as distinct from plasmon production which is a many electron excitation. If E_T be the energy of the transition and E_p the primary energy, the energy of the outgoing electron will be $E = E_p - E_T$. The single electron excitation theory was first proposed by Rudberg and Slater (1936).

It is shown in Chapter 5 that it is possible to explain some of the observed energy losses of the metals silver and copper in terms of the separate excitation of the s and d electrons, particularly if consideration is given to the fact that the electronic mass should be replaced by the appropriate effective mass m*, which will be different

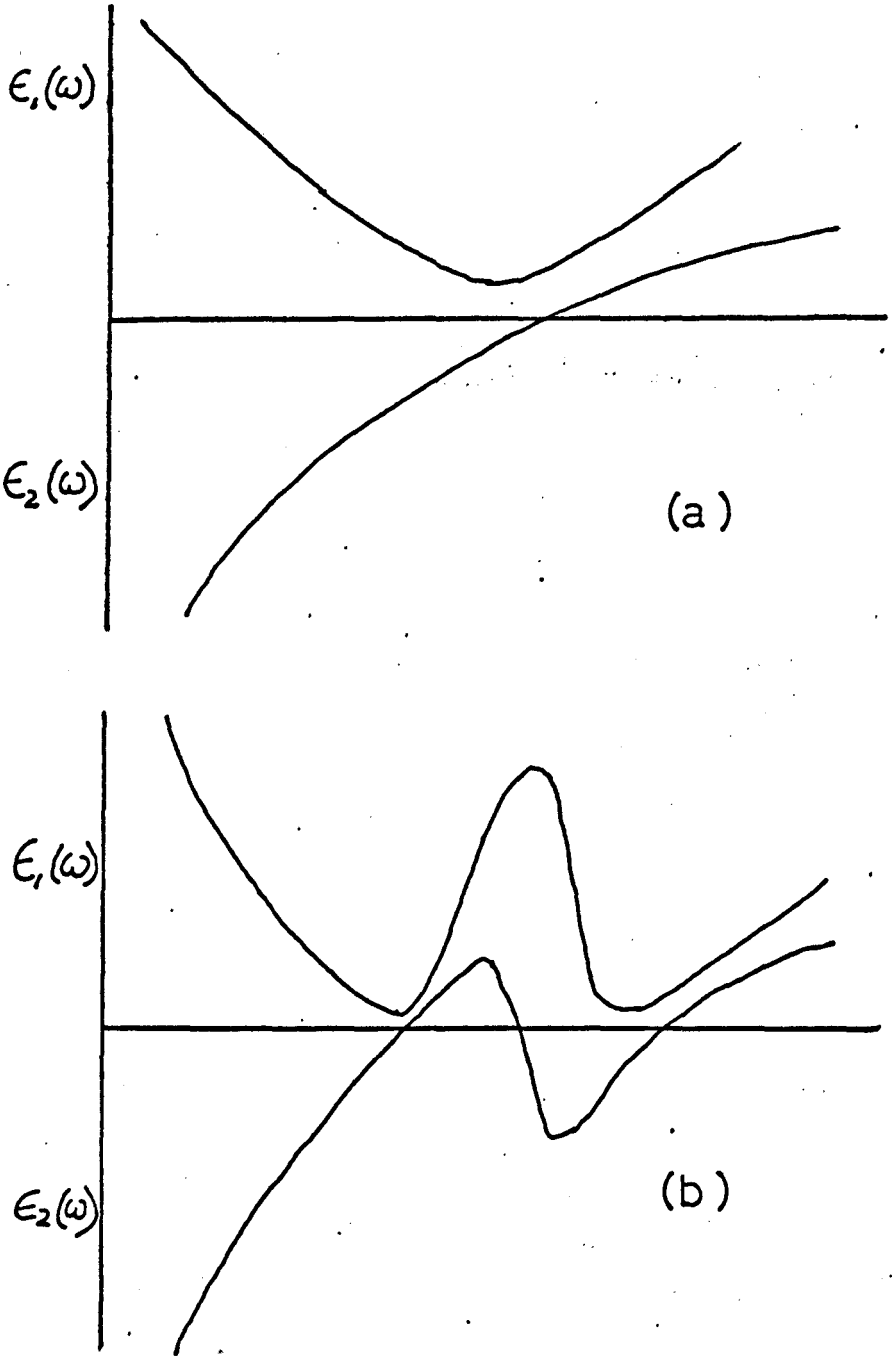

Figure 1.4 Behaviour of complex dielectric constant

the s and d electrons. Joshi (1969) calculated the bulk plasmon energy of copper assuming different effective masses for the s and d electrons, but did not consider a low energy loss of the s electrons alone.

An alternative approach in the case of the transition and noble metals considers the effect of neighbouring interband transitions on the dielectric theory of Nozieres and Pines (1958, 1959), Marton et al. (1955) and others. It is not appropriate to give a rigorous account of the theory here, but an outline of the method as used by Willis (1972) is as follows.

The complex dielectric constant $\varepsilon(\omega)$ is given by

$$\varepsilon(\omega) = \varepsilon_1(\omega) + i\varepsilon_2(\omega)$$

and in a nearly free electron model

$$\varepsilon_1(\omega) = 1 - \omega_p^2 \omega^{-2} + \varepsilon_1^c(\omega)$$

where $\varepsilon_1^c(\omega)$ is the lattice contribution. $\varepsilon_2(\omega)$ which represents the absrrption is very small and varies as

$$\varepsilon_2(\omega) = \omega_p^2 \gamma \omega^{-3}$$

where γ is the collision frequency. (See for example Hodgson 1970).

The schematic behaviour of ε_1 and ε_2 with frequency is shown in Figure 1.4(a). The major contribution to ε is real and negative at low frequencies and positive at high frequencies. The frequency ω_o at which $\varepsilon_1(\omega)$ passes through zero is given by

$$\omega_o^2 = \omega_p^2\left[1 + \varepsilon_1^c(\omega_o)\right]^{-1}$$

The presence of an interband transition of a frequency near ω_o can distort the $\varepsilon_1(\omega)$ function as shown in Figure 1.4(b) causing $\varepsilon_1(\omega)$ to cross the axis more than once. Plasma oscillation can then occur at these frequencies ω_1 and ω_2 either side of ω_o at which $\varepsilon_1(\omega)$ crosses the axis and $\varepsilon_2(\omega)$ is small.

ε_1 and ε_2 are related to the real and imaginary parts of the refractive index, n and k; hence measurements of n and k as a function of photon energy $h\omega$ can yield useful information on the characteristic loss spectrum.

The theoretical position with regard to the interpretation of characteristic energy losses from transition and noble metals remains uncertain, so that the processes assigned to the observed losses are no more than tentative in many cases. The situation has been more complicated until recently since much of the experimental data has not been reliable because of the effects of unknown contaminants. Careful measurements in an ultra high vacuum environment using current cleaning and surface monitoring techniques help to overcome these difficulties.

d) Ionisation losses

If an incident electron interacts with a bound electron and one of the electrons ends up with energy near the Fermi level, the other electron may be ejected from the solid with an energy corresponding to the primary energy minus the binding energy of the level involved.

For this electron to be detected as a characteristic energy loss, there must be an enhanced transition probability near the ionisation potential of the level. An ionisation loss is really a special case of an inter-band transition loss. Bishop and Riviere (1970) reported the observation of ionisation losses, and warned that they can be confused with Auger electron peaks if spectra with different primary energies are not taken. Gerlach, Houston and Park (1969, 1970) used special cross modulation techniques in the identification of ionisation losses, and pointed out the possible use of the technique as a direct measure of electron binding energies. Ionisation loss spectroscopy is, however, only successful for those metals and levels where there is an enhanced transition probability near the ionisation threshold. These elements usually have a high fluorescent yield and may also be suitable for examination by appearance potential spectroscopy (Park, Houston and Schreiner 1970).

e) Summary

The plasmon loss theory of Pines and others has proved very successful in interpreting the characteristic energy losses from metals where the valence electrons form a free electron gas. In other cases the explanation of the observed energy losses is more difficult and the effect of inter- and intra-band transitions has to be taken into account. In certain favourable cases ionisation losses may be used for the study of the binding energies of surface atoms. Contamination can have a pronounced effect, particularly on surface plasmon losses, and great

care is necessary in the examination of the loss spectra of reactive surfaces, to ensure that the results obtained are characteristic of the clean surface.

1.3.3 Auger spectroscopy

a) Introduction

The discovery by Auger (1925) of the process of electron emission that now bears his name was as a result of the interaction of X-rays with atoms. It was Haworth (1935) who first attempted to identify small peaks in the energy distribution of secondary electrons with processes involving transitions between the energy levels of the parent atoms, and Lander (1953) who correctly identified the peaks as due to Auger emission. Despite the fact that he predicted that "the characterstic peaks have sufficient intensity to make the technique interesting as a means of surface analysis", the apparent lack of sensitivity at that time precluded further studies. Harrower (1956) also observed Auger electrons in the secondary electrons from molybdenum and tungsten, but it was not until the breakthrough of Harris (1968), who differentiated the energy distribution function electronically, that interest revived.

Another significant advance was made by Weber and Peria (1967) who demonstrated that the display type LEED system could be readily modified for obtaining differentiated Auger spectra. It is perhaps because so many of these instruments were in use at that time that the literature on Auger spectroscopy has 'mushroomed' at such a great rate

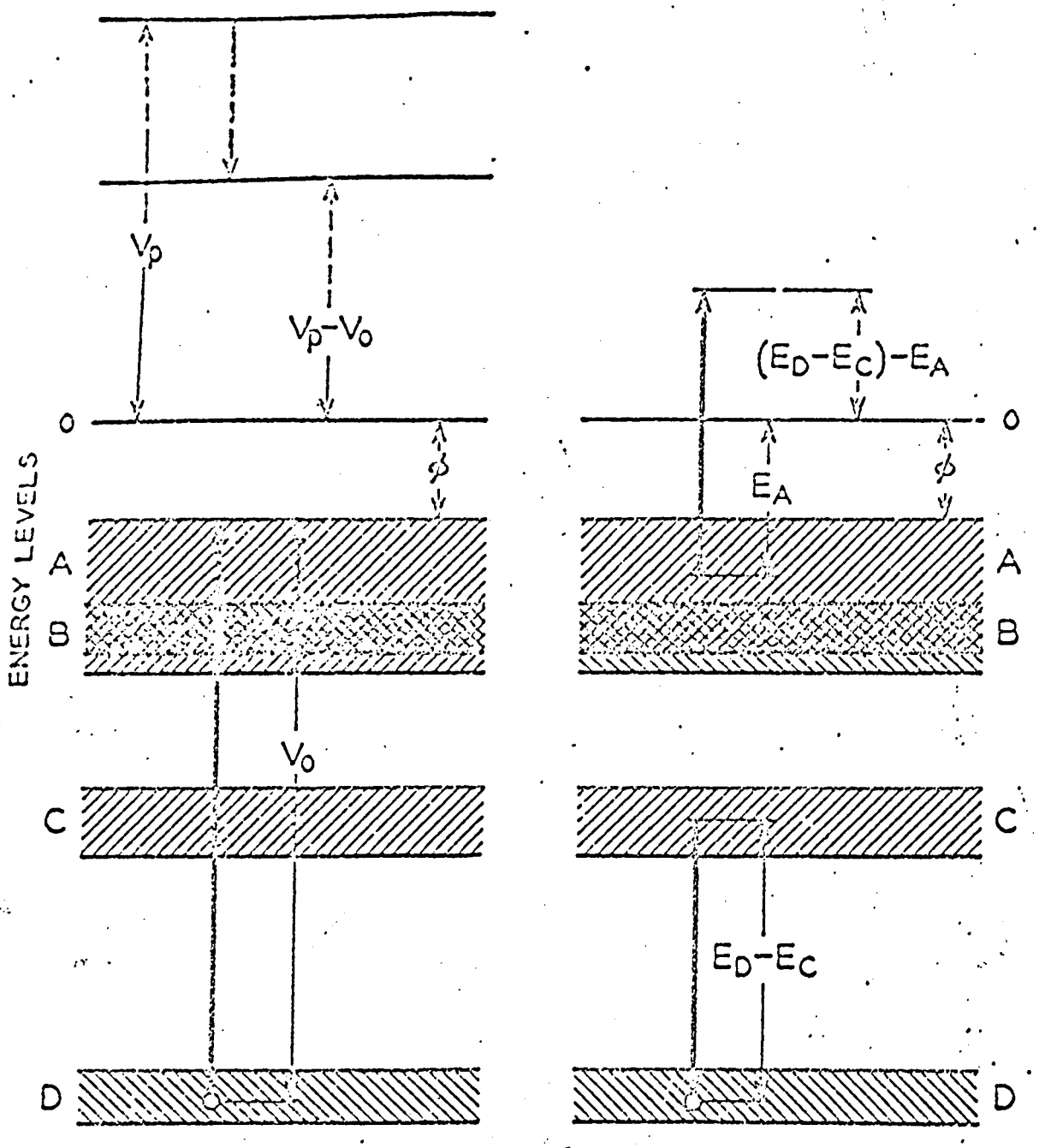
ENERGY LEVELS
V_p
$V_p - V_0$
0
ϕ
A
B
V_0
C
D
PRIMARY LOSING ENERGY TO AN ELECTRON IN BAND D
(a)
$(E_D - E_C) - E_A$
E_A
AUGER PROCESS
(b)

Figure 1.5

in a few years. Excellent comprehensive reviews on Auger electron spectroscopy have been made by Riviere (1968), Palmberg (1969), Chang (1971) and others.

b) The Auger process

When a material is irradiated with X-rays or electrons of a sufficient energy, some of its energy levels become ionised as is shown in Figure 1.5(a): a hole has been created in band D, leaving the atom in an excited state. The atom can then relax by absorption of an electron from an upper level, shown in Figure 1.5(b) as an electron from band C dropping to fill the vacancy in D. The resulting energy $(E_D - E_C)$ is then available for the emission of a photon, if the selection rules permit. Alternatively the energy may be transferred to another electron (from band A) which will be released with an energy given approximately by

$$E_{DCA} = E_D - E_C - E_A$$

Should the 'up' and 'down' electrons have originated in the same band, B, then the energy is given by

$$E_{DBB} = E_D - 2E_B$$

The overall process is called the Auger emission process, and the resulting electrons termed "DCA" and "DBB" Auger electrons respectively.

c) Calculation of Auger current

In order to calculate the magnitude of Auger current to be expected, Bishop and Riviere (1969) have split the Auger process into its constituent events. Firstly it is necessary to estimate the probability of photon production. The method of Auger spectroscopy uses primary ionisations of up to 3keV, which restricts the investigation to the outer few shells of most elements. In this case it may be shown that the probability of photon emission is about 0.03, for most metals, so that it can be assumed that most ionisations below 2keV produce Auger electrons.

The first step in the Auger process is the ionisation of an inner level, and the cross section for ionisation must first be considered. Bishop and Riviere (1969) suggested that the modified Born approximation of Worthington and Tomlin (1956) for X-rays should prove adequate, in the absence of more suitable quantum mechanical expressions.

The numerical form of this expression for the cross section Φ is given as:

$$\Phi E_c^2 = 1.3 \times 10^{-13}.b.\frac{1}{U}.\ln\{4U/[1.65 + 2.35\exp(1-U)]\} \text{ cm}^2(\text{eV})^2$$

where E_p is incident electron energy

E_c is the critical ionisation potential for the level

$U = E_p/E_c$

$b = 0.35$ for a K level

0.25 for a L level.

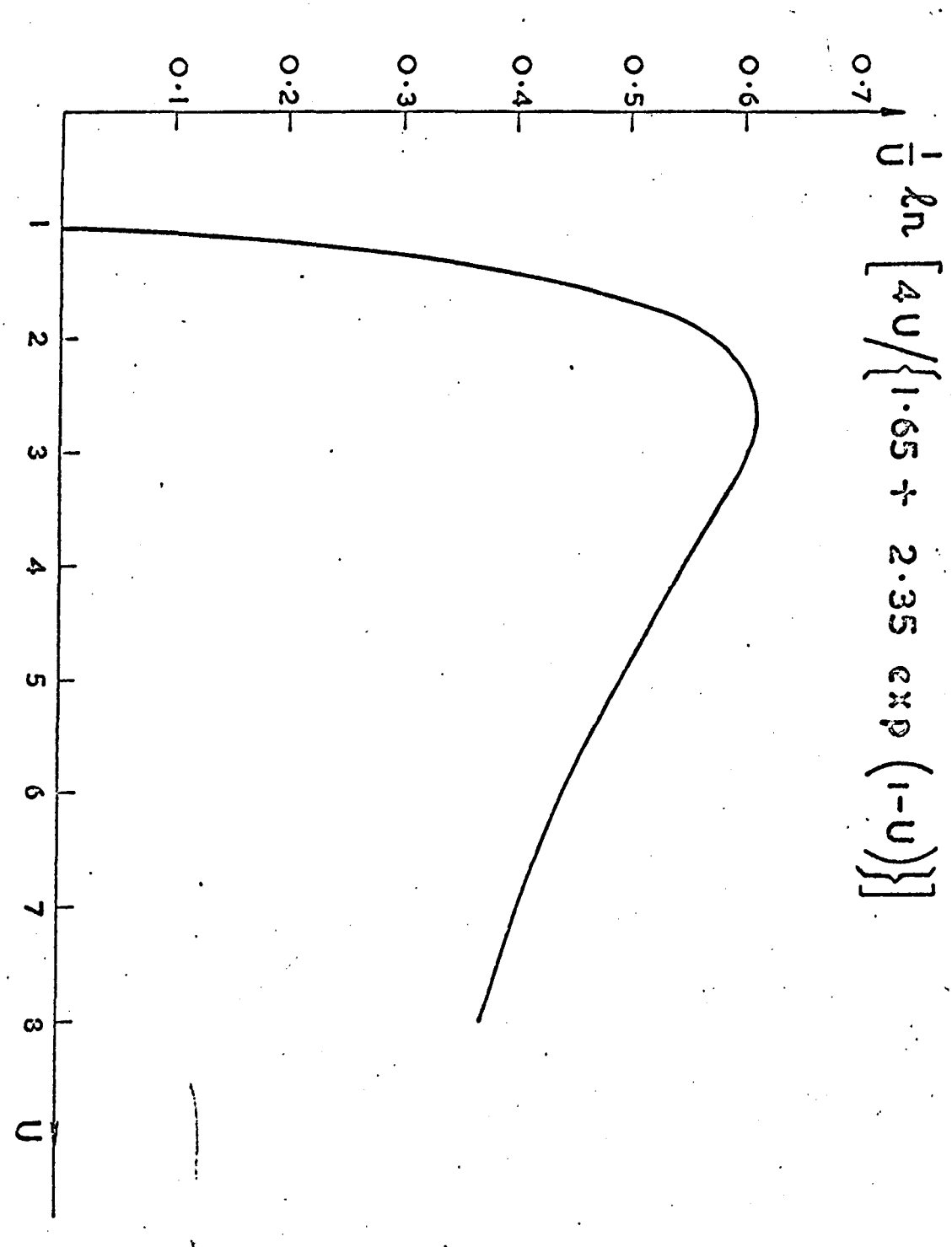

Figure 1.6 Primary ionisation cross section

This quantity is shown graphically as a function of U in Figure 1.6. It rises steeply from zero at U = 1 as required and maximises at a value of U = 2 to 3, then decreasing slowly. The main error in this expression is that it neglects the contribution from backscattered electrons to the ionisation; we saw earlier in 1.2 that backscattered electrons are very efficient in producing secondaries, and presumably they are also efficient in producing ionisations. The probable effect of the inclusion of backscattered electrons into the expression is to move the maximum Φ to slightly higher values of U and lessen the fall off with increasing U. The form of the expression for the ratio of Auger current i_{Auger} to primary current i_o for a thin film of one monolayer is given by Bishop and Riviere as:

$$i_{Auger}/i_o = N(\frac{\Omega}{4\pi})\ r\ \text{cosec}\ \phi\ \Phi\ (U)$$

where N is the number of atoms per square cm of surface,

Ω the solid angle subtended by the analyser,

r the backscattering factor and

and ϕ the angle of incidence of the primary beam.

Inserting reasonable figures into the above expression leads to a value for i_{Auger}/i_o of about 10^{-5} for normal incidence. This may be increased by nearly an order of magnitude for a smooth surface and near grazing incidence because of the cosec ϕ dependence.

The fact that the Auger current is at best about 0.01% of the primary current illustrates the difficulty experienced by the early workers, who were attempting to detect these small peaks. The steady background current in the energy distribution varies from about 1% of i_o in region II of Figure 1.2 to about 100% of i_o in region III. Any attempt to increase the amplification of the peak merely alters the background level by an equivalent amount, eventually saturating the detection equipment. It should be noted, however, that over the majority of region II the background is only slowly varying, so that by differentiation of the energy distribution it is possible to reduce the background substantially enabling much higher gains to be employed. It was the realisation of this fact by Harris (1968) which formed the basis of the technique of Auger spectroscopy.

d) Calculation of the Auger energy

From the diagram of the Auger process in Figure 1.5b it would appear that the calculation of emitted Auger energy is quite simple; true, it is possible to obtain an approximation to the observed energy using the simple formula:

$$E_{DCA} = E_D - E_C - E_A$$

but increased accuracy is obtained if more consideration is given to the processes involved.

Firstly the energy of the outgoing Auger electron is decreased by the work function of the target material; however the measured energy is

increased by the contact potential difference between the target and analyser leading to:

$$E_{meas} = E_{DCA} - \phi_T + (\phi_T - \phi_A)$$

$$= E_{DCA} - \phi_A$$

Thus the work function correction is independent of the target material and depends only on the analyser, which is (hopefully) constant for any particular apparatus.

The binding energies of electronic energy levels are measured with the atom in a singly ionised state. Either the energy required to ionise a particular level is measured by photoemission spectroscopy or X-ray absorption spectroscopy, or the energy difference involved in moving a vacancy between two levels is measured, as in X-ray emission spectroscopy.

The final state of an Auger emission, however, leaves an atom doubly ionised, so the effect of this is to alter the energy levels in a way which is not readily calculable. A good approximation to the energy is obtained by using for the energy of the outgoing electron the energy level of the element of next higher atomic number (Burhop 1952, p.75), so that for atomic number Z

$$E_{DCA}(Z) = E_D(Z) - E_C(Z) - E_A(Z+1)$$

Chung and Jenkins (1971) criticised the above expression for $E_{DCA}(Z)$, arguing that since the transitions E_{DCA} and E_{DAC} are quantum mechanically

identical, a more rigorous formula could be written as:

$$E_{DCA} = E_{DAC} = E_D(Z) - \tfrac{1}{2}\left[E_C(Z) + E_C(Z+1)\right]$$

$$- \tfrac{1}{2}\left[E_A(Z) + E_A(Z+1)\right]$$

In most cases, however, the "Burhop" formula gives almost as good (or bad!) an agreement with experimental values as the "C & J" formula, as we have shown in Chapter 4, particularly when a realistic work function correction for the analyser is made.

e) Chemical effects

Where one or both of the final vacancies of an Auger process arise in the valence band, considerable changes can occur in the energy and width of the Auger line when the parent atom is in different chemical environments. It is well known that the binding energy of core electrons in atoms is shifted when the charge state of the atom is changed, and also that changes also occur in the 'shape' of the density of states of the valence band. Measurements of these shifts in energy have been made for many years by the technique of soft X-ray emission spectroscopy, but have been rather hard to interpret because of the difficulty of locating the Fermi level in many cases.

This difficulty has been largely overcome in ESCA measurements of high precision where the determination of changes in binding energy has produced a valuable tool for the identification of oxidation states in compounds.

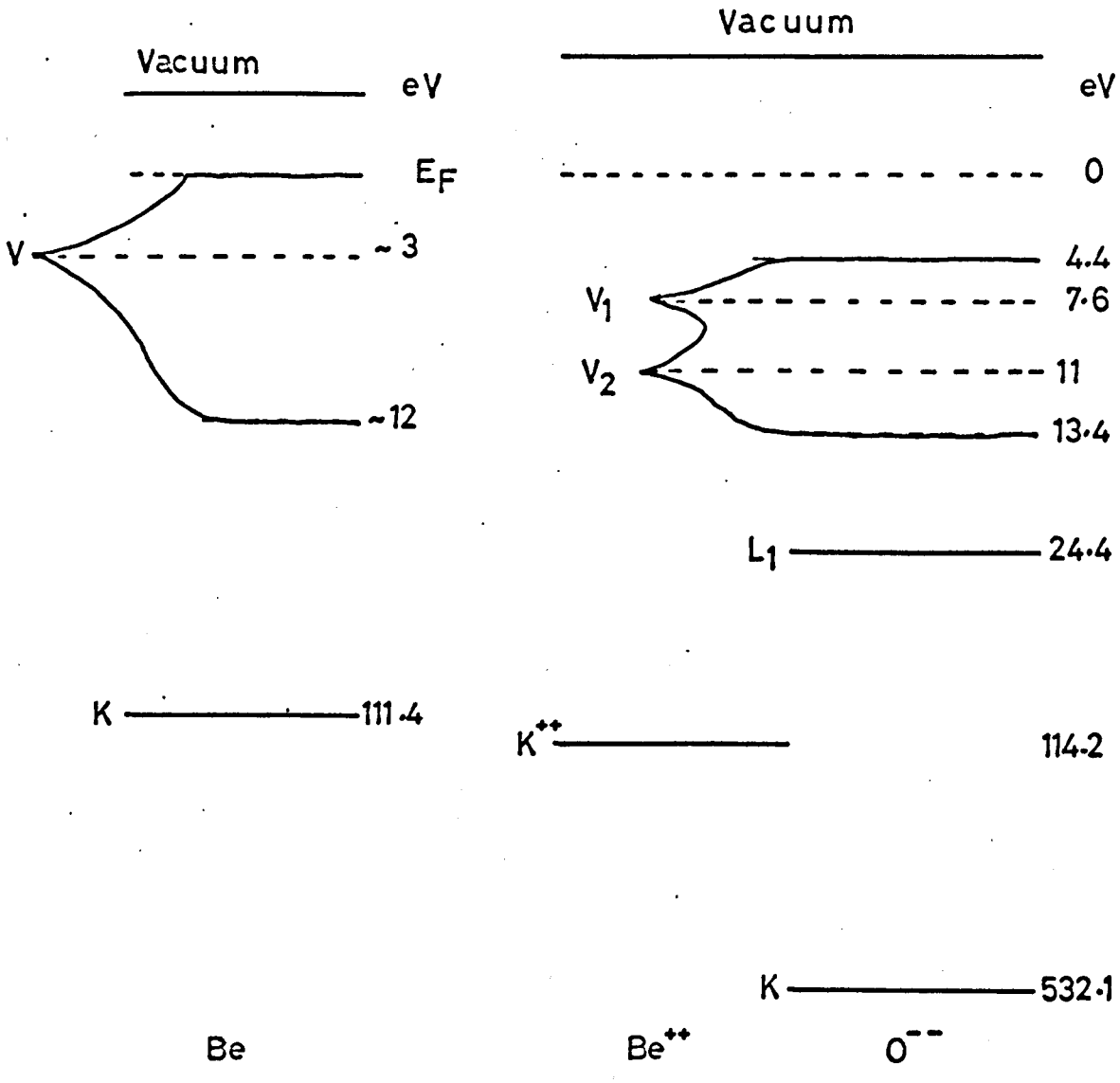

Figure 1.7 Energy band diagram for Be and Be O

X-ray measurements have generally shown only small shifts since it is the difference between two levels which is measured, and these levels will probably have shifted by similar amounts. In Auger spectroscopy the difference between three levels is measured, so that the shifts observed should be closer to the observed ESCA shifts, though the interpretation is somewhat more complex.

Suleman and Pattinson (1971) observed a large chemical shift on oxidation for the KVV Auger transition of beryllium of 10eV, and a shift of 13eV in the $L_{2,3}VV$ line of aluminium. These shifts were too large to be explained purely on the basis of small shifts in the energy levels of the elements, and furthermore Be^{++} has only two electrons per atom, which would make a simple Auger process seem impossible!

The interpretation of these peaks involves cross transitions between the Be^{++} (or Al^{+++}) levels and the O^{--} levels shown diagrammatically in Figure 1.7 for the case of beryllium from Suleman (1972).

The main beryllium peak observed before oxidation is at 104eV and the simple calculation E_K - 2V gives a value 105.4eV. It is not easy in this case to make a "Z+1" correction for the ionized state of the atom, but it would tend to increase the binding energy of the final electron and so reduce the calculated Auger energy. This shift is perhaps implied since no work function correction (which would have the opposite effect) has been made.

After the oxidation the Be K shell shifts downwards in energy by about 3eV and there are two peaks in the density of states of the valence

band at about 7.6 and 11eV, with an average population of one electron in each. The calculated new $K^{++}V_1V_2$ Auger transition would be at 95.6eV, compared with the value of 94eV which was measured.

Other small peaks in the observed spectrum of oxidised berylloum could be correlated with cross transitions of the type $K^{++}L_1V$ between the beryllium, oxygen, and common valence band levels.

Haas, Grant and Dooley (1971) also discussed the shifts in Auger lines of Mo (110) Nb (110) and Ta (110) with oxidation, and also examined the shape of the KVV carbon peak in different chemical environments, identifying different peak shapes for carbon as adsorbed CO, a carbide, and diamond. Small chemical shifts will become more readily detected when more modern high resolution energy analysers are in general use.

f) Fine structure

Studies of the fine structure of individual Auger transitions have been limited in many cases by the resolution of the equipment used, either as a result of poor instrumental resolution or the need for a large modulation amplitude for adequate sensitivity. However the future for such studies looks very rosy with the development of the high resolution high sensitivitycylindrical mirror spectrometer of Palmberg, Bohn and Tracy (1969) and variants thereof.

There are a number of causes of the observed fine structure in Auger spectra. Where the Auger transition involves the valence band, small satellite peaks may well reflect peaks in the density of states of the valence band; other interpretations can sometimes be made involving

characteristic gains and losses of the Auger electrons (Suleman and Pattinson 1971 and this thesis, Chapter 4).

Jenkins and Chung (1971) claimed a degree of correlation between energy loss peaks, low energy "gain" peaks and satellites around observed Auger peaks on a copper surface; comparisons with their work are given in Chapters 4, 5 and 6. Consideration should also be given to configurational effects, as was pointed out by Seigbahn et al. (1969). The final state of an Auger transition leaves an atom with two holes. If these are in the same shell, then the different final state configurations will have different energies. This was illustrated par excellence in the case of the X-ray induced Auger spectra of the noble gases given by Seigbahn et al. (1969), where the splittings observed under high resolution correlated almost exactly with those calculated for the configurational states involved.

In attempting the interpretation of the fine structure around Auger peaks, life is complicated by the number of possible mechanisms which could give rise to this structure: structure in the valence band, characteristic gains and losses, and configurational effects. This particular field is still relatively unexplored, and the use of new instruments of high sensitivity and resolution opens up an area of tremendous interest.

g) Summary

Much important information can be gained from the study of Auger electron spectroscopy. First and foremost it has proved to be the

only reliable tool for surface chemical analysis. Weber and Peria (1967) by the controlled evaporation of caesium on to clean silicon claimed sensitivities of 1% of a monolayer and a linear dependence of Auger peak height on surface coverage up to a monolayer. The work of Palmberg and Rhodin (1968) involved controlled evaporation of silver on gold, from which escape depths of only 4Å for the 72eV peak and 8Å for the 362eV peak were determined.

Although these results were taken during the early development of the technique, they serve to illustrate the high sensitivty and extreme surface nature of the Auger analysis, as compared to other techniques. It is thus an ideal contamination monitor for such studies as LEED, characteristic energy losses etc., where a characterised surface is essential. Certainly LEED theory has benefitted greatly from the correlation of patterns and surface chemistry.

The other aspect of Auger spectroscopy is more academic but just as valuable. Studies of fine structure and satellite peaks can give tremendous insight into the basic interactions involved and provide stimulating fodder for theoreticians.

At the present time quantitative surface analysis is limited to a few well defined systems, where previous calibrations have been made using other techniques; theoretical calculations of Auger current are as yet only approximate.

1.3.4 Characteristic energy gains

This section deals with region III of the secondary electron energy distribution. The large peak near zero energy can be explained on the "cascade" theory of Wolff (1954). A primary electron will make several collisions inside the solid creating many secondaries, and the 'slow' peak would be a delta function at zero energy but for the effect of the work function of the material.

Recently, small peaks have been observed superimposed on the slow peak (Willis et al. 1971) and they have been accentuated by differentiation of the energy distribution function (Jenkins and Chung 1971 and this thesis, Chapter 6). These peaks are observed to be reasonably independent of primary energy and incident angle though some changes in amplitude have been noticed. At present there are two possible explanations for these peaks, involving plasmon gain processes and conduction band states above the vacuum level.

Just as an electron in a solid can lose energy by the excitation of a plasmon it is conceivable that an electron can also gain energy as a result of the absorption of a plasmon. It may then be emitted from the solid with its initial energy plus the plasmon energy. The most likely initial energy is not (as Jenkins and Chung suggested) the slow electron peak energy, but rather a peak in the density of states of the valence band.

The alternative explanation put forward by Willis et al. involves direct (optical) transitions between critical points in E, K space.

If calculations of the energy bands of metals are made, it is found that high symmetry points exist above the vacuum level. It is possible that incoming electrons can excite electrons into these high energy states by direct transitions. These states correspond to "allowed" energy levels in the solid where the electrons possess sufficient energy to escape, if they are travelling in the right direction. Two mechanisms are then possible: the electrons in these states may be emitted with an energy corresponding to their initial state; or they may relax via a direct transition to another symmetry point, emitting an Auger electron from another level.

It is not possible to distinguish at present between these two explanations with any confidence, but the apparent lack of real correlation between the observed energy loss and energy gain spectra observed in Chapters 5 and 6 seems to imply that different processes are involved in the two cases. It thus would seem preferable at present to assign the characteristic gain peaks to conduction band states rather than plasmon gains.

The plasmon gain theory does, however, give an adequate explanation of the satellite peaks found above certain Auger peaks; e.g. Suleman and Pattinson (1971) for the case of aluminium. The mechanism envisaged in this case involves the absorption or emission of a plasmon by the Auger electron. The work of Jenkins and Chung attempted to correlate the loss and gain peaks observed in the case of copper, but the number of peaks which are seen in the slow peak region seems to

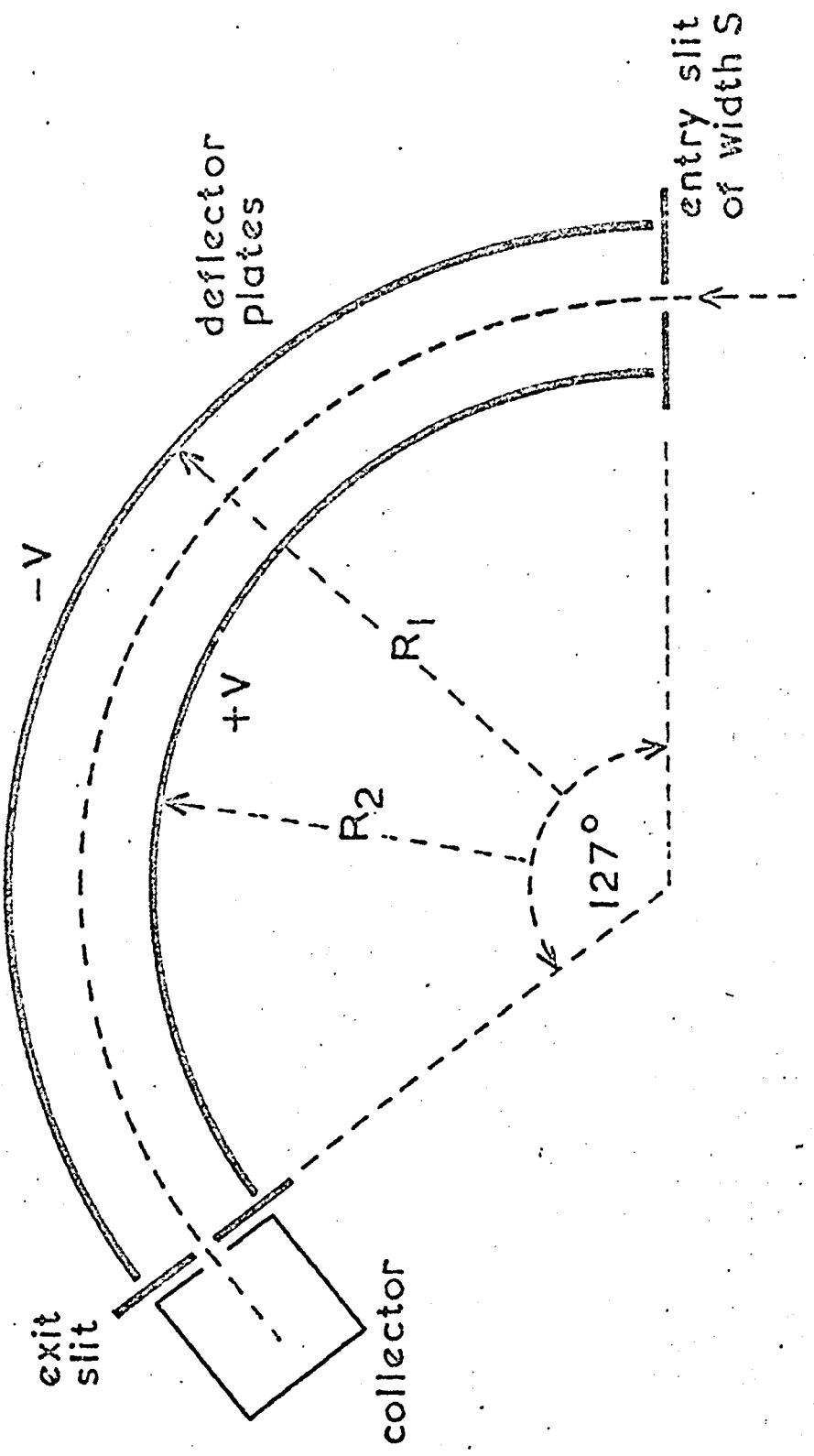

Schematic diagram of the 127° analyser

Figure 1.8

fit in more readily with the large number of possible optical transitions. Waths and Mathieu (1972) postulated a somewhat different plasmon gain process for the case of Auger electrons, involving the dymamical screening by the conduction electrons of the core hole created by the primary ionisation. By a suitable choice of hole and plasmon lifetime they were able to obtain a similar ratio between the plasmon gain, plasmon loss and main Auger peaks as found by Suleman and Pattinson (1971).

1.3.5 Energy analysers and detection methods

a) Introduction

In this section we describe the more commonly used electron energy analysers. No mention is made of magnetic spectrometers, though these were the type used for the early work of Farnsworth (1925). Two main kinds of energy analyser are considered, the "high pass" retarding field, and the electrostatic velocity type. A brief mention is then made of the detection system required with each type of analyser.

b) 127° electrostatic analyser

The early work of Harris (1968) was done using an electrostatic sector analyser similar to the one developed by Hughes and Rojansky (1929) and shown schematically in Figure 1.8.

If V is the applied deflecting potential on the plates of radii R_1 And R_2, then electrons with an energy corresponding to V_D will be refocussed at the exit slit if

$$V = V_D \ln (R_1/R_2)$$

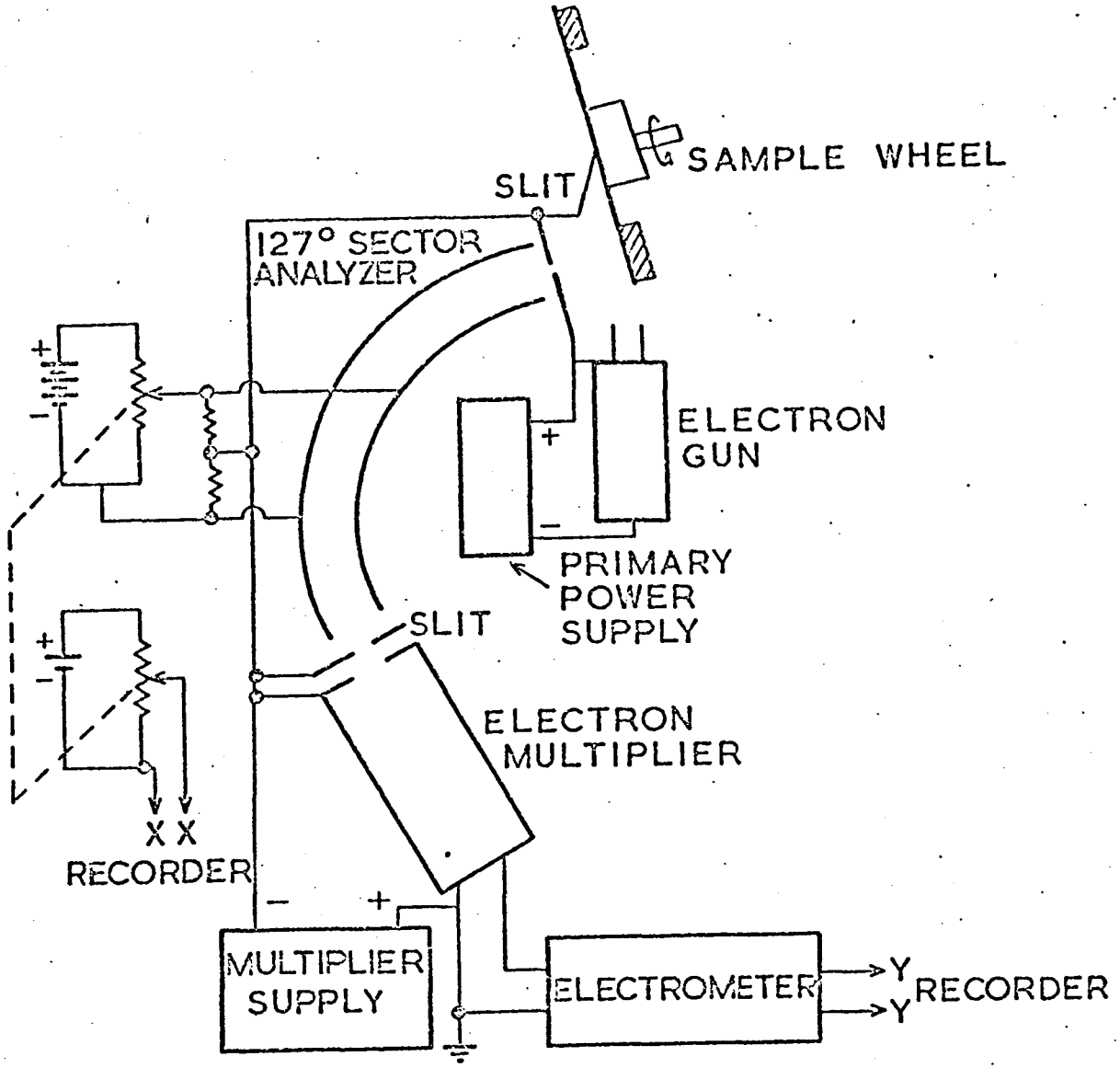

Figure 1.9

Experimental arrangement of Harris (1968)

It has been shown that the resolution and refocussing are optimal at an angle between the entrance and exit planes of $127^{\circ}17'$. Hence, this analyser has become known as the "127° Analyser".

For a reasonable transmission, the slit widths have to be set to give a resolution of about 1%; the low collection angle Ω, means that the overall sensitivity of the device is quite small, and an electron multiplier is required for an adequate signal.

The circuit arrangements used by Harris (1968) is shown in Figure 1.9. The d.c. output of the analyser yields the energy distribution directly, and by a.c. modulating the deflector voltage and detecting the a.c. component of the collected current, the differential of the energy distribution is readily obtained.

c) Retarding field analyser

Auger electron spectroscopy using a modified LEED system as an energy analyser was first carried out by Tharp and Scheibner (1967). They obtained the energy distribution curve by the technique of electrical differentiation of the retarding field plot, in which a small perturbing a.c. voltage is applied to the retarding grid and the a.c. component of the collected current detected in a manner similar to that described by Leder and Simpson (1958). Subsequently Weber and Peria (1967) and Palmberg and Rhodin (1968), by a further differentiation of the energy distribution obtained much greater sensitivity for Auger spectroscopy.

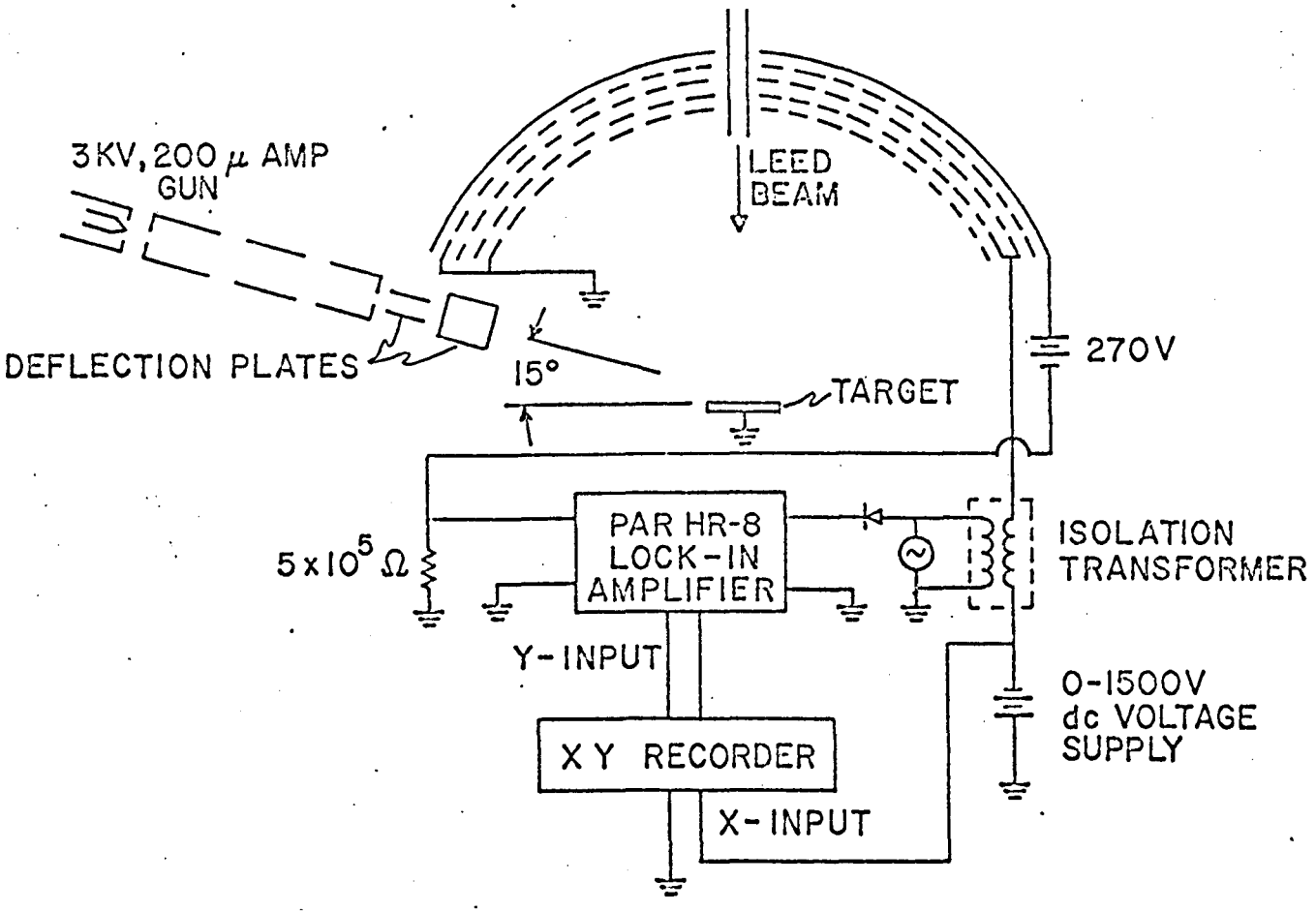

Retarding field analyser of Palmberg and Rhodin (1968)

Figure 1.10

The arrangement used by Palmberg and Rhodin is shown in Figure 1.10. The inner grid of the LEED optics is convected to target potential, the middle grid to a source of variable d.c. and the outer grid is also earthed, to reduce the capacitative pick-up between the grid and collector. The secondary current is collected on the specially treated conducting fluorescent screen used for the LEED display, which is maintained a few hundred volts positive to reduce secondary emission and charging effects.

If the d.c. voltage applied to the retarding grid by V_R, then an electron with energy corresponding to V will just be transmitted if it is travelling radially and $V = V_R$. The spherical surface of the grids is not an equipotential surface because of the potential variation between the grid wires. Calculation by Taylor (1969) based on the work of Liebmann (1947) showed that this problem was so severe as to degrade the resolution of the retarding field analyser to about 2%, with the mesh sizes and grid separations in common use. This problem was overcome by Palmberg (1968), who used two retarding grids separated by a small distance.

Taylor also pointed out that as the electrons pass through the inner grid from the field-free region to the retarding field region they will suffer a divergence at each of the cells of the mesh; this can be minimised by the use of fine mesh and by employing an inner grid radius of about half the mean radius of the retarding grids.

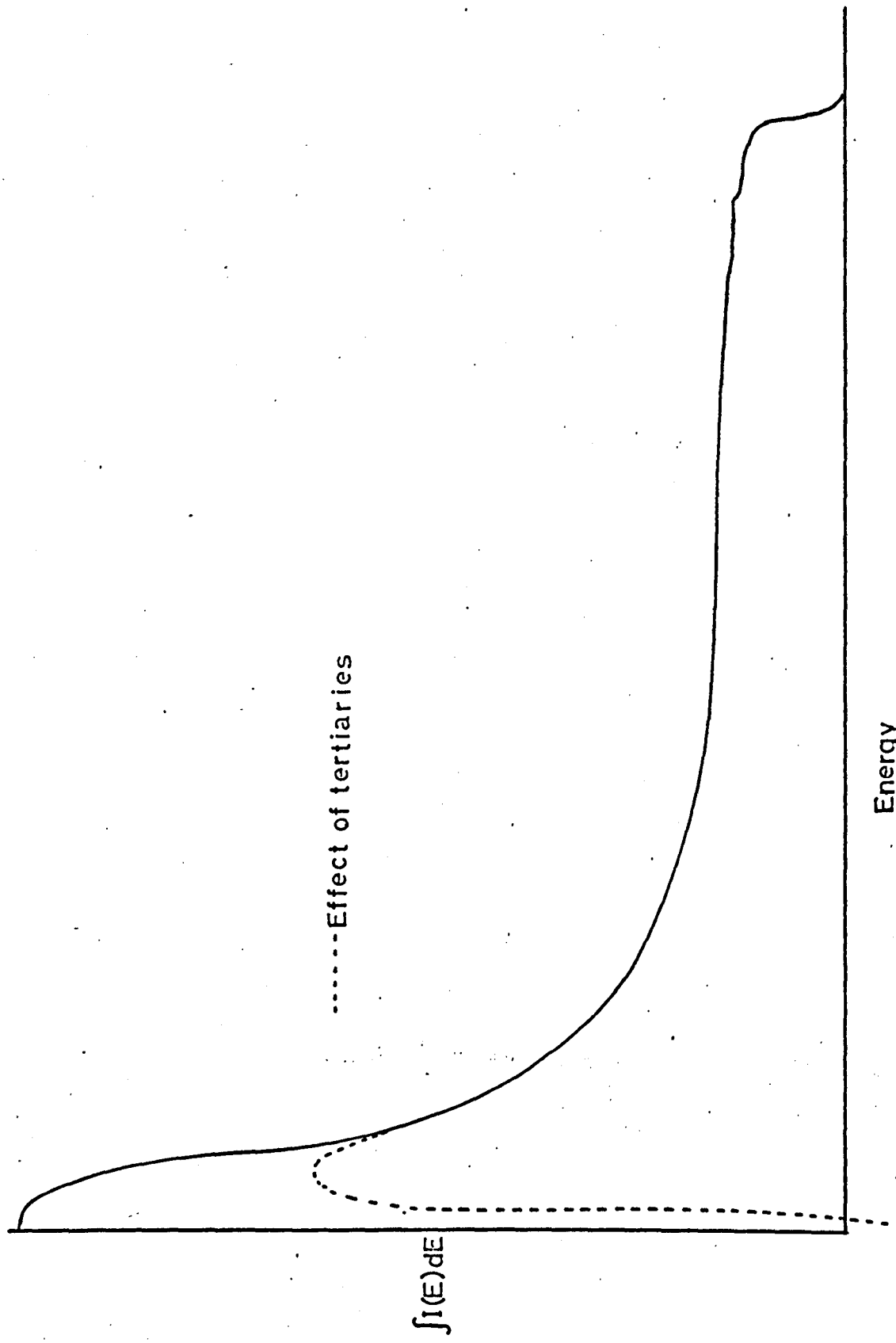

Figure 1.11 Transfer characteristic of a retarding field analyser

Taylor demonstrated the improvement in resolution obtained with these modifications on the shape of a 1keV elastic peak in his apparatus. For the "single grid" analyser the width of the peak was 24eV and it appeared at about 1025eV. When two retarding grids were used the width decreased to 5eV (0.5%) and the peak position moved to 1000eV; the amplitude was also increased by a factor of about 3. When the radius of the inner grid was reduced to its optimum value the resolution improved to better than 0.3% (3eV) and the amplitude of the elastic peak increased by a further factor of about 2.5.

Since the early work of Palmberg and others, retarding field analysers have become widely used as Auger spectrometers in combination with LEED systems. Because, however, the resolution of these devices can vary by as much as an order of magnitude, and instrumental "peak shifts" of up to 3% can occur with "single grid" analysers, much care has to be taken in comparing the results of different workers in the field.

In contrast with the 127° analyser, the retarding field device is a "high pass" velocity filter. The d.c. output, or retarding plot, then corresponds to the integral of the energy distribution from the voltage under consideration up to the elastic peak. A schematic retarding field plot, (corresponding to the integral of Figure 1.2) is shown in Figure 1.11. The dotted line shows the effect of secondary electron emission from the collector; at low values of retarding grid potential (below 50V) these secondaries can find their way back to the target reducing the collected current. A positive collector bias ensures that all the (low

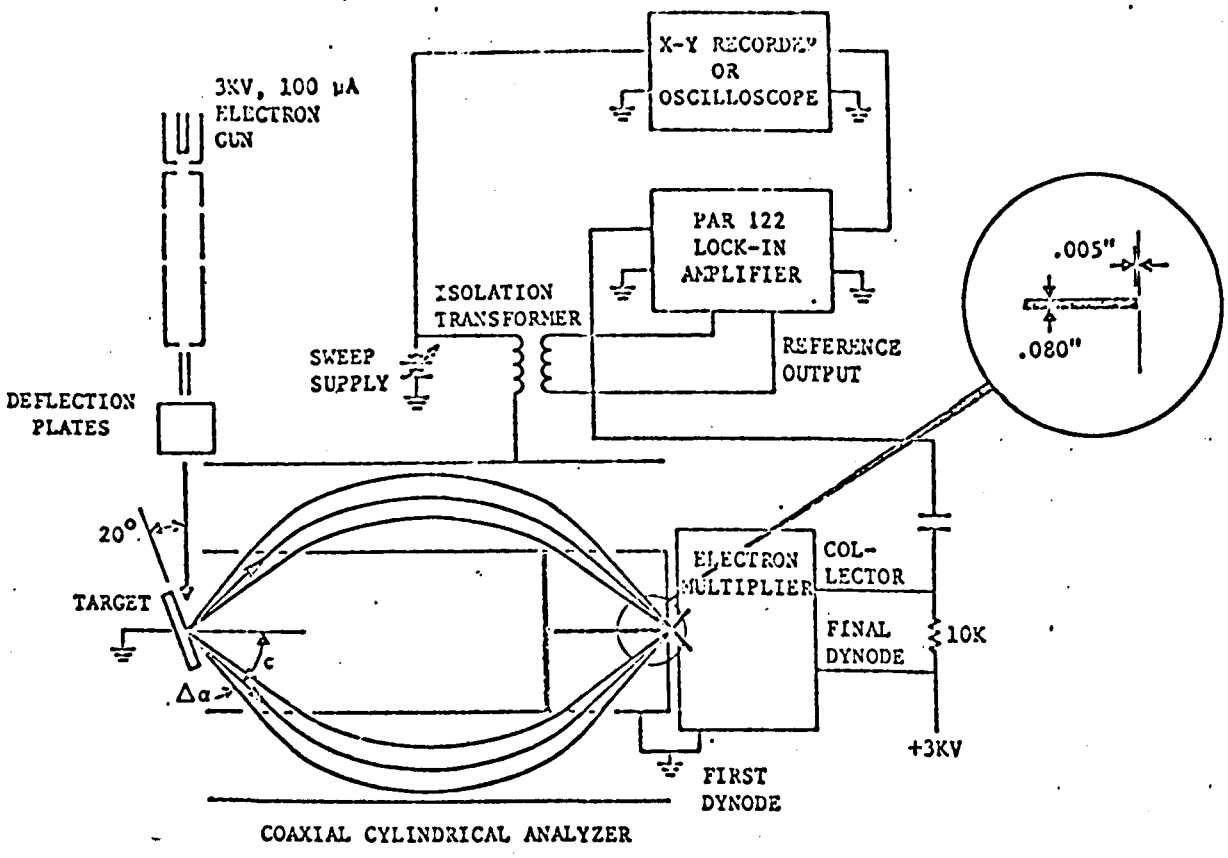

The cylindrical mirror analyser

Figure 1.12

energy) secondaries are reflected back by the retarding grid to the collector.

In order to extract the energy distribution it is necessary to modulate the retarding grid potential and detect the a.c. component of the collected current. Weber and Peria (1967) further showed that by detecting only that part of the secondary current at twice the modulating frequency, it was possible to obtain the differential of the energy distribution.

d) Cylindrical mirror

A significant advance in the state of the art of Auger spectroscopy was made with the application of the focussing properties of the coaxial cylindrical analyser. The advantage of this instrument in secondary emission studies is its comparatively large acceptance angle, and high transmission, comparable to that of a retarding field analyser.

The experimental arrangement used by Palmberg, Bohn and Tracy (1969) is shown in Figure 1.12. At a particular value of the potential difference between the cylinders, U, a beam of electrons of energy V will be transmitted. The detailed mathematics of the energy analysers is rather complicated, but it has been treated thoroughly by Pessa, Aksela and Karras (1969), Sar-El (1967), Roy and Carrette (1971) and others. It is possible to operate with axial focussing or with focussing on the surface of the inner cylinder, and the irises defining the entrance and exit angles and divergence have to be adjusted with great care. The alignment problems for high resolution may be less severe

if the tandem analyser advocated by Zashkvara et al. (1966) is employed. Haas, Thomas and Dooley (1972) have built such an instrument and obtained high resolution and transmission.

An instrument with an equivalent performance to that of a cylindrical mirror analyser has been described by Basset, Gallon and Prutton (1972). The instrument consists of a high transmission concentric hemispherical analyser with an intrinsic resolution of about 1% in conjunction with the pre-retarding lens of 10:1 retardation ratio. The combination thus possesses a resolution of 0.1%. The instrument is more directional that the cylindrical mirror, and consequently has a lower collection angle Ω. It will perhaps find more application in studies of the angular distribution of emitted electrons, studies of which are not practicable with a cylindrical analyser.

e) Comparisons and conclusions

A useful comparison between the signal to noise performance of the 127° and retarding field analysers was made by Taylor (1965).

If suitably "quiet" electronics is used the main contribution to the noise is shot noise in the collected current. Under these conditions, the performance of the two analysers is fairly similar with the retarding field analyser being superior for low excitation voltage and wide Auger peaks, and the 127° analyser leading for the case of high excitation voltage and narrow peaks. There is a dependence on primary energy because the current reaching the collector of a 127° analyser is that in an energy window ΔV, whereas in the retarding field

analyser there is additional noise from the integrated background current up to the elastic peak.

The 127° analyser is highly directional, so is of use where it is desired to measure the angular distribution of secondaries as well as their energy distribution. The retarding field analyser can, on the other hand, be used for total Auger yield determinations at a variety of incident angles.

For analytical surface chemistry and examination of fine structure in Auger peaks, there is no doubt that the cylindrical mirror analyser wins "hands down", with the hemispherical analyser (and pre-retarder) coming a close second where angular distribution studies are to be made. In addition to their high resolution, these instruments have a high transmission, comparable to that of a retarding field analyser. The shot noise contribution is, however, reduced by two or three orders of magnitude, over the retarding field analyser.

This enables much faster scan times to be employed or a reduction in the exciting beam current to lower levels at which less surface damage occurs.

The remaining advantages of retarding field analysers are their relative simplicity (partially offset by the increased complexity of the detection system), the ease with which existing LEED systems can be modified into Auger spectrometers, and their tolerance of somewhat higher magnetic fields. Because of this reason, and their intrinsically poor resolution at low energies, the operation of electrostatic analysers

becomes very difficult at energies below about 20eV in the region of the slow electron peak. For studies of crystal surfaces cylindrical analysers may be able to be used in conjunction with RHEED systems (Readhead and Armstrong 1970).

1.4 Related fields of surface study

1.4.1 Introduction

It is perhaps appropriate to mention at this stage a few other techniques which are employed in surface studies. Historically low energy electron diffraction (LEED), first discovered by Davisson and Germer (1927) has provided a powerful tool in the study of crystalline surfaces. High precision measurements of electronic binding energies by Siegbahn and co-workers (1967) using photoelectron spectroscopy (ESCA) have also proved extremely valuable in furthering the understanding of atomic states; their measurements have also provided the basis for the calculation of Auger electron energies.

More recently another technique for determination of binding energies at surfaces have emerged, namely Appearance Potential Spectroscopy (Park, Houston and Schreiner 1970). These three techniques are described briefly in the following sections, though we should mention that the techniques of characteristic X-ray spectroscopy (Sewell, Mitchell and Cohen 1969), thermal and electron-impact desorption have not been treated (Ehrlich 1966 and Redhead 1970).

1.4.2 Low energy electron diffraction

The diffraction of electrons by crystals is somewhat different from the diffraction of X-rays. Whereas the high penetration depth of X-rays yields information on the three dimensional structure of the bulk crystal, electron diffraction is primarily a surface effect dependent

on the two dimensional surface order. The primary energies used are from about 10 - 1000eV, corresponding to electron wavelengths of from about 4 - 0.4Å.

For a discussion of the experimental arrangement of a display type LEED apparatus, let us refer back to Figure 1.10. The primary electrons strike the specimen crystal plane normally, and by biasing the middle grid at the gun cathode potential, the elastically reflected electrons alone are allowed to pass through to the screen; this is maintained at a few kV positive, so that the electrons are accelerated sufficiently to produce a bright spot. Strong diffraction occurs when the wavelength of the primary electrons is a simple fraction of the atomic spacing.

The information which can be obtained from LEED data is limited at present by the theoretical position, and the complete interpretation of diffraction patterns will always be rather a complex problem. It has found particular application in the study of such problems as the adsorption of gases on to crystal surfaces.

Tracy and Palmberg (1969), for example, studied the binding energy of CO on Pd and Ni (100) surfaces as a function of surface coverage. For the case of Pd, they found three distinct ranges of surface density; at low coverages a disordered adsorption, near 0.5 monolayers an ordered structure, and at higher coverages a compressed surface arrangement with low binding energy.

As has been mentioned previously, the interpretation of LEED patterns has been greatly helped by the incorporation of Auger spectroscopy as an analytical tool; by using the same electron gun, the same area of crystal can be examined by each technique, and the changes in surface chemistry associated with changes in observed LEED patterns monitored.

1.4.3 Photoelectron spectroscopy

In the high precision photoelectron spectrometer developed by Seigbahn and colleagues (1967, 1969), the sample under investigation is bombarded with radiation, and the energies of the emitted photoelectrons analysed. Typically Al Kα (1480eV) and Mg Kα (1350eV) X-rays are used for excitation although UV radiation is useful for studies of the valence band.

The interpretation of ESCA spectra is very simple, for, if E_b be the binding energy of the level to be ionised and hν the energy of the primary radiation, the measured photoelectron energy, E_{pe}, is given by:

$$E_{pe} = h\nu - E_b - \phi_a$$

where ϕ_a is the work function of the electron analyser.

The binding energy is thus determined directly, and chemical shifts due to different oxidation states of the valence electrons may be readily observed. Using this technique the electron binding energies of

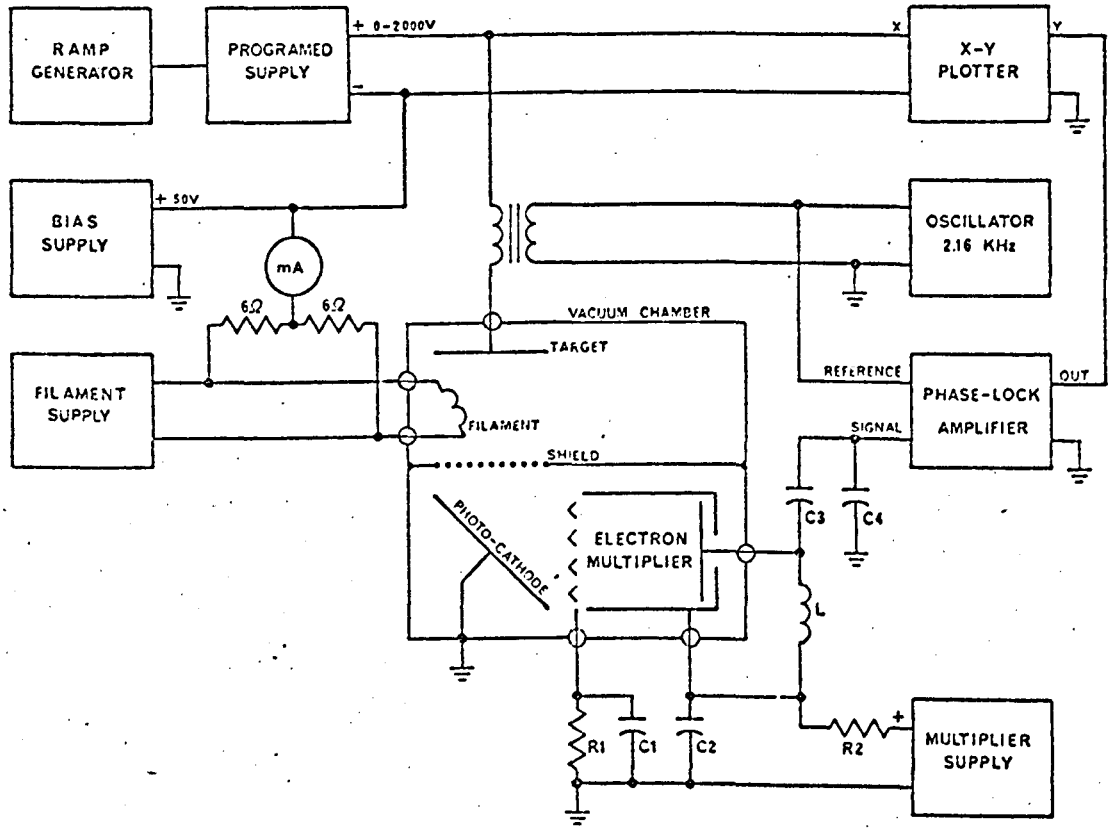

Soft x-ray appearance potential spectrometer (Park et al)

Figure 1.13

nearly all of the elements have been determined with a precision approach approaching 0.1eV. The method relies on the emission of electrons with energies of up to 1.5keV without subsequent energy loss; consequently the information obtained is predominantly from the surface region. It is advantageous, therefore, to conduct investigations in an UHV environment, but it is only recently that such instruments have become commercially available. Using an ESCA instrument, it is also possible to examine Auger transitions, and in favourable circumstances all the levels participating in the transition can be determined. ESCA measurements are generally more convenient than X-ray emission or absorption measurement, since the background count is lower, and they have advantages over methods involving electron stimulation in that they are equally suitable for conductors and insulators.

1.4.4 Appearance potential spectroscopy

In this simple method of binding energy determination, the sample is bombarded with a high current low current density electron beam. Photons and excited neutrals are released and strike a photo cathode releasing electrons, which can be detected. The biasing has to be suitable arranged so that secondary electrons are prevented from reaching the photo cathode or detector.

The experimental arrangement first published by Park, Houston and Schreiner (1970) is shown in Figure 1.13. Later they reported (Park and Houston 1971) that it was possible to dispense with the electron

multiplier if a suitable geometry was chosen, and the vacuum chamber could be used as a photo cathode.

If the derivative of the photo current is measured as a function of primary energy, peaks appear at energies consistent with the energy required to ionise inner levels.

Haas, Thomas and Dooley (1972) have shown that it is possible to modify a retarding field LEED-Auger system so that it becomes a LEED-Auger-Appearance potential spectrometer. However, they also mention that since the sum of the transition probabilities for Auger and photon decay is unit, those elements with strong Auger peaks may have weak photon peaks and vice-versa.

For example, they were unable to detect sulphur by the Appearance potential method on an outgassed vanadium sample, even though the Auger peak from sulphur contamination was large. As we mention later in Chapter 2, we saw no peaks from the $M_{4,5}$ levels of silver in an attempt to perform Appearance potential spectroscopy.

Tracy (1971) showed by direct comparison with Auger spectroscopy, that Appearance potential spectroscopy is about equally sensitive to Cr, Ti, Ge and Ni, but unable to detect Cn, Ag or GaAs. The technique is as yet not fully developed, and it may well prove to have a useful contribution to make to the study of surfaces.

1.5 Conclusions

In the previous sections we have given a general introduction to the phenomena associated with secondary electron emission.

In the following chapter we discuss the design and construction of an equipment for the study of the total yield, and energy distribution of secondaries, produced by electron bombardment. Initially, the investigation was concentrated on studies of the characteristic energy losses and Auger spectra of evaporated films of metals, but at a later stage further detailed examination of small peaks superimposed on the 'slow' electron peak was made.

CHAPTER 2

APPARATUS AND EXPERIMENTAL TECHNIQUE

2.1 Introduction

This chapter is dedicated to an approximately chronological account of the development of the equipment used in the present investigation. Firstly, in the following sections 2.1.1 to 2.1.3 we discuss certain general features of the design of the apparatus, and in sections 2.2 and 2.3 show how these ideas were implemented in the construction of the first and subsequent equipment. Of necessity, certain results were taken during the development stage, and we shall make use of these to demonstrate the limitations of the initial equipment and its progressive improvement. Certain other considerations (e.g. financial) meant that some improvements were not available until quite a late stage.

Initial experiments were carried out using a spherical vacuum chamber that was already in existence. It will be demonstrated in section 2.2 how the first energy distribution measurements were made and the first Auger peak seen. The resolution achieved was poor, however, presumably because it was a single retarding grid analyser. Physical considerations precluded the inclusion of extra grids and consequently a large chamber was designed and built; this is described in section 2.3.

2.1.1 General features

The design aim of the apparatus was to produce an equipment capable of measuring the total secondary yield of materials, and also the energy distribution of those secondary electrons, produced by electron bombardment. Thomas (1967) studied the energy distribution of secondary electrons in a yield measuring apparatus, and his basic design was followed.

The secondary electrons are collected on a sphere of stainless steel which also forms the walls of a vacuum chamber; within this spherical shell are mounted a number of concentric spherical grids made of tungsten mesh, which serve as accelerating grids for the yield measurement and as elements of a retarding field analyser for the electron energy analysis. The spherical collector is divided into two hemispheres for access by a vacuum flange and a number of stainless steel tubes are welded in radially for the mounting of components. The target, which is situated at the centre of the sphere, and electron gun are arranged at right angles, and a rotary drive attached to the target enables the angle of incidence of the primary beam to be varied. It should be noted that an important feature of the 360° analyser is that it is possible to use a wide range of incident angles and still collect all the secondary electrons. A projection lamp filament mounted close to the target may be used for radiative heating of the target and will also bake the sphere to an (external) temperature of about 200°C.

For alignment of the electron beam, the target was replaced by a conducting fluorescent screen, and the focussing properties and beam position were checked over the range of energies for which the spot was visible (above 200eV). It was also found that the beam was deflected by the stray magnetic field at low energies, but this was reduced by shielding the ion pump magnets with a Netic* can and enclosing the chamber in a Conetic* screen.

* Perfection Mica Co. Chicago.

2.1.2 Vacuum features

As mentioned previously, investigations involving the secondary emission properties of surfaces may be critically dependent on the composition of the topmost surface layers. Consequently, it is necessary to conduct the investigations in the Ultra High Vacuum region ($<10^{-8}$torr) to minimise or control contamination from the residual atmosphere, and to employ methods of specimen preparation which yield atomically clean surfaces in the UHV. The systems used have thus been of all-metal construction, using EN58E (304) stainless steel for the chamber and plumbing, and copper gasket knife-edge seals. In order to eliminate hydrocarbon contamination and to maintain high pumping speeds at low pressures, "clean" pumps have been emplcyed: i.e. rough pumping down to $\sim 10^{-3}$ torr by a chilled molecular sieve sorption pump, and pumping in the High Vacuum region by a Titanium diode sputter ion pump (Ferranti FJD 50). Using these pumps, operating pressures between 10^{-8} and 10^{-10} torr have been consistently obtained, the actual pressure being determined by the baking cycles employed after pump-down. The composition of the residual gases in the vacuum system may be determined using a Varian quadrupole residual gas analyser, but as this particular instrument does not possess an integral electron multiplier, investigations have been limited to total pressures above about 10^{-8} torr. The Quadrupole has also been used for in situ leak testing, but the majority of component leak testing was accomplished prior to assembly using a more sensitive (20th Century) mass spectrometer leak detector. The two vacuum systems used are described in more detail in sections 2.2.1 and 2.3.1.

2.1.3 Electrical features

The detailed development of the electrical detection system for the various modes of operation is traced in sections 2.2.2, 2.2.3 and 2.3.2-4. It will be helpful to give an outline here of the basic features of the electrical system. The primary electrons are obtained from an electron gun with an indirectly heated oxide-coated cathode. Despite the fact that this type of cathode is known to poison on exposure to atmosphere, (e.g. Wagener 1954, Jacobs and Wolk 1949), satisfactory operation was obtained for a number of pumping cycles, by careful reactivation at low pressures; it was also found helpful to maintain a small current running through the filament to reduce absorption of water vapour while at atmospheric pressure. Some early results were also taken using a directly heated LaB_6 filament in the gun. The energy range used for primary electrons is limited by the characteristics of the gun and in practice has been from 100 - 3000eV at currents of between 1 and 150μA. The secondary current is thus of the same order of magnitude, and the detection of characteristic energy loss and Auger electron peaks involves the measurement of currents several orders of magnitude lower than this. It is evident that extreme care was needed in the design of the detection circuits to reduce noise and pickup to the lowest levels. Stabilised power power supplies and phase sensitive detection methods have been employed to reduce the noise to tolerable levels. Since the stainless steel walls of the vacuum chamber are used as the electron collector, the whole apparatus is enclosed in an aluminium screening can; care has also been

taken to avoid earth loop currents in the high impedance input circuitry to the electrometer amplifier. 50Hz pick-up was severe when the 'mains' earth was used, and all signal earths were derived from a grounded bus bar.

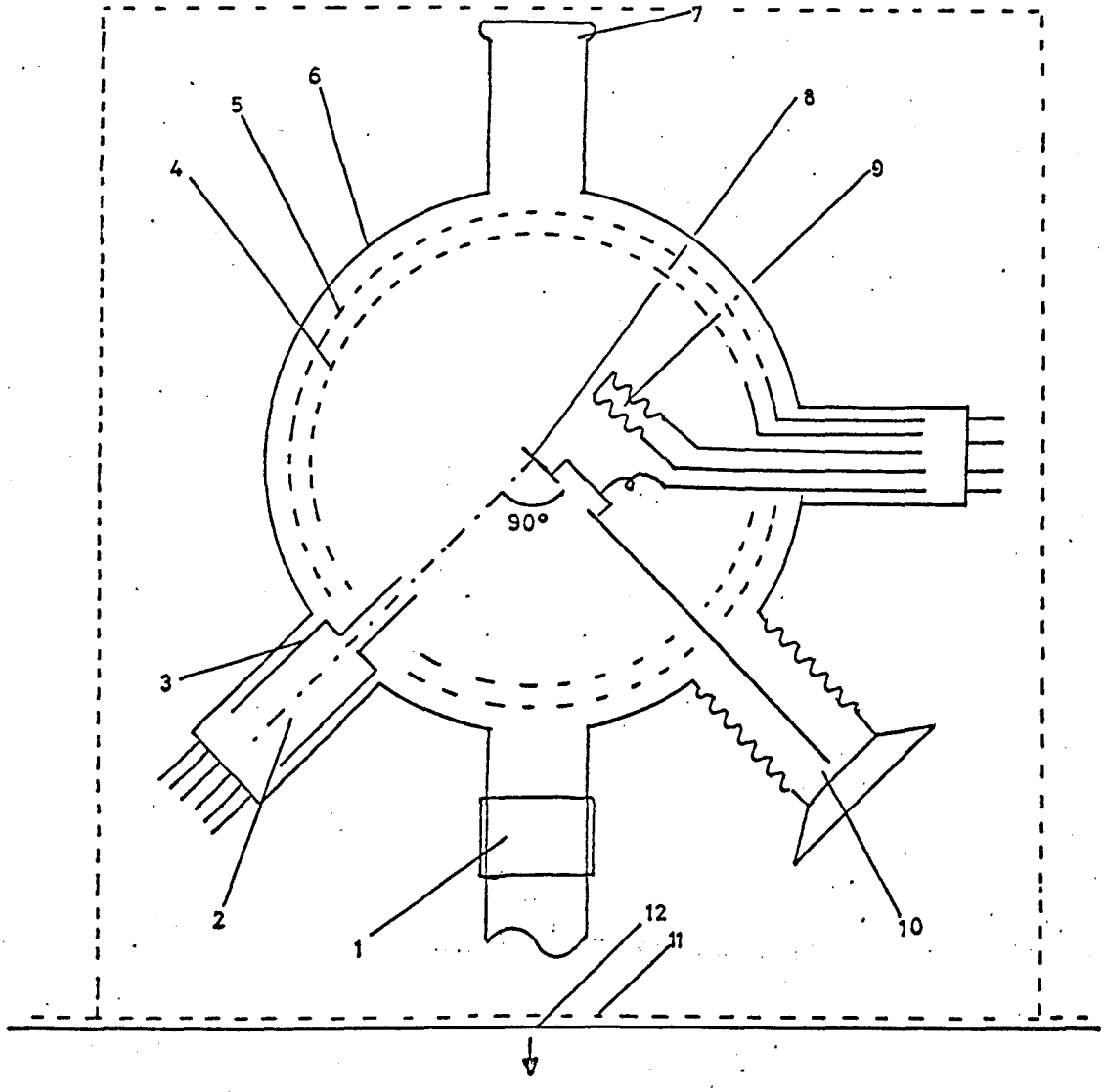

1 Ceramic Insulator
2 Electron Gun
3 Gun Screen
4 Inner Grid
5 Retarding Grid
6 Collector
7 Viewport
8 Target
9 Heater
10 U.M.Drive
11, 12 Magnetic Shields

Vacuum System

FIG. 2.1

2.2 Initial Experimental Arrangement

2.2.1 Vacuum system and components

A diagram of the vacuum system is shown opposite in Figure 2.1. The diameter of the spherical vacuum chamber (6) was about 150mm and this served as the electron collector, the ceramic insulator (1) being to isolate the chamber electrically from the remainder of the vacuum system which was earthed. The outer grid (5) had a diameter of about 128mm and was used as a retarding grid; the inner grid (4) of diameter 100mm was maintained at target potential. An earthed screen (3) was needed around the electron gun to prevent electrons reaching the collector directly from the gun electrodes, this screen was extended via a 6mm diameter nozzle into the field free region within the inner grid. Each grid consisted of two hemispherical grids connected together to form a sphere; they were fabricated by stretching 85% transparent Tungsten mesh over a spherical pyrex flask of the chosen diameter and carefully smoothing it over the flask until it began to take up the hemispherical shape. A nichrome wire ring which had been made a good fit over the flask was then pressed over the mesh on the flask, and welded on to the mesh all around the circumference. A number of holes were required in the grid and these were made by positioning small rings of wire in appropriate places and welding them to the mesh, before cutting the holes. Electrical connection was achieved by welding a small wire from the support ring to a multipin electrical feedthrough. The target (8) was mounted on an adjustable bellows and rotary motion feedthrough (10); using these it

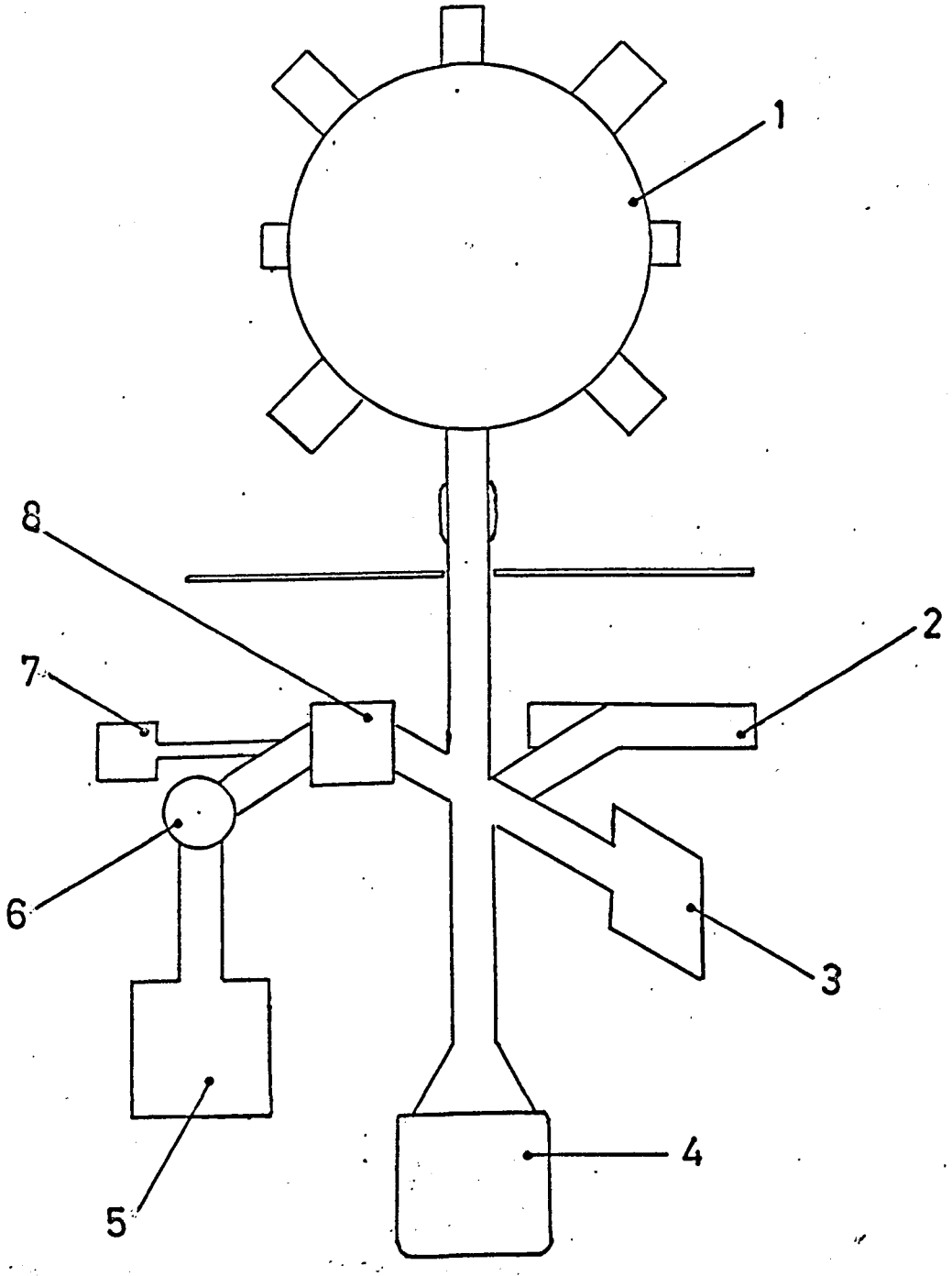

1. Chamber
2. Q.R.G.A.
3. Ion pump (8 l/s)
4. Ion pump (50 l/s)
5. Sorption pump
6. Viton tap
7. Pirani gauge
8. Bakeable tap

Figure 2.2 Schematic of pumping system.

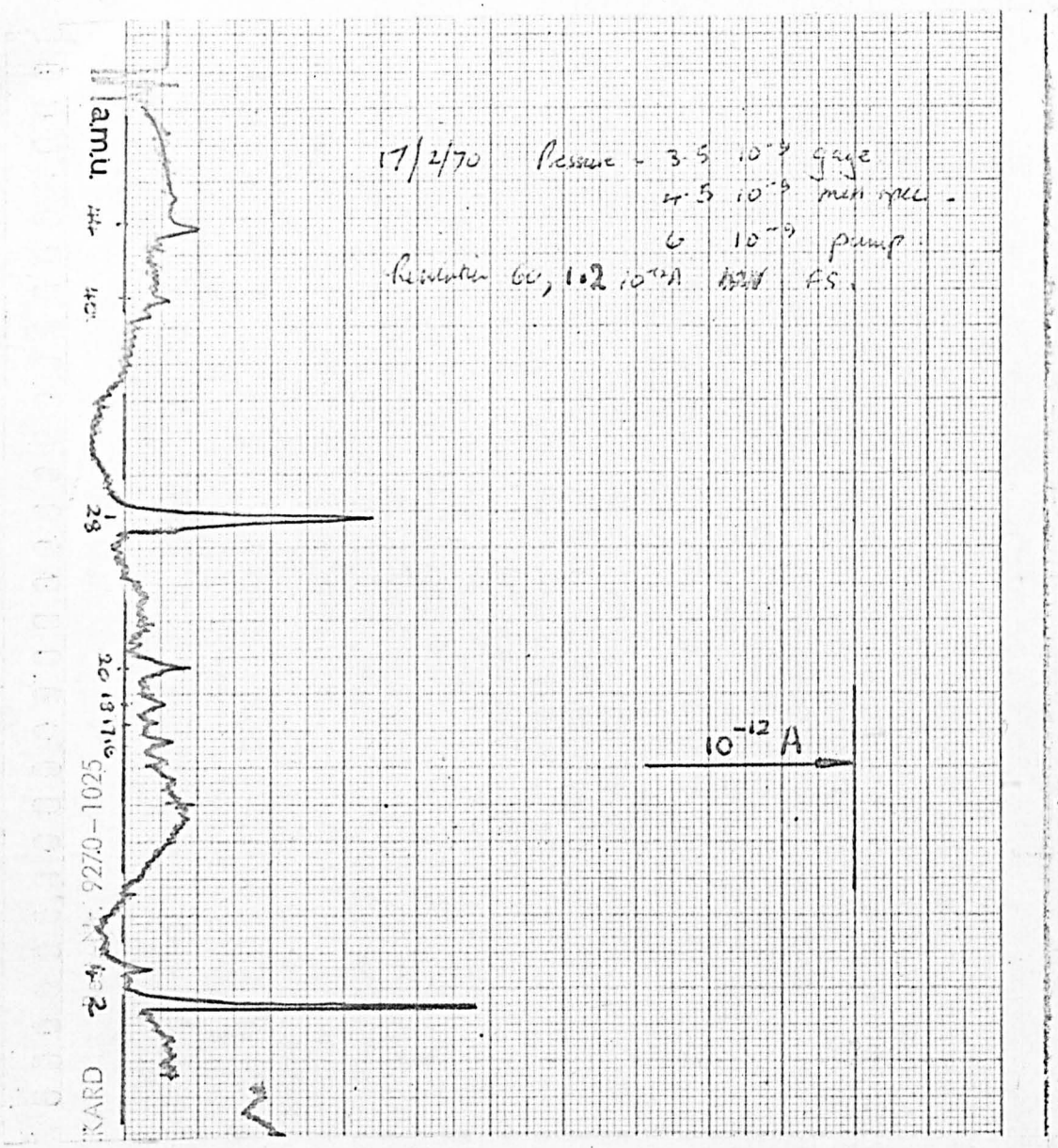

Figure 2.3 Residual gas spectrum of baked system

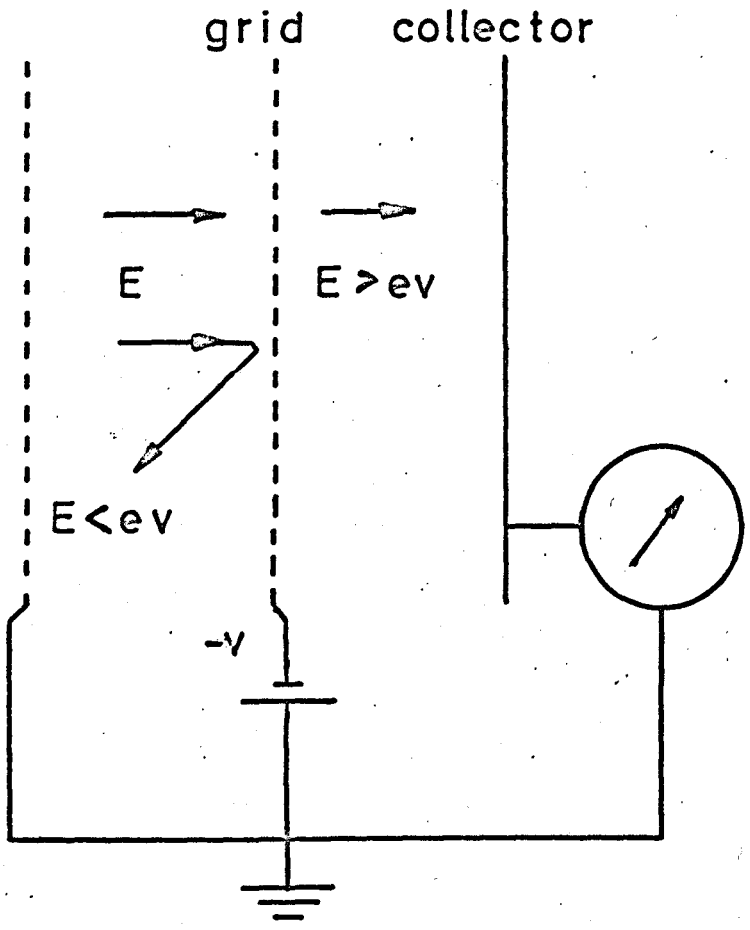

Figure 2.4 Basic retarding field analyser

was possible to position the target at the centre of the sphere and vary the angle of incidence and also place it near the radiant heater (9).

The pumping arrangement is shown in Figure 2.2. The chamber was bakeable to over 400°C by means of an external oven and the pumps and plumbing to over 200°C with heating tapes. The 8 l/s pump was found most useful during pumpdown, when the larger pump tended to overheat and outgas. After mild overnight baking the pressure fell typically to around 5.10^{-9} torr. Figure 2.3 shows a mass spectrum at this pressure obtained after outgassing the analyser filament. Most peaks are barely visible above the noise, masses 2 and 28 being the primary residuals; mass 2 is H_2^+ and 28 is due to N_2^+ and CO^+, the larger contribution being from CO as shown by the relatively large peak at mass 44 (CO_2^+), by comparison with the negligible peak at 14 (N_2^{++} and N^+). The level of noise on this plot demonstrates how,without an integral electron multiplier,this instrument was not useable below this pressure range.

2.2.2 First differential detection circuitry

A retarding field analyser is shown diagrammatically in Figure 2.4. It is essentially a high pass velocity filter and consequently the d.c. output current as a function of grid voltage V corresponds to the integral of the energy distribution of the transmitted electrons. In order to measure the energy distribution of the electrons it is necessary to differentiate the d.c. output (known as the transfer characteristic). This may be accomplished using the differentiating property of a phase sensitive detector; a small perturbation v sin ωt is applied to energy

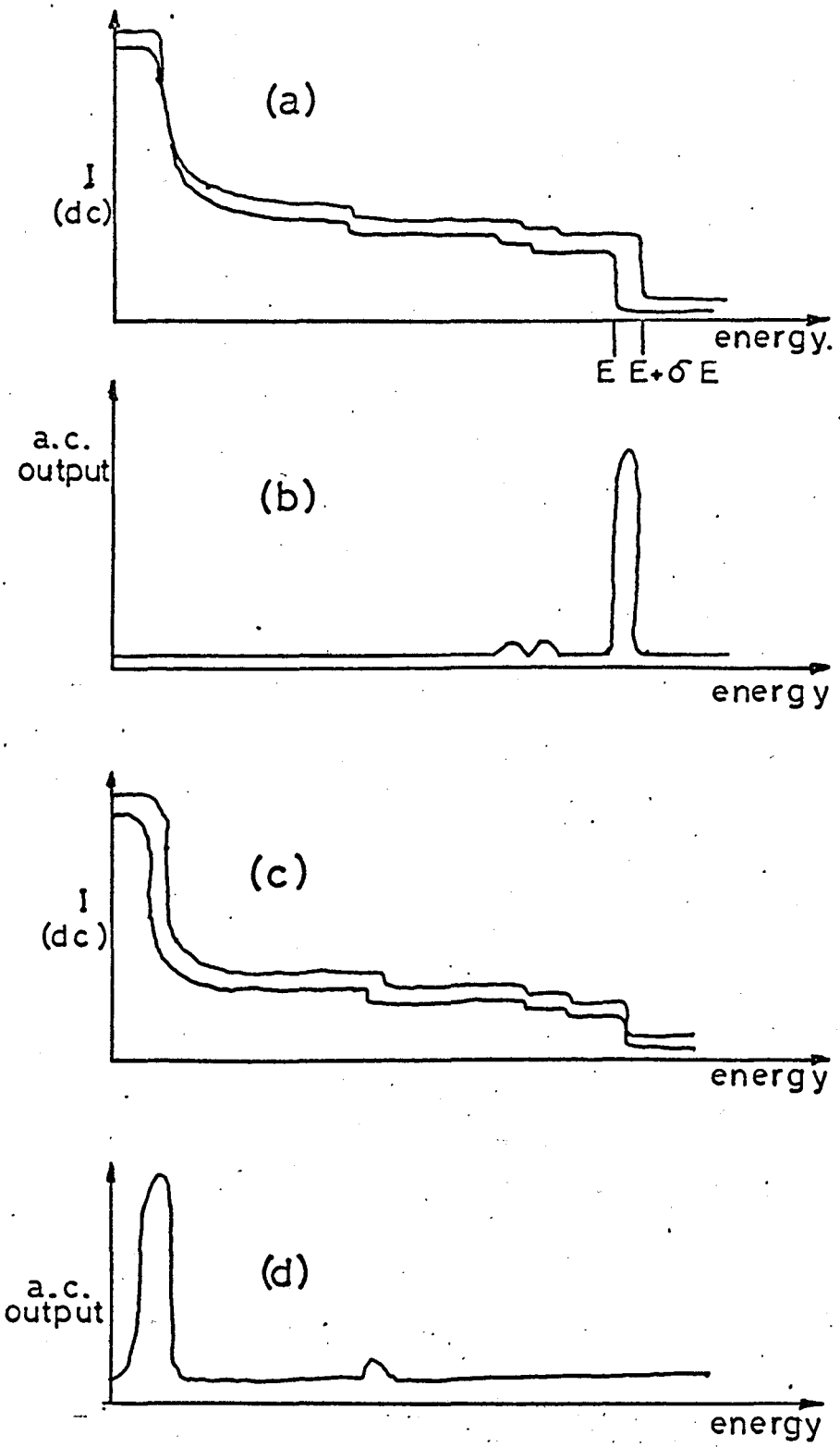

Figure 2.5 (a)(b) primary beam modulation
(c)(d) target modulation

Characteristics of retarding field analysers

modulate the electrons, and the amplitude of the collected current at frequency ω is proportional to the differential of the transfer characteristic.

This modulation may be accomplished in a number of ways in a secondary emission spectrometer:

1) The primary beam may be energy modulated,

2) The target potential may be modulated,

3) The potential of the retarding grid may be modulated.

Method 1) does not energy modulate the secondary electrons, in fact it amplitude modulates only that part of the spectrum which varies with primary energy, i.e. the elastic peak and associated characteristic energy losses. The 'slow' peak and Auger electron peaks are not modulated at all and thus do not contribute to the output signal. This is shown in Figure 2.5a, where the transfer characteristic of a retarding field analyser for primary energies E and E + δE is shown. Since the a.c. output at a voltage V corresponds to the difference between the two curves, only the Elastic peak and C.E.L. peaks will appear, as seen in Figure 2.5b.

Figures 2.5c and 2.5d show the effect of modulating the target potential. Since the energies of the elastic peak and energy losses are independent of the target potential, they will not produce an a.c. output whereas the 'slow' peak and Auger peaks will. For studying the entire secondary electron energy spectrum it is thus necessary to modulate the voltage of the retarding grid, since only by this method do we obtain an output from all the secondary electrons. The disadvantage of this method

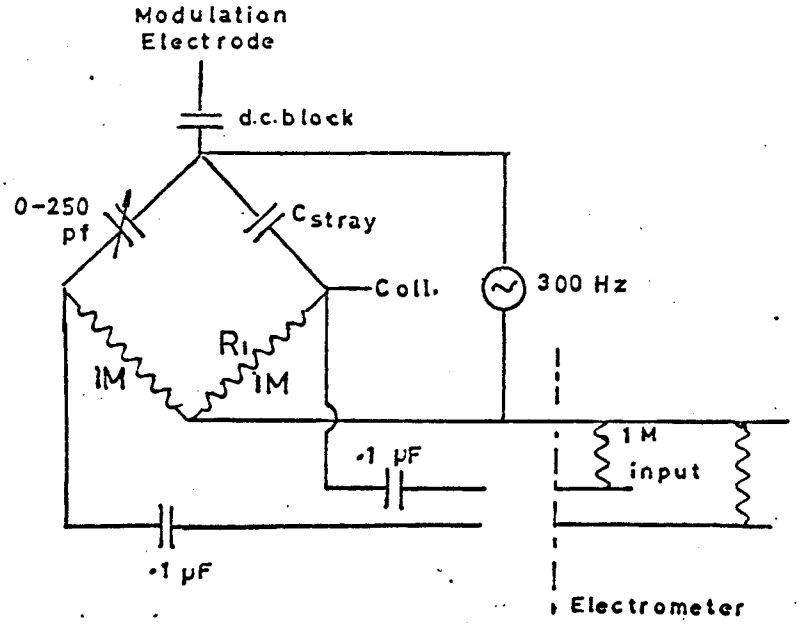

First Bridge

Figure 2.6

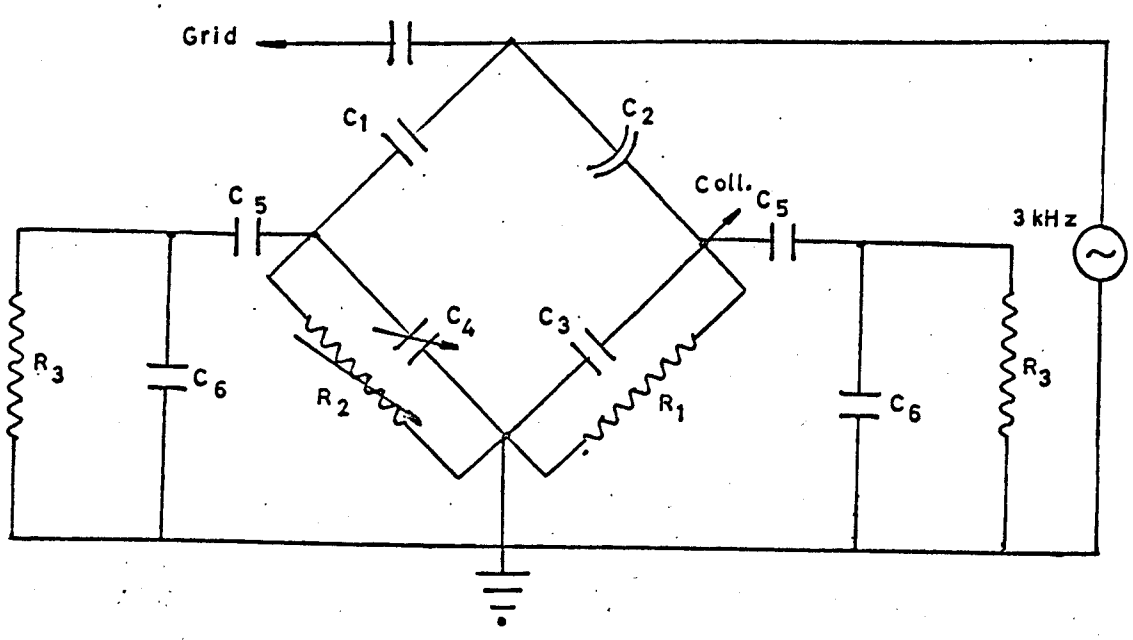

C_1 115 pF	C_4 270 - 320 pF	R_1 1 M
C_2 coil / grid	C_5 15 pF	R_2 570 - 670 k
C_3 coil / earth	C_6 ~ 20 pF cable	R_3 10M electrometer

Modified Bridge

Figure 2.7

is 'pick-up'; the capacitance existing between the retarding grid and the collector means that a proportion of the perturbing voltage applied to the grid appears at the collector, in quadrature with the a.c. component of the collected current. Because this latter current is so small, the pick-up signal is much greater than it and swamps the detection apparatus. A means has thus to be found of cancelling out this constant pick-up signal, so that the wanted signal may be amplified and detected. There are many ways of doing this, and, as J.C. Riviere once remarked, the number of pick-up neutralising circuits is equal to the number of workers in the field.

The first method tried used a bridge circuit similar to that used by Thomas (1967) shown in Figure 2.6. The capacitance between the grid and collector was measured to be about 110pF, so with the variable capacitor at this value no output should appear across the bridge. Unfortunately this design did not work on account of the stray capacitance of about 300pF between the collector and earth, appearing effectively across R_1. Satisfactory results were obtained with the circuit of Figure 2.7, where C_1 was set at 115pF and R_2 and C_4 were used to balance out the pick-up signal. The complete set-up is shown in Figure 2.8. The modulation frequency was increased to make it compatible with the second harmonic detection circuit; we shall show later in section 2.3 that this was an error, and it was later reduced to 30Hz! The maximum amplitude that could be used before overloading the input tubes with the pick-up signal was about 2V pk-pk. The electron gun was operated with

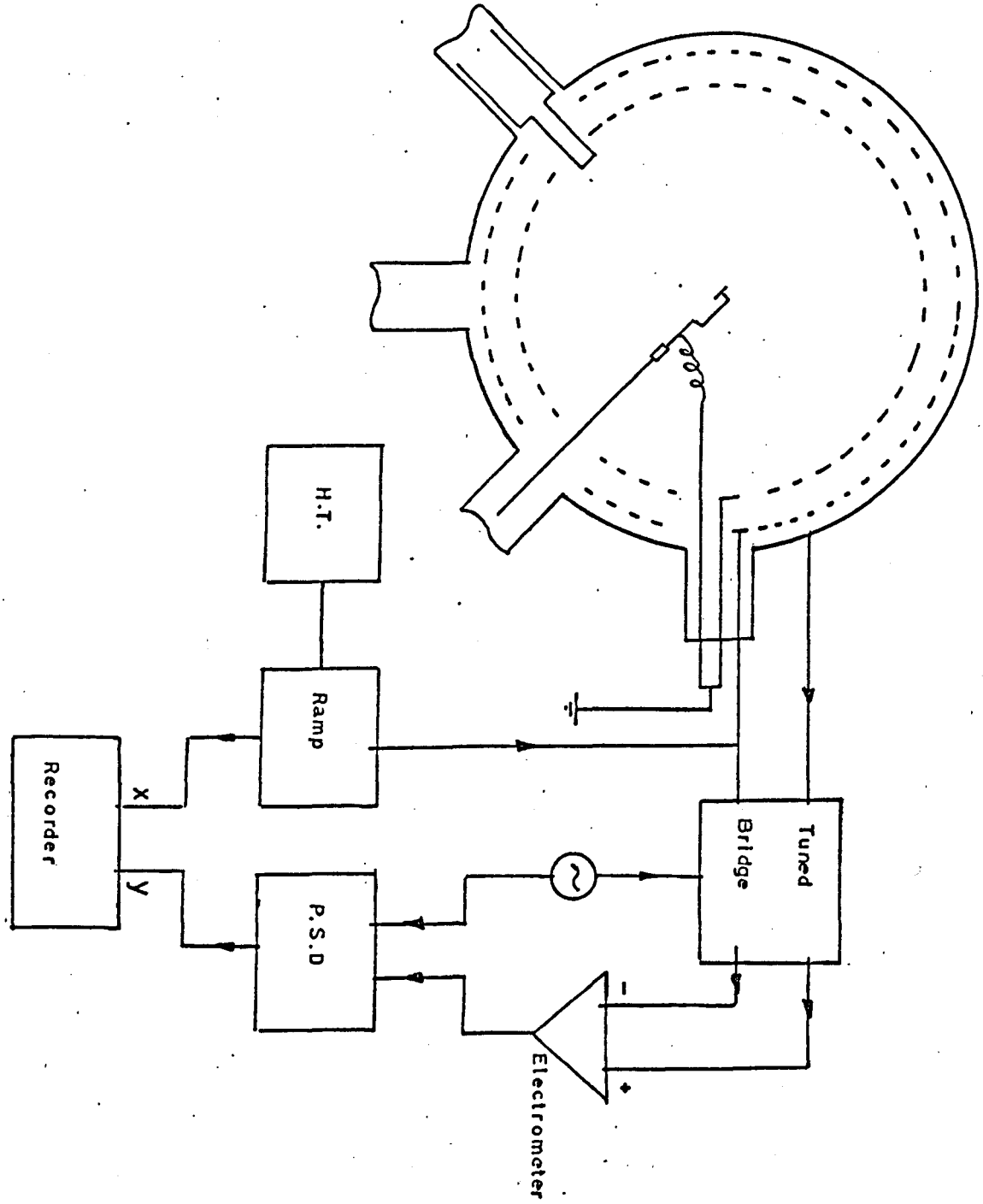

Figure 2.8 Block diagram of first-differential circuit

depressed cathode and earthed anodes so that the target could be kept at around ground potential.

The gun originally used was from the Mullard DG 7-32 cathode ray tube, but the transmitted current was only of the order of 100nA. A Vacuum Generators' Lanthanum Hexaboride directly heated cathode was fitted and the transmitted current rose to well over 1μA; however, it was discovered that there was a large fluctuation of order 10% in 20 minutes in the emission current of the gun, so the following method of stabilization was tried. Instead of supplying the grid and focus electrodes from batteries, they were fed from a resistor chain, incorporating negative feedback in such a way that as the emission current altered, the potential of the electrodes altered in the sense to reduce the change (Figure 2.9). The values of the resistors were chosen from consideration of the plots of the gun characteristics, and the need to reduce the current flowing through the cathode-focus-earth chain as much as possible to improve regulation at low emission currents; the use of this circuit reduced the fluctuations to about 2%, and further improvement was effected by transistor regulation of the filament current supply. Electrostatic X and Y deflection were provided to optimise the resolution by ensuring that the beam hit the target at the centre of the retarding grid.

The target and inner grid were maintained at earth potential so that the region around the target was field free. The potential on the outer grid was scanned between just above cathode potential and target

potential by means of a variable-speed motor-driven 10-turn helipot of 1MΩ total resistance. A 470kΩ series resistor was necessary to reduce the variation in a.c. impedance to earth of the grid circuit at the extreme ends of the potentiometer, and so ensure that the modulation amplitude and bridge balance remained constant. A picoammeter was used for checking that the beam was hitting the target and also for measuring the primary beam current; when the retarding grid potential was more negative than cathode potential, all the secondaries were returned to the target, hence the target current was a measure of the incident current. The a.c. output from the bridge was fed into a differential electrometer amplifier (Keithley model 603) and thence to the signal channel of the phase sensitive detector (AIM system 5). The unattenuated output of the oscillator was taken to the reference channel via a phase-shifter and squarer. A fraction of the retarding potential ($^1/10$) was applied to the X-channel of an XY recorder and the d.c. output of the phase sensitive detector applied to the Y-channel. The collector was biased at 60 volts above earth, since otherwise at low values of retarding grid volts tertiary electrons from the collector would find their way back to the target, resulting in a reduction of collector current in the region of the 'slow' peak.

2.2.3 Second differential detection circuit

Investigations of small peaks in the secondary electron spectrum are complicated by the large background current which limits the amount of gain available. This background can be greatly reduced by further

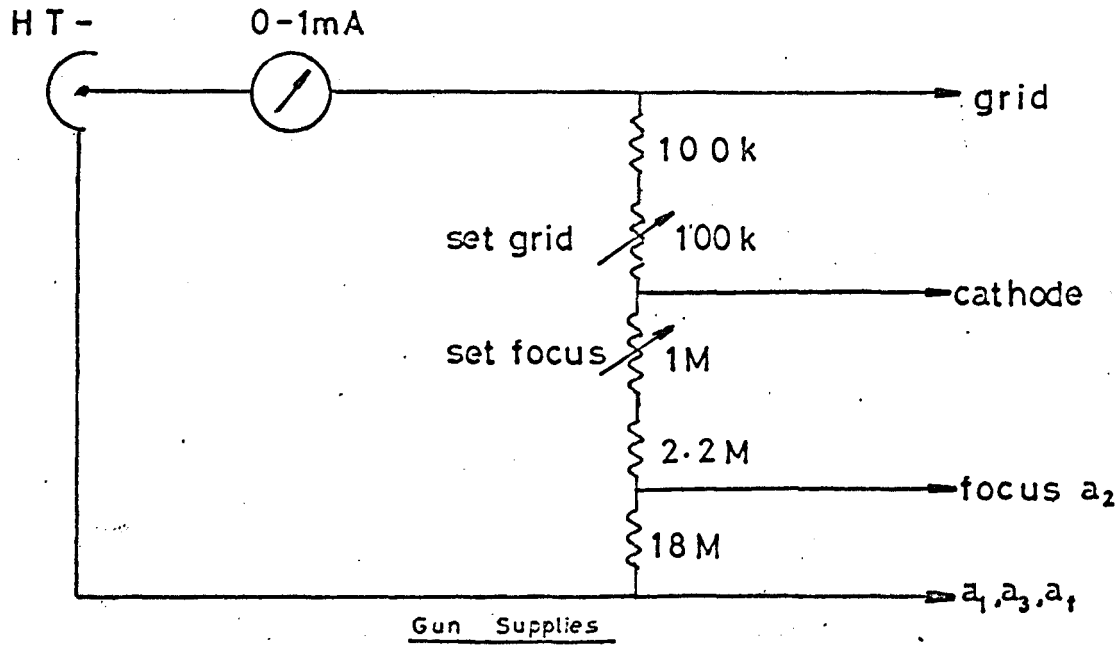

Gun Supplies

Figure 2.9

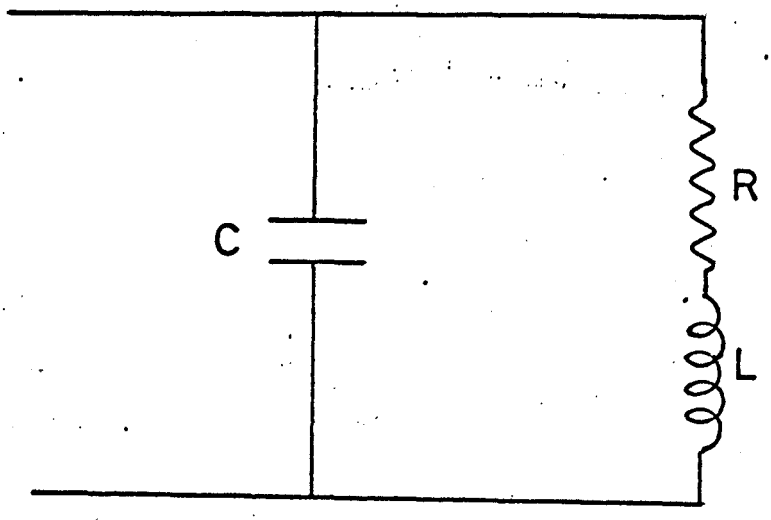

Figure 2.10 First tuned load circuit

differentiation, (Harris 1968), since a steady background signal has a differential of zero. Measuring the differential of the energy distribution involves detecting the second harmonic of the collected current of a retarding field analyser (Palmberg and Rhodin 1968); this is complicated by the large signal at the fundamental, which is mainly pick-up.
To overcome this problem a resonant load similar to that described by Gallon et al. (1969) was constructed and subsequently improved. It comprised an inductor tuned by the capacitance of the collector to earth, having a high resonant impedance at twice the modulating frequency and a low impedance at the modulation frequency.

A simple tuned circuit as shown in Figure 2.10 has a resonant frequency

$$\omega_r = 1/\sqrt{LC} \quad \text{if} \quad R << \omega_r L$$

The resonant impedance Z_r is

$$Z_r = L/RC$$

Now L and R may be considered as approximately proportional for a coil of a given design, so that for maximum resonant impedance C must be as small as possible. C is determined by the stray capacitance of the collector circuit to earth, and so is of order 500pF. In order to obtain a resonance in the frequency range 1 - 10kHz, a coil of inductance 0·5 - 50 henries and of low loss and self-capacitance was required; the only component immediately available to satisfy the above conditions was a T.V.

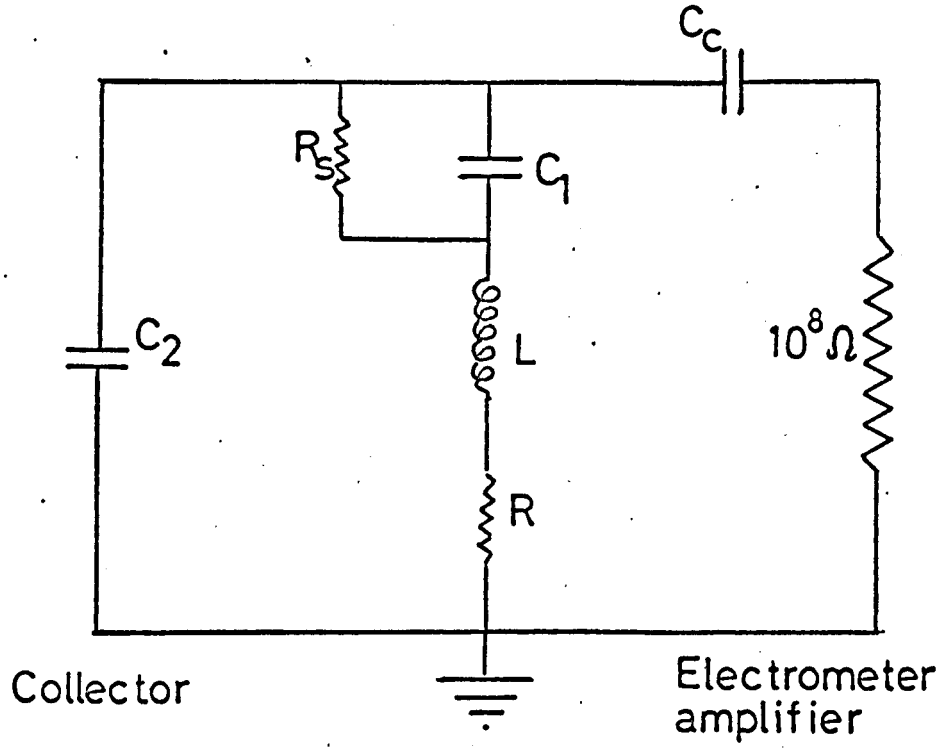

Figure 2.11 Modified tuned load

E.H.T. coil designed to operate at about 10kHz. It had an inductance of 4H and coil resistance 450Ω.

With 500pF across it:

$$\omega_r = 10^5/\sqrt{4\times 5} = 2{\cdot}3 \times 10^4 \quad \text{i.e.} \quad f_r = 3{\cdot}5\text{kHz}.$$

The resonant impedance is:

$$Z_r = \frac{L}{RC} = \frac{4\times 10^{10}}{450\times 5} = 1{\cdot}8 \times 10^7\Omega$$

At low frequencies the impedance will approximate to the impedance of the inductor, so that at the fundamental

$$Z_{(1{\cdot}8\text{kHz})} = \omega L = 4{\cdot}4 \times 10^6\Omega \text{ approx.}$$

The source impedance of the pick-up signal is the impedance of the grid-collector capacitance of 110pF at ω_r,

$$\therefore Z_{(p.u.)} = 4 \times 10^5 \text{ approx.}$$

Thus the tuned load in this design should reduce the pick-up signal by a factor of 10, produce a voltage of $4{\cdot}6 \times 10^{-2}$V/μA for the current at 1·8kHz and 18V/μA for current at 3·5kHz. This design was made to work, but improved pick-up rejection was obtained with a subsequent modification. In the circuit shown in Figure 2.11 an extra capacitor, C_1, has been inserted between the inductor and the collector, represented by C_2. Neglecting R_s for the moment, it can be seen from the Figure that L R and C_1 form a series tuned circuit, whose impedance is a minimum at a frequency

ω_o given by:

$$\omega_o = 1/\sqrt{LC_1} \quad \text{if} \quad R << \omega_o \times C_1 << R_s$$

and $Z_o = R.$

The effect of C_1 on the resonant frequency of the parallel tuned circuit of L,R and C_2 is of course that the resulting capacitance across the inductor is now

$$C = \frac{C_1 C_2}{C_1 + C_2}$$

The maximum impedance of the circuit now occurs at a frequency ω_∞, given by:

$$\omega_\infty = 1/\sqrt{LC} = \left(\frac{C_1 + C_2}{L\, C_1\, C_2}\right)^{\frac{1}{2}}$$

again if $R << \omega_\infty \times C_1 << R_s$

For detection of twice the modulation and rejection of the modulation frequency, we require that $\omega_\infty = 2\omega_o$.

Hence

$$C_1 + C_2 = 4C_2$$

i.e. $\underline{\underline{C_1 = 3C_2}}$

The resonant impedance, Z_∞, is again L/RC, or:

$$\underline{\underline{Z_\infty = \frac{4L}{3C_2R}}}$$

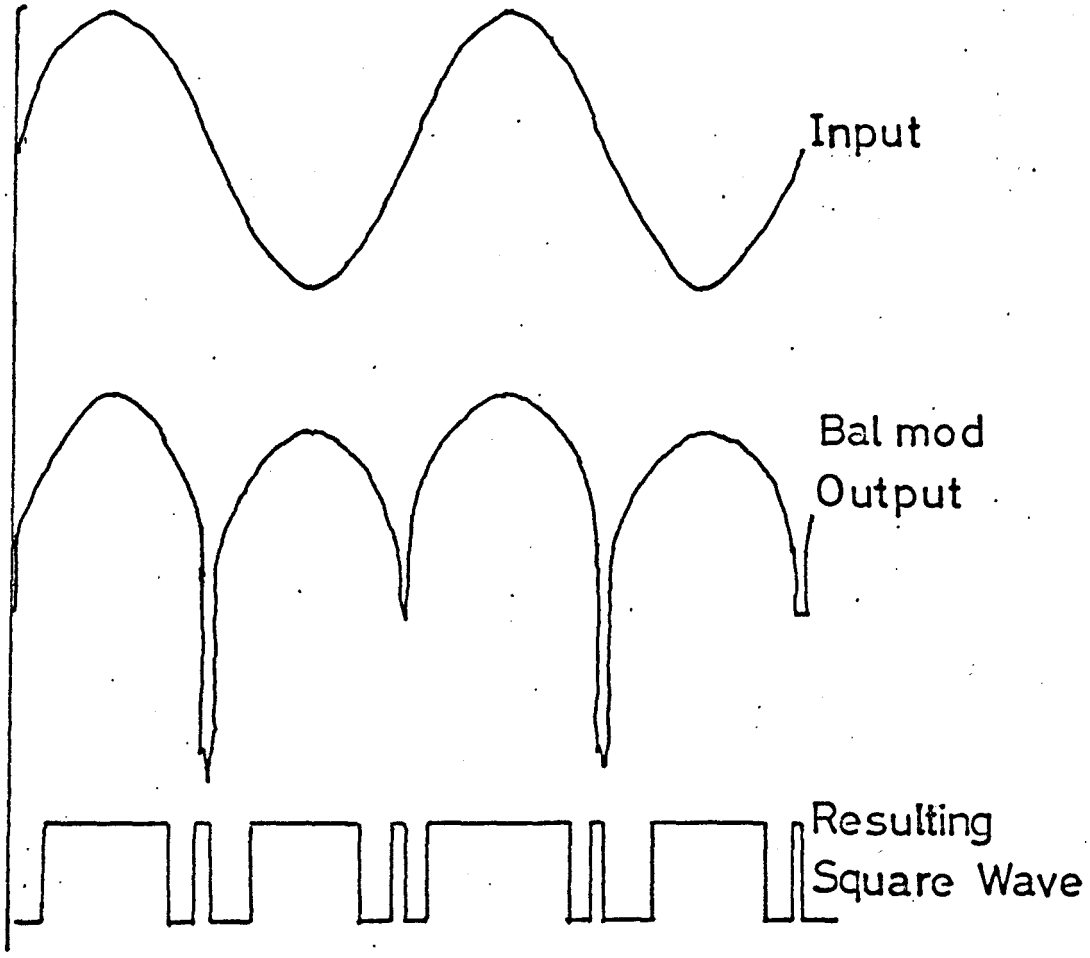

Figure 2.12

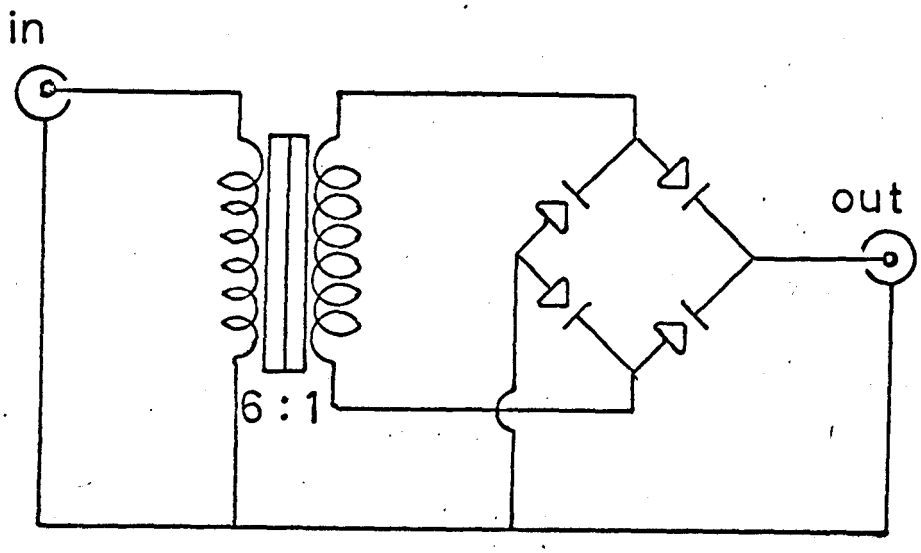

Figure 2.13

Frequency doubling for reference channel

Putting in the figures for the same coil,

C_2 = 500pF, C_1 = 1500pF, R = 450Ω, L = 4H

$$Z_\infty \simeq 24M\Omega$$

$$Z_o \simeq 450\Omega$$

These results are, of course, only approximate, since we have neglected the small self-capacitance of the coil and also the hysteresis losses in the ferrite core in deriving the impedances. Thus, the effect of the series capacitor C_1 has been to increase the resonant impedance (and hence the voltage at 2f for a given current) by 30% and to reduce the impedance at f (and hence the pick-up signal) by a factor of 100. The sensitivity at 2f is thus 24V/μA, the sensitivity at f 0.45V/μA, and the pick-up rejection 2 200, or 66dB. Of course, any second harmonic content of the modulating signal is not attenuated at all and appears in the pick-up signal.

R_s provides a path for the d.c. collector current and was chosen to have an impedance much greater than that of C_1 at f, ($\sim 4 . 10^4\Omega$); a value of 1MΩ was found to be adequate. A blocking capacitor C_c was then required to prevent the charging up of the input of the electrometer amplifier (represented by the $10^8\Omega$ resistor).

When setting up the second harmonic detection circuit, trouble was experienced with second harmonic distortion from the oscillator. The first oscillator used had a 2HD of 3% when it was measured. An alternative oscillator (Farnell LFM2) with a measured -50dB 2HD was then tried, but even this produced second harmonic pick-up in excess of the second

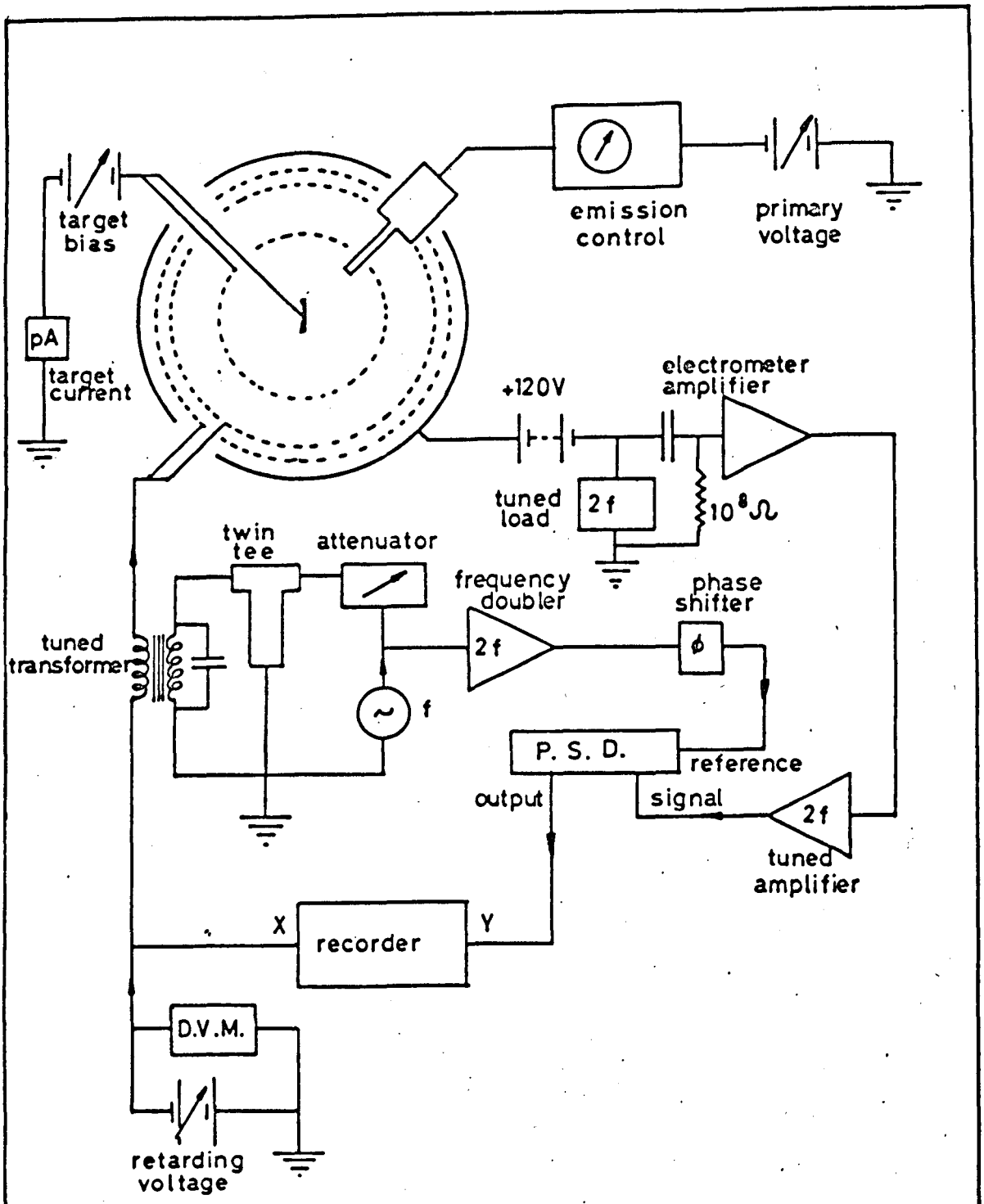

Figure 2.14 Second differential detection circuit

differential signal of all but the slow electron peak. A tuned input transformer circuit was then constructed, which as well as having a second harmonic rejection of 250:1 had a step-up ratio of about 2, enabling higher modulation voltages of up to 24V pk to be employed, and reducing the second harmonic distortion to -100dB.

Some difficulty was experienced in obtaining a good reference signal at 2f with good mark space ratio, and eventually the cheapest method tried was found successful. Initially the unattenuated (high impedance) output from the Farnell oscillator was fed to an emitter follower and thence into a P.S.D. operating as a Balanced modulator. With both inputs of the same frequency and phase, this should lead to full wave rectification. In practice there was trouble with switching spikes which caused spurious pulses from the phase shifter and squarer leading to the waveforms shown (exaggerated) in Figure 2.12. The mark-space ratio was improved by inserting a tuned filter at 2f, but this did not remove the switching spikes. Eventually we decided to try simple full-wave rectification of the reference signal, using a double wound step-down transformer to increase the impedance and provide earth isolation, as shown in Figure 2.14. The output from this arrangement was fed into a tuned filter and thence into the phase-shifter and squarer, producing a good square wave of unity mark-space ratio and no spikes.

The complete second harmonic detection circuit is shown in Figure 2.14. This circuit in its final form was also used with the second apparatus, and some components are described in section 2.3. The floating power supply used here for target bias, was first used as a 'baseline'

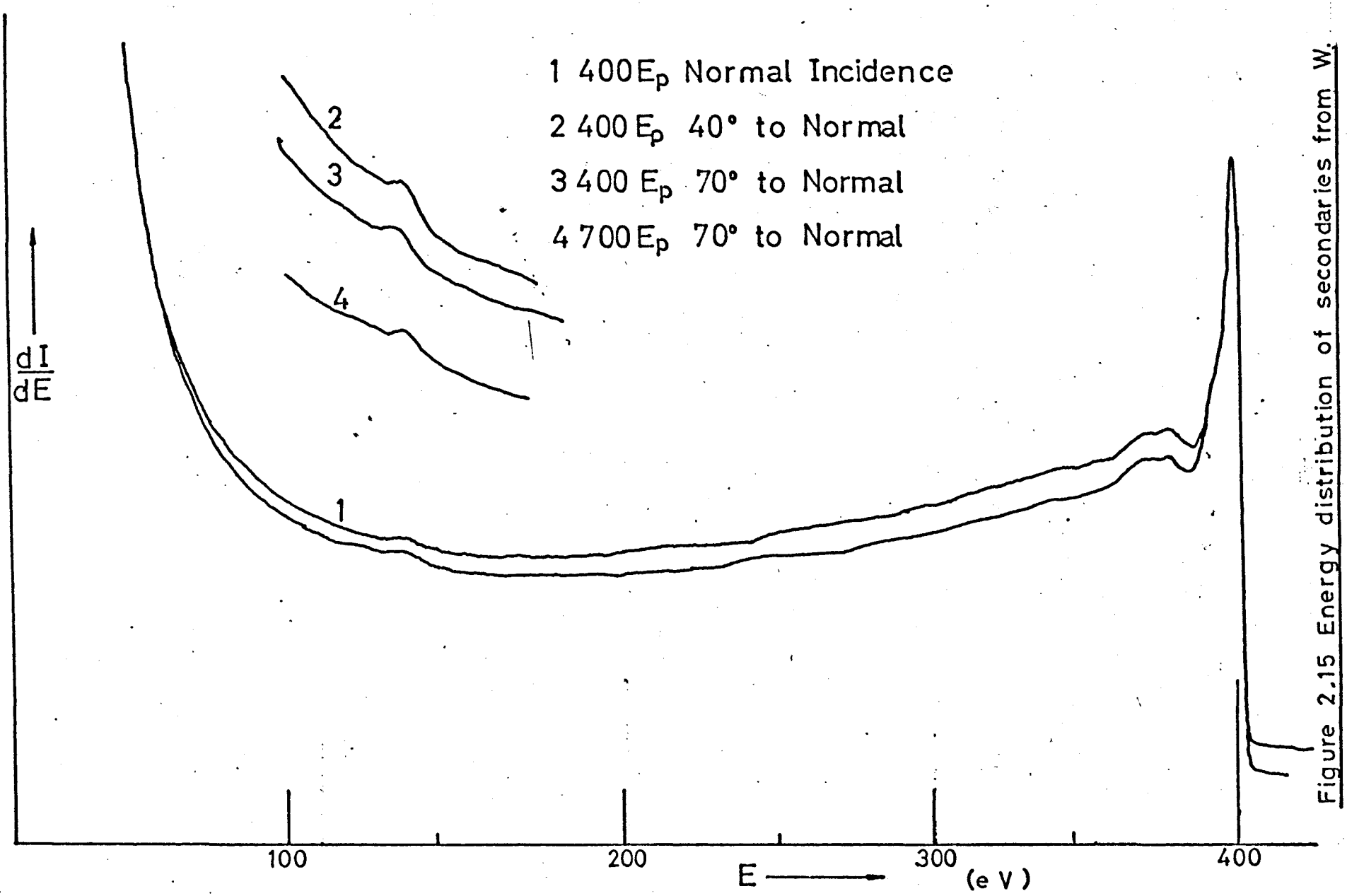

Figure 2.15 Energy distribution of secondaries from W.

supply in series with the output of the potentiometer, to enable sections of the spectrum to be scanned. However, a 'hum' signal developed on the output, presumably because neither output was earthed. This was reduced with an L C ladder smoothing network; since voltage scan rates were generally low (less than 1V/s) the time constant of the low pass filter did not interfere with the d.c. scanning.

2.2.4 Initial results and discussion

The first target used was a sheet of pure tungsten. Firstly, checks were made that the alignment of the target and electron gun were correct, and that the beam was hitting the target over a range of energies and incident angles. D.c. transfer characteristics of the analyser were then plotted, and when they seemed satisfactory the circuitry of Figure 2.8 was assembled so that we were able to plot the energy distribution of the secondary electrons.

An energy distribution plot of the unheated W surface is shown in Figure 2.15 for a primary energy of 400eV. The 'Resolution' as measured by the ratio $\Delta E/E$ for the elastic peak is seen to be about 2%. As well as loss peaks near the primary peak the spectrum showed a small bump near 150eV; this remained at the same energy, but increased in height on raising the primary energy and increasing the angle of incidence, as shown on the inset. It was therefore attributed to an Auger peak. After gentle heating, the spectrum shown in Figure 2.16 was obtained. The loss peaks found are compared with those of other workers in Table 2.I below.

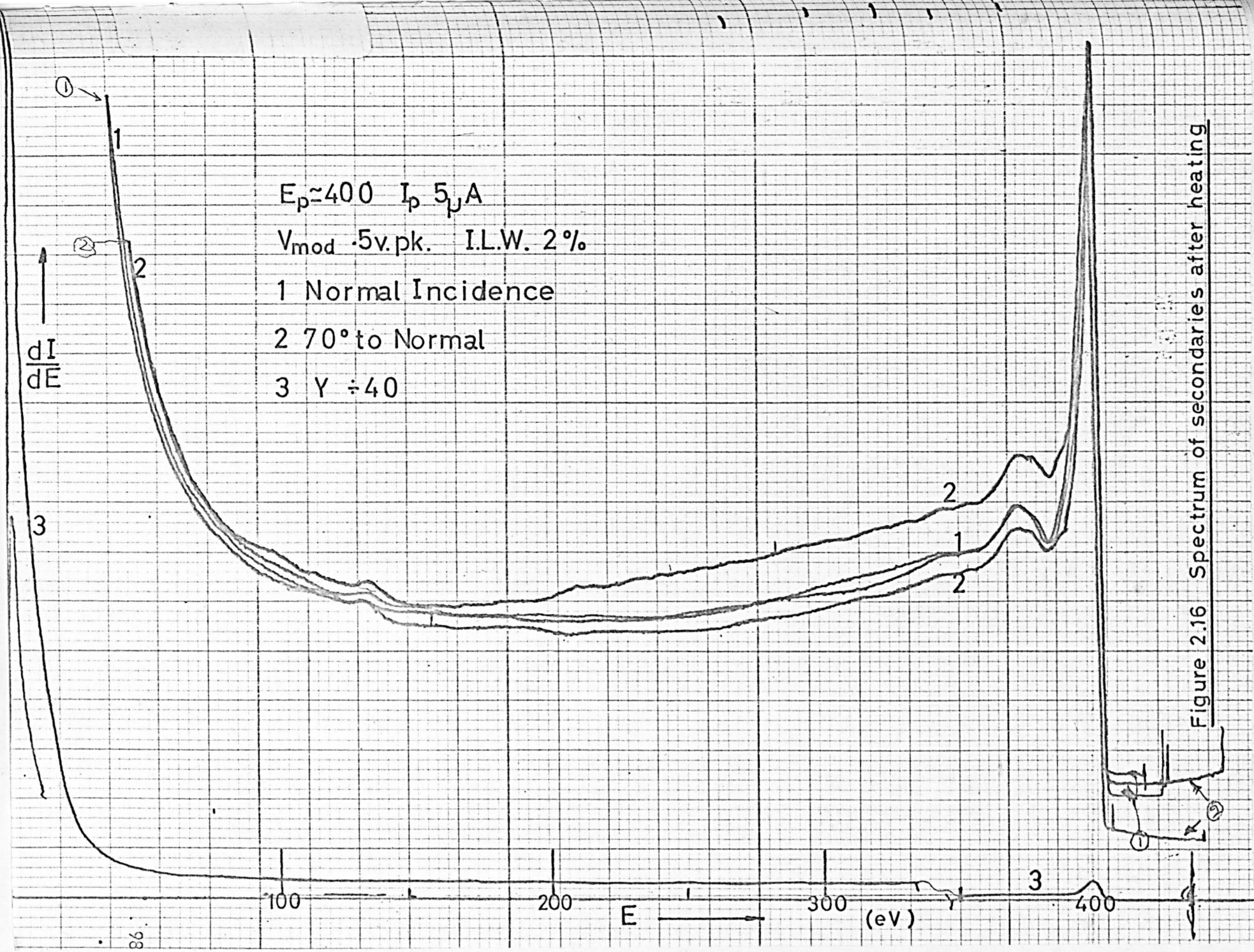

Figure 2.16 Spectrum of secondaries after heating

Table 2.I

Harrower 1956	Powell 1958	Tharp 1967	Allan 1969	Moss & Blott 1969	Suleman 1969	Present work
						4.5
			6.4	5.8		7.3
14.8	10.6	12.5	17.4	11.6	14.2	10.5
				23.3	21.6	22.8
26.8	24.3	25.5	24.7		-	27.4
			33.5	33.5	30.5	-
46.4	43.3	46	44.5	43.5	49.6	44.5
58	52.8	56	57	54	-	55.5
			75.2	69	71.7	-
88			86.6	81	86	-
					95	

The variation in these results shows how the values of the characteristic energy losses are dependent on specimen preparation. Only Moss and Blott and Scheibner and Tharp measured the Auger spectra, and only Moss and Blott could say that the contamination had been entirely removed.

Once the Auger peak at 150eV had been found, the second harmonic detection circuit was assembled and investigations were made of the

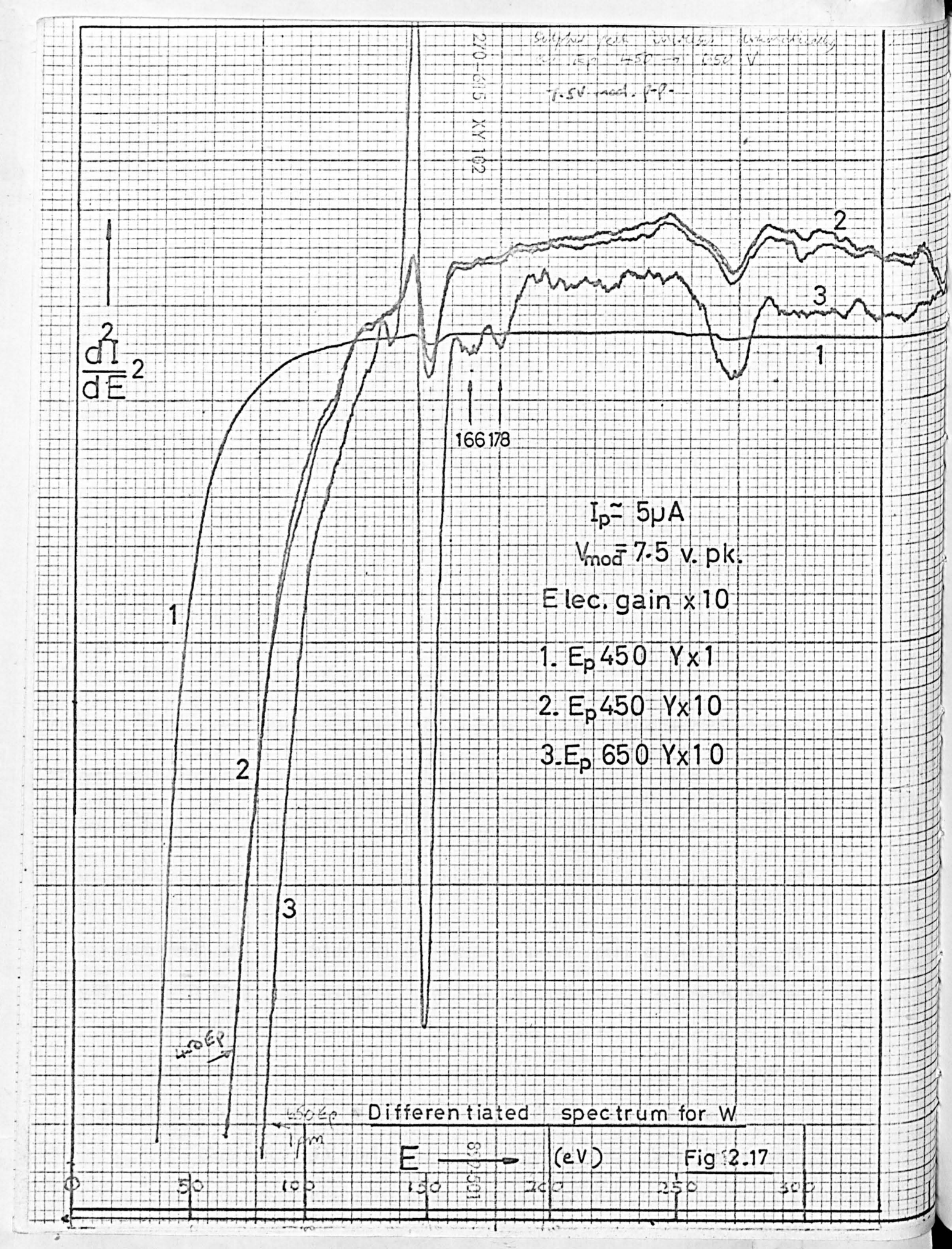

Differentiated spectrum for W

Fig 2.17

differential of the energy distribution, using the much higher modulation voltages that were then possible.

Figure 2.17 shows the effect of increasing the primary beam energy from 450 - 650eV. The peak at 150 volts was attributed to Sulphur contamination and that at 270 volts to the presence of Carbon by reference to the literature.

It was noticed that after electron bombardment for some time, at 650eV 5μA the sulphur peak decreased and the carbon peak increased as shown in Figure 2.18. On deflecting the beam, the S peak reappeared and the C peak diminished to about their original intensities. This correlation between C and S contamination was also reported by Sickafus and Colvin (1970); they observed the effect on heating a Nickel sample above 250^{o}C, but it would seem that even a modest electron beam of about 3mW/mm^{2} was sufficient to cause migration of Sulphur and/or Carbon on a dirty surface.

The small peaks seen at around 166 and 178eV in Figure 2.17 were the only tentative indications observed of Tungsten on the surface. As it was not possible to heat the surface to a sufficiently high temperature to remove the contamination, the Tungsten target was replaced by a double-sided target of Copper and Gold that had been evaporated outside the system in an oil-pumped coating unit. Figure 2.19 shows comparative spectra of the two films over the energy range 100 - 350eV. It can be seen that there is a large peak at 270eV on each surface, showing Carbon contamination, presumably from the coating unit. The spectra in

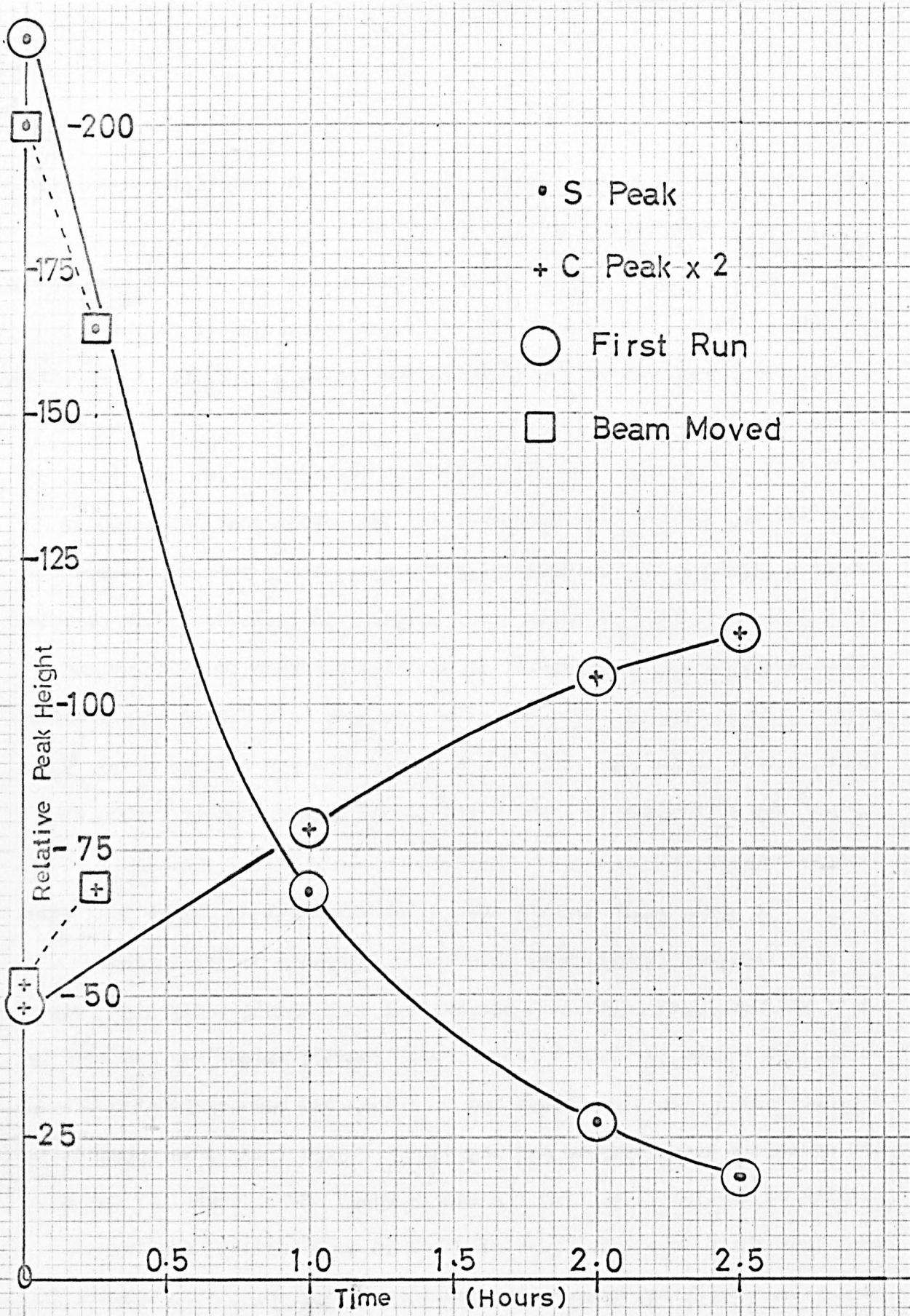

Figure 2.18 Effect of beam exposure on surface contaminants

this energy range were very similar and it was impossible to see the characteristic peaks of Gold at 150 and 250eV. These spectra were taken using the improved resonant load; note how it was possible with 8 volts modulation to increase the electrometer amplifier gain from 10 to 200.

Only very small peaks at 56 and 70eV were found on the Au surface and those on the Cu surface were even less prominent, owing to the contamination. No peaks in the high voltage range up to 1kV were found, probably because the low resolution of the analyser meant that at 1kV the instrumental width was at least 20 volts, and also this electron gun was rather temperamental above 2kV. The higher voltage Auger events are less sensitive to surface conditions than the low voltage ones because their mean free path is longer, so they should generally be found even if the low energy peaks are obscured by surface contaminants, provided their transition probability is large.

All attempts to improve the resolution of the analyser by realignment of the electron gun and target failed, and it was concluded that field penetration was limiting the resolution to the observed value of 2%. Taylor (1969) considered retarding field analysers from a theoretical point of view and came to the same conclusion; he recommended using two retarding grids separated by a small distance, and placing the inner screen grid midway between the Target and outer grids. This was just not practicable in the 150mm diameter sphere, as it would have meant using an inner grid of 50mm diameter, which would have left not enough room for the target heater, without cutting large holes in the

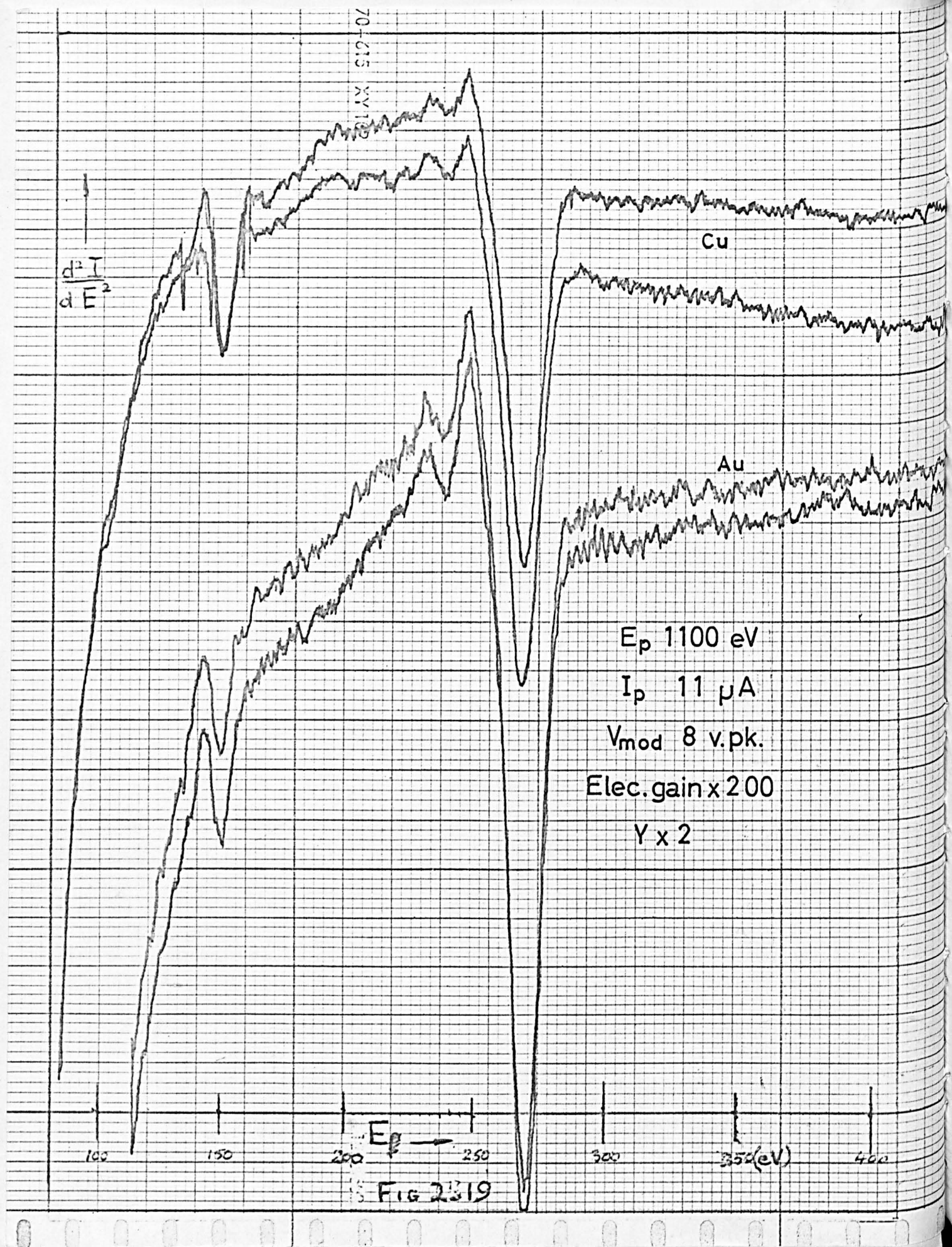
70-215 AV 1GV
$\frac{d^2I}{dE^2}$
Cu
Au
E_p 1100 eV
I_p 11 μA
V_{mod} 8 v.pk.
Elec. gain x 200
Y x 2
E_p
100
150
200
250
300
350(eV)
400

FIG 2319

grid, rather negating its purpose. These preliminary experiments had, however, proved the general applicability of the technique and the adequacy of the detection system. They also showed that if clean surfaces were to be examined by Auger spectroscopy, they could not be generated within the vacuum system by mere heating, or produced from evaporations in a coating unit, a fact which is now well known.

It was therefore decided to build a larger system so that three grids could be incorporated; a fourth grid to reduce the pick-up between the retarding grids and the collector as used by Palmberg and Rhodin, was not considered necessary, since the bridge circuits and tuned load performed so well. The more grids, the more the wanted current is attenuated on its way to the collector, and the smaller the separation between these grids becomes leading to breakdown problems. It was also decided to incorporate a molecular gun into the new system so that clean surfaces could be prepared by in situ evaporation. The development of this new system is described in the following section 2.3, together with the modifications to the detection system that were made.

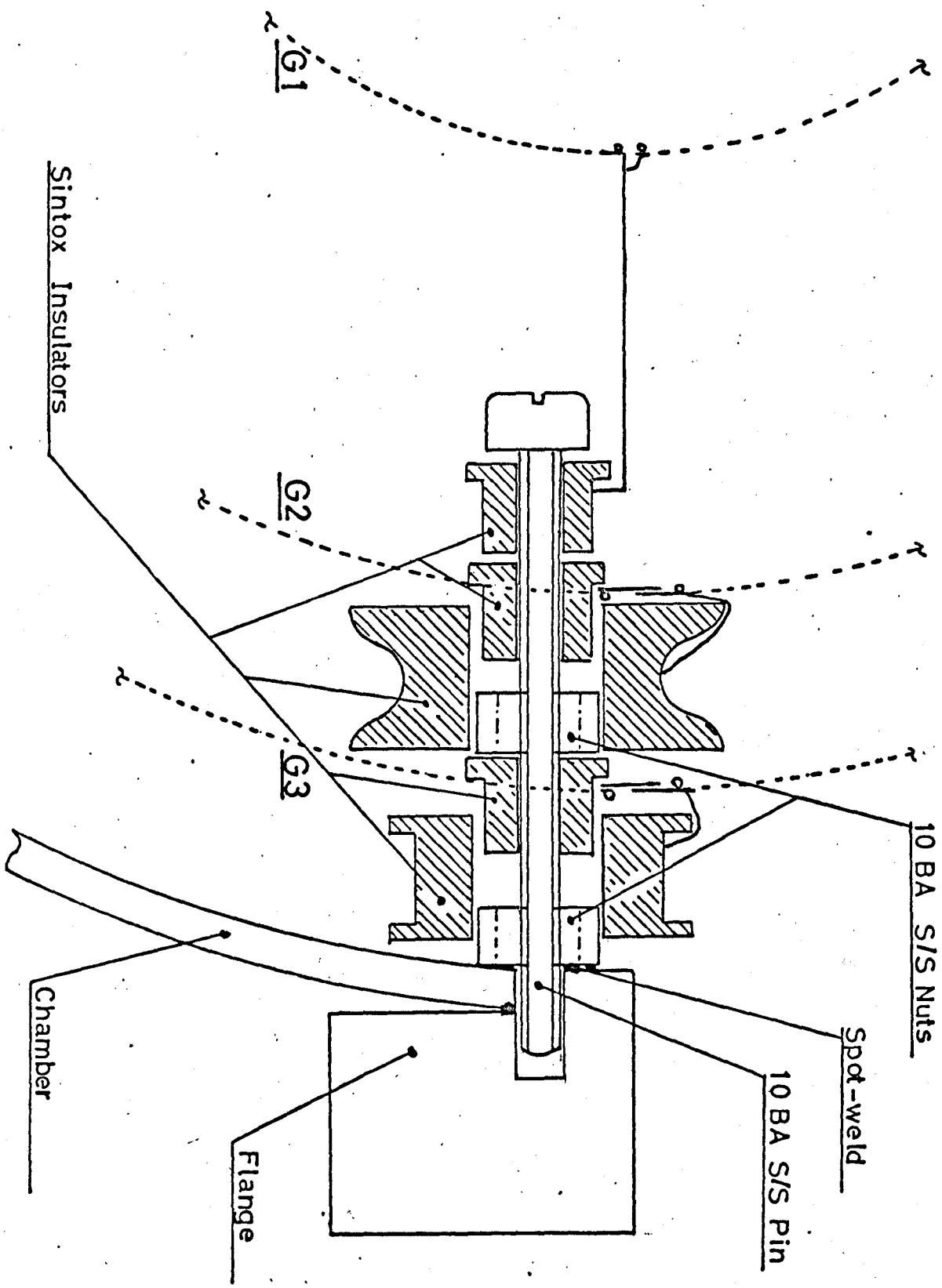

Figure 2.20 Grid connections

2.3 Subsequent Experimental Arrangement

2.3.1 Vacuum Chamber

Photographs of one half of the second vacuum chamber are shown in Plates 2.1 and 2.2. The diameter of the sphere was chosen to be about 200mm, suitable for use with a 10" copper gasket flange. All the grids were fixed into one hemisphere, simplifying the electrical connections, and enabling a rigid assembly to be constructed; the lower grids were secured using four 10BA stainless steel pins screwed onto nuts spotwelded onto the inside of the chamber flange, as shown in Figure 2.20. Sintox insulators were used as spacers, and the upper grids were pushed over the lower grids and held in place by .015" diameter Advance wire wrapped over the spacers.

The diameters chosen for the outer grids were 167mm and 187mm corresponding to the outside diameters of 2l. and 3l. spherical pyrex flasks. The .03mm x 4 lines/mm tungsten mesh used was not very rigid, and although it was easy to stretch around the flasks, it tended to distort on removal. We therefore decided to chromium plate the mesh whilst on the flask to maintain the shape; the method was similar to that described by Palmberg et al. (1964). The grids were so rigid after plating that it was not necessary to use a support ring around the holes that were cut in them. After plating, the grids were removed from the flasks and an Advance metal strip welded around their circumference to provide a firm location; Advance metal was employed rather than nickel

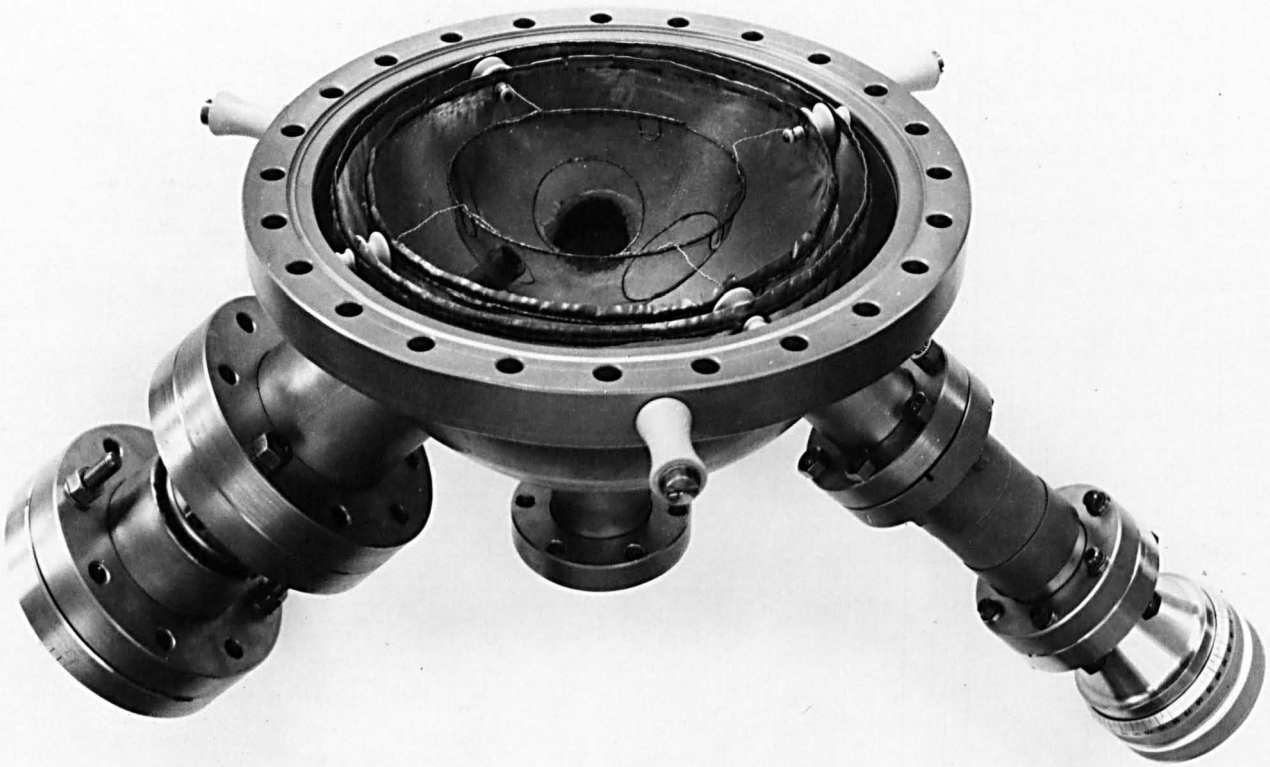

Plate 2.1

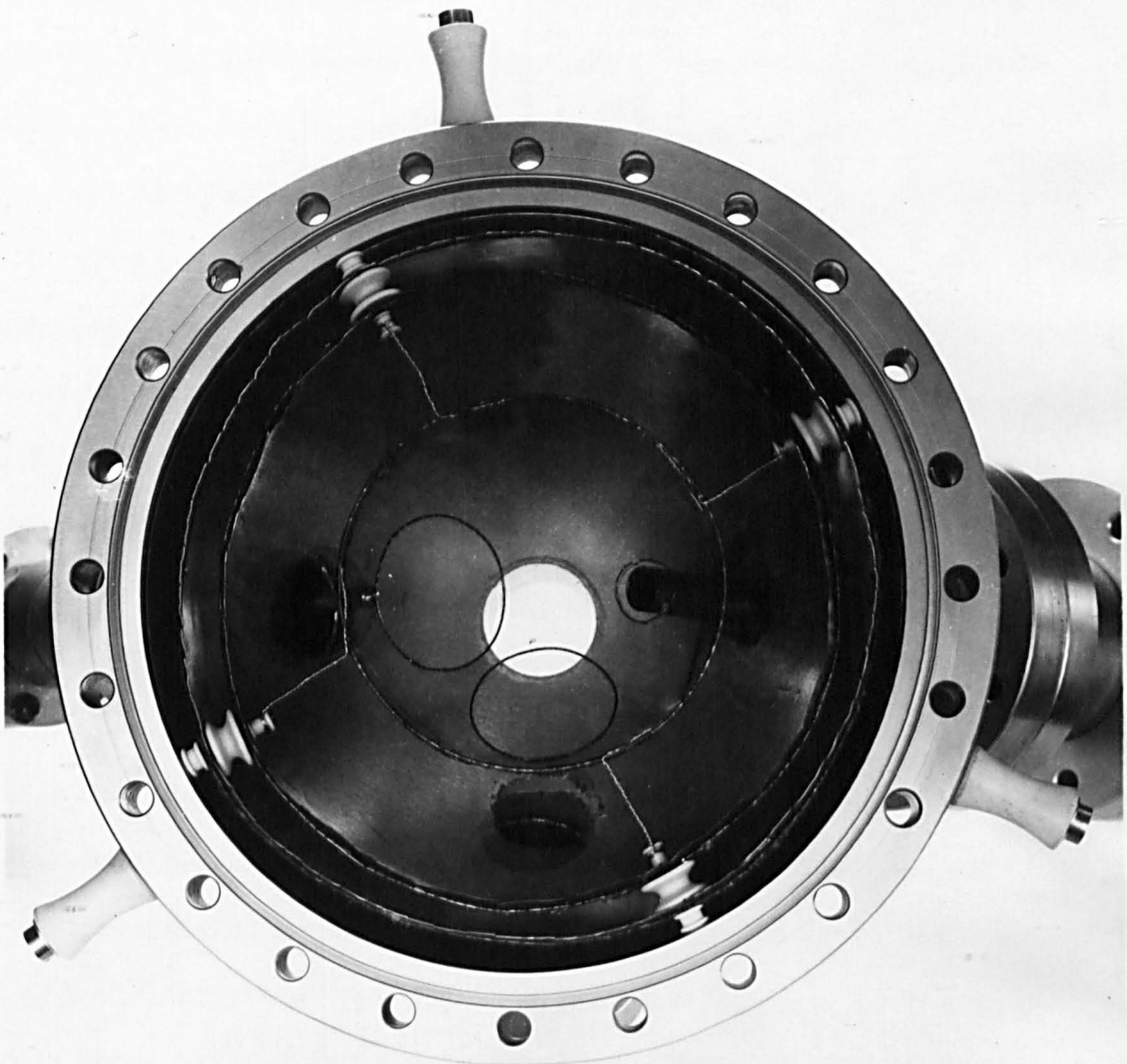

Plate 2.2

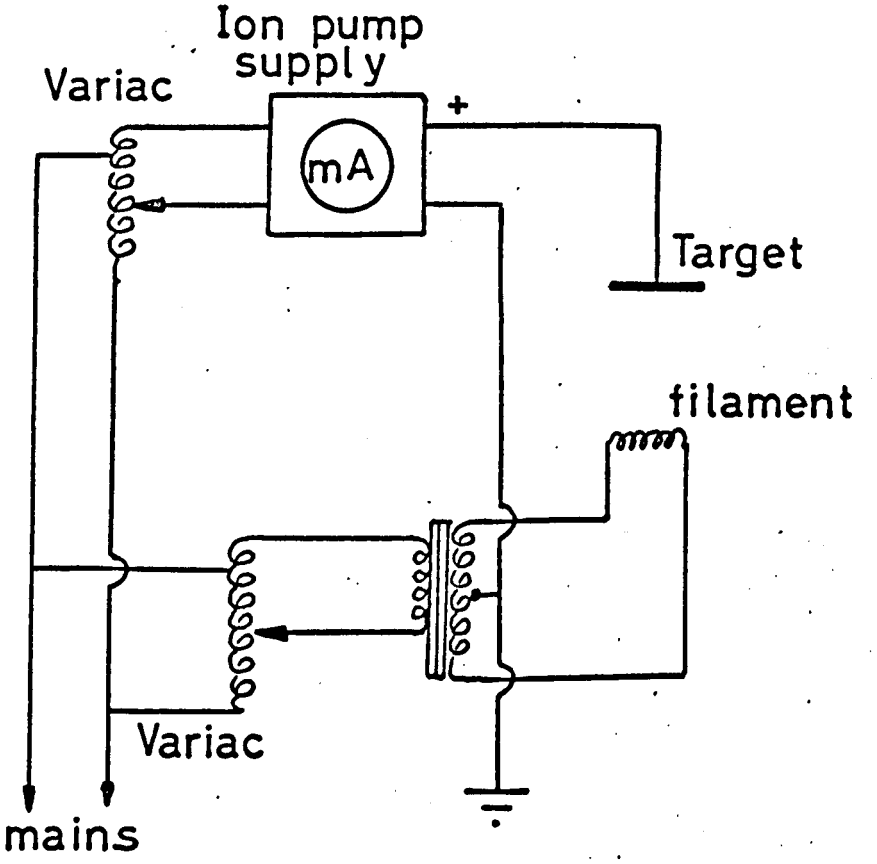

Circuit for electron bombardment

Figure 2.21

for connections since it is non-magnetic. G_1 was made as small as practicable and was 100mm in diameter,'Taylor's' optimum size being about 93mm; it was not chromium plated for the sake of increased transparency. We calculated that the plating reduced the transmission of each retarding grid to about 65%, so that the overall transmission became 38%. This was confirmed at about 40% by experiment.

Each hemisphere had a $2\frac{1}{2}$" diameter port welded in, one was used for a larger electron gun which was designed to operate at higher cathode voltages and in the other was fixed a three filament molecular gun for evaporations of the metals to be studied. The electron gun had a replaceable oxide-coated cathode, and, as previously mentioned, had a life of between five and six exposures to air. The gun mounting flange was insulated from the chamber by a ceramic section, to reduce the collection of stray electrons from the filament; and instead of mounting the target on a bellows, it was aligned at the centre of the sphere and fixed directly on a rotary motion feedthrough which was also isolated with a ceramic section from the main chamber. Using this more reliable electrical connection we were able to bias the Target up to 2kV for electron bombardment heating. The circuit used is shown in Figure 2.21; electrons were obtained from the projection lamp filament, which was isolated from the mains by a double-wound transformer, and the target potential from a 3kV ion pump power supply. The bombardment energy and current could be read off the power supply meter and controlled independentlyby two variacs, which altered the filament temperature and

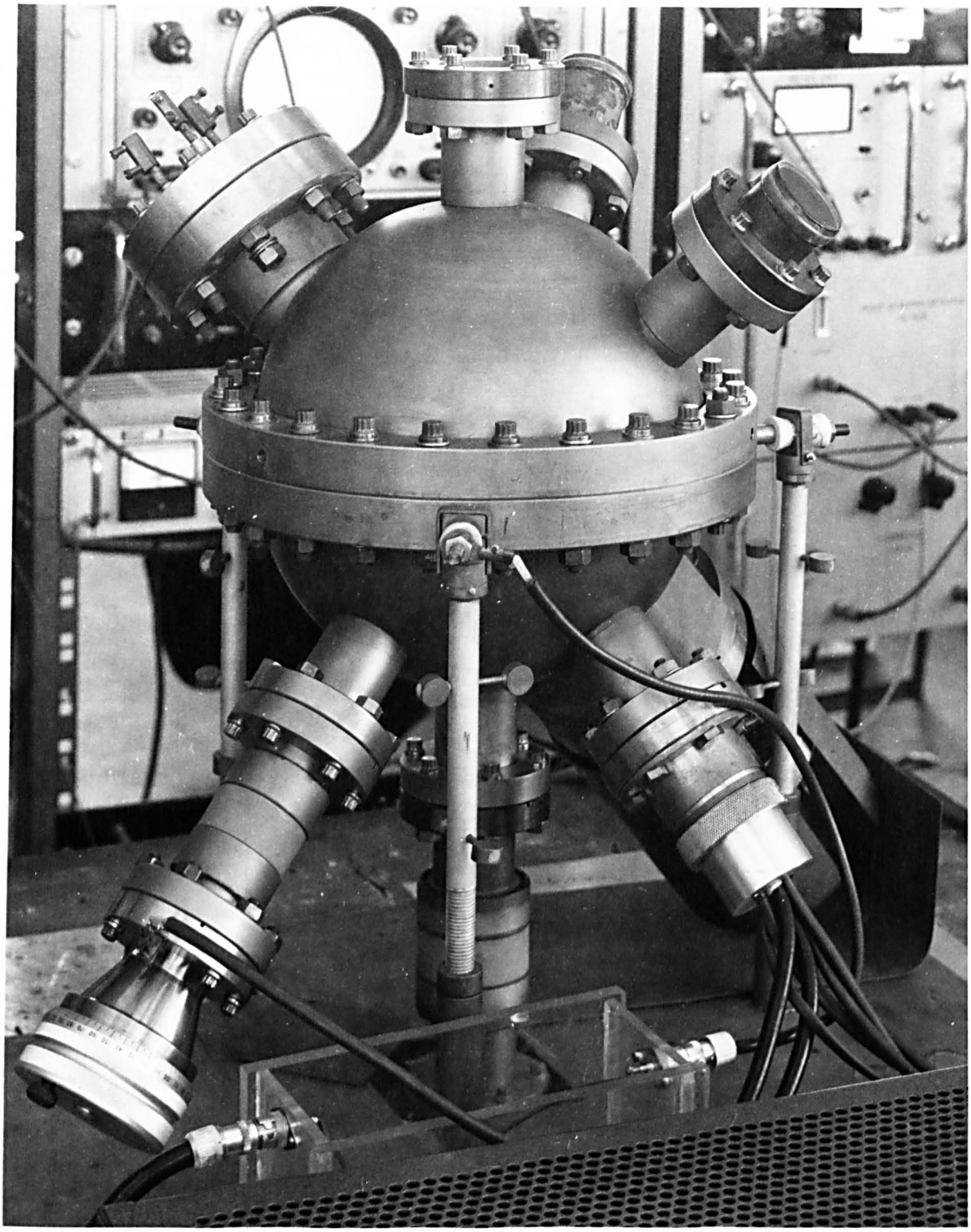

Plate 2.3

Plate 2.4

power supply voltage. We frequently obtained temperatures above 1000°C as evidenced by our inadvertently evaporating a titanium target on one occasion, and melting a stainless steel target on another! A close-up of the chamber is shown in Plate 2.3.

2.3.2 Instrumentation

No basic changes were made in the detection circuitry, shown previously in Figures 2.8 and 2.14, since the prototypes had performed so well; advantage was taken, however, of the arrival of some ferrite 'pot-core' formers to dispense with the E.H.T. coils which had been serving as inductors. Pot-core formers are made of special ferrite materials designed to reduce hysteresis losses. The particle size of the ferrites used determines the permeability and operating frequency for maximum Q. The formers used were Mullard 'Vinkors' from the 45mm range. Detailed curves for these were not available except that they had a maximum Q when used at frequencies of 1-10kHz. A photograph of the complete apparatus is shown in Plate 2.4. The first and second differential circuits were mounted together close to the apparatus to reduce noise and cable capacitance. They can be seen in the box at the front of the system. The tuned load inductor is on the left and the input transformer on the right. In the middle can be seen the bridge circuit for first differential detection; in order to increase the signal, the collector load resistor was increased to 5MΩ, and the modulating frequency reduced to about 30Hz. For the second differential mode the modulating frequency was about 3kHz, with detection at 6kHz, as

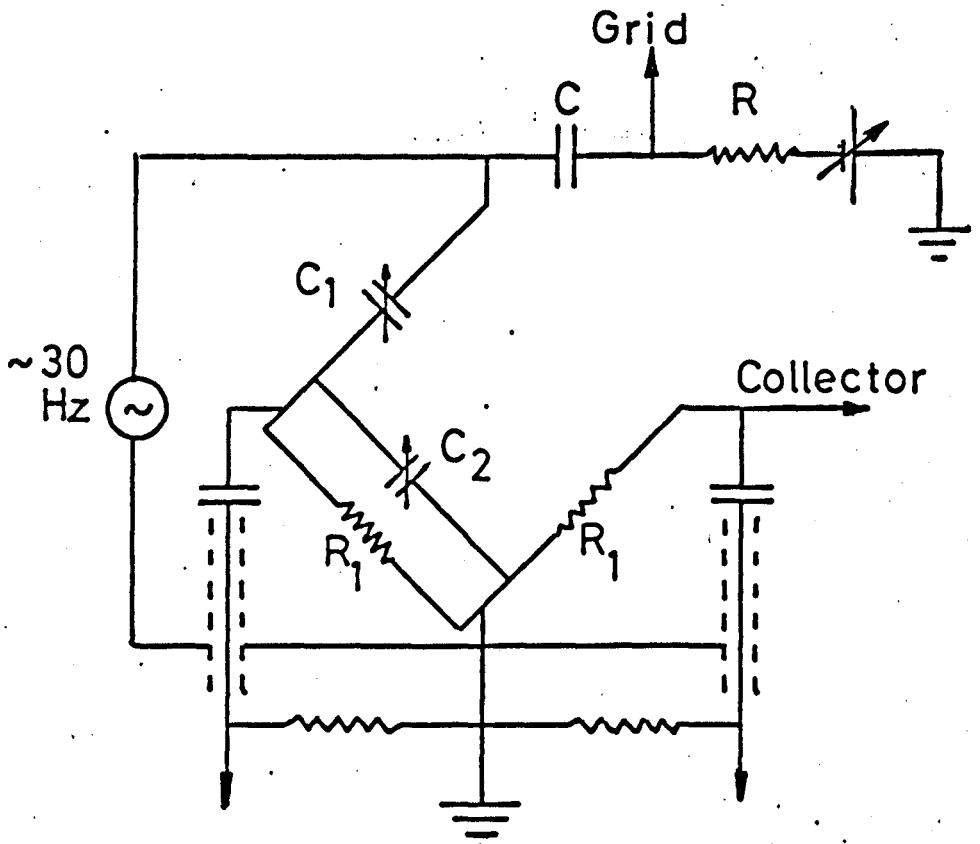

C 0.1μF 2 kV R 470kΩ
C_1 100-130 pF R_1 5MΩ
C_2 0-100 pF

Low frequency bridge circuit

Figure 2.22

a result of the different characteristics of the pot-core inductor.

The bridge circuit is shown in Figure 2.22; at a frequency of 30Hz, the impedance of the collector to earth capacitance is about 20MΩ, whereas at 3kHz, it is 200kΩ, hence the improvement in sensitivity. A phase shift exists across the C - R combination at lower frequencies, so that the balance point is frequency dependent, and the component values not quite those expected. We were now able to employ modulating voltages of up to 5V pk-pk before overloading the electrometer input valves.

The circuitry for second harmonic detection was unchanged except for the substitution of ferrite pot-core inductors for the older coils. The new tuned load circuit has been shown in Figure 2.11. R_s was increased to 3MΩ for increased rejection and so the collector battery was increased to +120V. Thus even when examining the slow peak region, where the retarding grid volts are low, collector currents of up to 20μA could be employed and the collector potential still remain above +50V, thus preventing tertiary electrons from interfering with measurements. The inductor was wound with 1160 turns of 32 swg silver plated P.T.F.E. insulated wire. Its d.c. resistance was only 34Ω, calculated inductance 2.2 henries, and resonant impedance 150MΩ. In practice the inductance was measured as 2.2 henries but losses in the core reduced the resonant impedance when used with the collector-earth capacitance to about 25MΩ. Because of the lower coil resistance we were now able to use up to 10V pk-pk modulation, before pick-up of the residual second harmonic

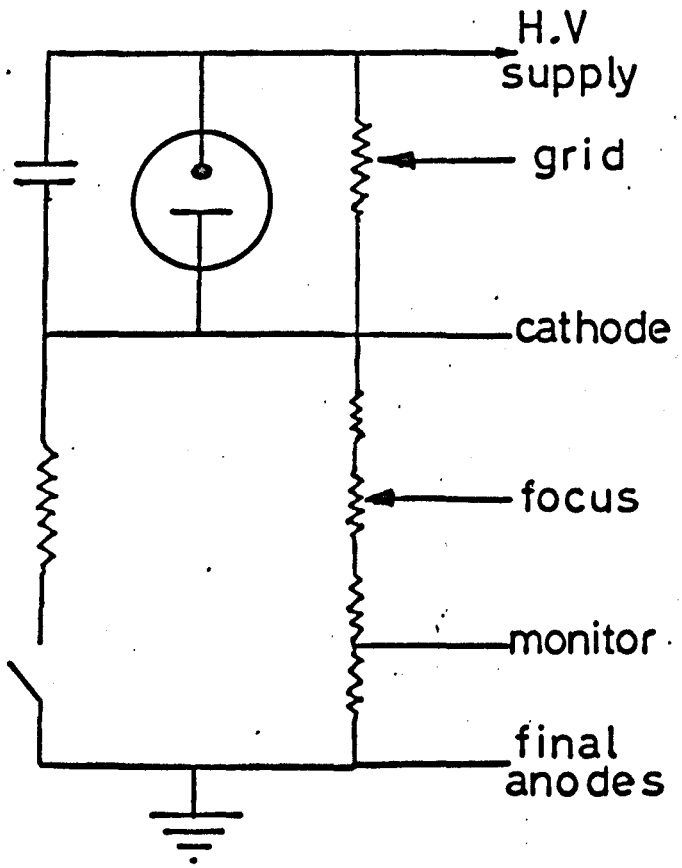

Modified electron gun control

Figure 2.23

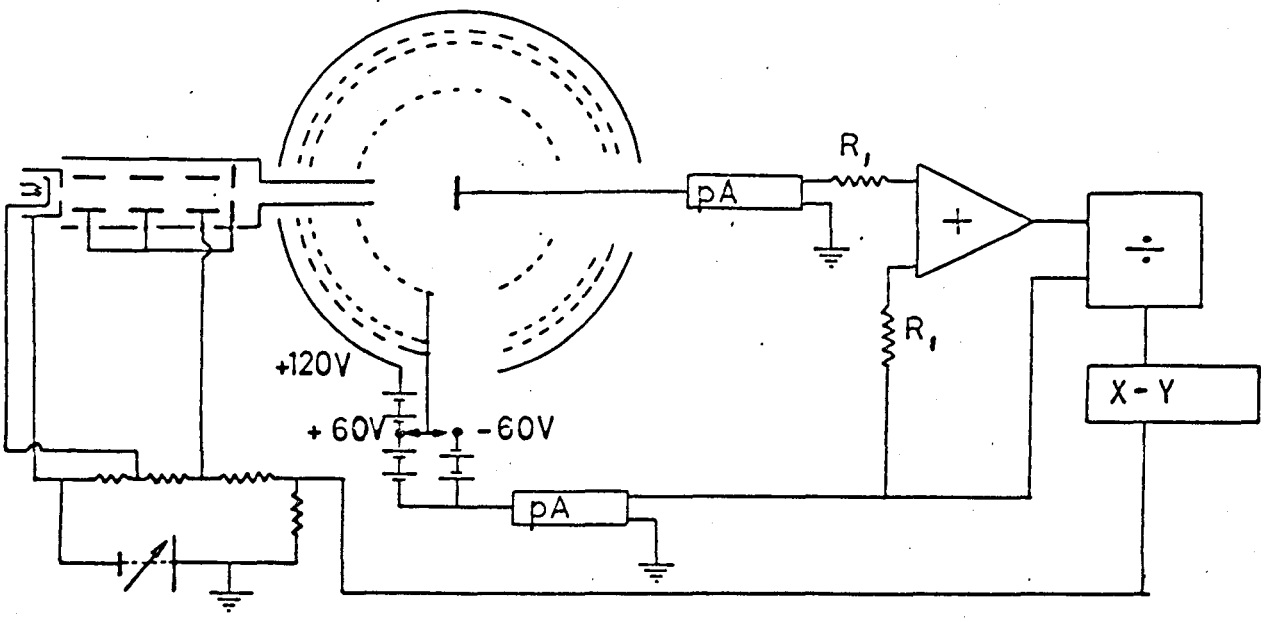

Circuit for yield measurement

Figure 2.24.

distortion exceeded the maximum input level of the phase sensitive detector, and by removing an amplifier, we could use 20V pk-pk.

Some changes were made in the power supplies to the electron gun, so that it could be operated at up to 2.5kV, and also be used for yield measurements. We found that at higher cathode voltages, the emission current of up to 2mA flowing through the grid control potentiometer tended to make it overheat and become noisy; we thus incorporated a neon tube in the circuit for use above 1kV, below this voltage the H.T. was applied direct to the grid as before. The modified circuit is in Figure 2.23.

2.3.3 Yield measurement

For yield measurements, the ramped H.T. was applied direct to the grid, and the switch opened, preventing the neon from striking; a fraction of the cathode voltage was applied to the XY recorder. The remainder of the yield measuring system was similar to that described by Thomas and Pattinson (1970) and is shown in Figure 2.24.

For measurements of the total secondary yield the three grids were connected to +60 Volts and the collector to +120 Volts; for measuring the backscattering coefficient, η, the polarity of the grid voltage was reversed. The value of 60 Volts was chosen because of the convenient availability of batteries. The presence of the extra grids does not affect the accuracy of the yield measurements, since they are all connected in to the collector circuit and their potentials ensure that no tertiary electrons can reach the target.

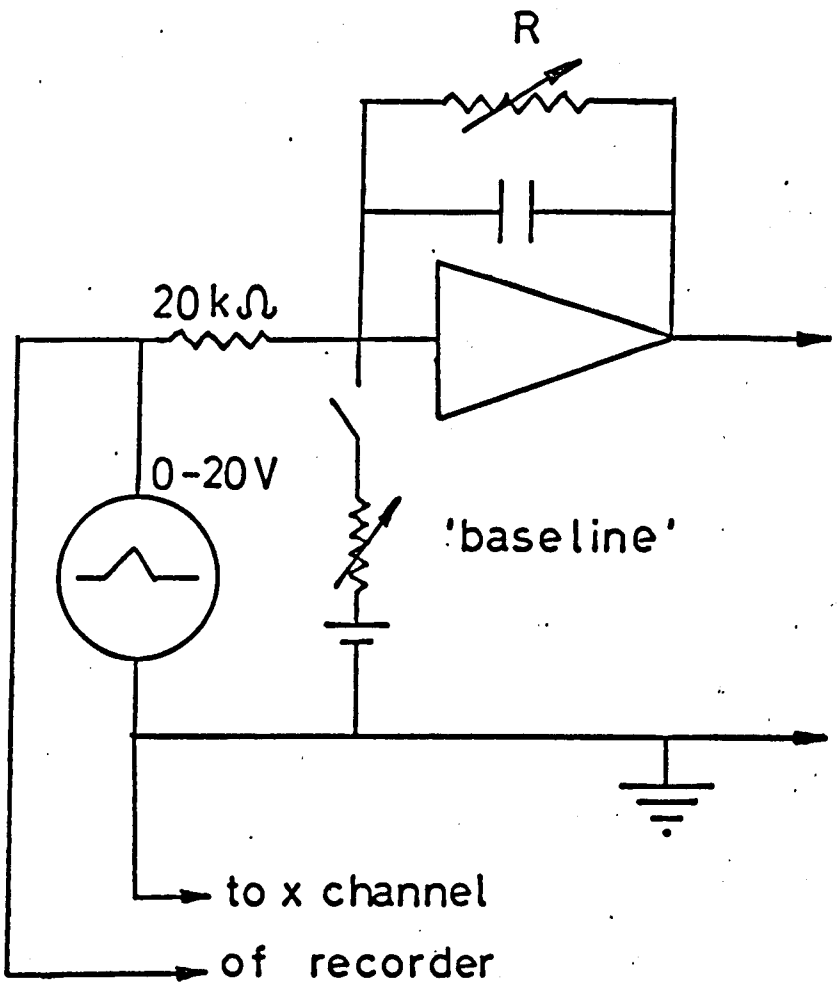

Figure 2.25 Ramp generator

2.3.4 Ramp generator

Towards the end of the research period, we were fortunately able to dispense with the motorised helipot and floating power supply, and replace them with an operational power supply and slow scan generator (Kepco OPS and FG-100). The arrangement is shown in Figure 2.25. The power supply is a high gain amplifier with negative feedback, so that under all conditions the input voltage and current must be zero; if a current i_o is fed in from an external source, the power supply attains an output voltage such that all the current flows around the feedback loop through the resistor R. In our case, R is 100kΩ or 1MΩ so that with 1mA output from the function generator the full scale output is 100V or 1kV respectively. In addition a variable 'baseline' can be provided, so that it is possible to scan from, say 500 - 600 Volts, by injecting a constant 0.5mA from the baseline control and 0 - 0.1 mA from the function generator, with the feedback resistor at 1MΩ. For the yield measurements a power supply with a 2MΩ feedback resistor can be used, giving an output voltage of 0 - 2 kV.

Another use was found for the floating power supply; by applying a positive voltage V to the target the effective primary energy is increased by V and the apparent energy of an Auger peak reduced by V. Target biasing may thus be used to increase the ionisation cross-section for high energy Auger peaks, and reduce the grid voltage required to see them. By using the floating supply between the target and the pico-ammeter, as shown in Figure 2.14, the target biasing could be achieved

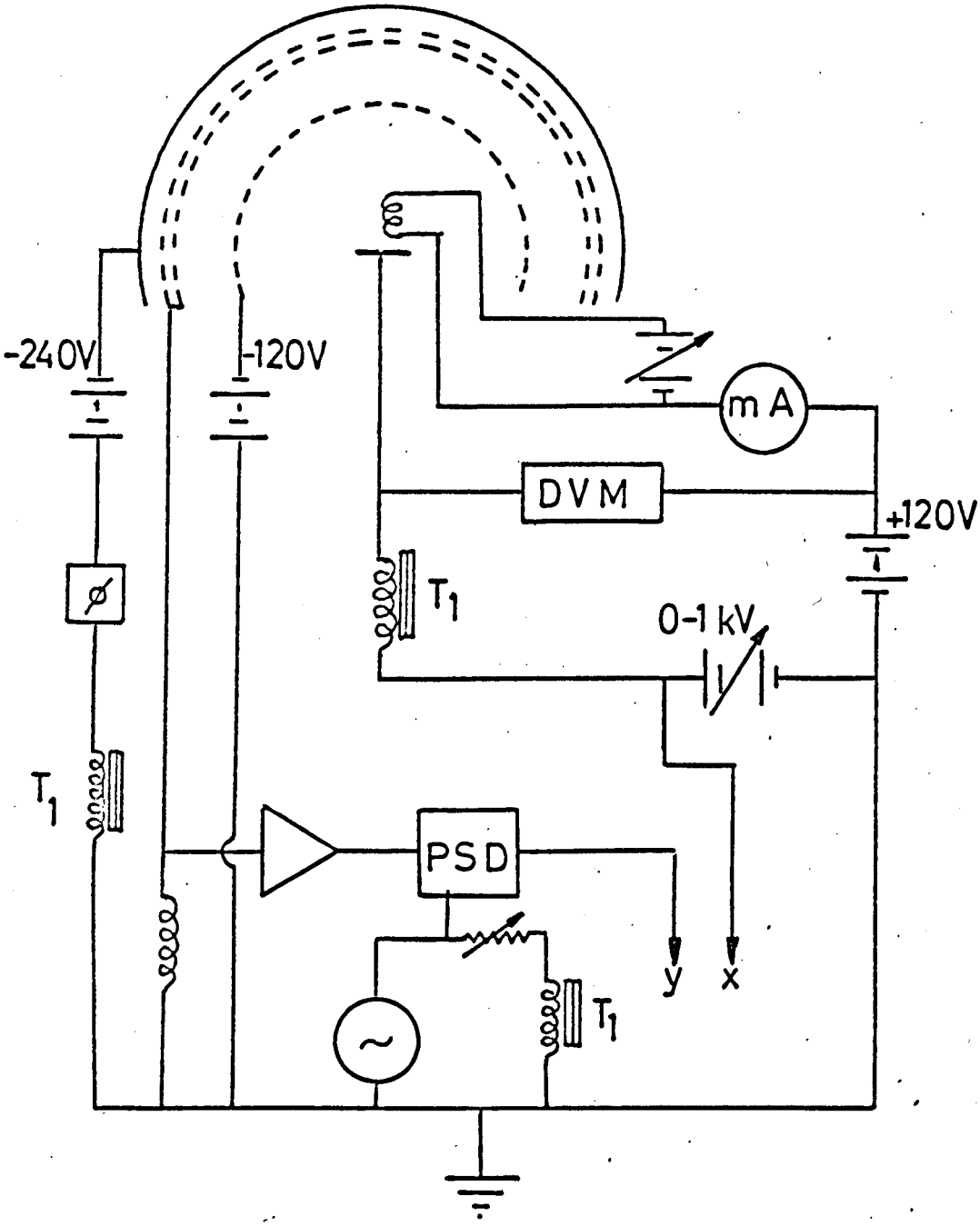

Figure 2.26 Circuit for appearance potential study

and the target current measured; to maintain the field-free region around the target, the inner grid was elevated to the same potential as the target. We also tried target biasing when examining the variation of surface and bulk plasmon intensity with primary energy; the idea was that by simply altering the potential of the target, it would be possible to alter the effective primary energy, keeping the current, and retarding grid voltage constant. This idea did not seem to work too well, since the amplitude of the elastic and loss peaks was much reduced when a few hundred volts was applied to the target (Chapter 5.7). Unfortunately we did not have the time to investigate the reason for this.

2.3.5 Appearance potential spectroscopy

Following publications by Houston and Park (1971), and Park and Houston (1970,71), we thought that it should be possible to use a retarding field analyser as an appearance potential spectrometer, so that we should be able to measure directly the binding energies involved in Auger transitions. The circuitry used is shown in Figure 2.26. The only modification to the vacuum system involved providing a filament as a source of electrons close to the target; for this we used a 6 Volt car headlamp filament.

It is necessary to choose the biasing potentials for the electrodes carefully, to ensure that neither 'primary' electrons from the filament nor secondaries from the target are able to be collected on the collector grids. To this end, the target and filament are biased

positively and the inner grid negatively with respect to the collector grids. X-rays leaving the target strike the walls of the vacuum chamber, liberating photo-electrons; since the collector grids, at earth potential, are the most positive electrodes between the inner grid and the chamber walls, the photo-electrons will be collected on these grids. Modulation is applied to the target through T1, which also supplies the reference channel of the P.S.D. and balancing modulation to the vacuum chamber walls, so that the pick-up signal from target to collector grids can be nulled. The circuit as a whole is similar to one described by Haas et al. (1972), but was, of course, developed independently.

Investigations were limited to a study of evaporated silver concurrently with Auger spectroscopy. Despite a protracted search, using currents of up to 1mA and detection circuitry capable of measuring 1pA, no trace of any signals was found. Apparently, appearance potential spectroscopy only works well for a few lucky metals, and silver isn't one of them! No doubt, the circuit shown is capable of appearance potential spectroscopy provided that the right target is used. Time limitations prevented further experiments in this direction.

2.3.6 Magnetic screening

The magnetic field in the vicinity of the sphere was too small for reliable measurements to be made with Hall probes; since the effect of the stray magnetic field on the performance of the analyser is deflection of the primary and secondary electron beams, this deflection

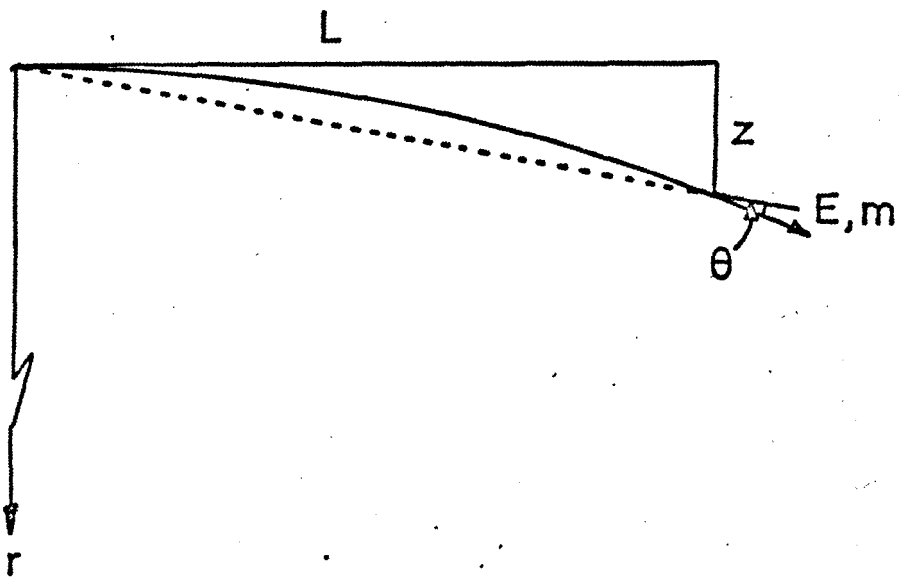

Deflection of electrons in a magnetic field

Figure 2.27

was employed in measuring the stray magnetic field.

We used a complete cathode ray tube with a length of 20cm from gun to screen. With reference to the Figure 2.27, the field B in Tesla is given by

$$B = \frac{2z}{L^2}\sqrt{\frac{2mV}{e}} \qquad \text{where } E = eV$$

We noticed that a vertical beam was undeflected, so the main component of the field was vertical. A horizontal beam of 500eV was deflected about 1 cm.

$$B = \frac{2 \times 10^{-2}}{4 \times 10^{-2}}\left[\frac{9.1 \times 10^{-31} \times 2 \times 500}{1.6 \times 10^{-19}}\right]^{\frac{1}{2}}$$

$$\approx \tfrac{1}{2}(6 \times 10^{-9})^{\frac{1}{2}}$$

$$\approx \underline{4 \times 10^{-5} \text{ Tesla or } 0.4 \text{ gauss}}$$

This is only about 2.5 times the earth's field, which shows that the Netic* screening around the ion pump magnet was efficient. When the measurement was repeated with a CoNetic* screening can surrounding the chamber, the voltage for $\frac{1}{2}$cm deflection reduced to ~100eV.

$$\text{i.e. } B = 1 \times 10^{-5}\text{T or } 0.1 \text{ gauss}$$

This was a 'worst case' measurement, and for the majority of the chamber volume, the field was less than this. Also, in order to measure the

* Perfection Mica Co., Chicago.

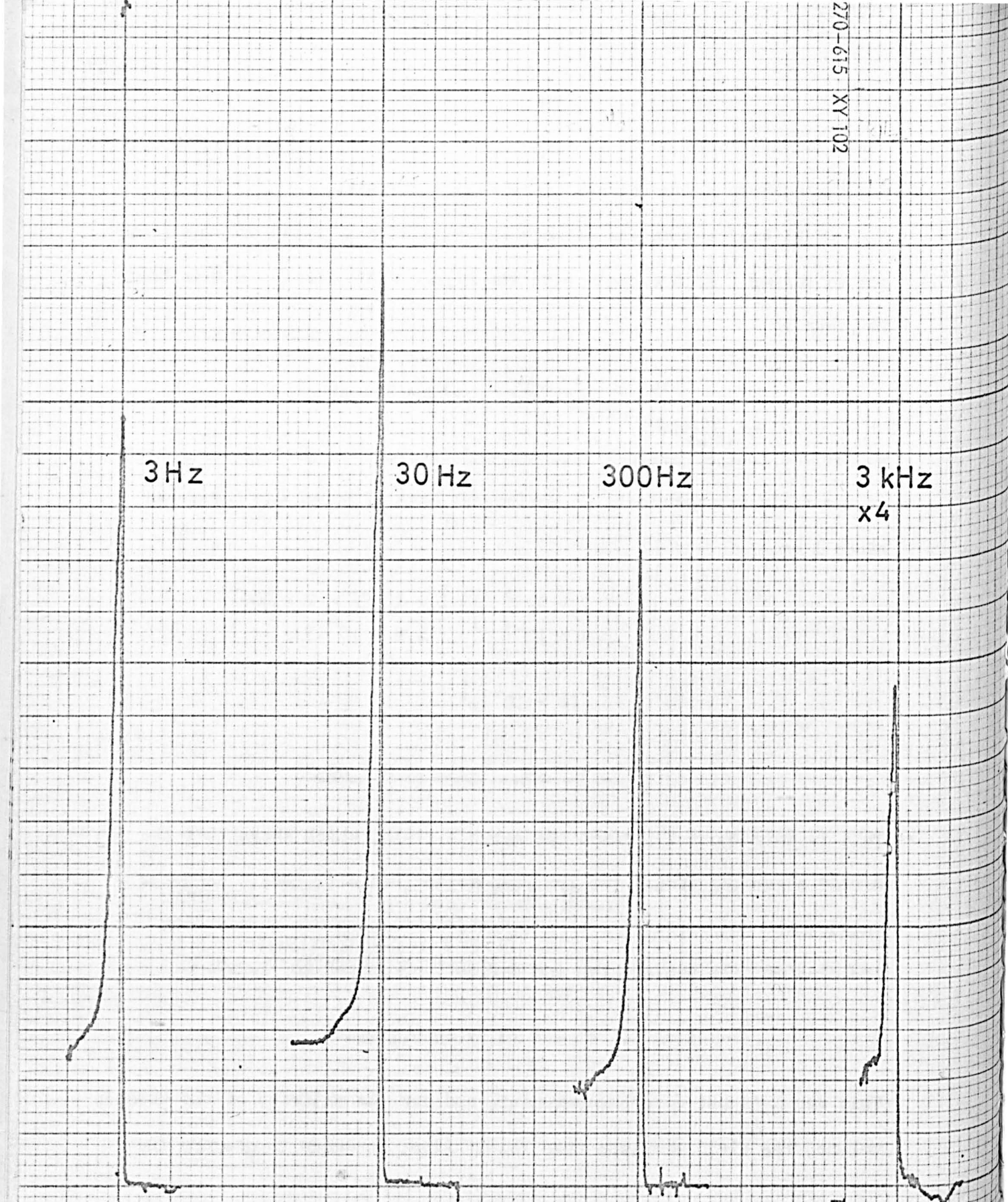

Figure 2.28 Elastic peaks using first bridge circuit

deflection it was necessary to remove some of the screen, which might also have increased the value obtained.

For considering the effect of the magnetic field on the resolution of a retarding field analyser, all we need is the cyclotron radius of the slowest electrons to be analysed in this field. Referring to Figure 2.27

$$r = \frac{1}{B} \frac{2mV}{e}$$

For 1eV electrons in a field of 1×10^{-5} Tesla

$$r = 0.4 \text{ m}$$

From the Figure

$$\text{Tan } \theta \approx \frac{R}{2r},$$

where R, the radius of the analyser grid is equal to L.

$$\text{Resolution} = \tan^2\theta = \left(\frac{R}{2r}\right)^2$$

So resolution is proportional to $\left(\frac{1}{r}\right)^2$, i.e. $\frac{B^2}{V}$

For present system where R = 9cm,

$$\text{Resolution at 1eV} = \left(\frac{9}{80}\right)^2 = (0.11)^2 \text{ or } \underline{1.2\%}$$

$$\text{Resolution at 10eV} = 0.1\%$$

This resolution is adequate for examining fine structure in the slow peak region from 0 - 25eV; without the screen the field is a factor of 4 higher, degrading the resolution to about 20%.

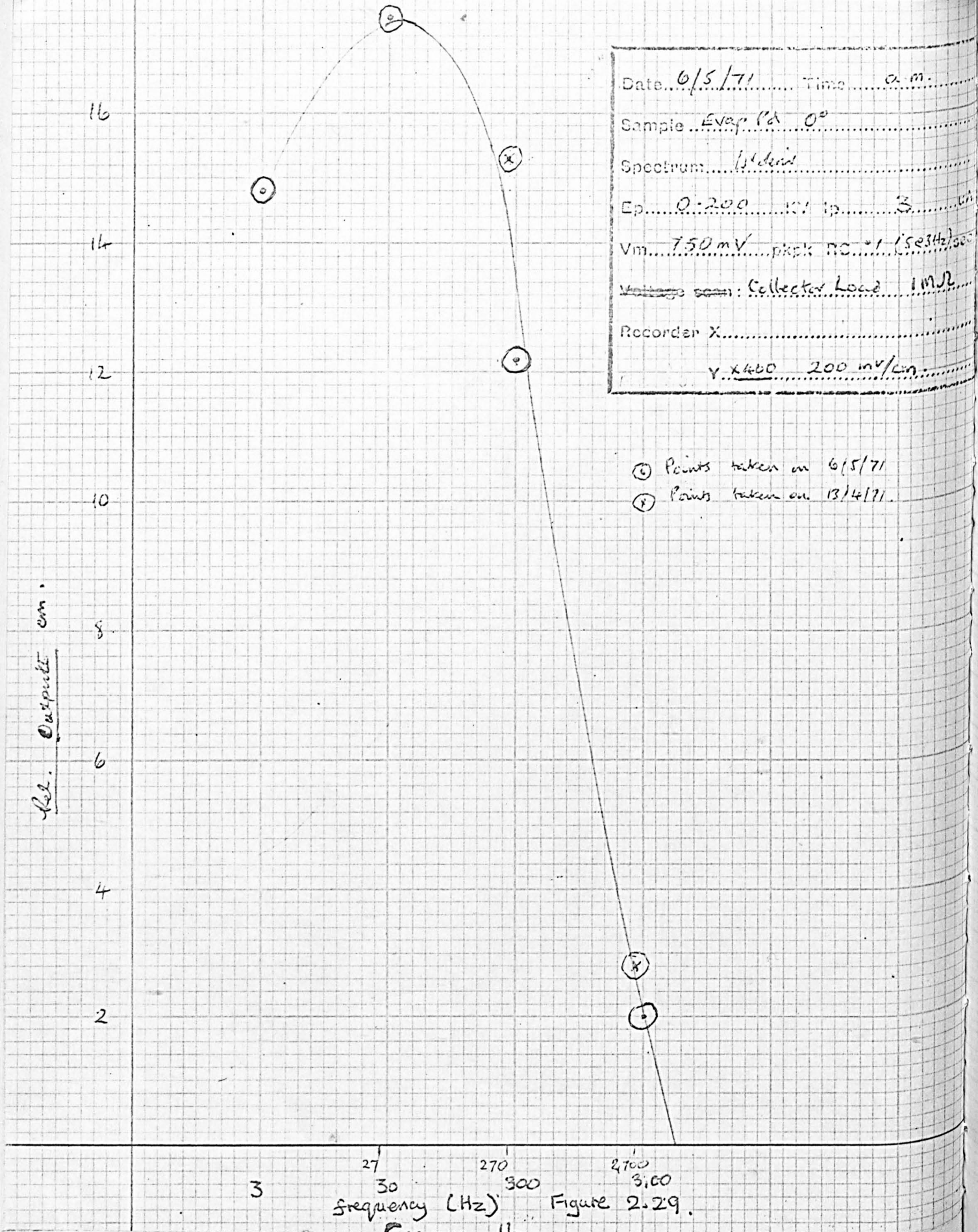
Date 6/5/71 Time a.m.
Sample Evap Pd 0°
Spectrum Helios
Ep 0-200 mV tp 3 ms
Vm 150 mV pick no. 1 (583 Hz)
Collector Load 1 MΩ
Recorder X
Y x400 200 mV/cm
Points taken on 6/5/71
Points taken on 13/4/71.
Rel. Output em.
16
14
12
10
8
6
4
2
27
30
270
300
2700
3,00
3
Frequency (Hz)

Figure 2.29.

Figure 2.30 Elastic peaks from modified bridge

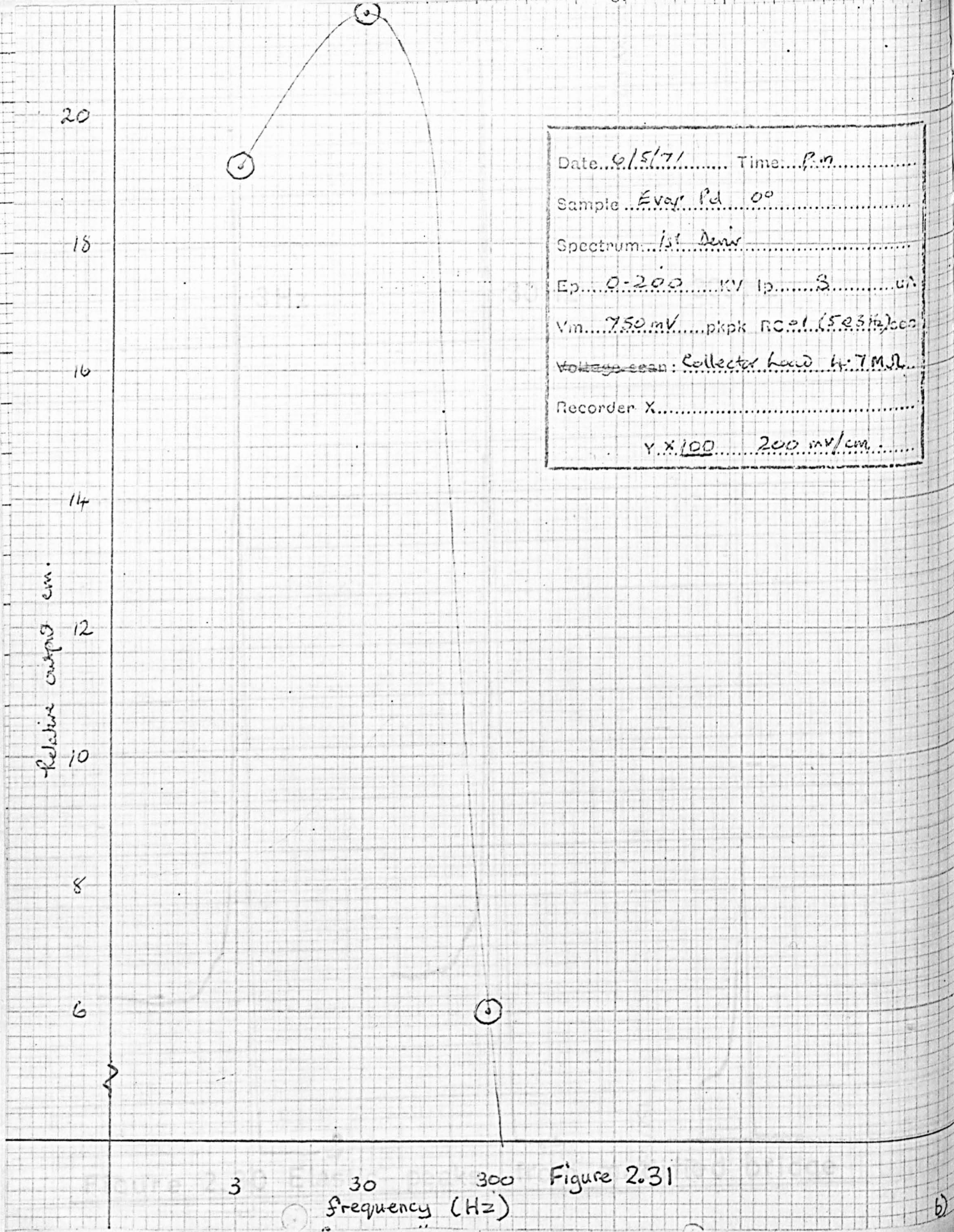
20
18
16
14
12
10
8
6
Relative output cm.
3
30
300
Frequency (Hz)
Date 6/5/71 Time p.m
Sample Evap Pd 00
Spectrum 1st Deriv
Ep 0-200 KV Ip 3 uA
Vm 750 mV pkpk RC=1 (5e3 Hz)
Voltage scan: Collector load 4.7 MΩ
Recorder X
Y X100 200 mV/cm

Figure 2.31

2.4 Comparative Results and Discussion

2.4.1 Modified bridge circuit

Figure 2.28 shows plots of the elastic peak on an evaporated palladium surface, taken using the original bridge circuit of Figure 2.7, at four different values of modulating frequency. We took care to keep all the other parameters constant, but, because of phase-shifts, it was necessary to rebalance the bridge at each frequency.

Figure 2.29 gives the variation of peak height as a function of frequency, including two results taken previously; it can be seen that the sensitivity at 30Hz is some 9 times that obtained using 3kHz, presumably because of the variation in the impedance of the collector to earth capacitance with frequency; as this impedance is about 20MΩ at 30Hz, we tried increasing the collector load resistor to 5 MΩ using the circuit shown in Figure 2.22. The elastic peaks we obtained under the same conditions as before, with the new circuit, and the electrometer gain reduced by a factor of four, are shown in Figures 2.30 and 2.31; the output at a frequency of 3kHz was too small to be worth recording. It is evident that the overall improvement resulting from a reduction in frequency and increase in collector load was a factor of about 44 in sensitivity. Also, with the new bridge circuit we were able to use modulation amplitudes of up to 5V pk-pk, before overloading the input tubes.

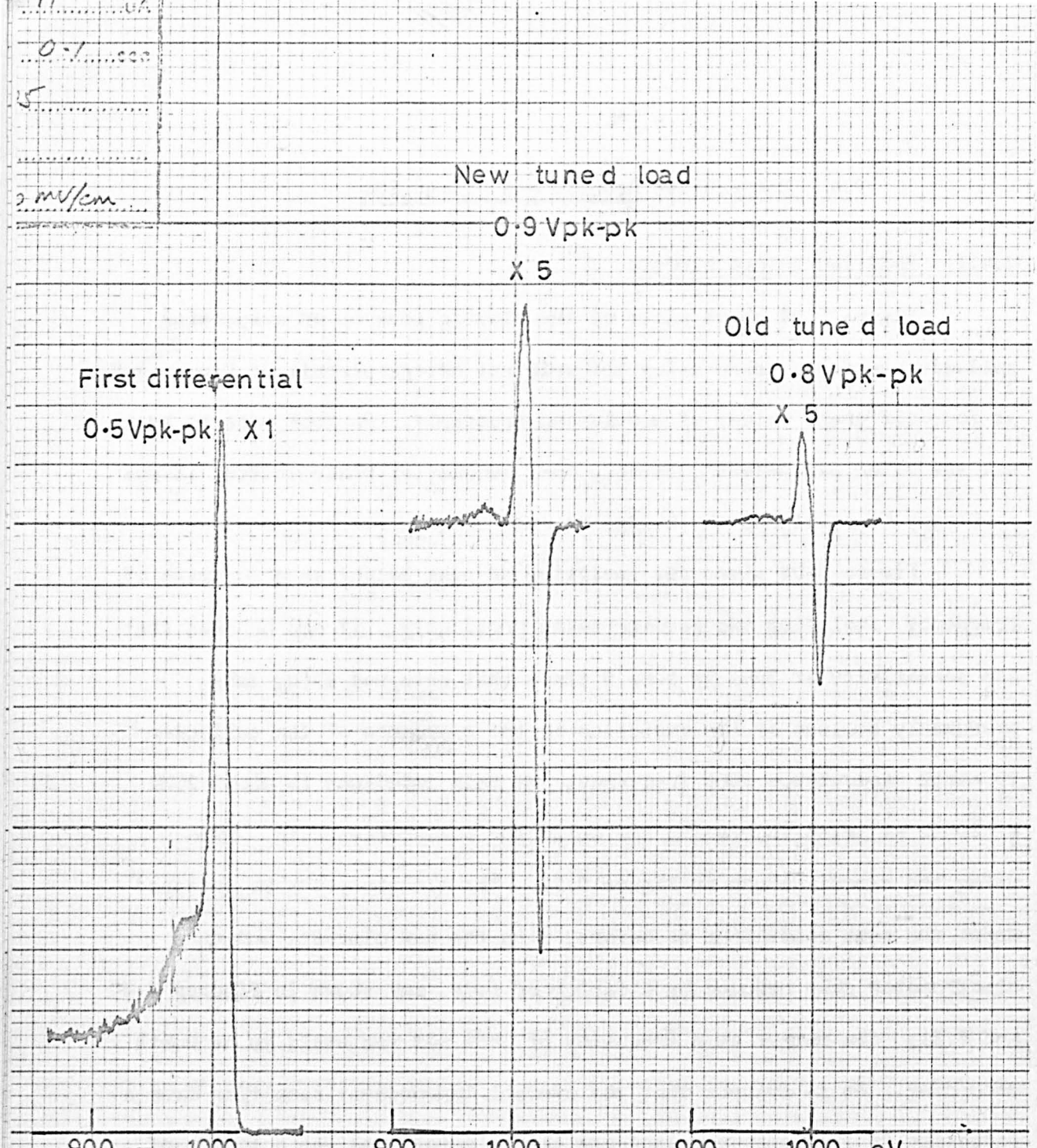

Figure 2.32 Comparison of first and second differential

154702-002

2.4.2 New tuned load

The effects of the new tuned load were less dramatic, but fortunately we did see an improvement in sensitivity as can be seen from Figure 2.32, which shows a differentiated elastic peak obtained using the new and old tuned loads, and, for comparison, the undifferentiated elastic peak using the new bridge circuit. The improvement resulting from the pot-core inductor was just over a factor of two; notice how at this modulation, the undifferentiated peak would be about ten times the height of that obtained by the tuned load. However, it should be remembered that the current in the second harmonic is proportional to the square of the modulation amplitude, while that in the first harmonic is directly proportional to the amplitude, so that a level of 9V pk-pk the second differential would be approximately equal sensitivity to the first differential.

2.4.3 Electron bombardment heating

In Figure 2.21 we showed the circuit used for electron bombardment heating, to obtain temperatures higher than could be reached by purely radiative heating from the projection lamp filament. This arrangement was first used on a titanium sample. Figure 2.33 shows the Auger spectrum of the titanium sample as inserted into the vacuum system; notice the large carbon peak at 268eV and the small peaks at 150eV (sulphur), 384 and 416eV (titanium), and 508eV (oxygen).

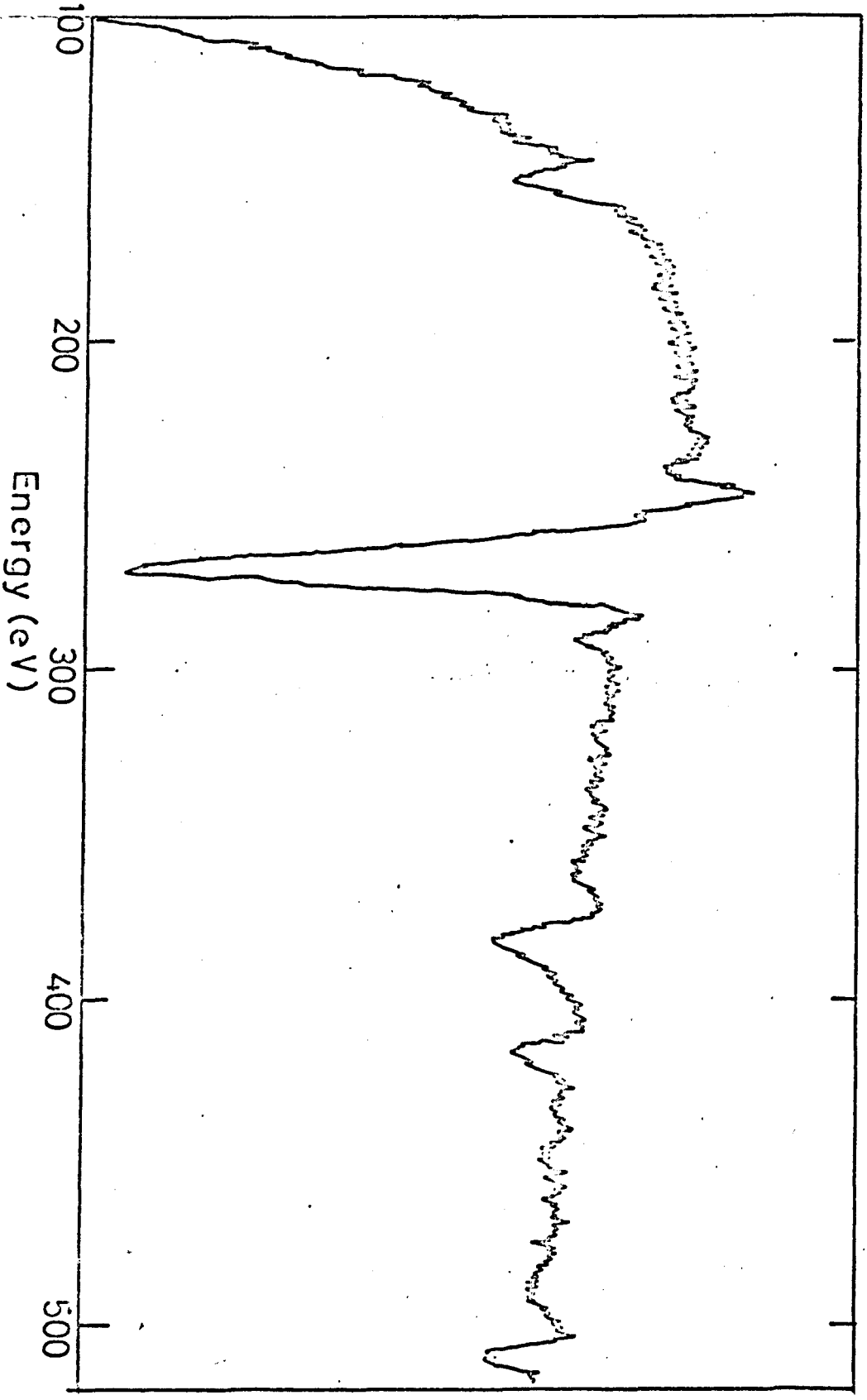

Figure 2.33 Auger spectrum of 'dirty' titanium

After the electron bombardment heating, during which some of the titanium seemed to be evaporated, the spectrum shown in Figure 2.34 was obtained; the carbon peak is much reduced and now appears at 270eV, but the sulphur peak has increased enormously, and is now at 148eV. The peak due to oxygen has disappeared completely, and the titanium doublet increased in amplitude. It is not clear whether the dramatic increase in the sulphur peak was due to diffusion from the bulk or from sulphur evaporated from the heating filament either as neutrals or negative ions arriving at the titanium surface; this spectrum is, however, very similar to that reported by Bishop, Riviere and Coad (1970, 1971), who were only able to obtain a contaminant-free titanium surface by recording the Auger spectrum while the specimen was maintained at 600°C. The Auger peaks found are compared with their results in Table 2.II below.

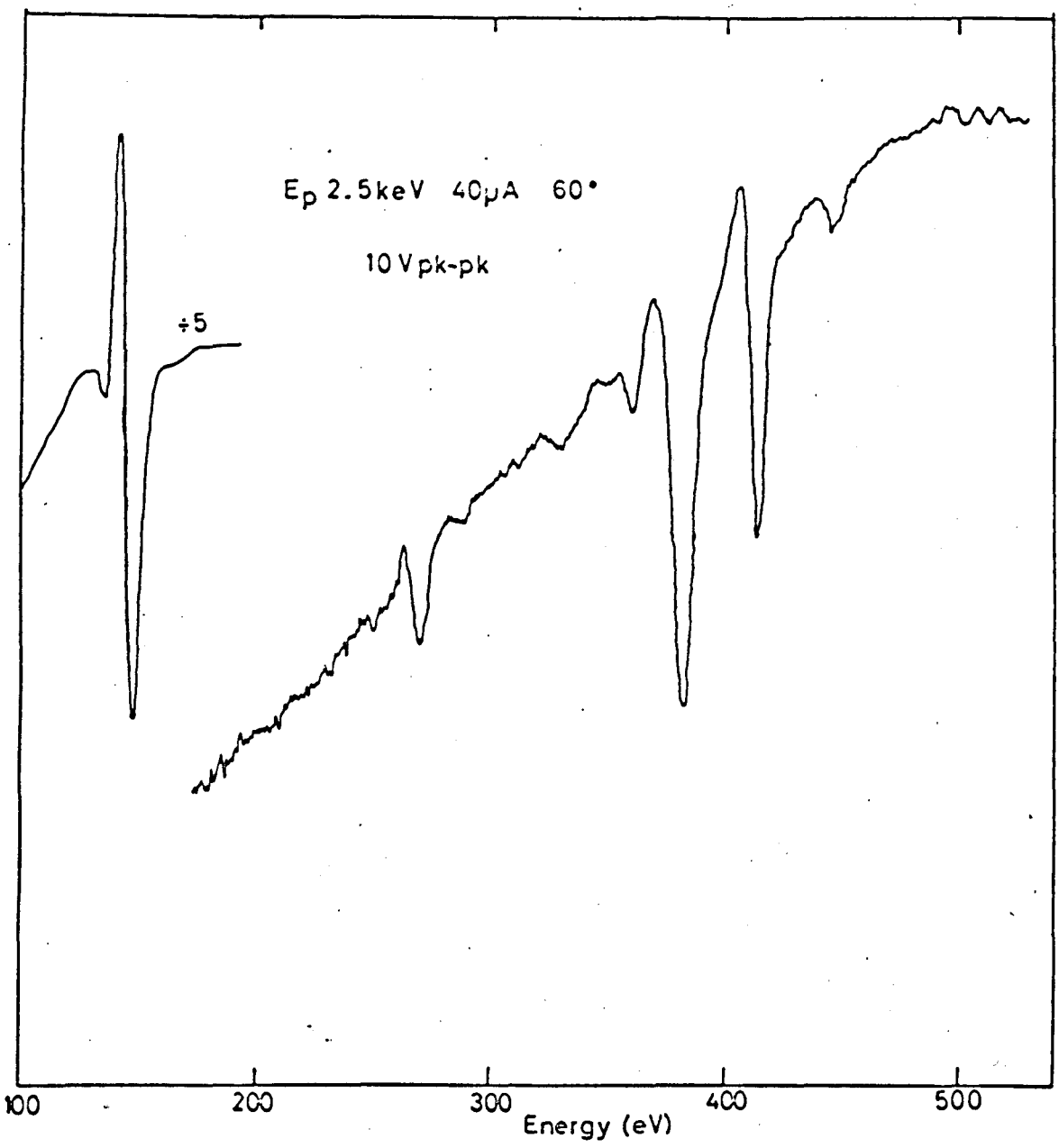

Figure 2.34 · Auger spectrum of titanium after electron bombardment

Table 2.II

Auger peaks observed on Titanium surface

Present Work	Bishop et al.	Element	Allocation
-	10	O	L_1VV
-	24	Ti	$M_{2,3}VV$
-	40	?	?
136	136	S	Plasma loss from 150eV peak
148	150	S	$L_{2,3}VV$
	180	Cl	$L_{2,3}VV$
270	272	C	KVV
328	330	Ti	$L_{2,3}M_1M_1$
	350	Ti	1st plasma loss from 382eV peak
360	362	Ti	$L_{2,3}M_1M_{2,3}$
381	382	Ti	$L_{2,3}M_{2,3}M_{2,3}$
414	416	Ti	$L_{2,3}M_{2,3}V$
444	450	Ti	$L_{2,3}VV$
	472	O	KL_1L_1
508	490	O	KL_1V
512	510	O	KVV

2.4.4 Conclusions

The development of a sensitive 360° retarding field analyser of secondary electrons has been described, together with the associated electronic differentiation systems. We shall demonstrate in the following chapters the high resolution of up to 0.2% obtained with this device; also the flexibility inherent in the design enabling measurements to be taken over a wide range of incident angles. Total secondary yield and backscattering coefficient determinations of surfaces whose surface composition may be related to an Auger spectrum have also been made, and the equipment is capable of measuring appearance potential spectra, though no such results have yet been obtained.

At this stage it is perhaps appropriate to reiterate our grateful thanks to Mr. G. Dudley and his staff for much patience and skill in fabricating and welding the experimental chamber and accessories, and their skill in sealing the few leaks that were located. Our thanks are also due to Messrs. M. Davies and J. Minshull from the Electronics Workshop for much help in the design of the circuitry, and the frequent maintenance of the more unreliable commercial instrumentation.

CHAPTER 3

AUGER ELECTRON SPECTROSCOPY AND SECONDARY ELECTRON EMISSION OF A Zr/Al BULK GETTER

3.1 Introduction

In this chapter we give an account of the first set of measurements made with the equipment described in the previous chapter. The material examined was a Zr/Al bulk getter, type St101, manufactured by S.A.E.S. Getters, Milan. It is an alloy of 84% zirconium and 16% aluminium in the form of a compressed powder, and was supplied in two forms, which were examined separately; in the first investigations the getter was in the form of pellets 7mm in diameter mounted on a thin 7mm x 10mm nickel ribbon*; subsequent measurements were also made of a so called 'coated getter'** with similar results.

The gettering properties and surface studies of this material have been reported by della Porta (1962), Kindl (1963, 1967), and Pisani (1967); it is a non-evaporable bulk getter, and may be of some technological importance in maintaining high vacuum conditions in, for example, high power microwave tubes (Tuck 1972). For this type of application, a knowledge of the secondary emission properties of the material is useful, since materials with high secondary electron yields can degrade the performance of electron tubes.

In this investigation, the total secondary yield and back-scattering coefficient of the material were measured at both normal and 75° incidence, during various stages of heat treatment. An Auger

* St 101/DF/50

** St 101/CT 8 x 6 D60

examination was also made of the surface, and comparative results were taken of the polished nickel surrounding the getter pellet.

The yield at normal incidence was found to decrease from an initial value of approximately 1.4 to a δ_{max} of 0.8 at an $E_{p_{max}}$ of 500eV. The getter behaved like a rough surface in that its yield did not vary appreciably with the angle of incidence. After heating to activation temperatures, strong zirconium Auger peaks and weak carbon and oxygen peaks were observed on the surface, but no trace of aluminium was found.

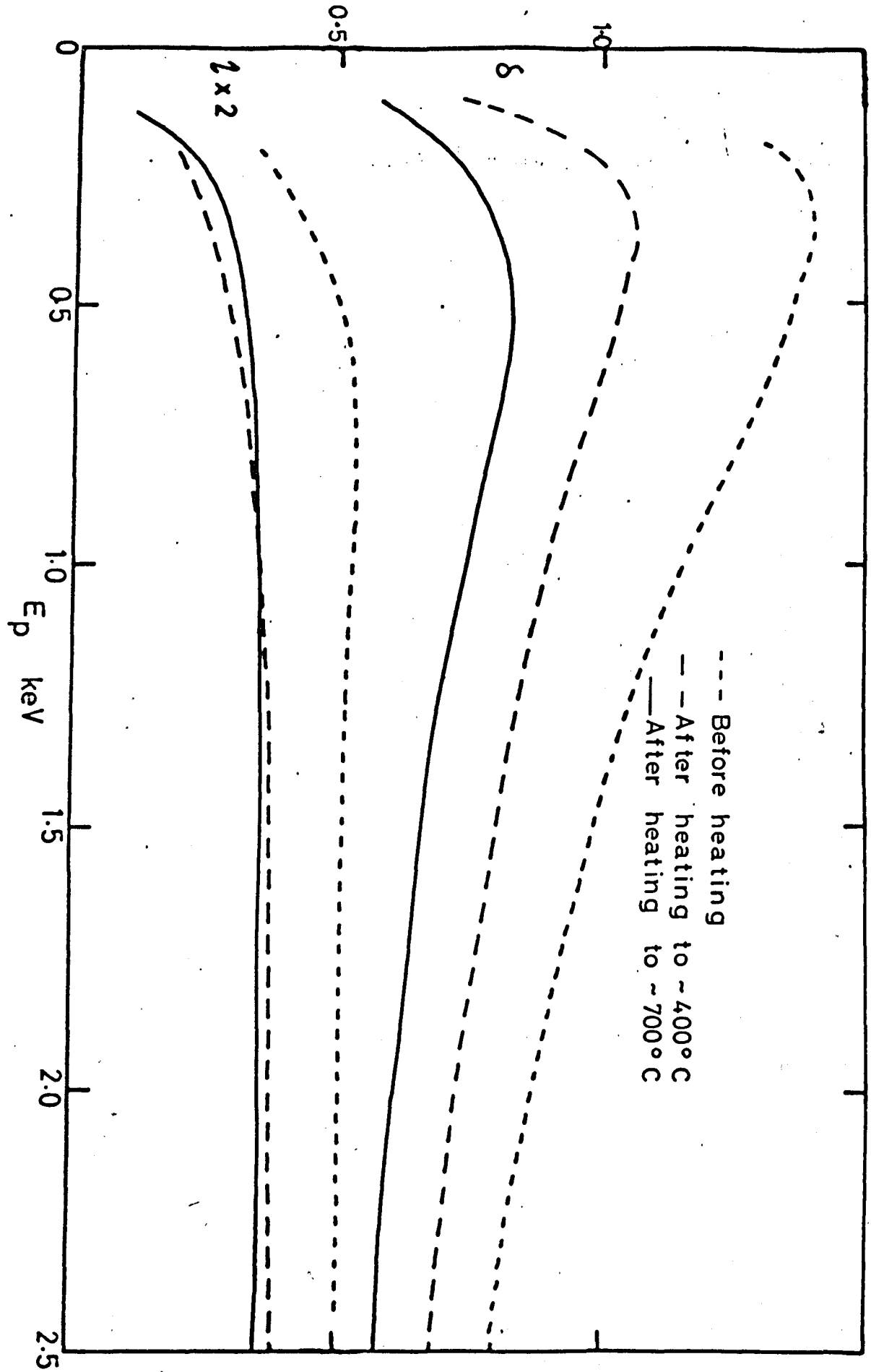

Figure 3-1 Yield curves of Zr/Al normal incidence

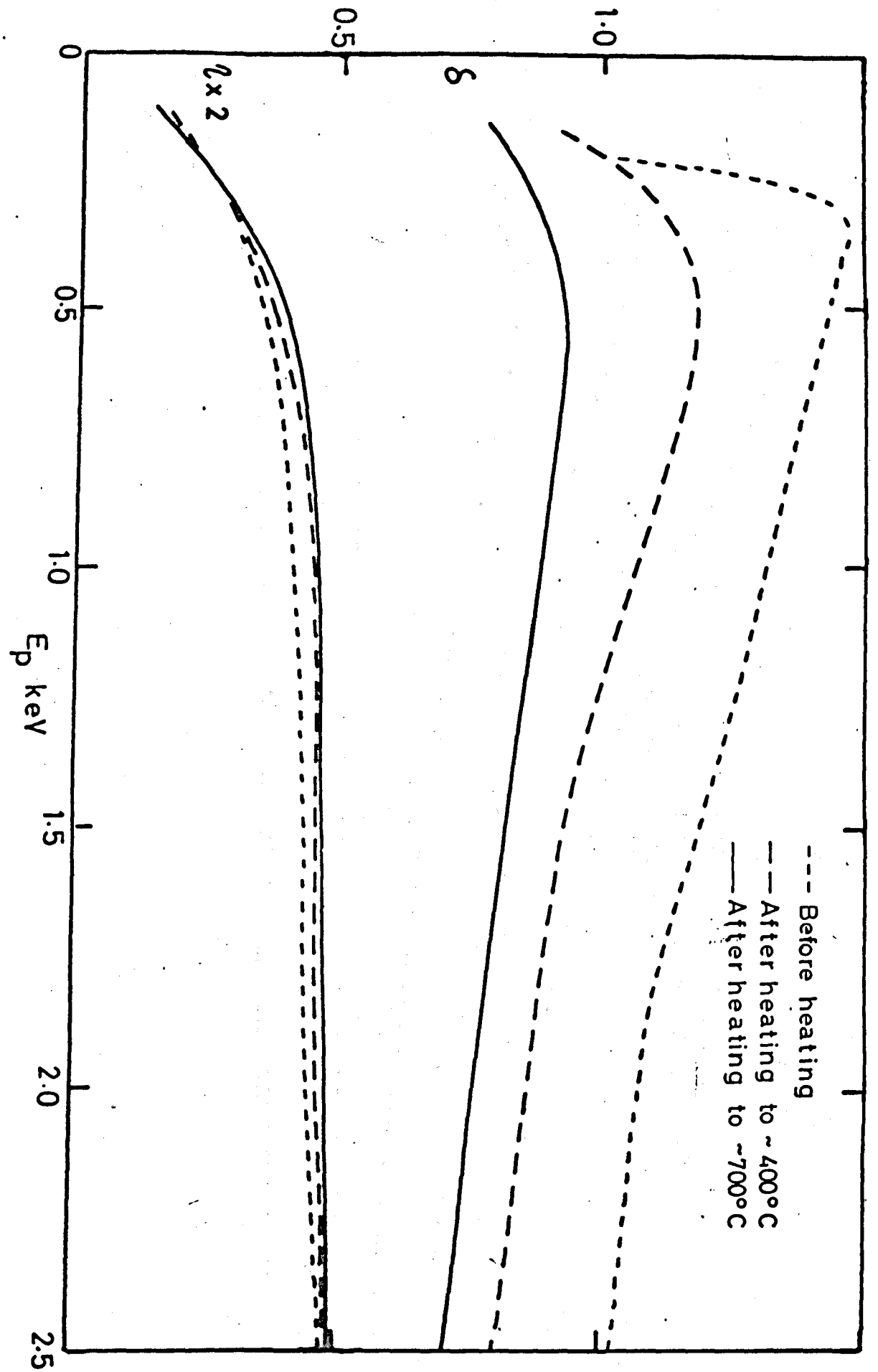

Figure 3-2 Yield curves of Zr/Al 75° incidence

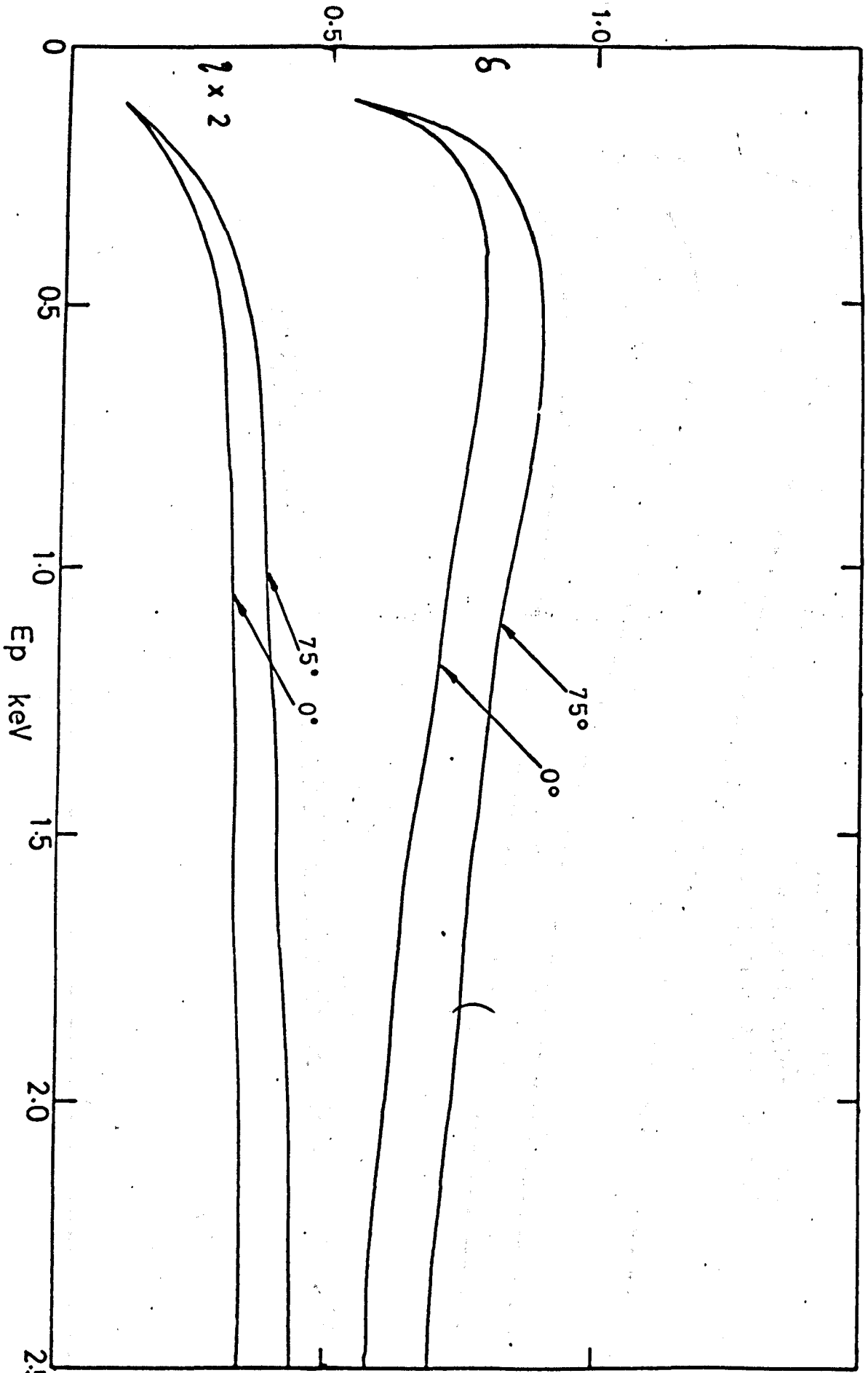

Figure 3.3 Yield curves of Zr/Al After final heating

3.2 Results

The yield measurements were made using the arrangement of Figure 2.25. Below about 1200 Volts the variation in E_p was accomplished using the motor-driven helipot. Measurements were additionally made up to an E_p of 2.5keV, and because a programmable power supply was not available at this stage, we employed a cruder method; the gun potential was varied by manually switching the power supply in increments of 100 Volts and relying on the long time constant in the supply to 'ramp' the voltage. Inevitably a 'spike' occurred on the plot every 100 Volts. Owing to the small size of the samples we found it necessary, particularly at grazing incidence, to make changes in the electrostatic deflection voltage with changes in E_p to maintain the beam on the surface. It was also found helpful to make occasional changes to the electron gun control grid potentiometer to reduce the variation in primary current, and hence improve the accuracy of the division.

Figure 3.1 shows the δ, E_p and η, E_p curves for Zr/Al at normal incidence. It can be seen that heating to 400°C reduced the total yield from an initial δ_{max} of 1.4 to 1.1; electron bombardment heating to about 700°C reduced it still further to 0.85. Figure 3.2 gives the corresponding curves for an angle of incidence of 75° to normal. The curves taken before heating were a trifle arbitrary, since the yield was very variable across the surface by as much as 20%. Figure 3.3 shows the yield curve we obtained after overnight heating followed by electron

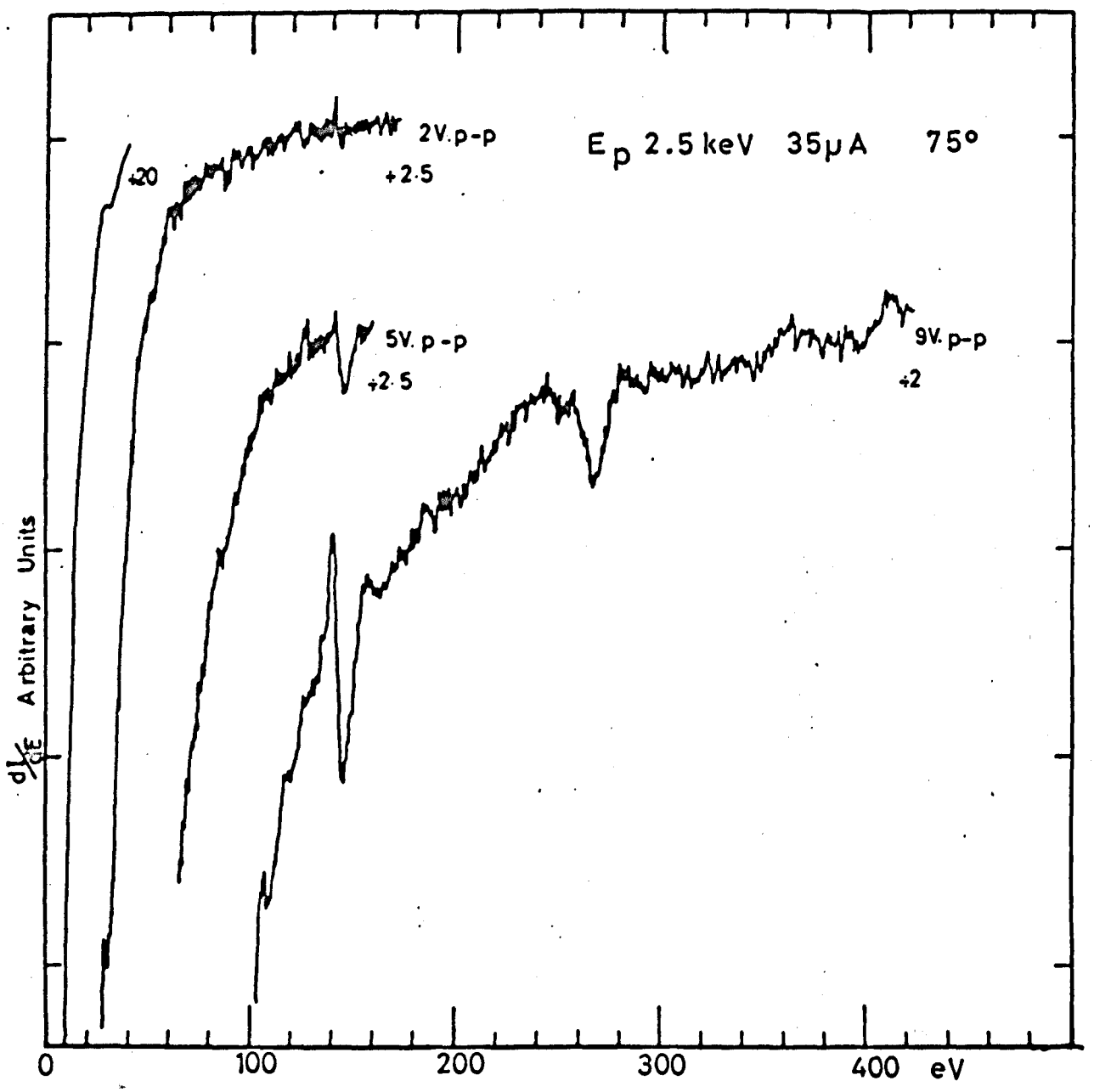

Figure 3.4 Auger spectrum of Zr/Al after heating to 400°C

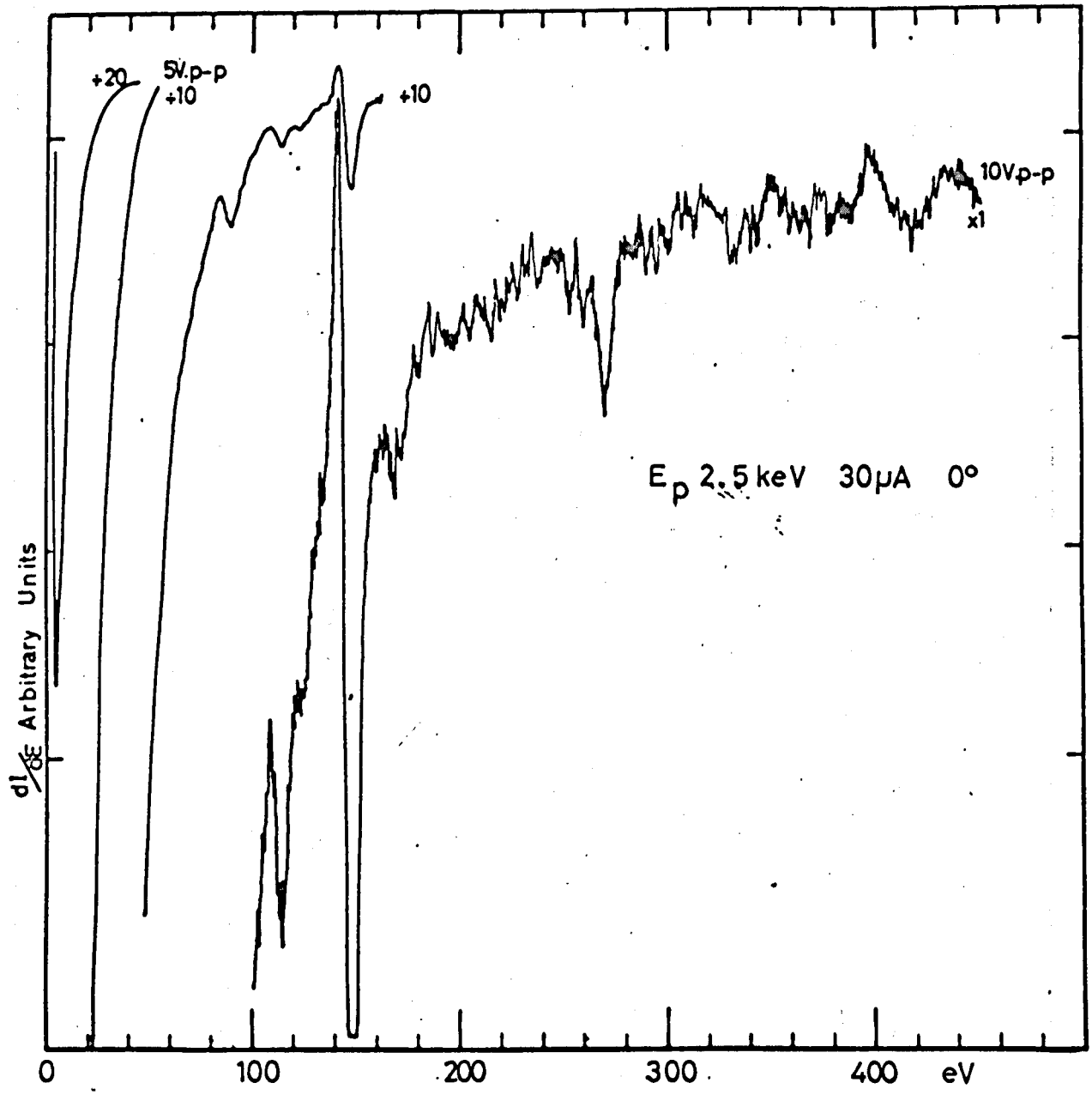

Figure 3.5 Auger spectrum of Zr / Al after heating to 700°C

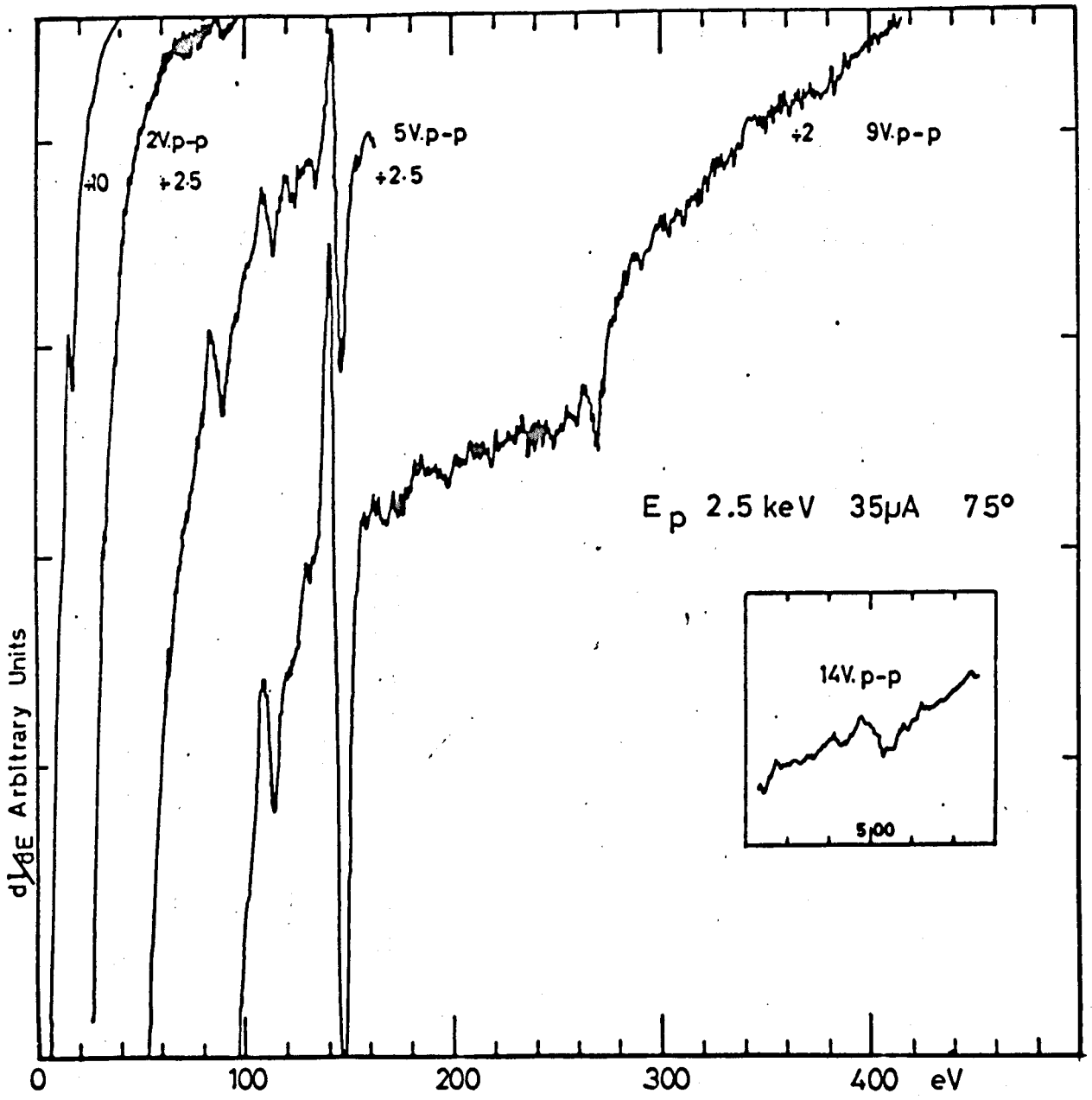

Figure 3.6 Auger spectrum of Zr/Al after heating to 700° C

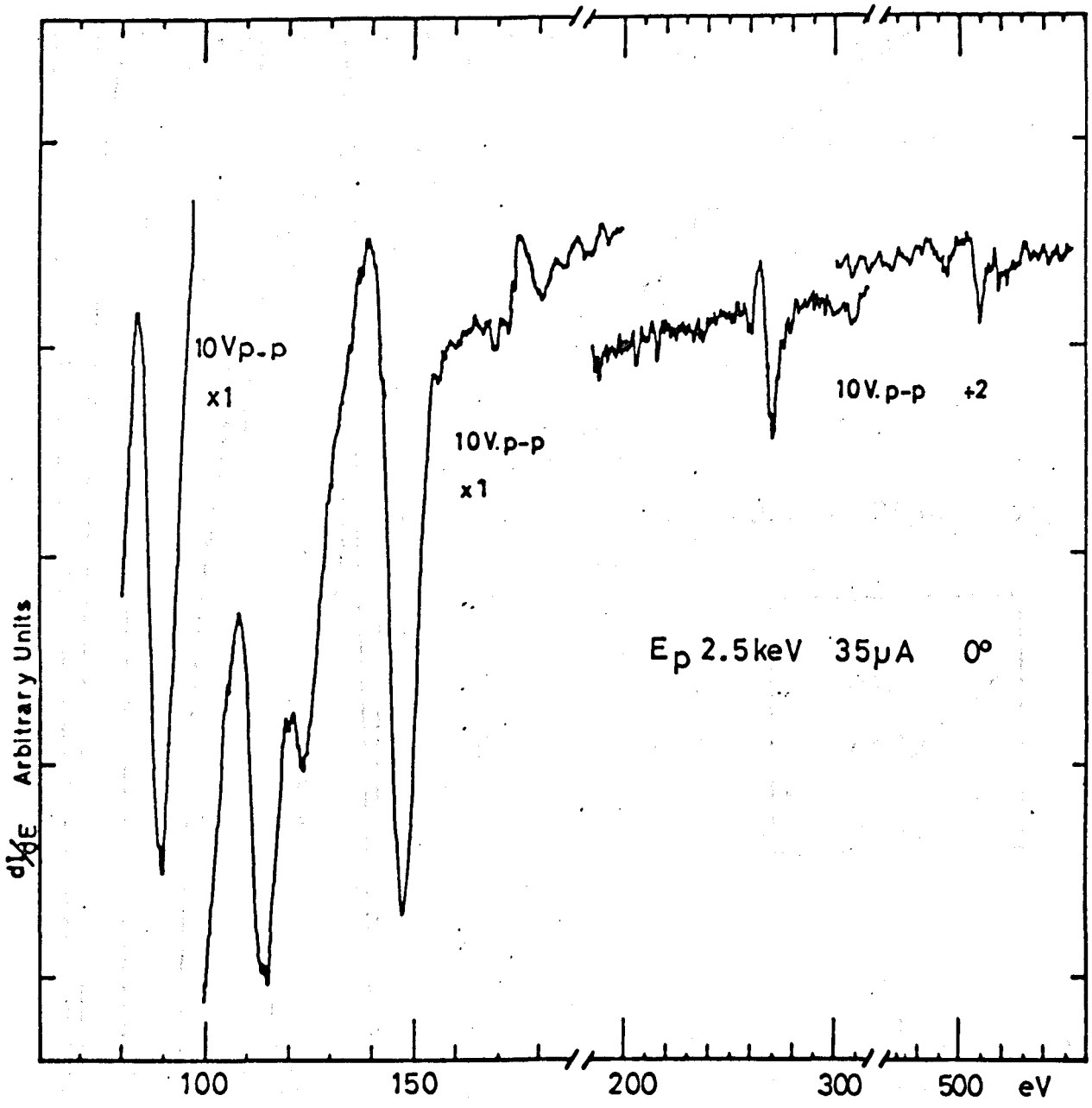

Figure 3.7 Auger spectrum of Zr/Al after final heating

bombardment heating to 800-1000°C. This final heating should have activated the surface (Kindl 1967). The upper curves refer to 75° incidence and the lower to normal incidence; it can be seen that the material exhibits the properties of a microscopically rough surface in that the yield shows little variation with angle of incidence of the primary beam. δ_{max} at normal incidence is 0.8 at 500eV, and η rises to 0.18 at 2.5keV; the corresponding values at 75° being 0.9 and 0.22.

The changes in the Auger spectrum of the sample after the heat treatment are shown in Figures 3.4 - 3.7. Except where indicated, a primary energy of 2.5keV 30 - 35μA was used; no peaks could be seen on the surface before heating to 400°C. In Figure 3.4, which is after the heating to 400°C, corresponding to the centre curves of Figure 3.2, the prominent peaks are at 150 and 270eV, with a small peak at about 110eV. The 270eV peak is identified as due to Carbon and the peak at 150eV could be either due to sulphur (150eV), or zirconium (148eV). The largest contribution to this peak is probably from sulphur because the other members of the zirconium triplet (148, 109, 90eV) are barely visible, as well as the presence of small satellite peaks at about 160 and 135eV which are characteristic of sulphur.

Figures 3.5 and 3.6 show the Auger spectra after flashing to 700°C at normal and 75° to normal incidence respectively, corresponding to the low yield plots of Figures 3.1 and 3.2. The spectrum taken at 75° shows greater sensitivity and lower noise than the curve at normal incidence, but the main features are the same. The carbon and oxygen peaks are reduced and the peak previously at 150eV has moved to 149eV,

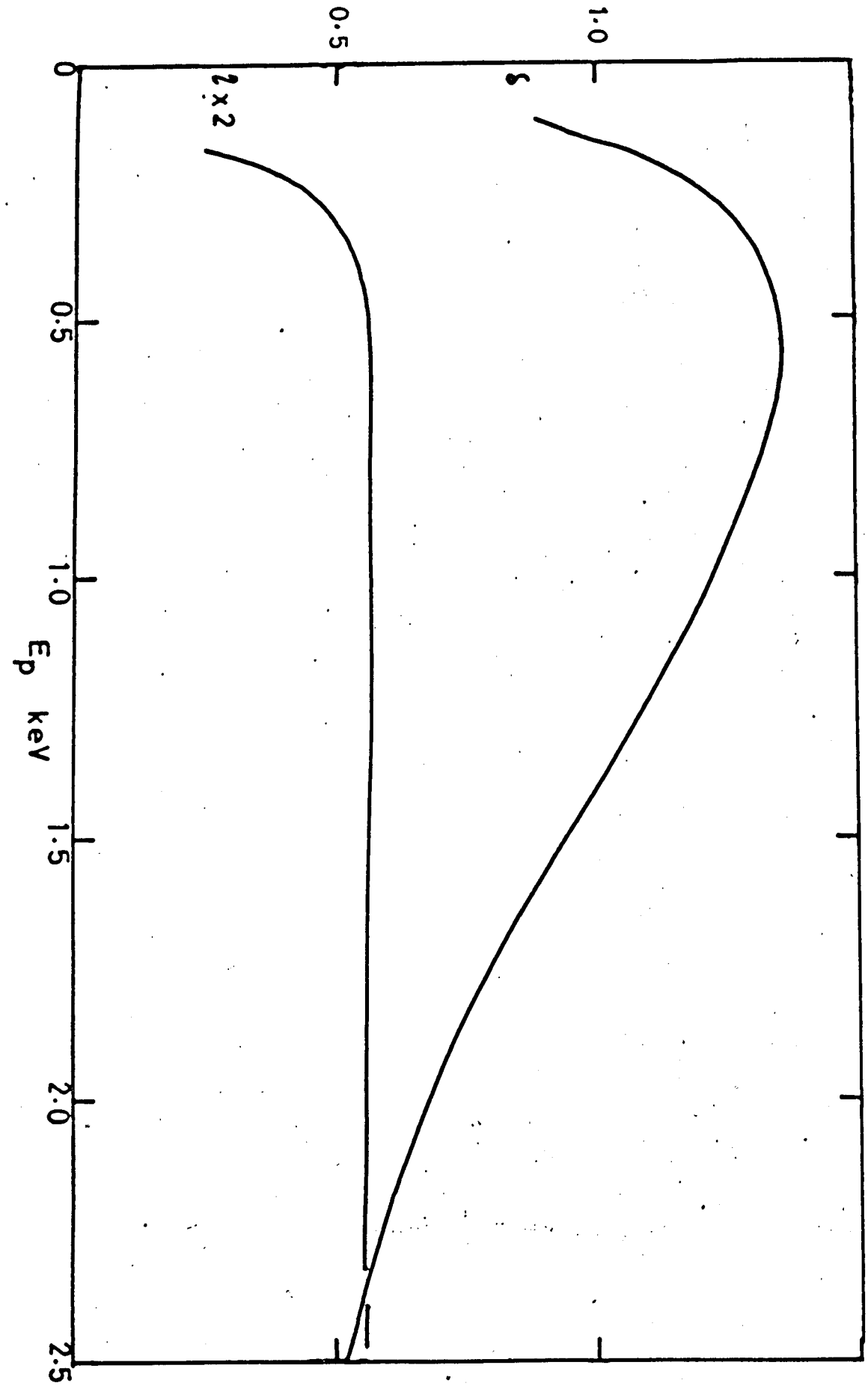

Figure 3.8 Yield curve of Zr/Al after heating to 700° C

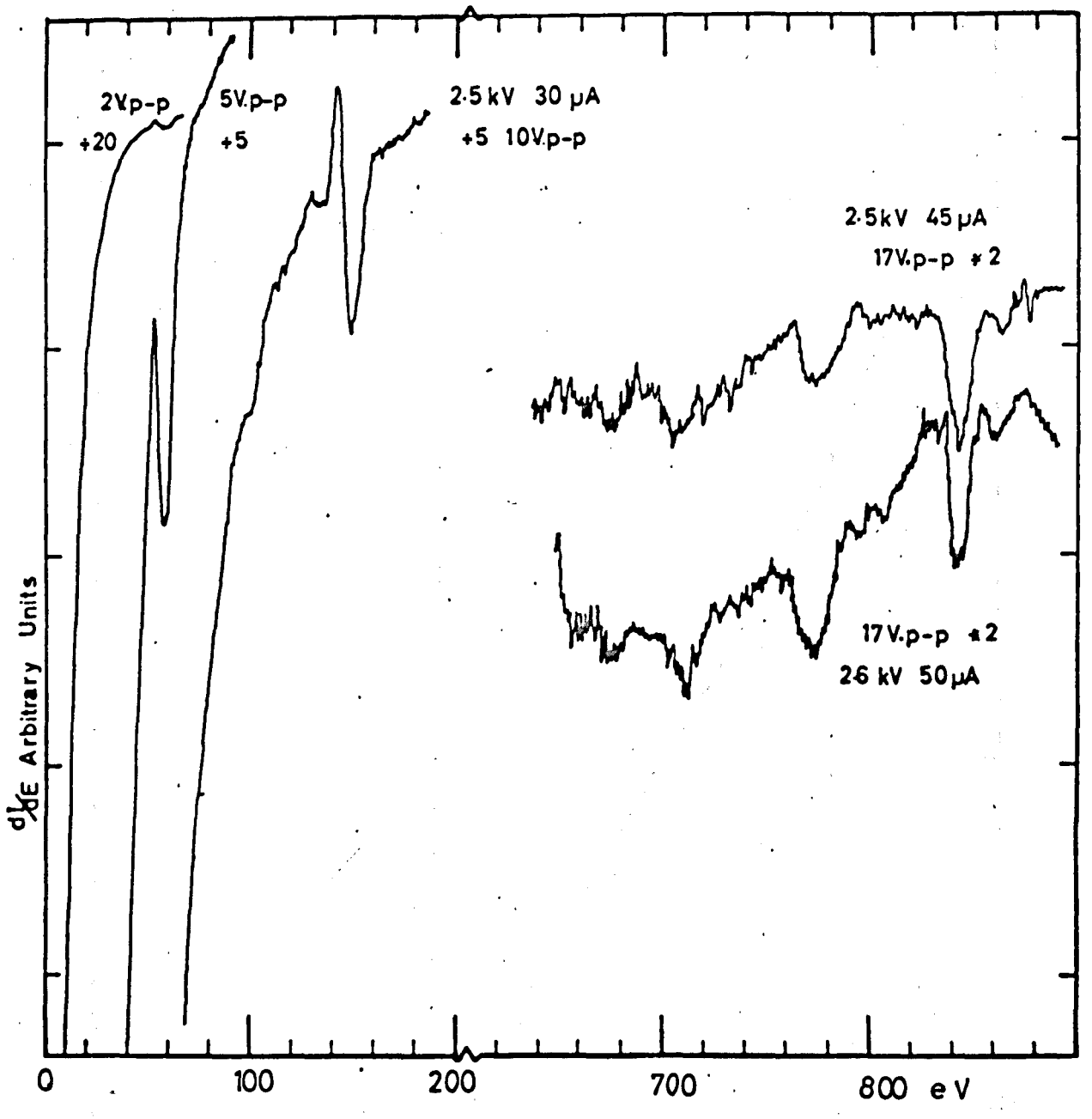

Figure 3.9 Auger spectrum of nickel surface

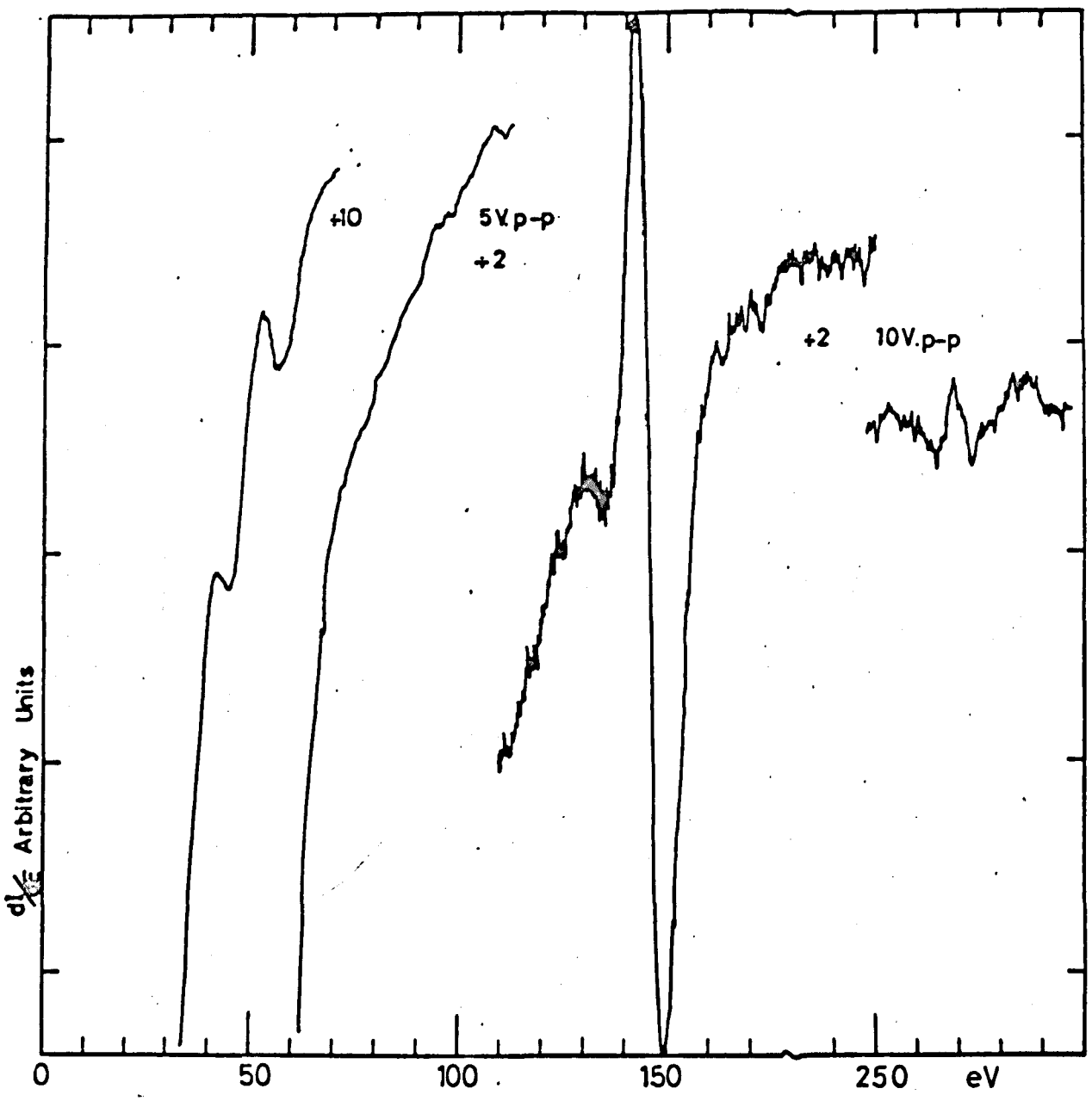

Figure 3.10 Low energy Auger spectrum of nickel after heating

indicating an increased contribution from zirconium; also peaks at 90 and 109eV have now increased. The relative increase in sensitivity at 75° can be seen to be only about 50%, presumably on account of the rough surface of the getter. The final heating to 800 - 1000°C which should have 'activated' the getter material, causes a further increase in the intensity of the zirconium peaks by comparison to those of the contaminants. The peak at 175eV reported by Haas et al. (1970) was not really confirmed, and it was noticed that there was no suggestion of an aluminium peak at 67eV or an oxidised aluminium peak at 52eV (Suleman and Pattinson 1971). From the bulk concentration of 16% aluminium, this lack of an Auger peak is very surprising.

Figure 3.8 shows the δ, E_p and η, E_p plot for the nickel surrounding the sample at normal incidence after the heating to about 700°C. The curve obtained is quite close to that obtained in this laboratory on a polished 'outgassed' nickel sheet, (Thomas and Pattinson 1968), but the value of η is slightly lower, perhaps on account of the larger suppression voltage used. In Figure 3.9 we show the Auger spectrum we obtained for the nickel surface under the same conditions, revealing strong sulphur contamination; the peaks seen at 60, 710, 770 and 850eV agree well with those observed by Coad and Riviere (1970), but it was interesting that we saw no carbon contamination. The resolution of the peaks is perhaps a bit poor, because it was necessary to deliberately deflect the beam from its optimum position onto the nickel. Further improvement in the nickel peaks was not really obtained after heating to 800 - 1000°C; it can be seen from Figure 3.10 that it was possible

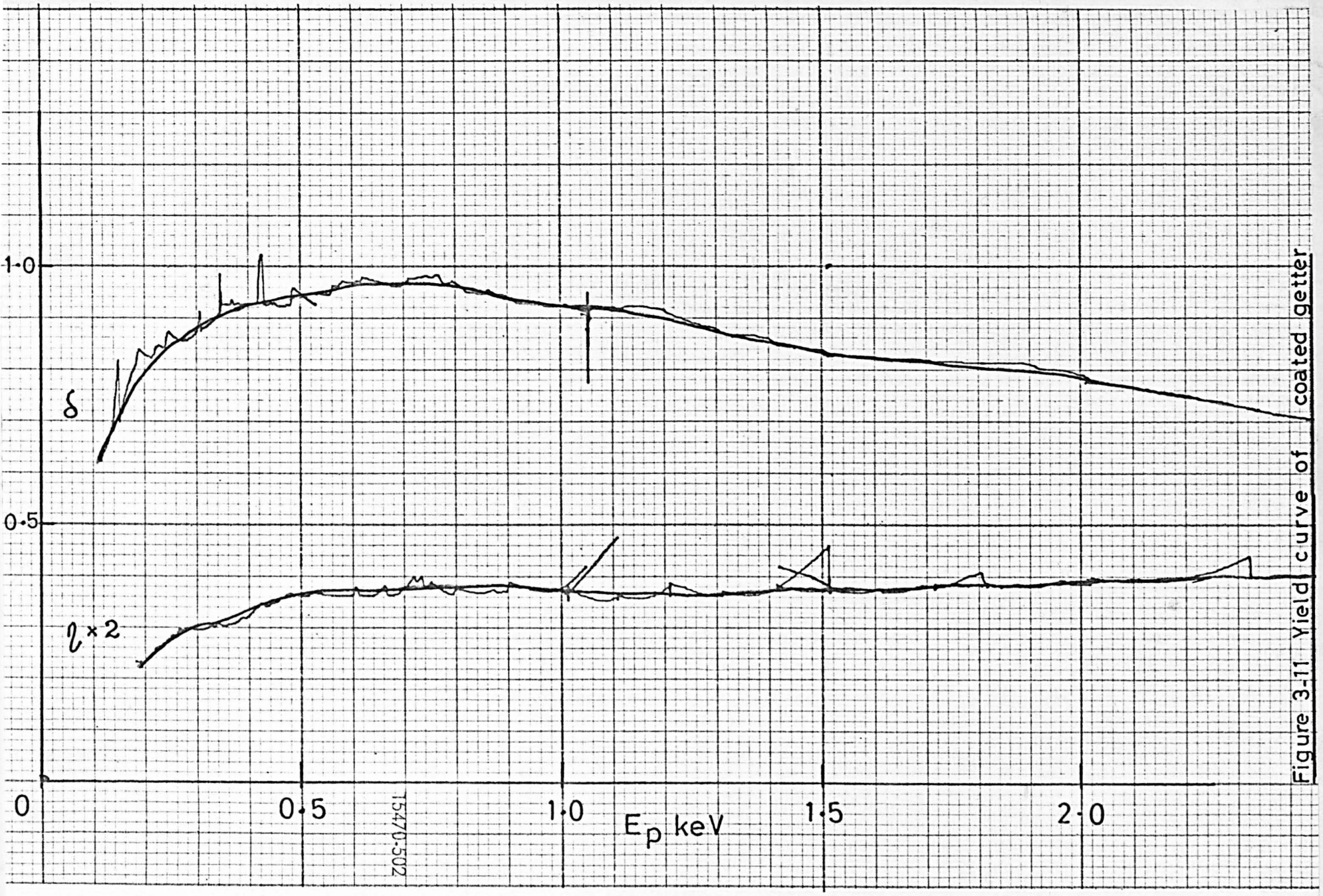

Figure 3-11 Yield curve of coated getter

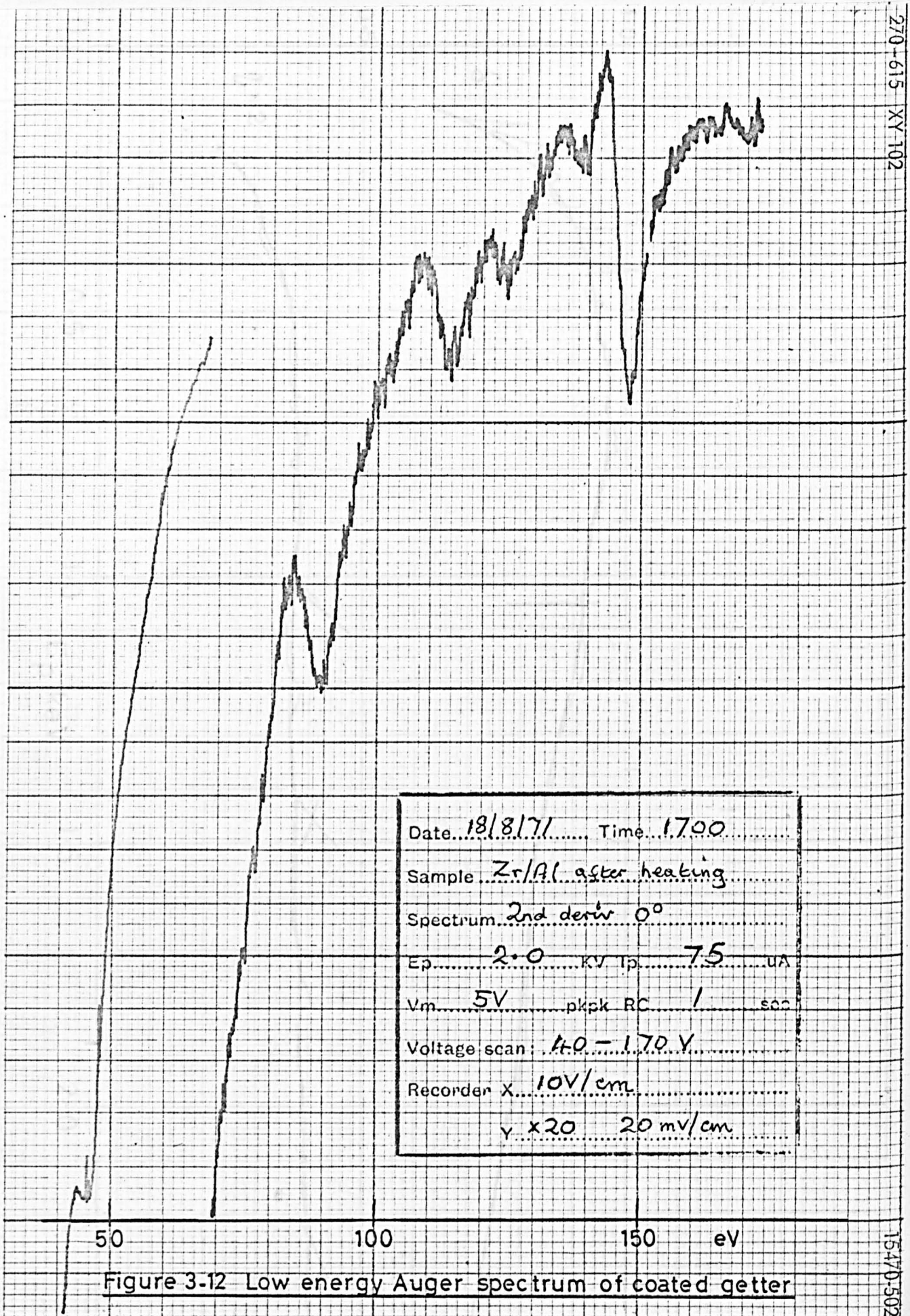

Figure 3-12 Low energy Auger spectrum of coated getter

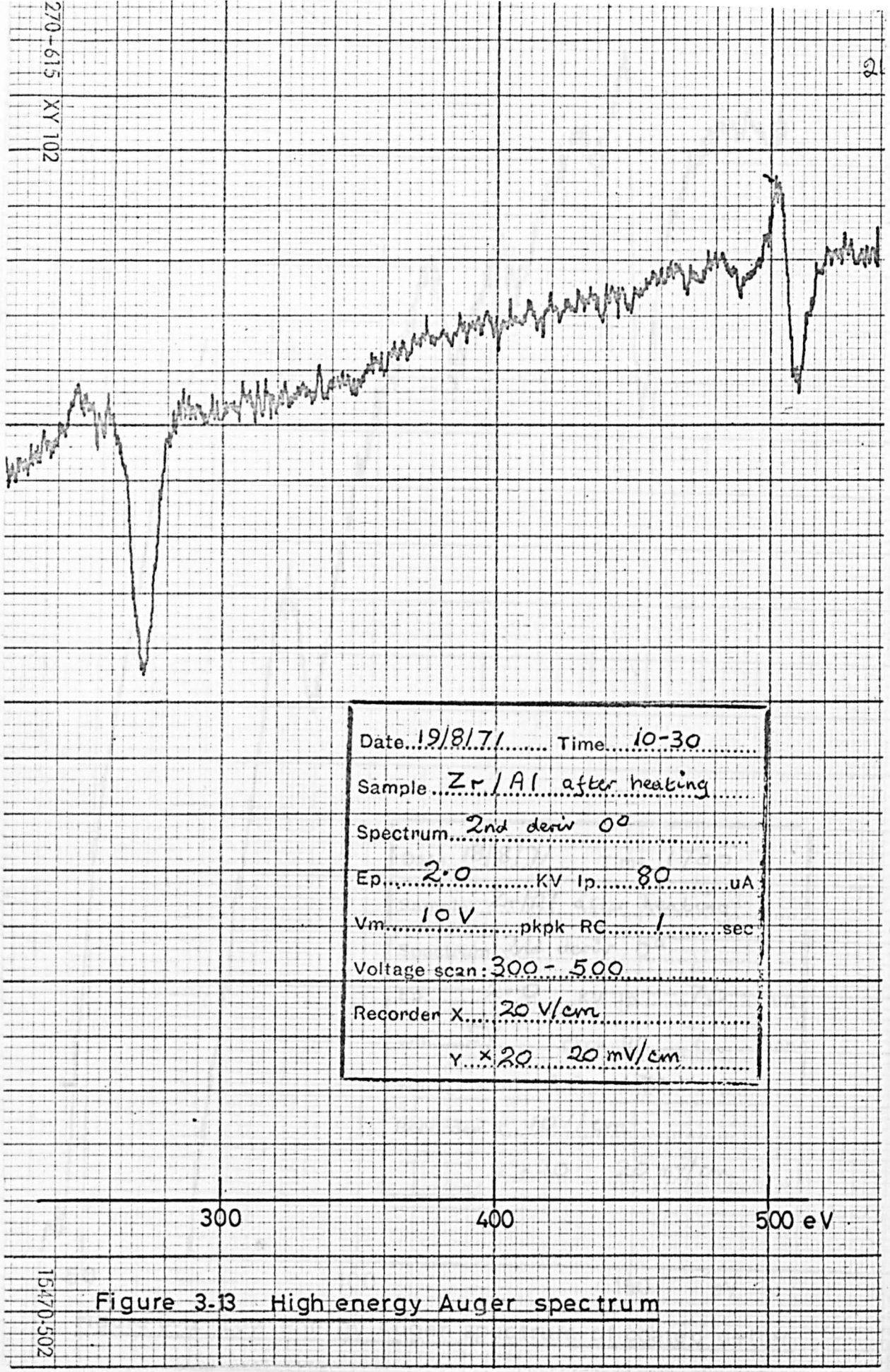

Figure 3-13 High energy Auger spectrum

to see an extra peak at 45eV, a small carbon and oxygen peak may also be seen, but they are of very low amplitude, perhaps due to the gettering action of the Zr/Al reducing the concentration of CO in the residual atmosphere.

The above work was then repeated on a sample of coated getter with similar results. We noticed that the yield of this material after activation was rather higher than that of the previous sample, as is shown in Figure 3.11; δ_{max} is about 0.9 at an $E_{P_{max}}$ of 700eV. We noticed that on examining the samples after removal from the vacuum system, it appeared that we had been a bit over zealous with the electron bombardment (again!) and caused some surface melting; this may account in part for the high value of δ_{max} observed. The Auger spectroscopy of the surface (Figures 3.12 and 3.13) revealed little extra, except that we were able to take advantage of a higher beam current to examine the zirconium peaks at higher resolution. The peak positions we observed with this lower modulation were 148, 139, 124, 114, 90eV with a small additional peak at 46eV. It should be noted that we still did not see any trace of aluminium on the surface.

3.3 Discussion

The values of the peaks we found on the Zr/Al surface after activation, are compared in Table 3-I below with the results of Haas and Grant (1970).

Table 3-I

Observed Auger Energies in Zr/Al

Present work (on Zr/Al)	Haas and Grant (on Zr foil)	Transition	Calculated Energy
N.R.	175	$M_4N_{4,5}N_{4,5}$ $M_5N_{4,5}N_{4,5}$	179.9 177.5
148	149	$M_4N_{2,3}N_{4,5}$ $M_5N_{2,3}N_{4,5}$	151.1 148.7
139		C.E.L.	~130
124	127	$M_4N_1N_{4,5}$ $M_5N_1N_{4,5}$	128.5 126.1
114	117	$M_4N_{2,3}N_{2,3}$ $M_5N_{2,3}N_{2,3}$	119.8 117.4
90	93	$M_4N_1N_{2,3}$ $M_5N_1N_{2,3}$	97.2 94.8
46	47	$N_1N_{4,5}N_{4,5}$	48.0
N.R. N.R.	34 23	$N_1N_{2,3}N_{4,5}$	20.0

	'Z'	'Z+1'
$N_{4,5}$	0.7	2.6
$N_{2,3}$	28.7	33.9
N_1	51.3	58.1
M_5	180.0	
M_4	182.4	
M_3	330.5	
M_2	344.2	
M_1	430.3	

Energy Level Diagram for Zirconium

Figure 3.14

The observed peaks always occur a few volts below their calculated position. This is because we have not made any allowance for the work function of the analyser grid, 4 - 5eV.

The calculated values were based on the formula of Burhop (1952) and allowance was made for the ionized state of the atom after an Auger transition by using the binding energy of the next highest element, niobium, for the binding energy of the final electron. The data used are shown in Figure 3.14, and are taken from the Tables of Bearden and Burr, who correlated the ESCA data of Siegbahn with the other published energy level data. The $N_{4,5}$ level of Zirconium is taken as the peak in the density of states in the valence band, from Holliday (1968).

It is evident that all the peaks observed on the surface may be interpreted in terms of transitions involving zirconium atoms only. Kindl (1967), by careful etching of the getter surface, identified various alloys of Zr/Al on the 'surface' of the getter, but of course this is the 'bulk' as far as Auger spectroscopy is concerned. It is possible that since the aluminium will be very mobile at the activation temperature, and even at the operating temperature (400^{o}C) of the getter, it could be constantly diffusing from the surface region to the bulk, maybe even carrying with it the gas atoms that have been pumped on the surface.

CHAPTER 4

AUGER ELECTRON SPECTROSCOPY OF EVAPORATED FILMS OF Pd, Ag, Sn, Sb, Cu and Al

4.1 Introduction

In this chapter we report the Auger spectra observed for the metals Pd, Ag, Sn, Sb, Cu and Al. Auger spectroscopy was used primarily to characterise the surface cleanliness for the subsequent investigations. During the Auger examination, extensive fine structure was discovered in the region of the 'slow' peak and we give an account of this part of the spectrum in Chapter 6.

Because of the superior resolution of this analyser, we were also able to discover fine structure not previously observed with retarding field analysers in the $M_{4,5}N_{4,5}N_{4,5}$ Auger peaks of Pd, Ag, Sn and Sb; on the other hand not all the fine structure around the $M_{2,3}VV$ Auger peak of copper, reported by Jenkins and Chung (1971) was observed. Our spectrum of clean aluminium was similar to that first reported by Suleman and Pattinson (1971), but the additional fine structure later found by these workers was not seen (1972).

The results we give for the spectra of Ag, Sn and Sb at high resolution are generally similar to those of Aksela, Pessa and co-workers (1971), who used a cylindrical mirror analyser; however, their work was performed under relatively poor vacuum conditions, and a confirmation of their findings in uhv on clean surfaces is here described. Also they only reported measurements of the main $M_{4,5}N_{4,5}N_{4,5}$ transition, whereas we list here other peaks that have been observed in the Auger spectra.

It will be shown that agreement between the observed energies of the peaks and their positions as calculated from the Burhop (1952)

formula and the formula of Chung and Jenkins (1971) is quite good when a correction of 5eV is made for the work function of the analyser grid. Since this correction is quite often 'forgotten' in much published work (particularly if it makes agreement between experiment and theory worse!) a work function correction has not been made to our tabulated results, but rather to their calculated values. This permits a more direct comparison between the results of different workers.

4.2 Stainless Steel Substrate

A highly polished stainless steel sheet was used as the substrate for the evaporations. It was cleaned by heating in vacuo up to its melting point by electron bombardment, giving the Auger spectrum shown in Figure 4.1. The upper trace covers the energy range 100-600eV, and the lower trace at higher gain was taken with the same range of retarding voltage applied to the grids, but with a target bias of 300V; it therefore covers the range of Auger energies of 400-900V w.r.t. the target potential. The largest peak is seen to be at 150eV, corresponding to sulphur, and it can be seen that other peaks are very small, and nearly lost in the noise.

All the metals examined were deposited onto the stainless steel by evaporation from tungsten or molybdenum baskets, which were initially cleaned by flashing in vacuo. It was not possible to examine the effect of heating on the evaporated films, since we found that previously evaporated material was being re-evaporated from the heating filament and contaminating the target surface.

The first evaporations of palladium were monitored with a quartz crystal, but its design was such that it ceased to work after the heating filament had been used, so we were forced to manage without. It would obviously have been helpful had we been able to use a bakeable film thickness monitor crystal. It was necessary to use the heating filament for internal baking and for heating the substrate prior to evaporations.

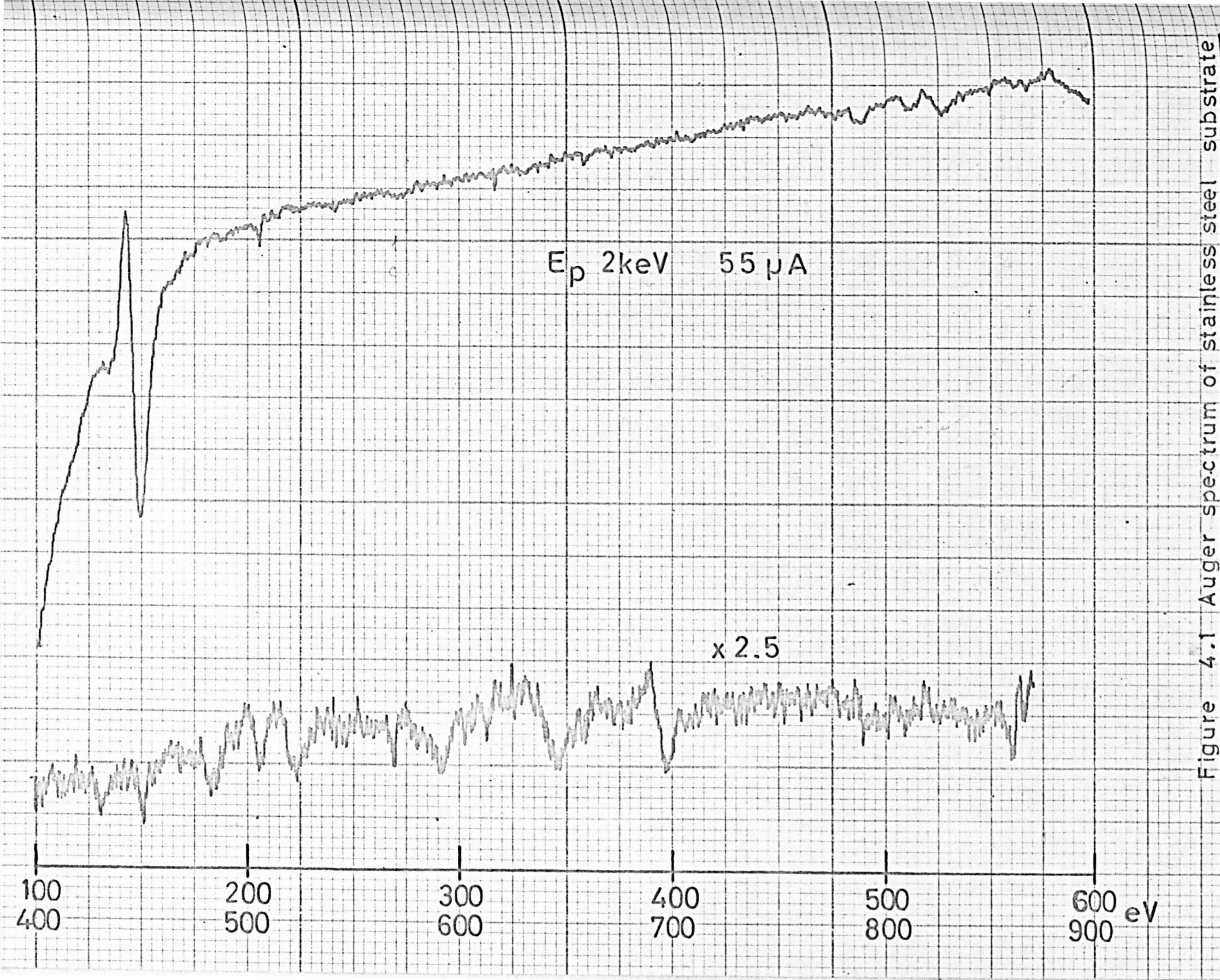

Figure 4.1 Auger spectrum of stainless steel substrate

The main peaks observed on the surface are listed below in Table 4-I.

Table 4-I

Energy	Element	Transition
698	Fe	L_3VV
645	Fe	$L_3M_{2,3}V$
590	Fe	$L_3M_{2,3}M_{2,3}$
520	O	$KL_{2,3}L_{2,3}$
505	O	$KL_1L_{2,3}$
485	O	$KL_{2,3}L_{2,3}$
450	Sb	$M_{4,5}N_{4,5}N_{4,5}$
430	Sn	$M_{4,5}N_{4,5}N_{4,5}$
150	S	$L_{2,3}M_1M_1$
135	S	Plasma loss from Auger peak

The small peaks assigned to tin and antimony probably result from previous evaporations of these metals not having been entirely removed by the target heating.

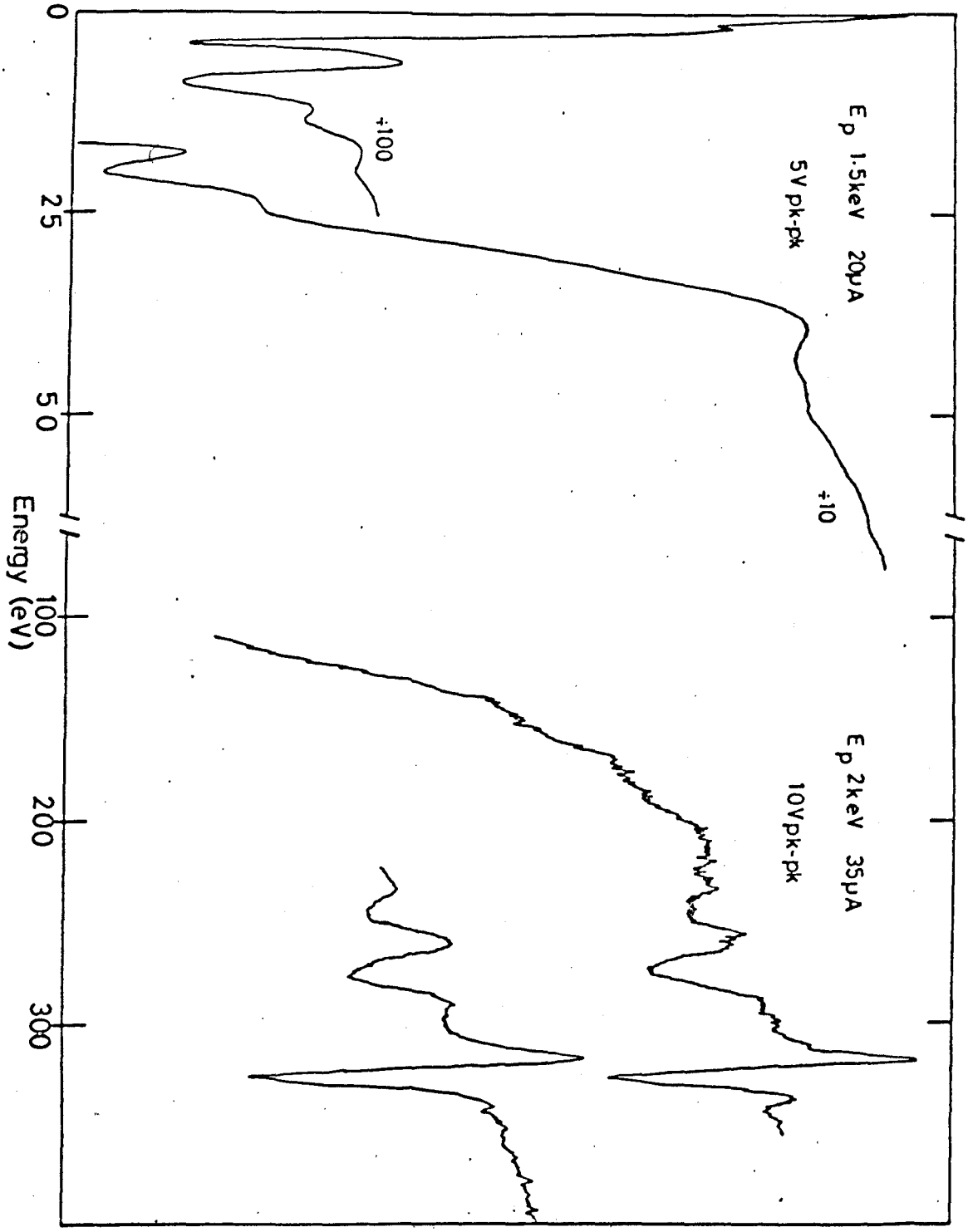

Figure 4·2 Auger spectrum of palladium

4.3 Palladium

4.3.1 Results

The first metal to be evaporated was palladium. Figure 4.2 shows the Auger spectrum observed for the palladium under low resolution and high sensitivity, i.e. with a modulation of 10V pk-pk. On reducing the modulation and carefully optimising the resolution, the spectrum shown in Figure 4.3 was obtained, and it can be seen that the main Auger transition first seen at 326eV has been resolved into two peaks at 328 and 324.5eV. The instrumental resolution of about 0.3% should lead to broadening of observed peaks at this voltage by about 1eV, so it can be stated with certainty that the overall width of about 10eV found for this doublet is intrinsic.

Two small peaks at 43 and 50eV were also found; more structure was found below 25eV and this region of the slow peak is examined in detail in Chapter 6. The Auger spectrum was re-examined regularly up to 43 days after evaporation and no change in the peak positions or evidence of contaminants was found.

4.3.2 Discussion

Two measurements of the Auger spectrum of palladium are known to us at present; those of the 'pioneers' of Auger spectroscopy, Palmberg and Rhodin, in 1968, and the results of the now equally famous group under Haas, in 1970.

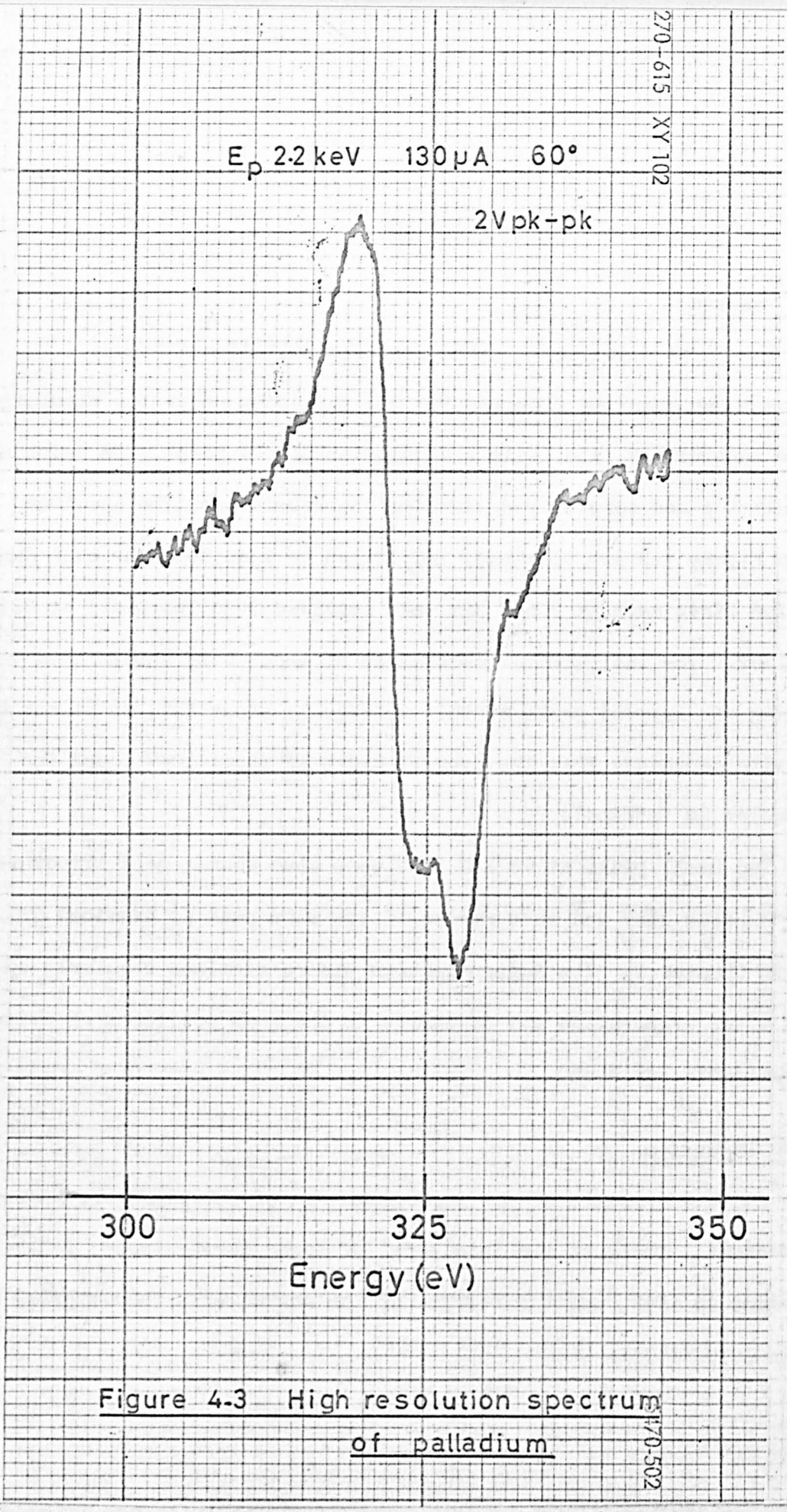

Figure 4-3 High resolution spectrum of palladium

Palmberg and Haas used three grid LEED system retarding field analysers for their Auger spectroscopy. The optimum resolution of these devices is known to be in the region of 2%, as has been mentioned in Chapter 1, and as we discovered on using the Mark I apparatus (Chapter 2); not only does this poor resolution cause a broadening of the peaks, but their apparent position is shifted in energy upwards by about 2%, on account of the field penetration of the retarding grid. The total effect on the high energy edge of a peak at 300eV could thus amount to about 3% or 9 volts. If this quantity is subtracted from the values of these workers, then closer agreement with our work is obtained. From the theoretical point of view, it would seem at first that the results of Hass and Palmberg are more in accordance with the values calculated from the Burhop (1952) formula. However, this 'agreement' is rather fortuitous, since it is necessary to add the work function of the analyser grid (about 5eV) to the measured energies for them to be relative to the Fermi energy of the target (Seigbahn 1967).

In Table 4-II we list our values for the Auger peaks together with those of Haas and Palmberg, indicating the assigned transition and calculated value on the basis of the Burhop formula; the column headed 'Z+1' includes his correction for the ionised state of the atom. The binding energies used for the calculations have been taken from the tables of Bearden and Burr (1967), and the energy level diagram derived from these values is given in Figure 4.4.

	"Z"	"Z+1"
$N_{4,5}$	1.5	3.3
$N_{2,3}$	51.1	59.2
N_1	86.4	95.2
M_5	334.7	
M_4	340.0	
M_3	531.5	
M_2	559.1	
M_1	669.9	
	eV	

Energy level diagram for palladium

Fig. 4.4

Agreement between our values and the calculated ones is much better when the work function correction is taken into account. No peak was observed resulting from an $M_{4,5}N_{2,3}N_{2,3}$ transition, neither was the $N_1N_{4,5}N_{4,5}$ peak, observed at 80eV by Haas, found. The two peaks at 50 and 43eV are assigned to N_2 and $N_3N_{4,5}N_{4,5}$ transitions, indicating a previously unreported splitting of the $N_{2,3}$ level of about 7eV. This is of the same order as the splitting of the equivalent levels of silver, 6.7eV.

Table 4-II

Present work	Palmberg and Haas	Allocation	Calculated		
			Z	Z+1	(Z+1)-5eV
328	337	$M_4N_{4,5}N_{4,5}$	337	335.2	330.2
324.5		$M_5N_{4,5}N_{4,5}$	331.7	329.9	324.9
300	n.r	C.E.L.	307	306	301
272	285	$M_{4,5}N_{2,3}N_{4,5}$	284.7	282.9	278
244	250	$M_{4,5}N_1N_{2,3}$	249.4	247.6	242.6
n.r	n.r	$M_{4,5}N_{2,3}N_{2,3}$	235	227	222
n.r	80	$N_1N_{4,5}N_{4,5}$	83.4	81.6	76.6
50	44	$N_2N_{4,5}N_{4,5}$	48.1	46.3	41.3
43		$N_3N_{4,5}N_{4,5}$			

Note that the splitting of the $M_{4,5}$ level of palladium was here measured as about 3.5eV, whereas the value from the Figure 4.4 is 5.3eV. The doublet as shown in Figure 4.3 is only just resolved on account of the large width of the component peaks, and it is possible that a deconvoluted curve might show greater splitting. The peak at 300eV cannot be explained purely as an Auger transition, and we have attributed it as due to an Auger electron which has suffered a characteristic energy loss. We have observed that the main energy loss peak in palladium is at 27eV (see Chapter 5), so that the predicted energy of an $M_{4,5}N_{4,5}N_{4,5}$ transition - 27eV agrees well with the observed value of 300eV.

In conclusion, the values found for the Auger peaks of palladium based on $M_{4,5}$ ionisation are some 10eV lower than previously reported, on account of the higher resolution of the present apparatus. Splittings of 3.5eV for the $M_{4,5}$ levels and 7eV for the $N_{2,3}$ levels have been resolved; in addition a new peak at 300eV has been found corresponding to a characteristic energy loss from the main Auger transition. Agreement between the observed and calculated peak positions is improved when a work function correction is made.

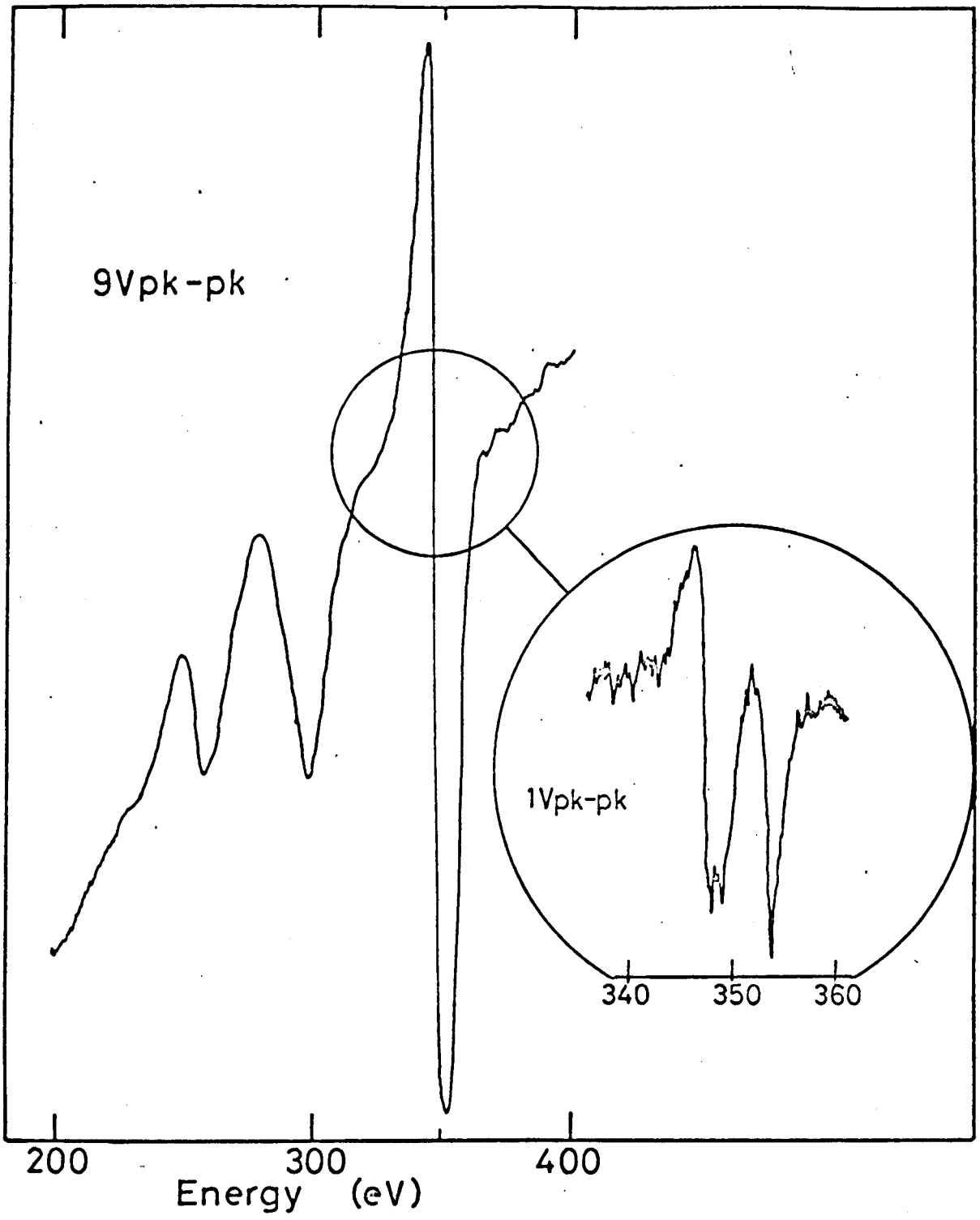

$M_{4,5}NN$ Auger spectrum of silver

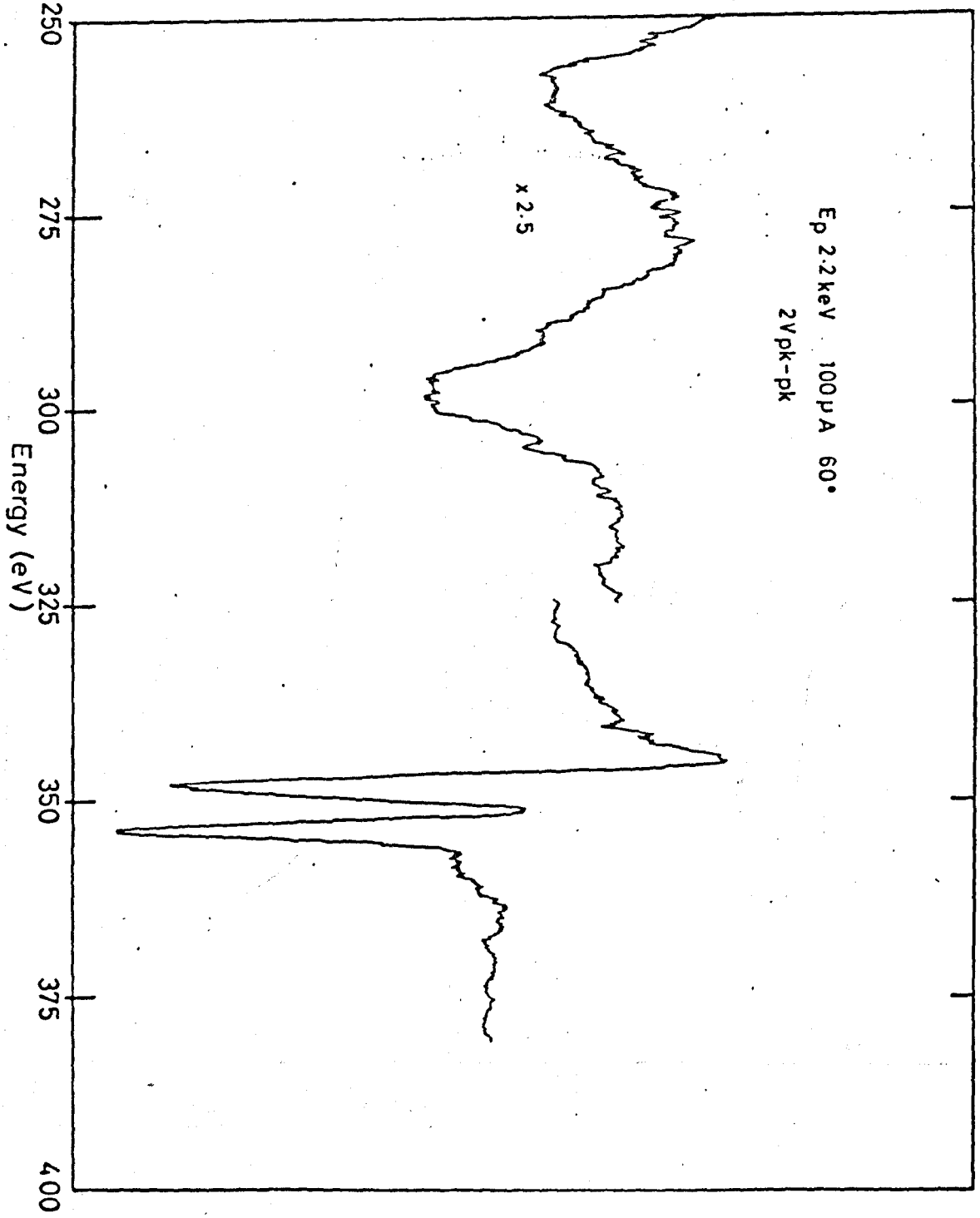

Figure 4.6 Medium resolution spectrum of silver

4.4 Silver

4.4.1 Results

The Palladium film was then covered with a film of evaporated silver. A low resolution spectrum of this surface is shown in Figure 4.5. One large and two satellite peaks may again be seen as in the case of palladium, the mean peak at 352eV being some 28eV higher than in the former case. When the modulating voltage is reduced to 3V pk-pk, the main peak splits into a doublet, as shown in Figure 4.6, the peaks appearing at 353.5 and 348eV; the two satellite peaks are not resolved into doublets, presumably because of their intrinsic width, but they appear to be spread over a range of energy of 296-301 and 257-262eV respectively.

With careful optimisation, and by using the very low value of 1V pk-pk modulation, the lower peak of the main doublet was further resolved into two peaks at 347.5 and 349eV, the upper peak appearing at 353.8eV. These results are the mean of six plots of the spectrum, two of which are shown in Figure 4.7, and one on the inset to Figure 4.5; because of the poor signal to noise ratio at this value of modulation, we found it necessary to use a time constant of 10 seconds in the d.c. integrator of the Phase Sensitive Detector, consequently each plot took over half an hour to complete at a scanning rate of about 0.02V/s. For some of the plots we used a target bias of 300 volts, to increase the effective primary energy and reduce the grid voltage to be scanned. It is evident that the equipment was being used at its sensitivity limit to obtain these results.

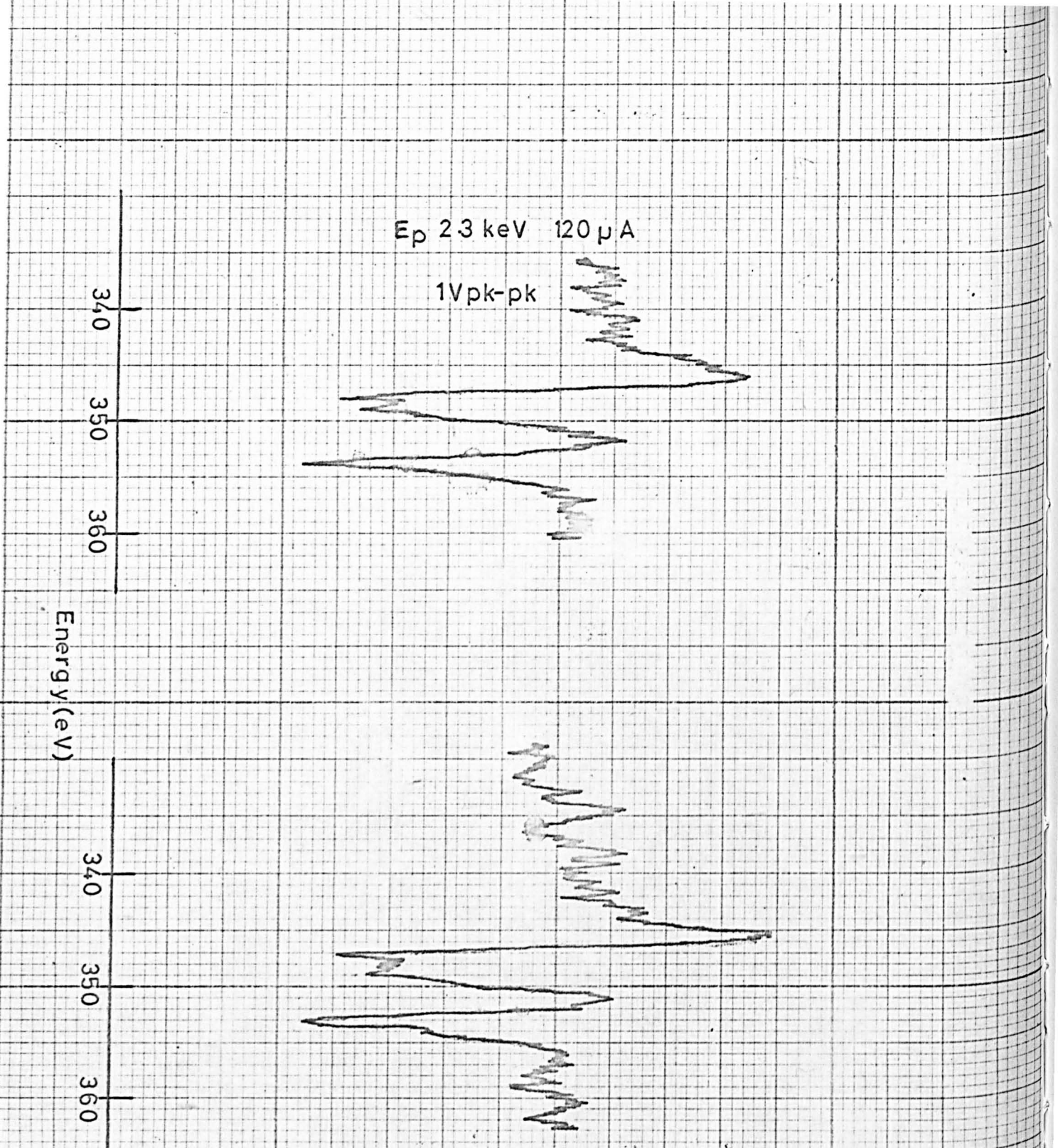

Figure 4.7 High resolution spectrum of silver

By way of comparison, we also took an undifferentiated spectrum of this region and show it in Figure 4.8. Notice how on the sloping background the satellite peaks are barely visible, whereas there is no suggestion of the main peak being split even into a doublet.

After the target had been exposed to air, we took a further low resolution plot of the surface and this is shown in Figure 4.9. The Auger peaks are now to be found at 268, 294, 304 and 350eV; in addition peaks at 150 and 508eV, representing sulphur and oxygen contamination can be seen. The main constituent of the peak at 268eV is probably carbon contamination.

4.4.2 Discussion

We compare our low resolution results on silver (Figure 4.5) with those of Haas and co-workers (1970) and Palmberg and Rhodin (1968) in Table 4-III below.

Table 4-III

Present work	Palmberg (1968)	Haas (1970)	Allocation
352	362	362	$M_{4,5}N_{4,5}N_{4,5}$
298	308	308	$M_{4,5}N_{2,3}N_{4,5}$
258	268	268	$M_{4,5}N_1N_{4,5}$
n.r.	80	n.r.	$N_1N_{4,5}N_{4,5}$
n.r.	45	n.r.	$N_2N_{4,5}N_{4,5}$
n.r.	35	n.r.	$N_3N_{4,5}N_{4,5}$
n.r	25	n.r.	$N_1N_2N_{4,5}$

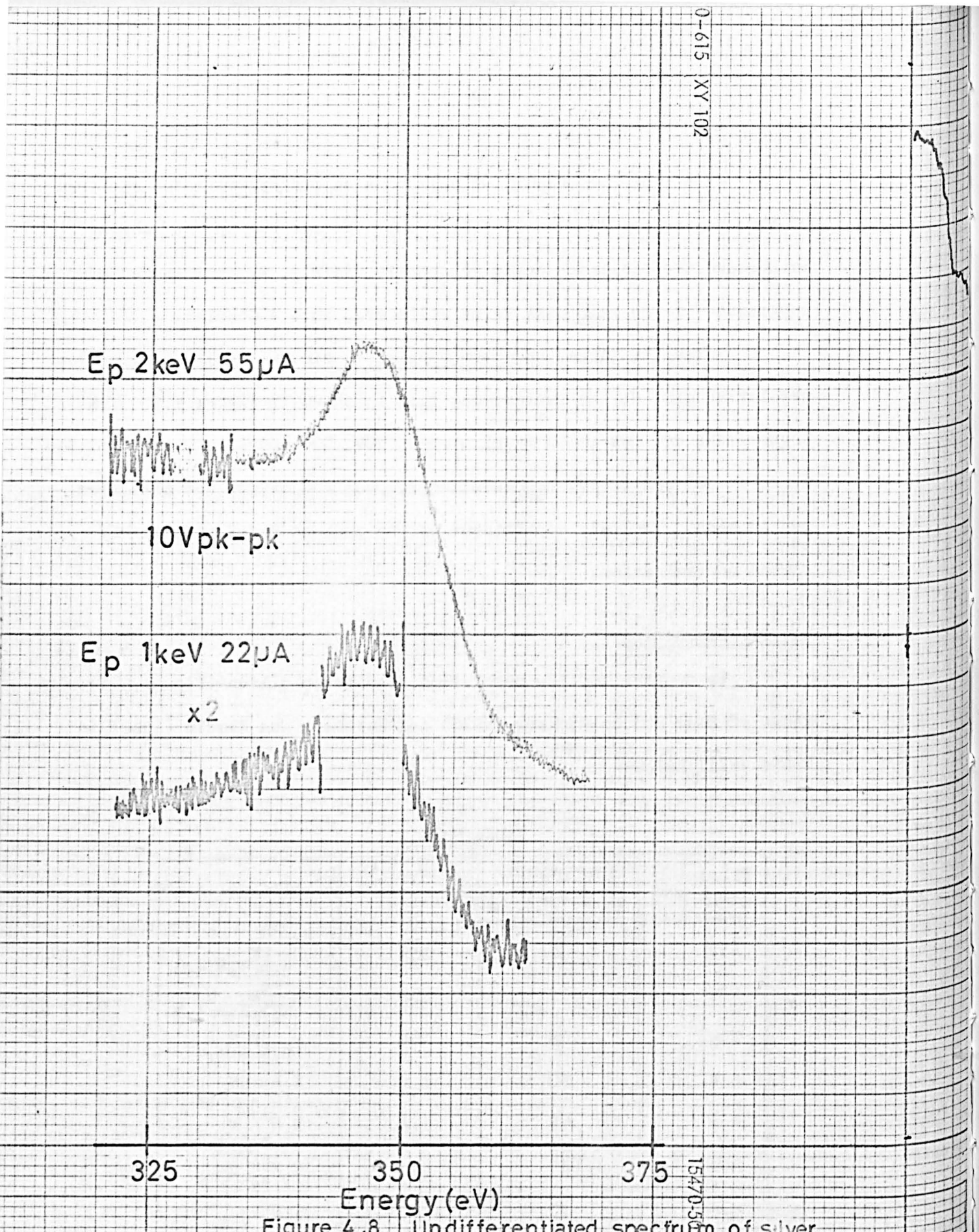

Figure 4.8 Undifferentiated spectrum of silver

Once again we notice that our results are some 10 volts lower in energy than those obtained by Palmberg and Haas. Only very weak peaks were observed at low energy and are not included in the table.

The medium resolution plots of Figure 4.6 show the main splitting of the $M_{4,5}N_{4,5}N_{4,5}$ transition into two peaks at 353.5 and 348eV; the $M_{4,5}N_{2,3}N_{4,5}$ transition appears to be spread over an energy range from 296-301eV and the lowest energy peak from 257-262eV. The calculated positions of the peaks according to Burhop's formulae are given in Table 4-IV below.

Aksela (1971), who developed the sensitive and high precision Cylindrical Mirror spectrometer, has measured the Auger spectrum of silver and found two strong peaks with a small shoulder on the lower peak. His results are compared with our high resolution plot of Figure 4.7 below in Table 4-IV. Because he referred the energies to the Fermi surface of the specimen, we have here subtracted an arbitrary 5eV from his tabulated energies, since it has not been customary to make the correction for the work function of the analyser in other published work on Auger spectroscopy.

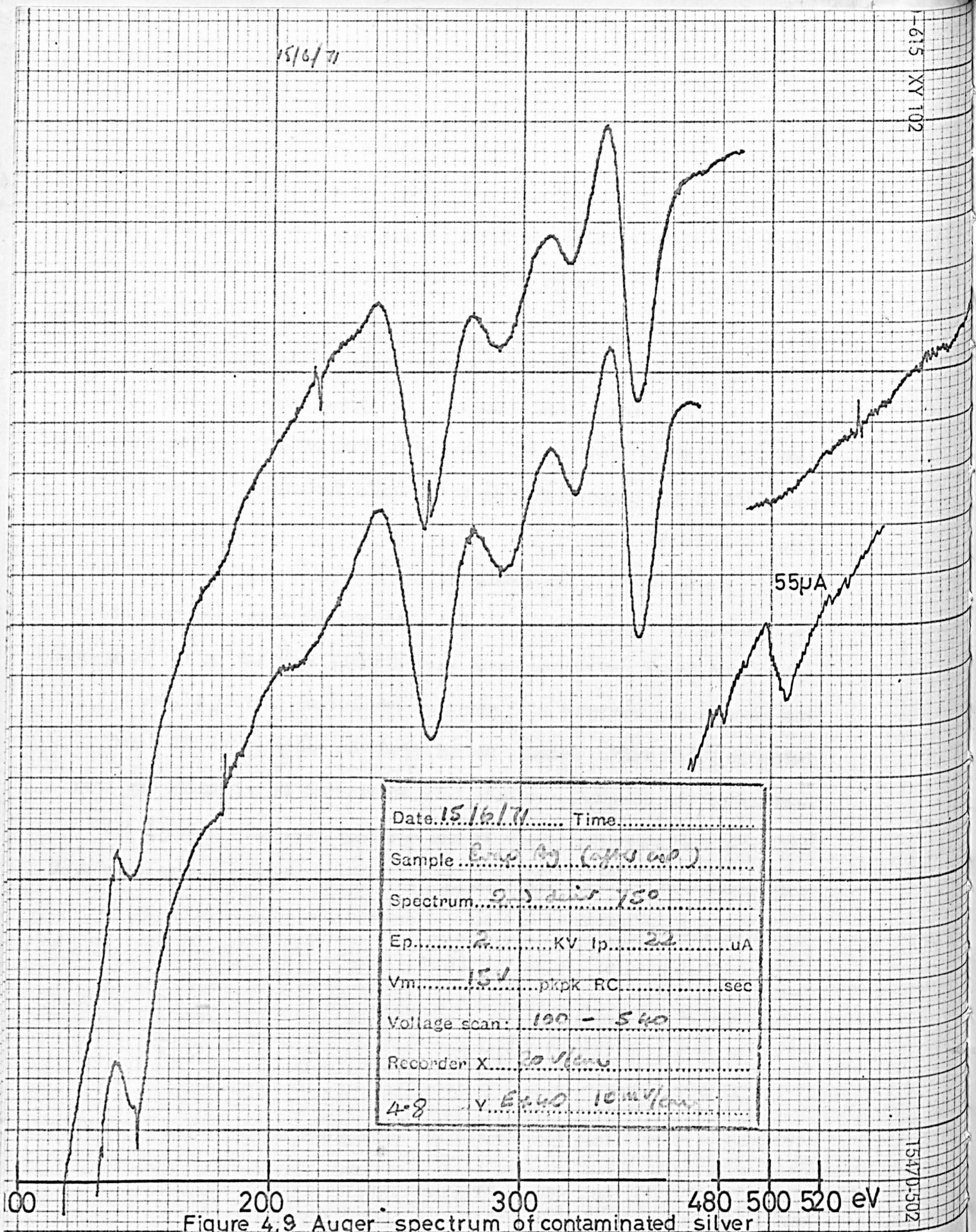

Figure 4.9 Auger spectrum of contaminated silver

Table 4-IV

Present work	Aksela (1971)	Allocation	Calculated		
			Z	Z+1	(Z+1)-5eV
353.8	354.8	$M_4N_{4,5}N_{4,5}$	366.2	360.2	355.2
349	349.6	$M_5N_{4,5}N_{4,5}$	360.1	354.1	349.1
347.5	348.4				
301		$M_4N_{2,3}N_{4,5}$		307-301	302-296
296		$M_5N_{2,3}N_{4,5}$		301-295	296-290
262		$M_4N_1N_{4,5}$		268	263
257		$M_5N_1N_{4,5}$		261	256
n.r		$M_4N_{2,3}N_{2,3}$		247	242
		$M_5N_{2,3}N_{2,3}$		240	235

It can be seen that the results of Aksela, minus work function, show excellent agreement with our values, and also with the calculated values, taking into account the work function. The main point of interest is that the splitting found for the $M_{4,5}$ level in our work is ~5.6eV, in Aksela's work, ~5.8eV, and the value from the tables of Bearden and Burr is 6.1eV, which is good evidence that the projected origin of the transition is correct. Aksela attributes the doublet found for the $M_5N_{4,5}N_{4,5}$ transition as being due to the different final state energies of the electrons which are in the $4d^8$ configuration.

		"Z"	"Z+1"
4d	$N_{4,5}$	3.3	9.3
$4p_{3/2}$	N_3	55.9	66.9
$4p_{1/2}$	N_2	62.6	
$4s_{1/2}$	N_1	95.2	108
$3d_{5/2}$	M_5	366.7	
$3d_{3/2}$	M_4	372.8	
$3p_{3/2}$	M_3	571.4	
$3p_{1/2}$	M_2	602.4	
$3s_{1/2}$	M_1	717.5	

Energy level diagram for silver

Fig. 4.10

The energy level values used for the calculations are shown in Figure 4.10, and are taken from Bearden and Burr (1967). The calculated values for the $M_{4,5}N_{2,3}N_{4,5}$ transitions in Table 4-IV also include the splitting of the $N_{2,3}$ level. It should be noted that the theory predicts a peak at 290eV, and referring back to Figure 4.5, a small bump at that energy can be found; this being identified, therefore, as an $M_5N_3N_{4,5}$ transition, the peak at 296 as $M_4N_3N_{4,5}$ plus $M_5N_2N_{4,5}$, and the peak at 301 as the $M_4N_2N_{4,5}$ transition.

The predicted position of the $M_{4,5}N_{2,3}N_{2,3}$ transitions is at about 238eV. No peak was observed at this point. The undifferentiated spectrum of Figure 4.8 shows the position of the composite $M_{4,5}N_{4,5}N_{4,5}$ transition as occurring at 347eV. The point of maximum slope on the high energy side is about 352eV which compares with the position found on the differentiated plot of Figure 4.5. Figure 4.8 was taken under the highest sensitivity condition, and demonstrates how the sensitivity and signal-to-noise ratio is improved when using the second differential.

The peaks found on the surface after exposure to air may be interpreted as due to the surface adsorption of CO and S on the silver, the extra peak at 324eV is probably a characteristic energy loss from the peak at 350eV, since the surface showed a loss of about 26eV when contaminated (Chapter 5).

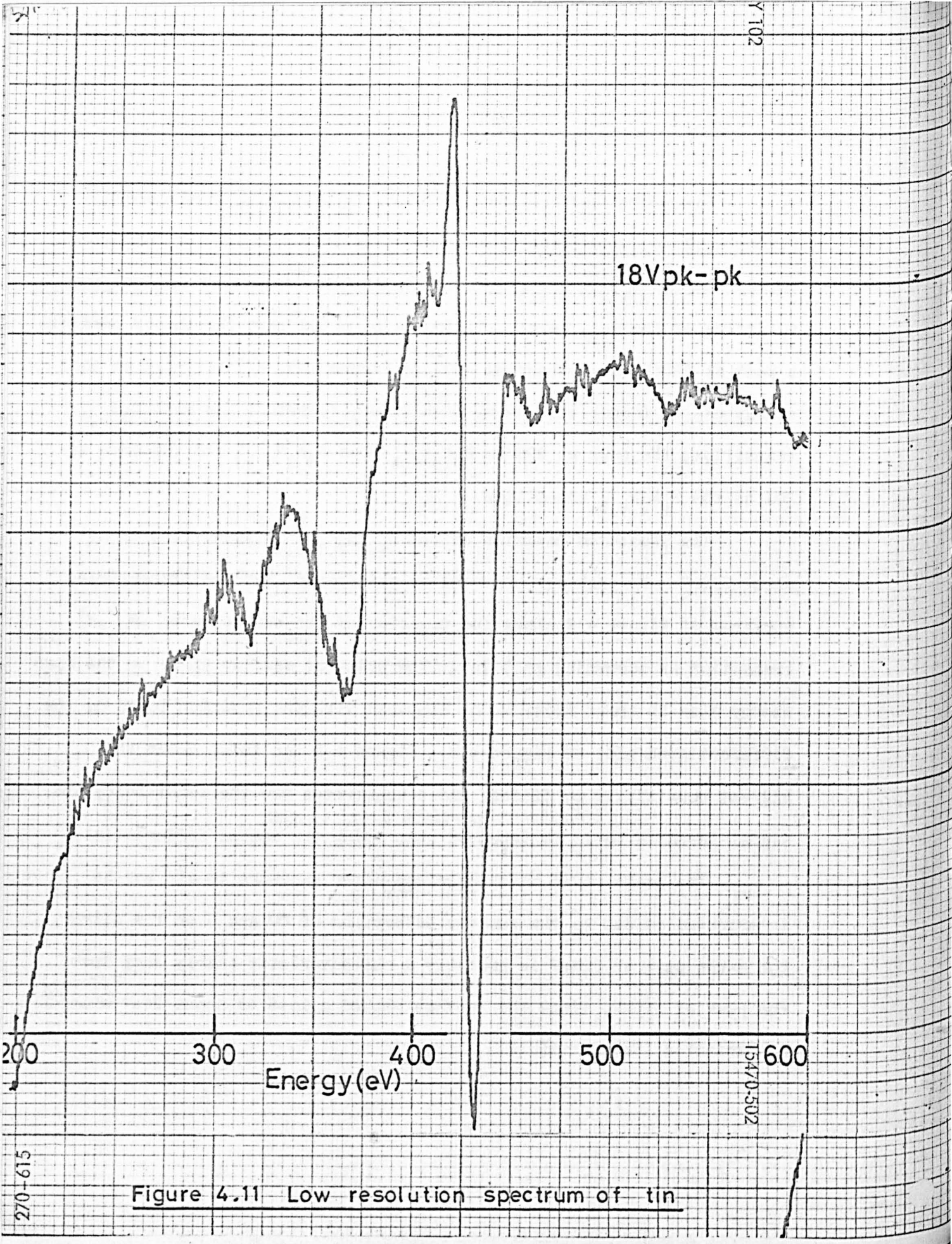

Figure 4.11 Low resolution spectrum of tin

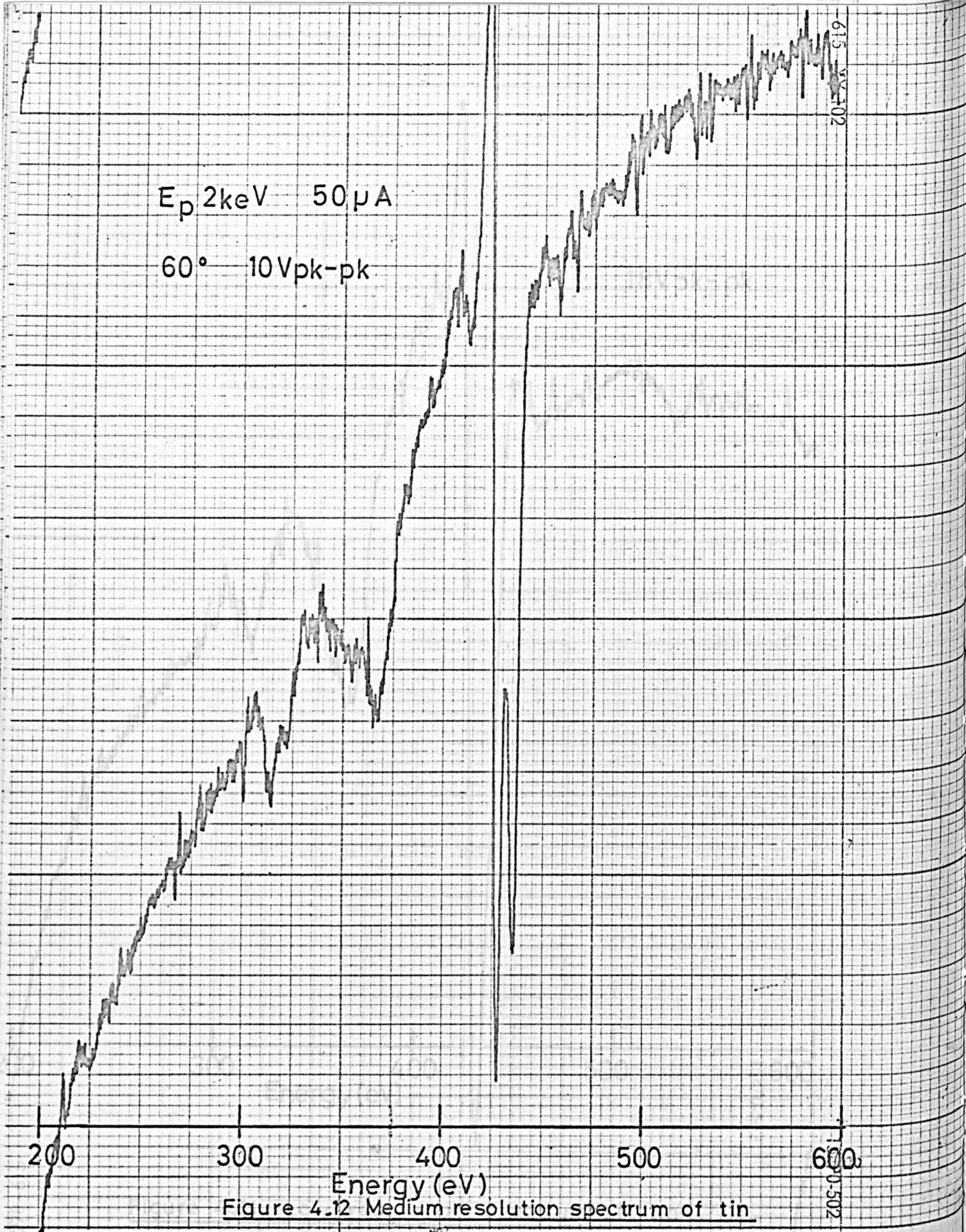

Figure 4.12 Medium resolution spectrum of tin

4.5 Tin

4.5.1 Results

Figure 4.11 shows a low resolution spectrum of evaporated tin, generally similar in appearance to that of palladium and silver. The main peak occurs at 431eV and there are two smaller peaks at 365 and 315eV. Once again, by careful optimisation of the resolution, we were able to examine the structure within the large 431eV peak, and in Figure 4.12 we can see the splitting of the peak just beginning to show up. This plot was taken with a modulating voltage of 10V pk-pk, and a time constant of 1 sec in the P.S.D. Further structure was apparent on reducing the modulating voltage still further to 2V pk-pk, and Figure 4.13 shows five scans over the energy range 430-435eV using a time constant of 10 seconds and with slightly differing settings of the x and y deflection voltages in an attempt to optimise the resolution of the structure. The fine structure observed by Pessa and others (1971) was not found in toto, but a splitting of the lower peak into two peaks at 424 and 426.5eV can be seen and the upper peak appears at about 432.5eV. Unfortunately, these plots were a trifle noisy, but the reproducibility of the five traces is quite good. No large peaks were found at lower energy except a peak at 150eV, which was probably sulphur contamination from the substrate.

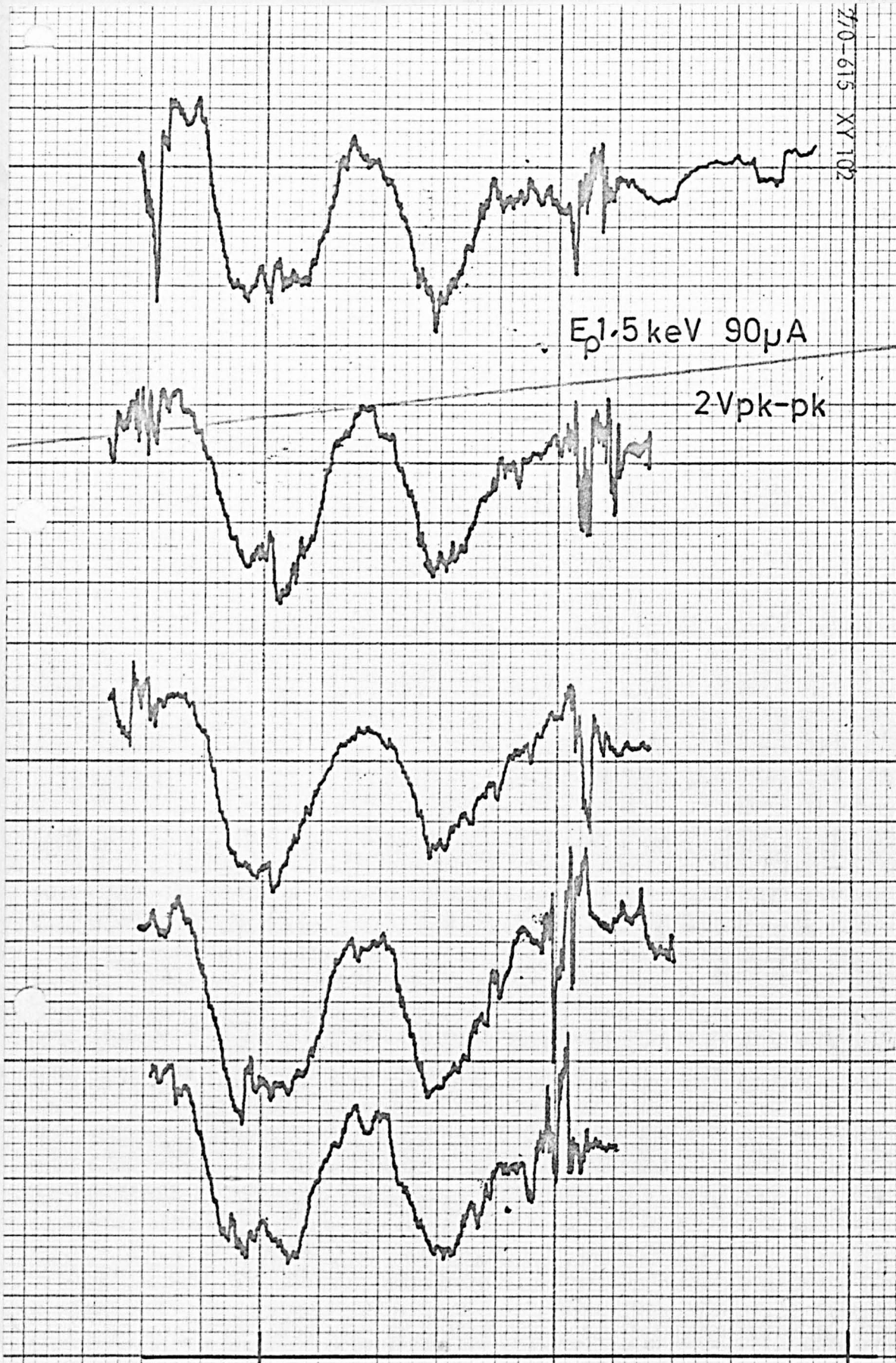

Figure 4.13 High resolution spectra of tin

4.5.2 Discussion

Neither Palmberg nor Haas has published the Auger spectrum of tin, possibly because of its low melting point. However, more recently, Jackson and Hooker (1971) have reported a spectrum obtained with a retarding field analyser, yielding peaks at 430 and 315eV. This is consistent with our measured values of Figure 4.11 of 431, 365 and 315eV, though it is strange how these authors were able to locate the 315eV peak without finding the peak at 365eV which is much larger.

In Figure 4.12, we not only see the splitting of about 7eV in the main peak but also that the peak at 365eV seems to be split into two peaks, a narrow one at about 365eV and a broad one at 350eV; similarly, the lower peak occurs at about 313 and 322eV. In Figure 4.13, the high resolution again allows us to perceive a widening of the lower energy peak of the main doublet into peaks at about 424 and 426.5eV.

These results are compared with those of Jackson and Hooker, and Pessa et al. less 5eV in the Table 4-V, where we have also included values read off the 'Varian Chart' of Strausser and Uebbing (1971) and since reproduced by Chang (1971), though the primary source of the data is not known. We have also included two columns of calculated peaks, based on the Burhop formula (1952) and the modified formula suggested by Chung and Jenkins (1970), both reduced by the work function correction. The energy levels used in the calculations are given in Figure 4.14. The column headed 'C & J' lists the levels used for the Jenkins and Chung expression, midway between 'Z' and 'Z+1'.

		"Z"	"Z+1"	"C+J"
$5p$	$O_{2,3}$	1.1	2.1	1.6
$5s_{\frac{1}{2}}$	O_1	0.9	6.7	3.8
$4d$	$N_{4,5}$	23.9	31.4	27.6
$4p$	$M_{2,3}$	88.6	98.4	93.5
$4s_{\frac{1}{2}}$	N_1	136.5	152.0	144.2
$4d_{5/2}$	M_5	484.8		
$4d_{3/2}$	M_4	493.3		
$4p_{3/2}$	M_3	714.4		
$4p_{\frac{1}{2}}$	M_2	756.4		
$4s_{\frac{1}{2}}$	M_1	883.8		

Energy level diagram for tin

Fig. 4.14

Table 4-V

Present work	Varian Chart	Jackson & Hooker	Pessa et al	Allocation	Calculated -5eV	
					C & J	Burhop
470 ?	475	n.r.	n.r.	M_4 O O	482	482
				M_5 O O	474	474
460 ?	460	n.r.	n.r.	M_4 $N_{4,5}$O	460	460
				M_5 $N_{4,5}$O	452	452
432.5	435	431	431.2	$M_4N_{4,5}N_{4,5}$	433.6	433.6
426.5 m	425		424.5	$M_5N_{4,5}N_{4,5}$	424.5	424.5
424.0		n.r.	422.5			
			419.8			
412	n.r.	n.r.	n.r.	C.E.L.	408-422	
365	377	n.r.	n.r.	$M_4N_{2,3}N_{4,5}$	367.1	368.3
350	370		n.r.	$M_5N_{2,3}N_{4,5}$	358.6	359.8
322	320	315	n.r.	$M_4N_1N_{4,5}$	316.4	320.4
313	315		n.r.	$M_5N_1N_{4,5}$	307.9	311.9

The values are again taken from the tables of Bearden and Burr (1967).

Notice again that there is no peak corresponding to the $M_{4,5}N_{2,3}N_{2,3}$ transition, and also that the agreement with 'C & J' is no worse than with 'Burhop'. The splitting of the $M_{4,5}$ level is measured as about 7.3eV, compared with Pessa's 7.7eV, the Varian Chart value of about 10eV and the value of 8.5eV from Figure 4.13. No peak corresponding

to the one at 419.8eV seen by Pessa was observed, but the small peak at 412eV seen in Figures 4.11 and 12 is allocated to a plasma loss from the M_5 transition. Strong surface and bulk losses of 11 and 16eV were observed for this tin surface (see Chapter 5) leading to predicted plasma losses from the $M_{4,5}N_{4,5}N_{4,5}$ transition at 422, 417, 413 and 408eV. The losses from the M_4 transition are obviously lost within the large M_5 transition, and its width, and the width of the losses from it, would make the resolution of separate peaks at 413 and 408eV almost impossible.

The splitting of 1.5eV observed for the M_4 transition is of the same order as the 2eV found by Pessa. Our values for the $M_{4,5}N_{2,3}N_{4,5}$ transitions do not agree as well with the predicted values as in the other cases, and there may be some contribution from an unknown splitting of the $N_{2,3}$ level, though the noise level makes accurate location of the position difficult. The small peaks at about 460 and 470eV in Figure 4.9 may be $M_{4,5}00$ and $M_{4,5}N_{4,5}0$ and two peaks in this position (but unassigned) may be found on the Varian Chart, indicated as weakly observed. The much larger peak at 525eV may be due to slight oxygen contamination.

In conclusion, we have seen splittings in the $M_{4,5}N_{4,5}N_{4,5}$ Auger transition of tin, which compare favourably with the results of Pessa; all the peaks listed on the Varian Chart due to $M_{4,5}$ ionisation have been found, together with the peak at 412eV, which we assign to a plasma loss from the $M_5N_{4,5}N_{4,5}$ transition. It is strange how Jackson and Hooker were able to see the relatively small peak at 3.5eV, but not

the larger one at 370eV - even though they were expecting it. The slight contamination observed on the surface may have been caused by diffusion of contaminants from the substrate. Since the melting point of tin is low, and the thermal conductivity of the stainless steel substrate also is low, it is quite possible that the electron bombardment of the primary beam caused local melting or diffusion of contaminants from the substrate.

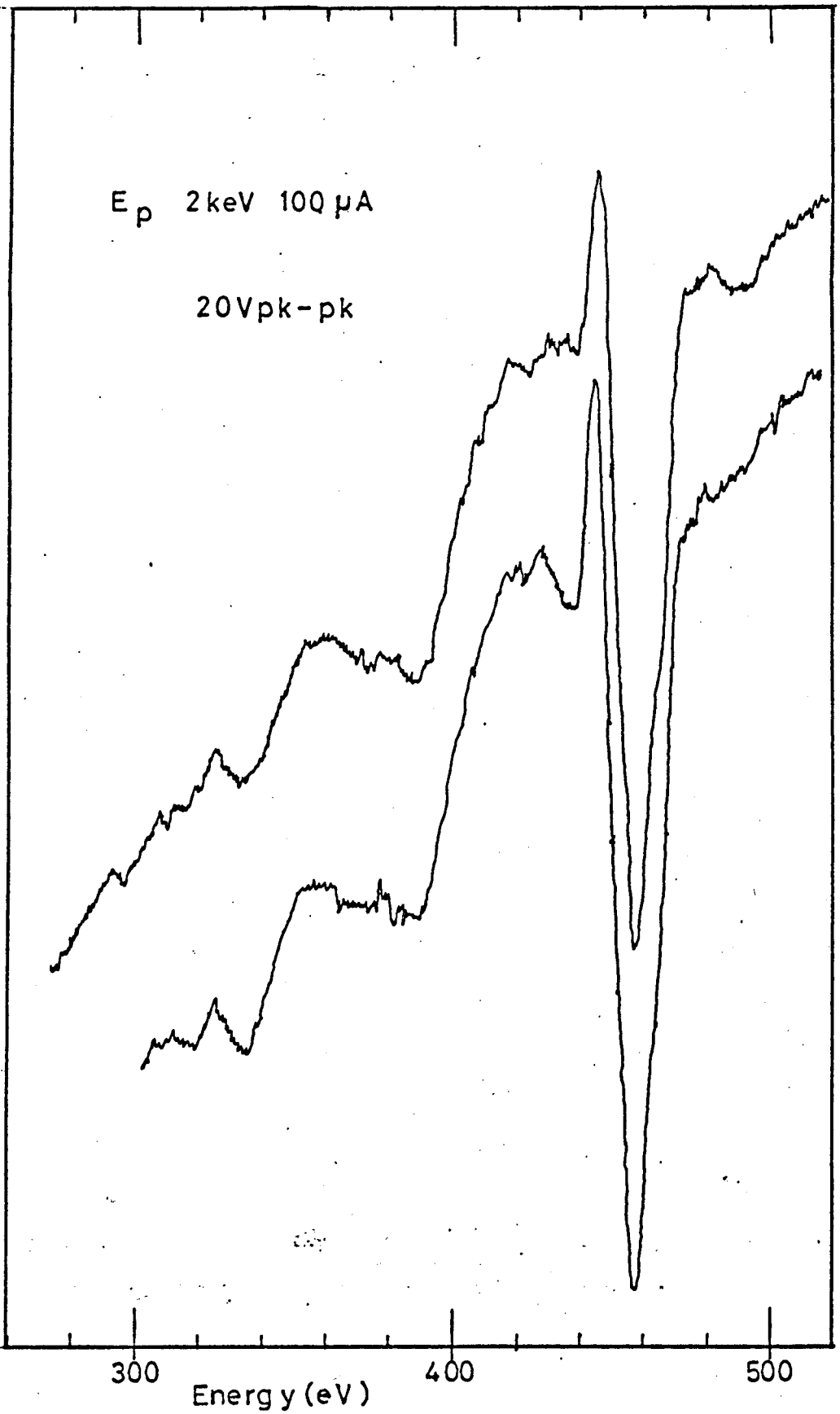

Figure 4.15 Auger spectrum of antimony

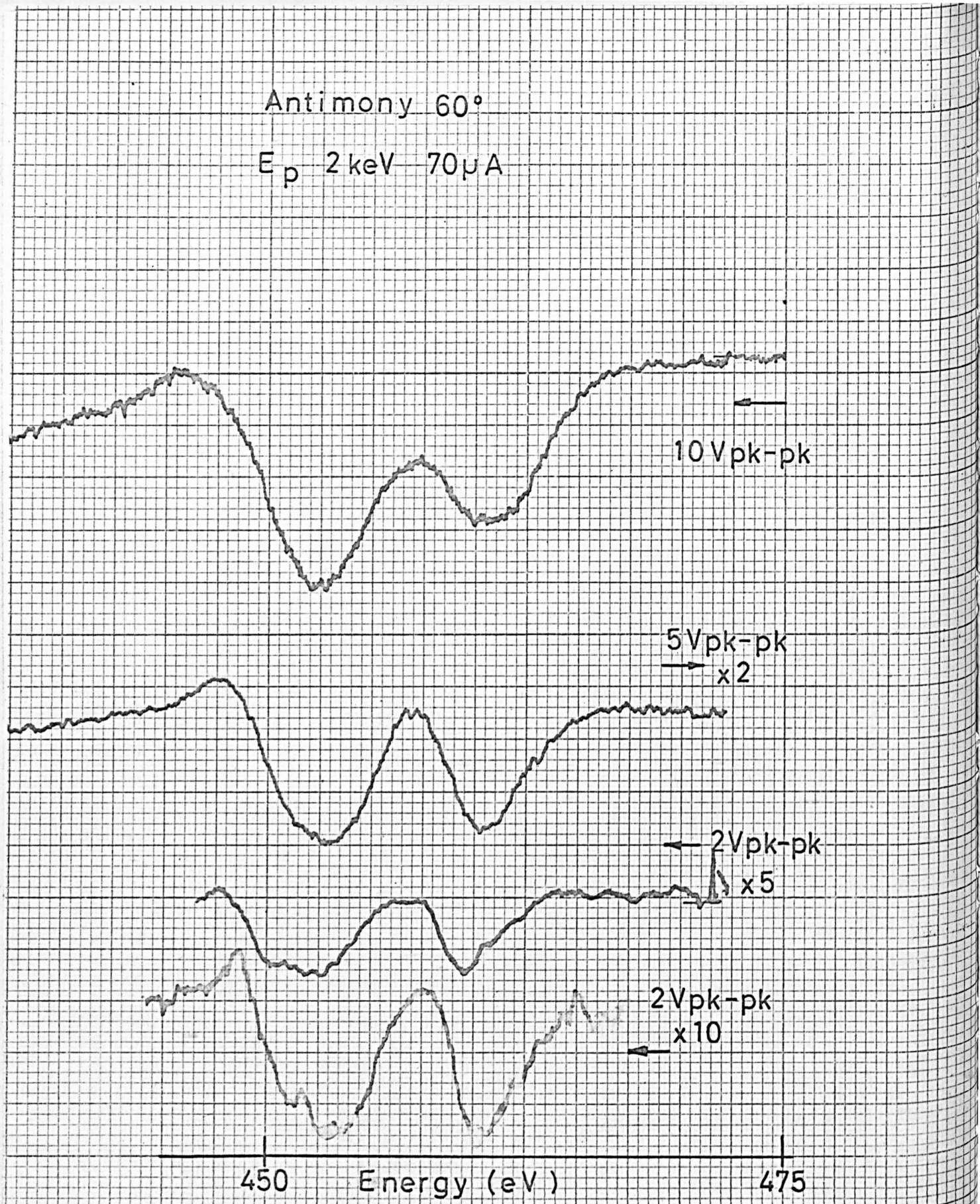

Figure 4.16 Effect of modulation amplitude on spectrum.

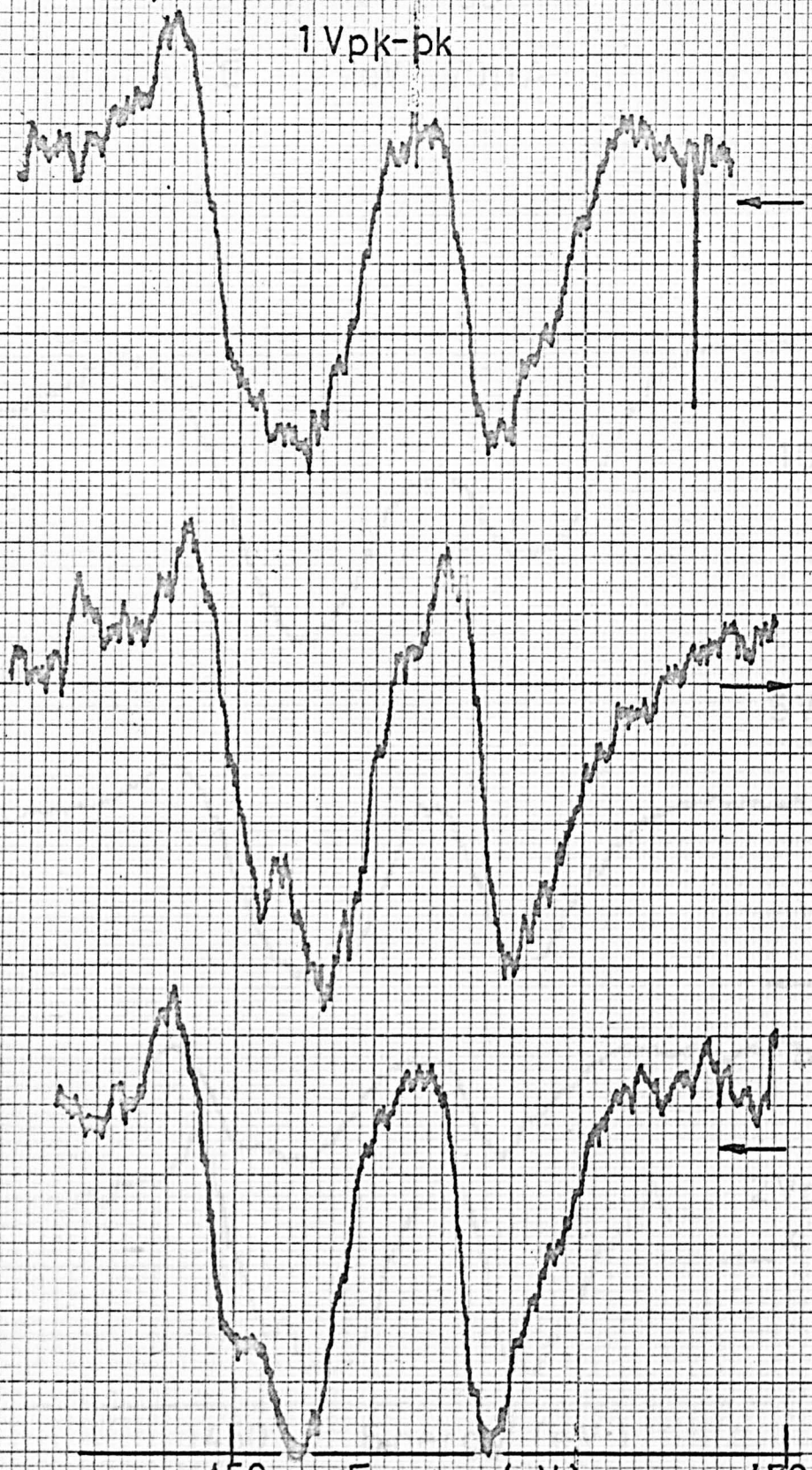

Figure 4.17 High resolution antimony spectrum

4.6 Antimony

4.6.1 Results

Low resolution spectra of the evaporated antimony surface are shown in Figure 4.15, together with the effect of a Target bias of 100 volts. The shape of the two spectra is almost identical, the 100 volt bias causing a 20% increase in peak height. These traces were taken with a modulating voltage of 20 volts pk-pk. The progressive increase in the resolution of the fine structure around the lower peak of the doublet is demonstrated in Figure 4.16, where the amplitude of modulation is reduced from 10 volts to 5 volts andfinally 2 volts.

In Figure 4.17 we show three scans over the doublet, using 1 volt pk-pk modulation. The lower peak which is at 452.5eV in the upper trace of Figure 4.16 has been resolved into peaks at 450.5 and 452.2eV, these being the mean of plots taken scanning in opposite directions. The upper peak appears at 459.5eV, and since the width of this line is about 2V, there would be little to gain from using a lower value of modulating voltage, except increased noise! It is interesting to notice that even at the low scanning speed of about .01V/s, a slight shift in peak position is evident in the plots taken in opposite directions.

No convincing peaks were seen at lower energies, except some in the slow peak region.

	"Z"	"Z+1"	"J+C"
$O_{2,3}$	2.1	2.3	2.2
O_1	6.7	11.6	9.2
$W_{4,5}$	31.4	39.8	35.6
$N_{2,3}$	98.4	110.2	104.3
N_1	152.0	168.3	160.2
M_5	527.5		
M_4	536.9		
M_3	765.6		
M_2	811.9		
M_1	934.7		

Energy level diagram for antimony

Fig. 4.18

4.6.2 Discussion

The published data on the Auger spectrum of antimony are very scarce. We here compare our results with the Varian Chart of Strausser and Uebbing (1971), with the high resolution work of Aksela et al. (1971) and with theoretically calculated values based on the energy level diagram of Figure 4.18, with data from Bearden and Burr (1967). Once again the results of Aksela et al. and the theoretically calculated values have been reduced by an arbitrary 5eV.

Table 4-VI

Present Work 4.15 4.16	4.17	Varian Chart	Aksela et al.	Allocation	Calculated -5eV J & C	Burhop
n.r.		500	n.r.	M_4OO	519	519
				M_5OO	510	510
490		490	n.r.	$M_4N_{4,5}O$	491	493
				$M_5N_{4,5}O$	481	484
461	459.5	462	460.7	$M_4N_{4,5}N_{4,5}$	460.7	460.7
	452.2		453.5			
452.5		452		$M_5N_{4,5}N_{4,5}$	451.3	451.3
	450.5		451.5			
436		n.r.	n.r.	C.E.L.	435-450	
388		390	n.r.	$M_4N_{2,3}N_{4,5}$	392.0	393.7
370		382	n.r.	$M_5N_{2,3}N_{4,5}$	382.6	384.3
		342	n.r.	$M_4N_1N_{4,5}$	336.1	340.1
332						
		332	n.r.	$M_5N_1N_{4,5}$	326.7	330.1

Once again, the main peaks can be attributed to $M_{4,5}NN$ transitions, no peak corresponding to the $M_{4,5}N_{2,3}N_{2,3}$ transition being seen. The splitting of the $M_{4,5}$ level from our work is seen to be ~8.3eV, compared with the values of 10eV from the Varian Chart, 8.2eV from Aksela et al. and 9.4eV from Figure 4.18. Also the new peak observed at 436eV is allocated to a plasma loss from the main peak; surface and bulk plasma losses were observed from this antimony film at 11 and 16eV; (see Chapter 5) so the calculated position of a bulk plasma loss from the M_5 transition is 435eV. The large width of the parent peak would make resolution of the surface plasma loss (440eV) very difficult. The losses from the M_4 transition, at 450 and 455eV, are of course masked by the M_5 transition. It is rather difficult to locate the positions of the lower energy peaks precisely, because of the poor signal-to-noise ratio and the large background slope, the origin of which is not clear.

In conclusion, the splittings of the $M_{4,5}N_{4,5}N_{4,5}$ transition in antimony agree well with the work of Aksela et al., and the results at low resolution are similar to those tabulated on the Varian Chart, with the addition of a peak at 436eV, attributed to a plasma loss from the M_5 transition.

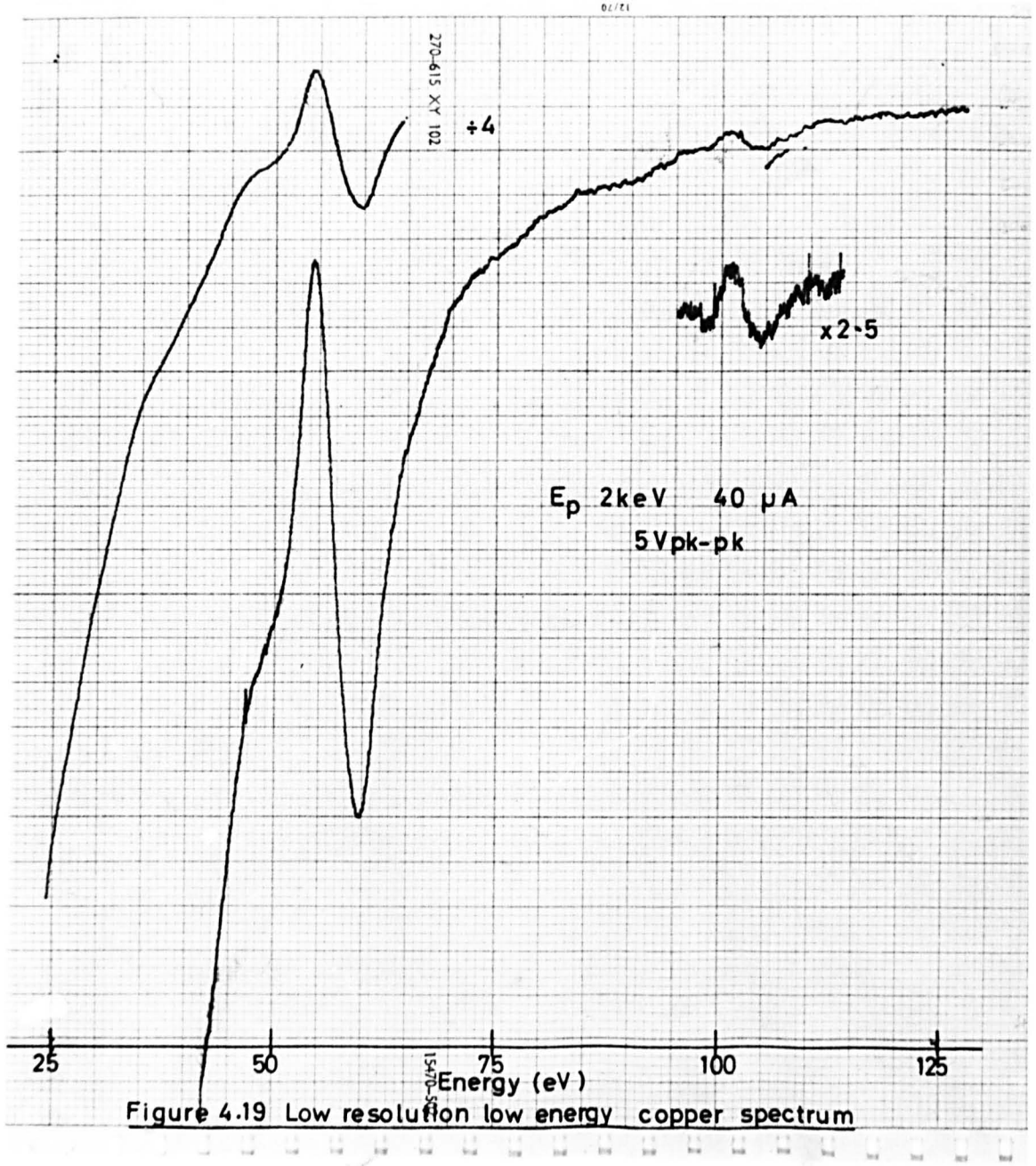

Figure 4.19 Low resolution low energy copper spectrum

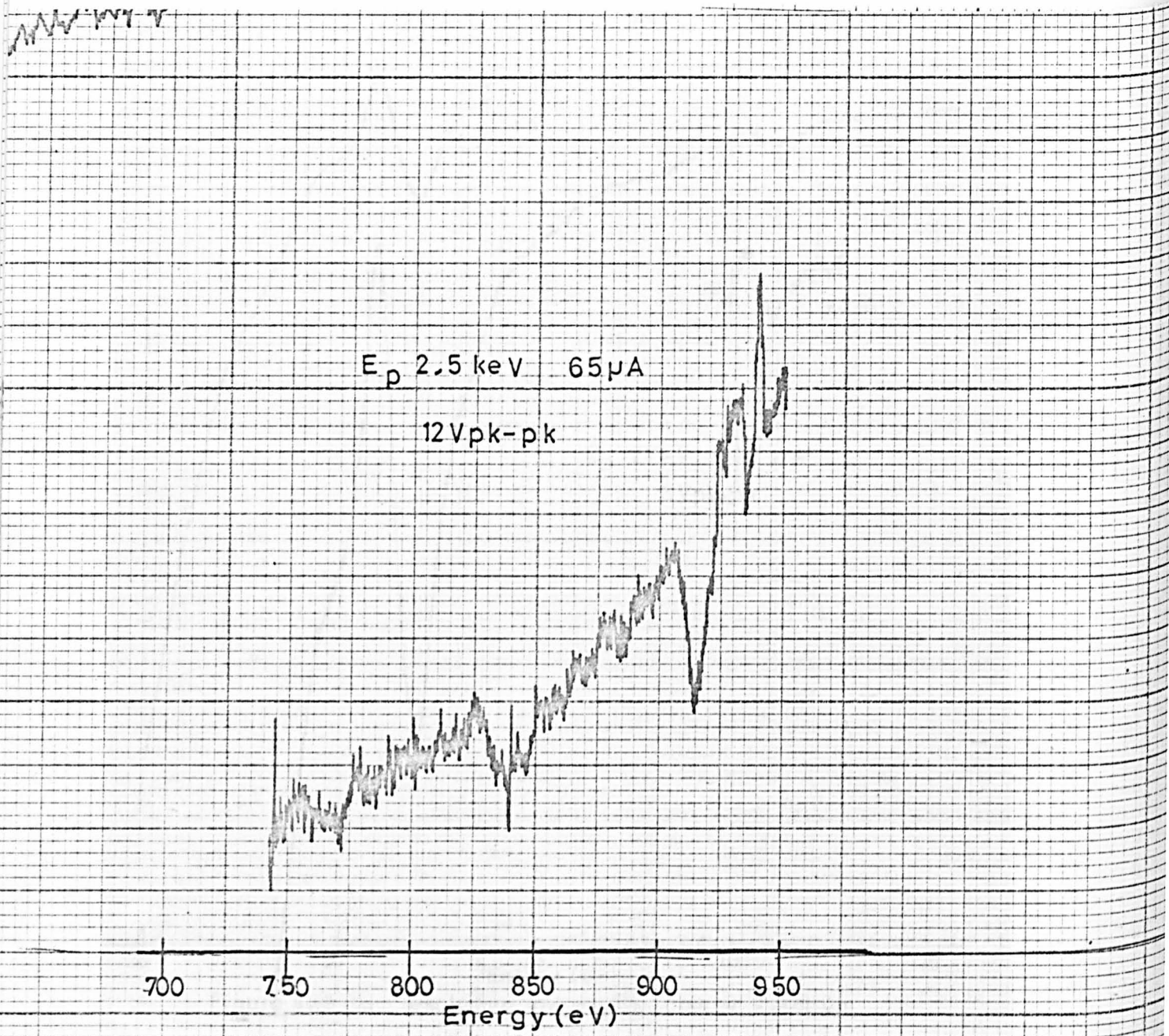

Figure 4.20 High energy spectrum of copper

4.7 Copper

4.7.1 Results

The next metal studied was copper; we show the main low energy Auger peaks observed in Figure 4.19. They appear at 59.5 and 104.5eV; in addition we were just able to distinguish from noise the high energy triplet at 913, 843 and 770eV as seen in Figure 4.20. On reduction of the modulating voltage, the peak originally at 59.5eV shows a distinct splitting into two peaks at 57 and 59.5eV as can be seen in Figure 4.21, which was taken using 2V pk-pk modulation.

On further reduction of the modulation to 1V pk-pk, the slope of the 'slow' peak was sufficiently reduced for us to be able to plot the whole of the spectrum from 0-60eV. The trace in Figure 4.22 shows additional Auger peaks at 20, 25, 33 and 36eV as well as a whole host of peaks below 15eV, which are of course discussed in C apter 6; the splitting of the 57 and 59.5eV peaks is now very clear, although their amplitude is low on this plot in order that we can display a greater range of the spectrum. We were not able to locate all the small satellite peaks on either side of this doublet that have been reported by Jenkins and Chung (1971b), but perhaps the signal-to-noise ratio in our case masked their presence.

4.7.2 Discussion

The energy level diagram of copper is shown in Figure 4.23 and in Table 4-VII we list the peaks seen together with the results of

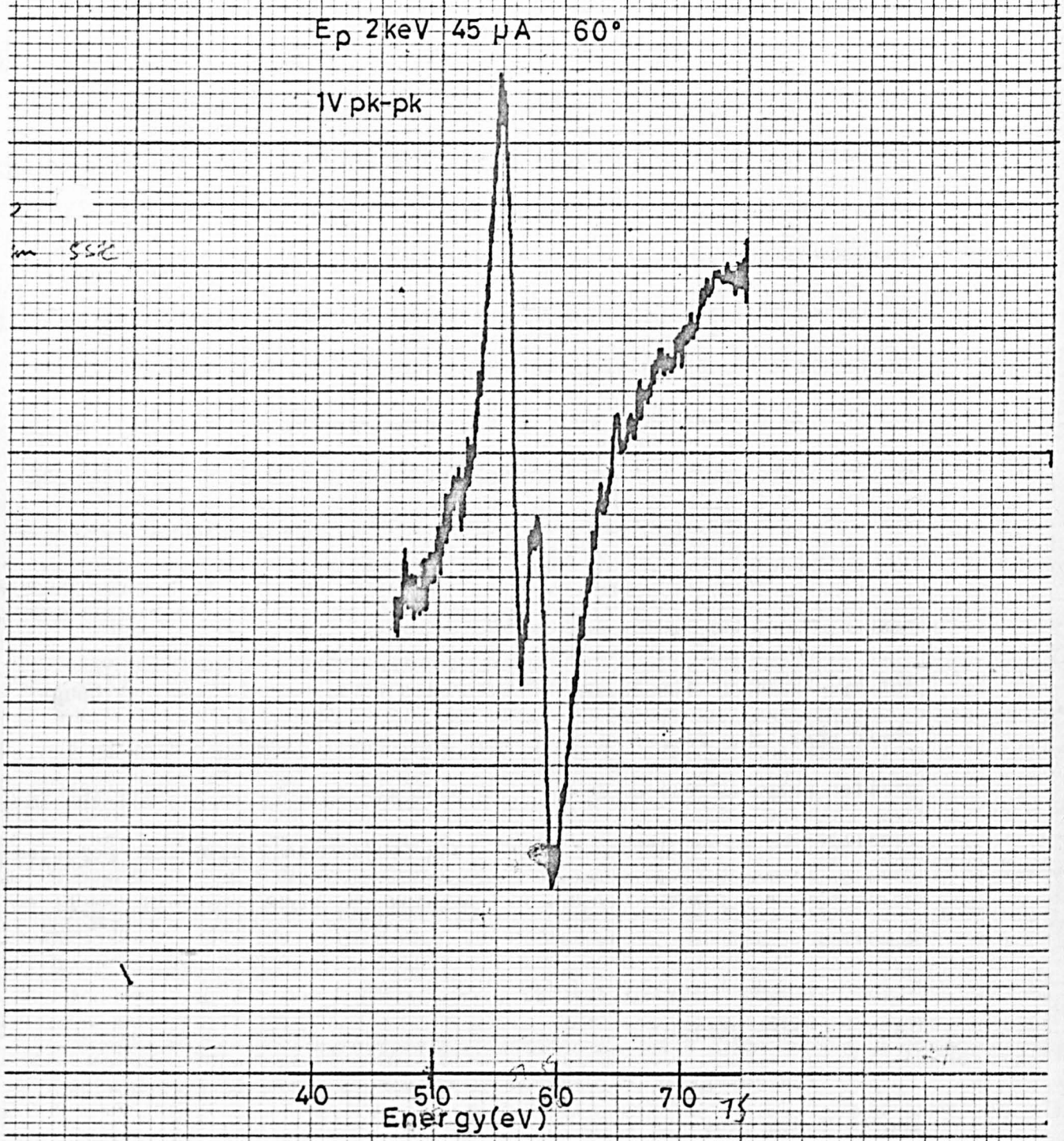

Figure 4.21 High resolution copper Auger peak

other workers; the calculated values in this case are taken directly from the paper of Jenkins and Chung (1971a) and no corrections for the analyser work function have been made. In common with most other workers, only those peaks labelled by Jenkins and Chung as Strong or Very Strong were observed; they were fortunate in being able to use up to 300μA of primary current to gain in signal-to-noise ratio, whereas our plots were taken with about 40-60μA. The results of Palmberg were, of course, taken with the single grid analyser and the effect of the field penetration at the higher voltage end has been to cause his results to be about 30 Volts high.

It is not clear from their paper if Jenkins and Chung made a work function correction to their observed energies, but it is not likely, even though their results are quite close to those of Aksela et al., who did make the correction.

The peaks observed at high resolution by Jenkins and Chung (1971b) around the $M_{2,3}M_{4,5}M_{4,5}$ doublet are shown at the bottom of the Table, together with the amended values for the main peaks. In their earlier paper, they positioned them at 62 and 59eV, some 2eV higher than our values, but in the second paper they amended these to 60.6 and 57.6eV, which are in much closer agreement. The small changes of slope found at 65 and 50eV are the only indications in the present work of the fine structure they observed as characteristic energy gains and losses. Further comparisons with their work on the other sections of the secondary electron spectrum of copper are given in the relevant sections of Chapters 5 and 6.

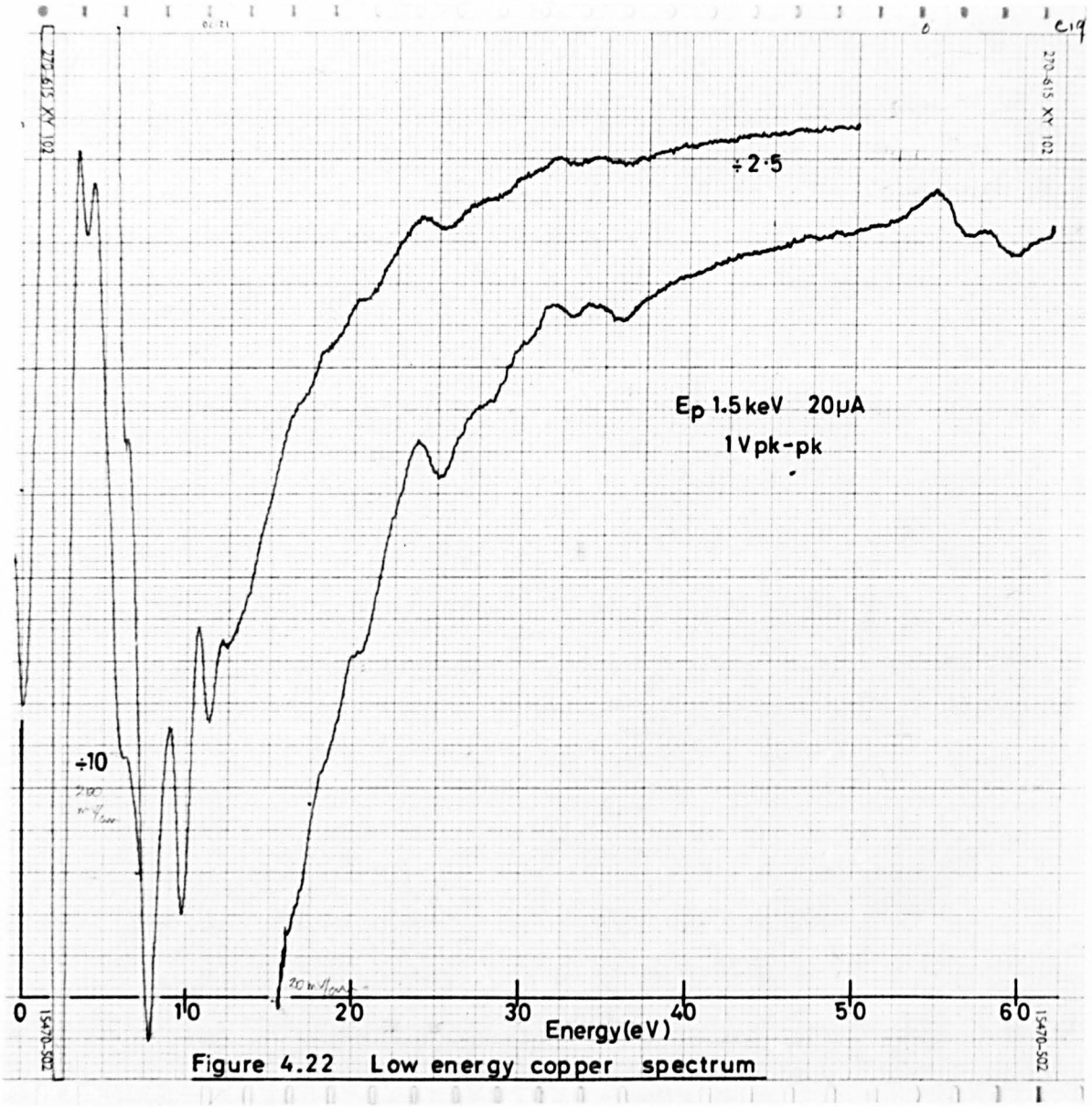

Figure 4.22 Low energy copper spectrum

TABLE 4-VII

Present Work	Jenkins & Chung	Suleman 1971	Harris 1968	Palmberg 1967	Aksela 1971	Allocation	Calculated J & C
-	1090 (VW)	-	-	-	-	$L_1M_{4,5}M_{4,5}$	1085
-	939 (M)	938				$L_2M_{4,5}M_{4,5}$	940
913	919 (VS)	918	925	950	918.9	$L_3M_{4,5}M_{4,5}$	919
	885 (VW)					$L_1M_1M_{2,3}$	887
	864 (M)					$L_2M_{23}M_{45}$	865
843	843 (S)	846	850	875	846.4	$L_3M_3M_{4,5}$	846
					839.2	$L_3M_2M_{4,5}$	845
	-	838				$L_1M_1M_1$	839
	815 (W)					$L_2M_1M_{4,5}$	815
	800 (W)					$L_3M_1M_{4,5}$	797
	791 (M)					$L_2M_{2,3}M_{2,3}$	791
770	772 (S)	773	780	795	777.2	$L_3M_{2,3}M_{2,3}$	771
	735 (M)					$L_2M_1M_{2,3}$	742
	717 (M)					$L_3M_1M_{2,3}$	722
	690 (W)					$L_2M_1M_1$	694
	679 (W)					$L_3M_1M_1$	674
104.5	109	107		109		$M_1M_{4,5}M_{4,5}$	109
	69.0						
	65.0					C.E.G.	
65?	62.5						
59.5	60.6	61		62		$M_2M_{4,5}M_{4,5}$	62
57	57.6					$M_3M_{4,5}M_{4,5}$	59
	52.3						
50?	49.7					C.E.L.	
	42.6						
	37.6						
36						$M_1M_3M_{4,5}$	42
33						$M_1M_2M_{4,5}$	39
25							

	"Z"	"Z+1"
$M_{4,5}$	1.6	8.1
$M_{2,3}$	73.6	86.6
M_1	119.8	135.9
L_3	931.0	
L_2	951.0	

Energy level diagram for copper

Fig. 4.23

In conclusion, the sensitivity of the apparatus for the high energy copper peaks has been found to be low compared with the work of Jenkins and Chung, who had a much larger primary current at their disposal; perhaps for a similar reason, it was not found possible to resolve all the fine structure reported by these workers around the low energy copper peak. It is possible, however, that the peaks that they observed at 42.6 and 37.6eV, and associated with characteristic energy losses are in fact the Auger transitions $M_1M_{2,3}M_{4,5}$.

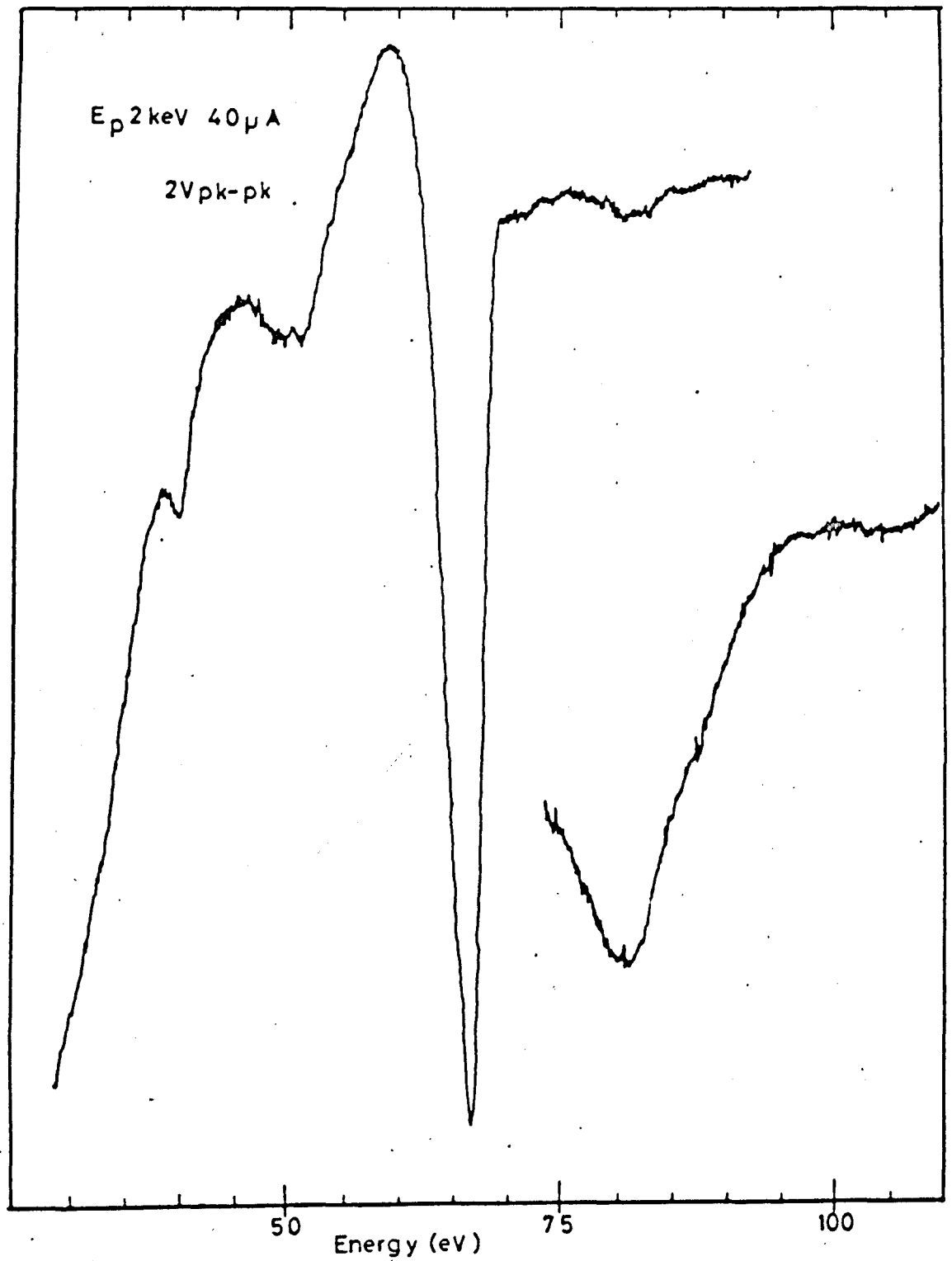

Figure 4.24 Auger spectrum of aluminium

4.8 Aluminium

4.8.1 Results

This section deals with the Auger spectrum of aluminium. As mentioned in the introduction, it is similar to that originally reported by Suleman and Pattinson (1971), and the additional fine structure later observed by these workers was not found. The main feature of the spectrum, shown in Figure 4.24, is the large peak at 67eV, smaller peaks at 51 and 82eV and very small peaks at about 105 and 40eV. The main information gained from this spectrum was the fact that the surface was clean, since very small amounts of chemisorbed oxygen cause a radical change in the spectrum (Suleman and Pattinson). A number of attempts were made to plot the high energy Auger peaks, but breakdown problems and a very poor signal-to-noise ratio joined forces to thwart all efforts.

The Auger spectrum was taken several times throughout the subsequent measurements of characteristic energy losses (Chapter 5) and energy gains (Chapter 6) and at no time was any oxygen peak or oxidised aluminium peak observed, showing that the residual pressure of oxygen in the apparatus must have been extremely low.

4.8.2 Discussion

Table 4-VIII gives a comparison between the present work, that of Suleman and Pattinson (1971, 1972) and of Quinto and Robertson (1971). The calculated values are those of Suleman and Pattinson, who explained

	V_1	0.2
M_1	V_2	3.5
	V_3	6
$L_{2,3}$		73.1
L_1		117.7

Energy level diagram for aluminium

Fig. 4.25

their higher resolution results with reference to the observed valence band structure of aluminium (Ashcroft 1966) which contains three peaks, labelled V_1, V_2 and V_3 whose energies from the Fermi level are about 0.2, 3.5 and 6eV. If we assume that in the vicinity of any particular atom the most likely configuration of the three valence electrons is one at each peak of the density of states, then transitions of the type LV_1V_1, LV_2V_2, LV_3V_3 will have a low probability, because on average only one electron is in each energy level. However the situation is complicated by the fact that it is virtually impossible to build into the calculations any correction for the ionised state of the atom after the transition; and for an element of low atomic number like aluminium, this change will be relatively large, e.g. the binding energy of the Si $L_{2,3}$ level is 99.2eV, of the M_1 level 8eV and the $M_{2,3}$ level 3eV. The absence of a work function correction would make the calculated position of a peak about 5eV high, but on the other hand, absence of a correction for the ionisation may make it low by up to 7eV. All that can be hoped is that in this case the two effects tend to cancel.

TABLE 4-VIII

Present work	Suleman & Pattinson 1971	Suleman & Pattinson 1972	Quinto & Robertson 1971	Allocation (S & P)	Calculated (S & P)
				$L_1V_1V_1$	117.3
				$L_1V_1V_2$	114.0
				$L_1V_1V_3$	111.5
105	---	107		$L_1V_2V_2$	110.7
	---	93.5?		$L_1V_2V_3$	108.2
	---	89.8?		$L_1V_3V_3$	105.7
82	82	82.4	81	Plasmon Gain	82
		73		$L_{2,3}V_1V_1$	72.6
				$L_{2,3}V_1V_2$	69.3
67	67	67.1	67	$L_{2,3}V_1V_3$	66.8
				$L_{2,3}V_2V_2$	66
		58.5		$L_{2,3}V_2V_3$	63.5
		55		$L_{2,3}V_3V_3$	61
50	52	49.7	52	Plasmon Loss	52
		45.4		$L_1L_2V_1$	44.5
40		40.3	39	$L_1L_2V_2$	41.2
				$L_1L_2V_3$	38.7

It can be seen that the agreement between the observed peaks and their theoretical position calculated on this basis is not terribly good, and one is tempted to look for other possible explanations to the fine structure. Taking the results of Suleman and Pattinson, we note that the separations of the observed peaks above the main Auger peak at 67eV are 6, 15.4, 22.8 and 26.5eV from it, and the separations of the peaks below are 8.5, 12, 17, 21.6 and 27eV. It is impossible to compare the relative heights of these peaks because of the large change in the background slope, but it is not unreasonable to suggest that they are all examples of characteristic energy losses and gains. If we now move the median energy from 67 to 66eV (we are, after all, measuring the high energy edge of a wide peak), the "gains" and "losses" appear as shown below; some of the observed energies corresponding surprisingly well with the measured values of surface and bulk plasmons (Chapter 5).

Table 4-IX

"Gain"	"Loss"	Plasmon Energies
7	7.5	
	11	1S 11
16.4	16	1B 15.5
	20.6	
23.8		2S 22
27.5	26	B+S 26.5

The similarity between these results and those of Jenkins and Chung (1971b), who studied the low energy copper peaks now becomes apparent. We make further comparisons with peaks observed at low energies in Chapter 6. Jenkins and Chung (1971c) have recently published a paper on aluminium covering Auger electron and characteristic gain and loss phenomena. They obtained Auger peaks at 33, 40.7, 52.0, 67.6 and 83eV. Further discussion of their results is included in Chapter 6.

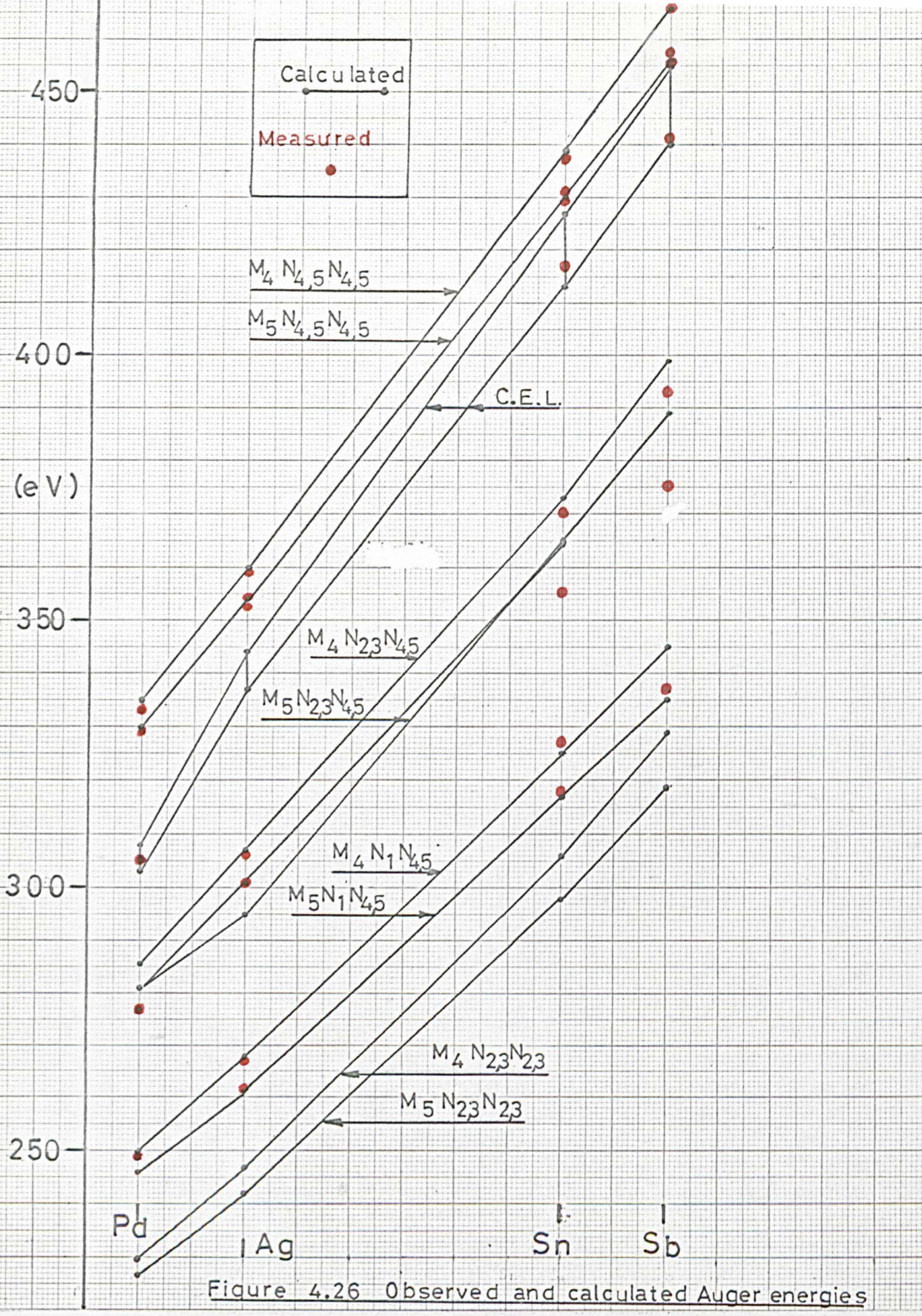

Figure 4.26 Observed and calculated Auger energies

4.9 Conclusions

In this chapter we have demonstrated the performance of the equipment as an Auger spectrometer. Although Auger spectroscopy was originally intended as an analytical tool for the confirmation of surface cleanlinesss, the high resolution of this particular analyser has made possible observation of fine structure not previously recorded with this type of device. It is possible, also, that this high resolution is the reason for the results described being lower in apparent energy than most other recorded work; with the notable exception of Aksela and Pessa, the results of most workers have been so high in comparison with the calculated peak positions that they have 'neglected' to make a work function correction to their recorded results. However, the fact that the convention of measuring the high energy edge of a peak has been adopted, means that where large modulation has been used or the intrinsic width of a peak is large, a "correction" is implicit in the observed value.

Figure 4.26 shows graphically the peaks observed and the calculated positions of the $M_{4,5}NN$ Auger transitions of the metals Pd, Ag, Sn and Sb plotted against atomic number. The calculations are based on the "Burhop Z+1" formula, and in this case we have added the work function correction to our results, so that all energies are relative to the Fermi energy of the target. The observed energies have been plotted in red for clarity. It is very tempting to explain the splitting

TABLE 4.X

Xenon $M_{4,5}N_{4,5}N_{4,5}$ Auger transition energies and a comparison between the energies relative to the $^1D_2$ line and the same energies calculated under the assumption of intermediate coupling. (See also appendix B). Errors in parentheses.

Line number	Kinetic energy (eV)	Relative energy (eV)	Calculated relative energy (eV)	Interpretation
1	537.5(5)	4.75(10)	5.23	$M_4N_{4,5}N_{4,5}(^3F_4)$
2	535.7(3)	3.02(7)	3.44 3.61	$M_4N_{4,5}N_{4,5}(^3F_{2,3})$
3	534.5(3)	1.73(7)	1.54	$M_4N_{4,5}N_{4,5}(^3P_2)$
4	533.7(5)	0.97(7)	0.68 0.92	$M_4N_{4,5}N_{4,5}(^3P_{0,1})$
5	532.7(3)	0	0 0.01	$M_4N_{4,5}N_{4,5}(^1D_2)(^1G_4)$
6	527.3(3)	−5.41(7)	−6.09	$M_4N_{4,5}N_{4,5}(^1S_0)$
7	524.9(3)	4.76(7)	5.23	$M_5N_{4,5}N_{4,5}(^3F_4)$
8	523.3(3)	3.18(7)	3.44 3.61	$M_5N_{4,5}N_{4,5}(^3F_{2,3})$
9	521.8(3)	1.71(7)	1.54	$M_5N_{4,5}N_{4,5}(^3P_2)$
10	521.0(4)	0.95(7)	0.68 0.92	$M_5N_{4,5}N_{4,5}(^3P_{0,1})$
11	520.1(3)	0	0 0.01	$M_5N_{4,5}N_{4,5}(^1D_2)(^1G_4)$
12	514.6(5)	−5.53(10)	−6.09	$M_5N_{4,5}N_{4,5}(^1S_0)$

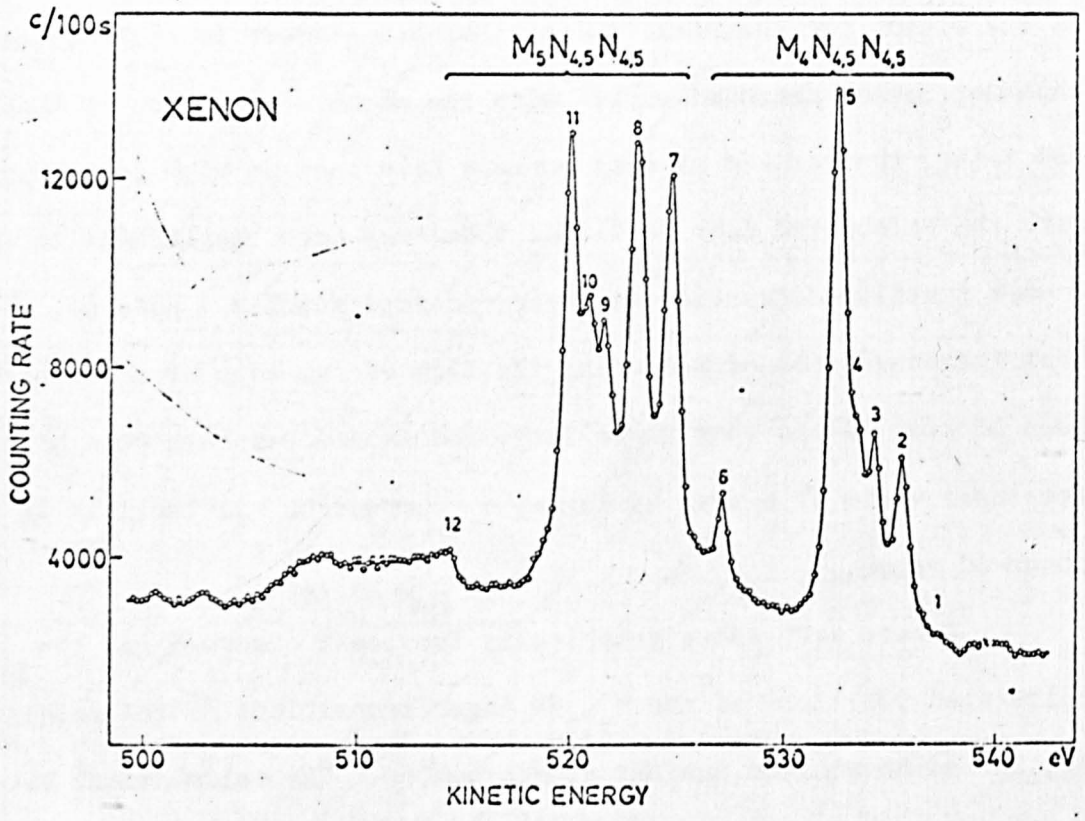

Fig. 4.27 Xenon $M_{4,5}N_{4,5}N_{4,5}$ Auger electron spectrum with resolved fine structure of the final state. The spectrum was excited by electron impact.

of the $M_5N_{4,5}N_{4,5}$ transition on the basis of a plasma loss from the M_4 transition; the observed energies agree very well in the case of tin and antimony, but there are two reasons for dismissing this hypothesis: the amplitude of the peak is much too large compared with the plasma loss from the M_5 transition. The agreement is sadly astray for the case of silver, where a splitting of the lower peak is observed when no plasma loss from the peak is seen and the predicted energy does not agree with the observed losses for silver.

Seigbahn et al. (1969) have studied the Auger spectra of the noble gases, both with X-ray and electron stimulation. In the spectra of gases, of course there are none of the broadening effects associated with measurements in the solid state, and no plasma losses associated with the peaks. Consequently they were able to resolve a great deal of fine structure for these gases, and we show in Figure 4.27 their $M_{4,5}N_{4,5}N_{4,5}$ Auger spectrum of Xenon, the closest noble gas to the metals we have been studying. It should be noted that some six peaks were observed for each main transition, but the relative amplitudes in the two cases were different. The measured energies (Table 4 - X) accorded very well with those calculated for the possible final states of the $4d^8$ configuration, based on an intermediate coupling scheme.

It is not clear why the relative amplitudes of the transitions to different final states differ for the M_5 and M_4 based transitions; presumably some selection rule is operating. However the result of this asymmetry between the two transitions is to make the apparent width

of the M_5 transition much greater than that of the M_4 transition, and to split it more or less into two peaks, with final states $(^1D_2)$,$(^1G_4)$ and $(^3F_4)$, $(^3F_{2,3})$. If we make this (rather rash) assumption that the final state splittings will be proportional to the $M_{4,5}$ splitting, and that they will have similar relative amplitudes for the metals we have been studying, then we can estimate the splittings and apparent widths for the two peaks as would be observed under our lower resolution conditions. These estimates are given in Table 4-XI, where the 'width' of the M_5 peak has been taken as peaks11-7 and that of the M_4 peak as peaks 5-3 in Figure 4.27. The measured widths are the half heights (or rather depths) of the high resolution plots.

Table 4-XI

Element	$M_{4,5}$ splitting	M_5 width		M_4 width	
		Obs.	Est.	Obs.	Est.
Xe	12.6	5.2	-	1.5	-
Sb	9.4	5	3.9	2.5	1.1
Sn	8.5	4.5	3.5	2.5	1.0
Ag	5.9	2.7	2.3	1.7	0.9
Pd	4.7	n.r.	1.9	n.r.	0.7

As mentioned earlier, the instrumental resolution of about 0.3% would lead to additional broadening of observed peaks in this energy range by about 1eV, so bearing this in mind, it would appear that the assumptions are justified at least qualitatively.

In no case were the transitions $M_{4,5}N_{2,3}N_{2,3}$ or $M_{4,5}N_1N_1$ observed, and it is quite strange that in the case of tin and antimony the strongest observed transitions did not involve the valence band, but were still of the $N_{4,5}N_{4,5}$ type. The selection rules for Auger transitions are not well understood (if at all!) and it is not clear why the $M_{4,5}N_{4,5}N_{4,5}$ transition predominates as it does for these elements. Certainly there are 10 electrons in each of the d-levels involved, thus enhancing the transition probabilities by sheer weight of numbers, but this is perhaps not a sufficient criterion. If we recall the Auger peaks seen in the case or zirconium (Chapter 3), it will be remembered that the main transition observed was the $M_{4,5}N_{2,3}N_{4,5}$, and a strong $M_{4,5}N_{2,3}N_{2,3}$ was also seen, as distinct from the case at this end of the transition series. Zirconium, of course, has only two 4d electrons, so the fact that the main transitions involve the six 4p electrons points to an increased transition probability when the levels involved are full, due perhaps to a strong hole-hole interaction.

Although the fine structure that has been reported by other workers around the low energy Auger peaks of copper and aluminium has not been found, it is suggested that in both cases the satellite peaks result from characteristic gain and loss mechanisms; for aluminium some of the observed peaks of Suleman and Pattinson (1972) correspond to surface, bulk and multiple plasma losses and gains, and this interpretation appears to be equally as valid as one based on the influence of the valence band structure.

In a general way the results presented demonstrate the retarding field analyser used at its limit of resolution and sensitivity, and it is most likely that they will soon be surpassed by measurements using a cylindrical mirror analyser, which should offer improvements in both resolution and sensitivity, particularly when the differential of the energy distribution is plotted. The measurements in the following chapters demonstrate an area in which perhaps the retarding field analyser will still maintain its supremacy; the flexibility of being able to use a variety of incident angles and still collect all the secondary electrons, and the measurement of the very slow electrons with energies up to about 25eV. It is also true to say that it is not possible to make secondary yield measurements with the cylindrical analyser!

CHAPTER 5

CHARACTERISTIC ENERGY LOSSES OF Pd, Ag, Sn, Sb, Cu and Al

5.1 Introduction

This chapter is concerned with characteristic energy loss measurements made on the metals whose Auger spectra have been described in the previous chapter. The energy loss measurements were made immediately after an Auger investigation had confirmed the surface cleanliness. We used primary energies from 100eV to 1keV and angles of incidence of from normal to 75° to normal incidence, in order to assist in the identification of surface and bulk plasma losses; some losses observed have also been attributed to core ionisation and inter-band transitions. The thorough examination made of the energy loss spectrum of Aluminium has allowed us to measure the variation in the ratio of the amplitude of the surface and bulk losses with primary energy and incident angle. For analysis of the data on aluminium we are most grateful to the Physics Department of the University of Birmingham for allowing us the use of a Dupont Curve Resolver.

The methods of measuring the characteristic energy losses are of two main types: transmission measurements through thin foils, where energies of several keV have been employed, using electron microscopes or particle accelerators for the primary radiation; and reflection of comparatively slow electrons, which are analysed by retarding field or electrostatic velocity analysers. The narrowest plasma loss peaks have been seen using the transmission method. This is as a result of the well known plasmon dispersion relation (Pines 1956), since for small scattering angles the width of the energy

loss will be small, whereas if we integrate over all scattering angles, as is the case with the reflection measurements, the observed lines will be broader. The surface cleanliness of the samples used in transmission measurements is perhaps more in doubt, because of the difficulties associated with the preparation of thin self-supporting films. It is much more likely that the surfaces involved in the measurements of Powell (and others in Australia) were cleaner, since they employed in situ evaporation; this work was performed over ten years ago, so that the vacua involved were 'high' rather than 'ultra-high', and they did not have the benefit of Auger spectroscopy for monitoring the surfaces.

The results described in the following pages generally confirm the work of Powell's group; comparisons have also been made with values obtained by the other methods where appropriate, and more recent work where available.

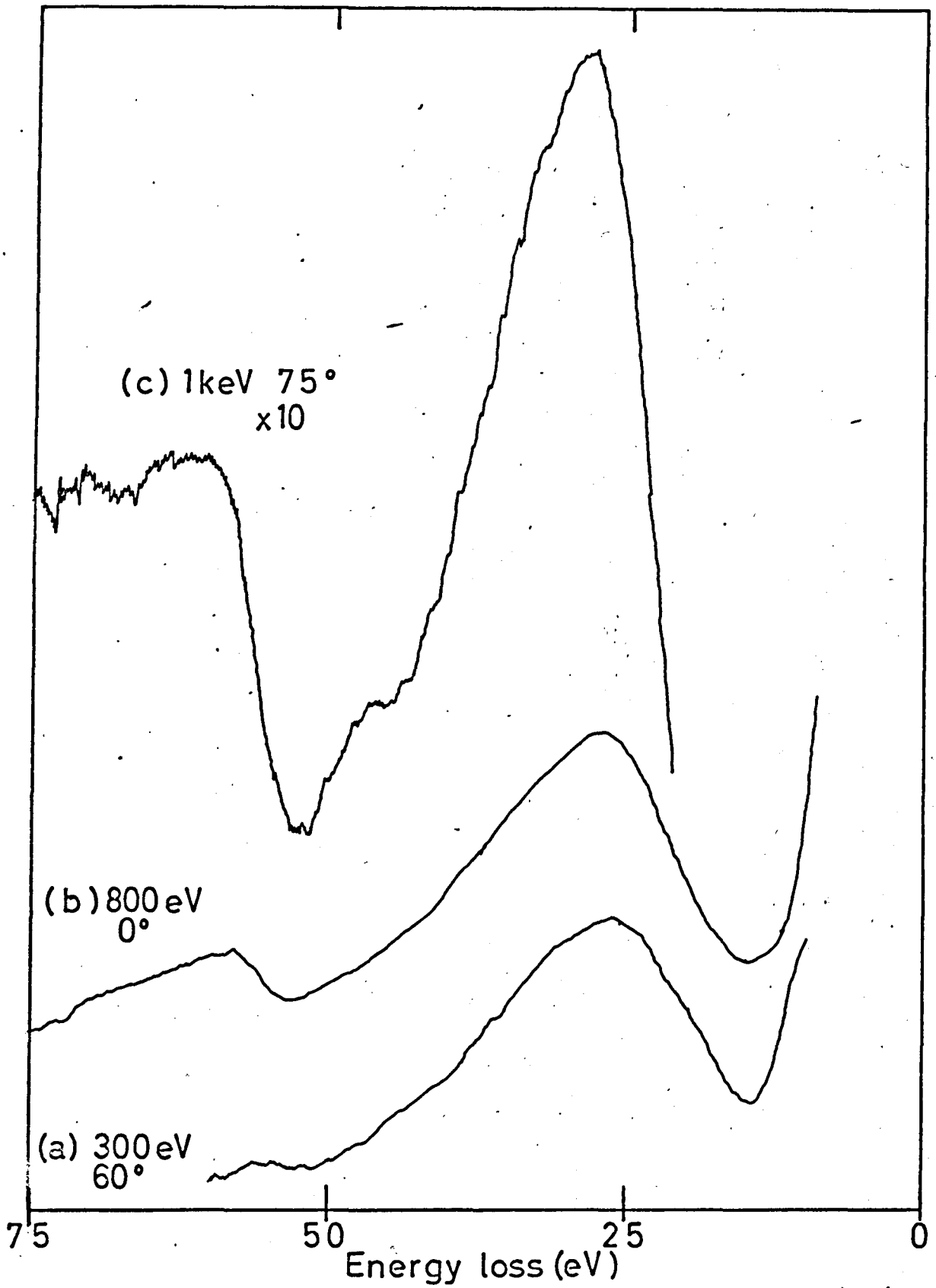

Figure 5.1a Energy loss spectrum of palladium

5.2 Palladium

5.2.1 Results

The first electron energy loss spectra from evaporated palladium are shown in Figure 5.1a. The primary energies used were 300, 800 and 1,000eV. The main loss is seen to be at 27eV, and on raising the primary energy a peak appears at 58eV together with a small peak at 46eV. The loss peak at 27eV is nearly symmetrical in shape, whereas that at 58eV has more of the appearance of an absorption edge.

These were perhaps the least complete and reliable of the energy loss results, since at this early stage we were still experiencing alignment and magnetic shielding problems. A re-measurement of the energy loss spectrum at primary energies of 250, 300 and 1000eV is shown in Figure 5.1b. Thelosses now appear at 7, 15, 26, 33 and about 47eV.

5.2.2 Discussion

In Table 5-I we compare the present values for the characteristic energy losses with the results of Powell and Swan (1959) and Marton and Leder (1954).

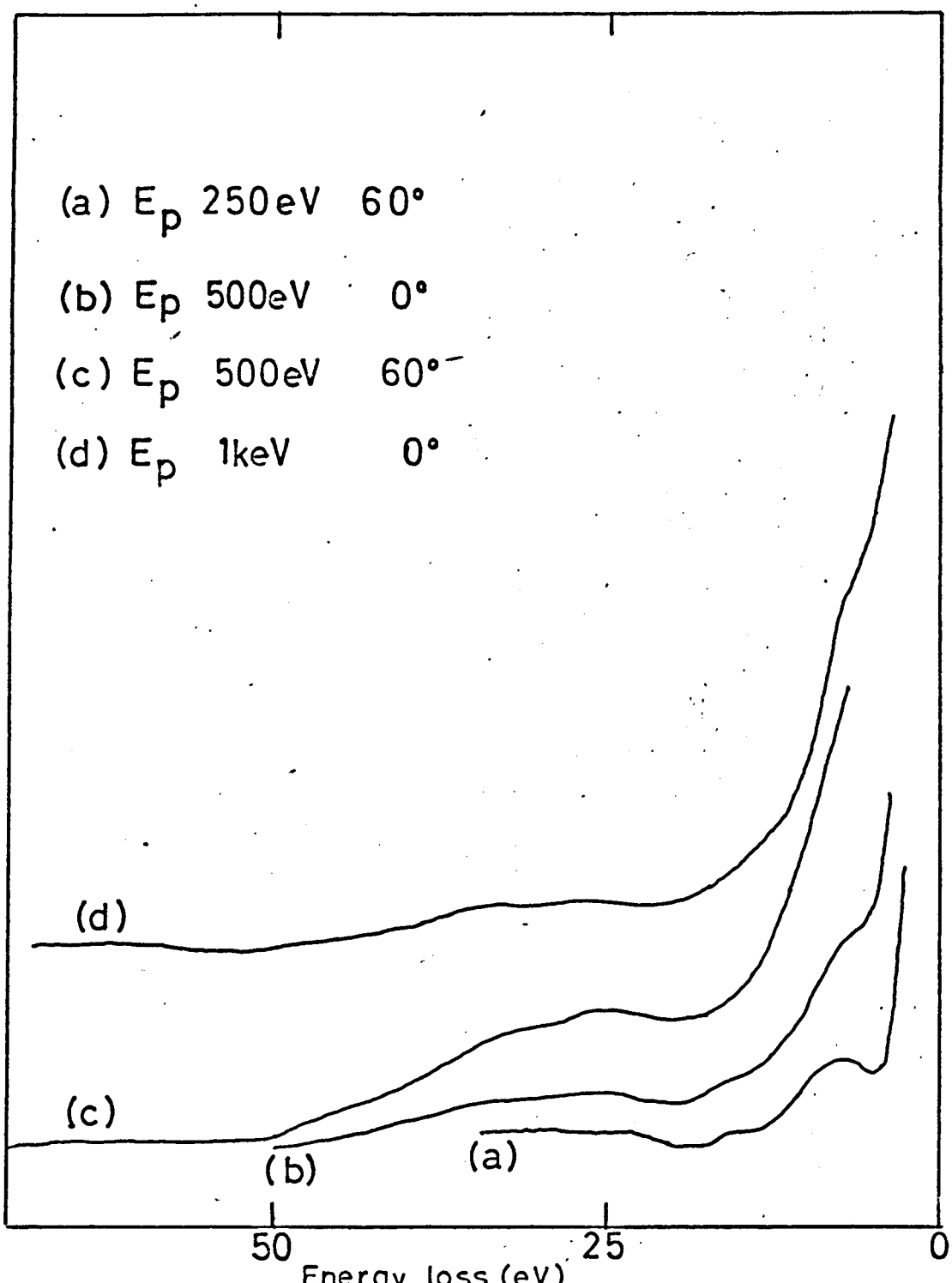

Second measurement of loss spectrum of palladium

Figure 5.1b

Table 5-I

Present work (a)	Present work (b)	Marton and Leder	Powell and Swan
	7		6.8
	15	15	16.0
		22	20.2
	26		25.5
27			
	33		
46			31.9
	47		
58			

The values obtained in the second measurement are much closer to those of Powell and Swan than the first determination. The analysis of the energy loss spectra of the transition and noble metals is complex and not well understood, and presumably, for palladium a variable number of d electrons can enter into collective oscillation.

The theoretical free electron value for the bulk plasmon in palladium with 10 electrons per atom is 31eV, with the corresponding surface loss at 22eV. There is also an interband transition $N_1 - N_{2,3}$ of energy 34.7eV (see Figure 4.4), and the strong coupling between this and the bulk loss could also depress the observed value.

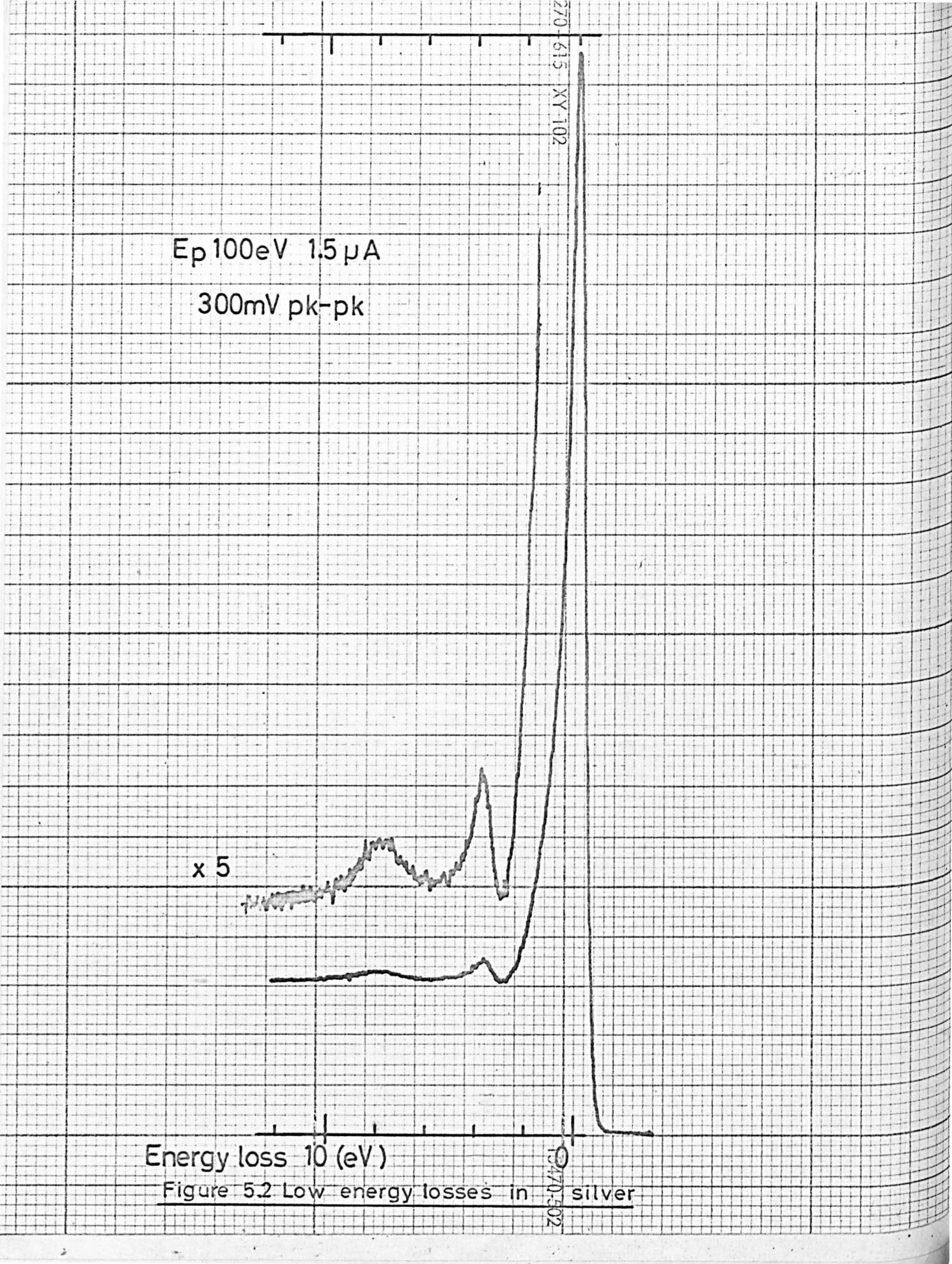

Figure 5.2 Low energy losses in silver

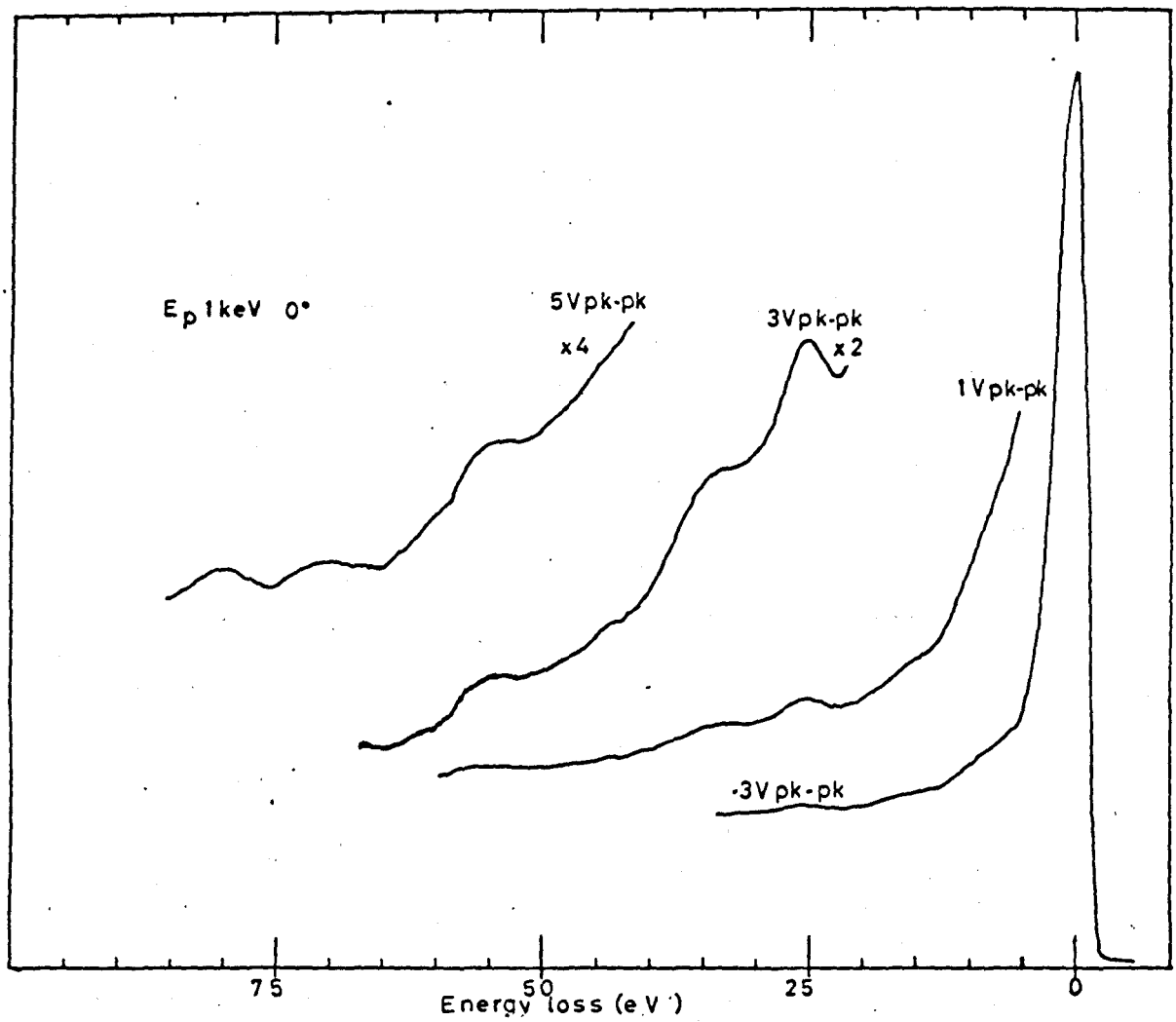

Figure 5.3 Energy losses of silver

5.3 Silver

5.3.1 Results

The energy distribution of secondaries in the vicinity of the elastic peak for silver with a primary energy of 100eV is shown in Figure 5.2. Two losses at 3.8 and 7.6eV are apparent. When the primary energy is raised to 1keV, these losses completely disappear, and in Figure 5.3 we can see losses at 16, 25, 34, 44, 55, 70 and 80eV. In Figure 5.4 we show the energy loss spectrum for a range of primary energies from 150eV to 1keV. In Table 5-II are listed our observed losses as a function of the incident conditions, and with reference to the appropriate figures.

Table 5-II

Ep	θ	Losses										Figure
100	0	3.8	7.8	(most accurate)								5.2
100	0	3.8	7.8									
1000	0			16	26	34	44	54	58	70	80	5.3
150	0	4	8		26							5.4a
205	0	3.5	7.5									5.4b
500	60	3.5	7	15	25	33						5.4c
500	0		8		26	34	45	54		70	80	5.4d
1000	0			16	25	34	44	54	57	70	80	5.4e

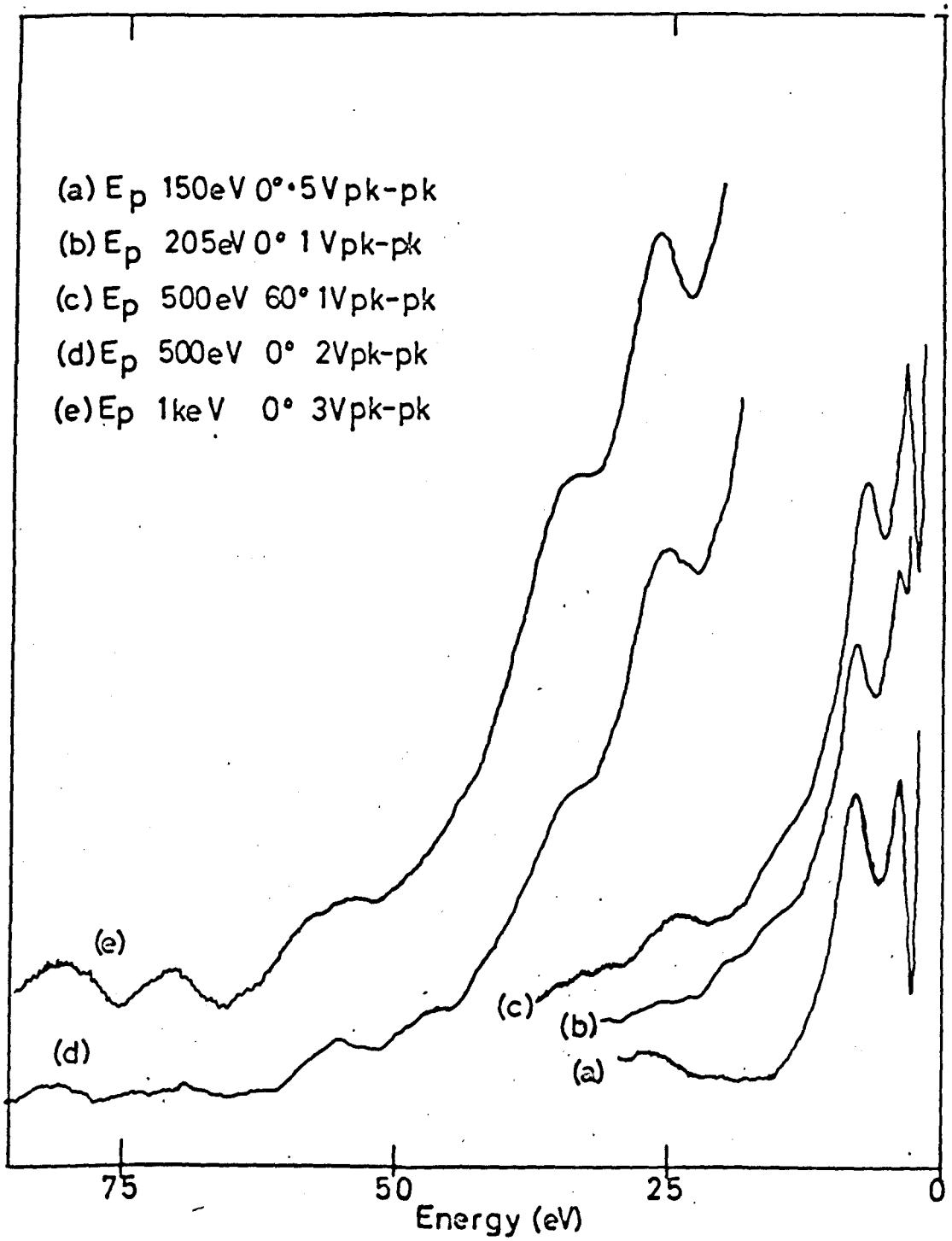

Figure 5.4 Energy loss spectra of silver

5.3.2 Discussion

Figure 5.5 shows the energy loss spectrum for a number of primary energies after exposure to air. Only the 16eV and 25.5eV loss are now visible, the low losses having disappeared. Figure 5.6 lists all the possible energy loss values for silver. Because of its rapid increase in amplitude with angle of incidence, the 3.8eV loss is assigned to a surface plasma loss associated with the 5s electrons. This could be lowered by the possible $N_{4,5}$ → Fermi level transition.

Table 5-III

Present work	3.8	7.8		16		25.5	34,44	54,57	70,80	R
Suleman (1971)	3.7	7.5				25.4	34.2	55.3,57		R
Seah (1971)	4	7.4	11.5	16.5		24.4	40,44.8			R
Robins (1961)	4.1	7.3		17.2		25.0	33.5			E
Allen (1969)	4.2	7.3	12.6	16.6	21.9	26.0	32,37.5,43.1	47		E
Thomas (1967)	4.1	8.6	13.5	16.7	23.4	25.5	33.5,43.1			R
Rudberg (1930)	4.6	7.4				24.8				T
Marton (1955)	3.4	7.0		16.7		24.8				T
Jull (1956)	3.3	6.8		14.3		23.8	44.8			T
Watanabe (1956)	3.4	7		16.7		24.8				T

The last column indicates the method of measurement:

R - retarding field; E - electrostatic analyser; T - transmission.

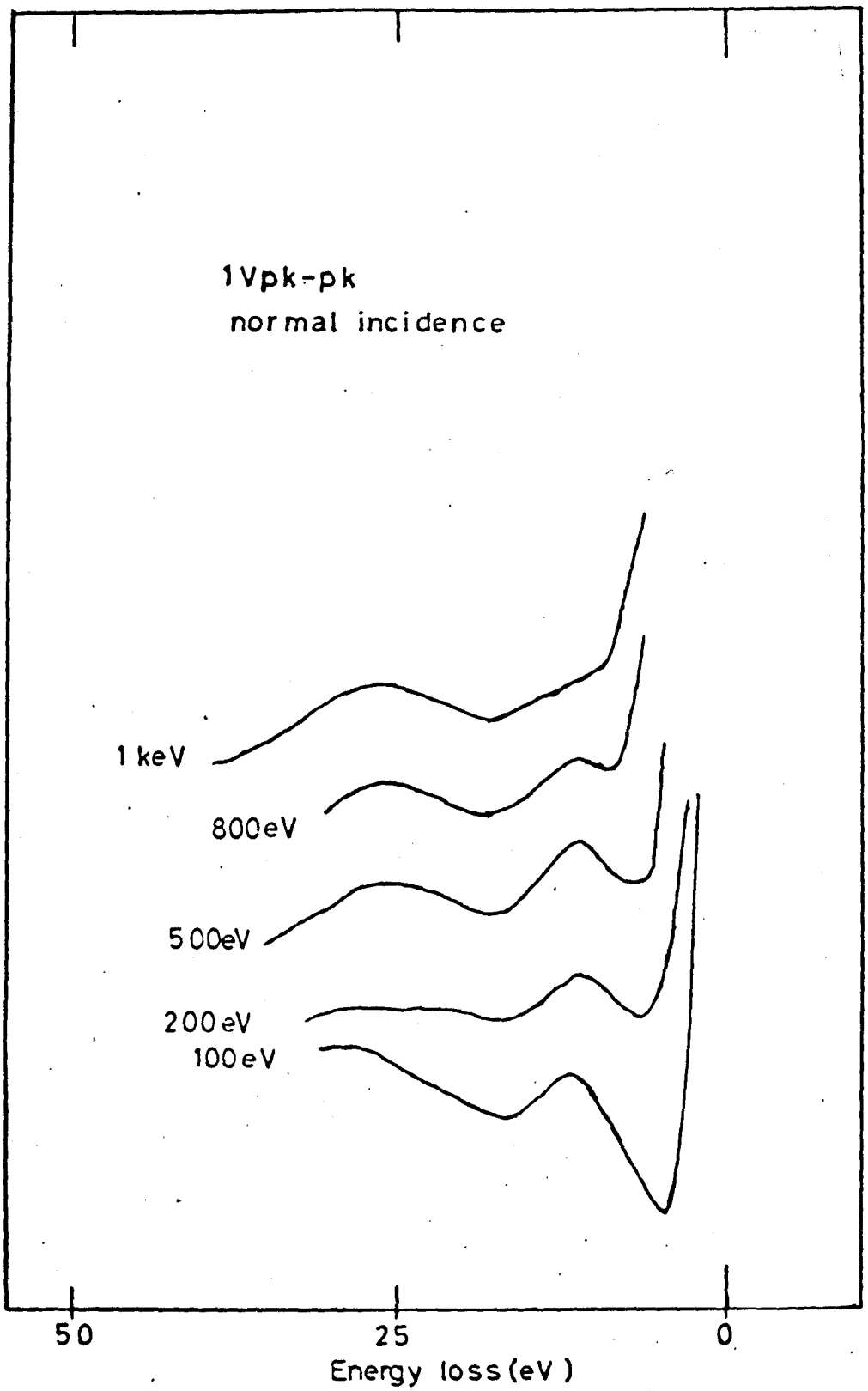

Figure 5.5 Energy losses of contaminated silver

The loss at 7.8eV is then the bulk plasma loss associated with 5s electrons. There could also be a contribution to this loss from possible $N_{4,5}$ - Vacuum level transitions at about 8eV. Work of Seah (1971) on the angular variation of the 4eV loss diffracted from a single crystal also confirms the allocation of a surface loss.

As the primary energy is raised the beam also excites all the 4d electrons into oscillation and the 25.5eV loss is assigned to the bulk loss associated with the ten 4d electrons. The loss at 16eV could then be either two 7.8eV bulk losses or the surface loss associated with the 25.5eV bulk loss. The latter interpretation is preferred, because of the disappearance of the 3.8 and 7.8eV losses at higher primary energies, whilst the 16eV loss remains visible. The losses at 34 and 44eV could result from the interband transitions N_1 - $N_{2,3}$ together with the 16+ 25.5eV compound loss. The losses at 54 and 57eV could also be $N_{2,3}$ - $N_{4,5}$ interband transitions or two 25.5eV losses.

The losses at 70 and 80eV are a bit more difficult to interpret; neither have they been previously reported. They seem too large in amplitude to be multiples and combinations of the 25.5 and 16eV losses, but they do not fit any calculated interband or ionisation loss, unless it is ionisation of the $N_{2,3}$ level to an allowed level about 15eV above the Fermi level, which is not very likely!

The observed losses after exposure to air provide further possible evidence for the low lying losses being associated with the 5s electrons; these losses completely disappear on the contaminated surface.

Plasma losses

free electrons per atom	$\hbar\omega_p$ B	$\hbar\omega_p/\sqrt{2}$ S	B+S	2B	2B+S	3B
1	8.9	6.3	15.2	17.8	-	-
10	28	20	48	56	76	84

Interband transitions

$N_1 \rightarrow N_2$	32.6
$N_1 \rightarrow N_3$	39.3
$N_3 \rightarrow N_{4,5}$	52.6
$N_2 \rightarrow N_{4,5}$	59.3
$N_1 \rightarrow N_{4,5}$	91.9

Ionisation Losses

	to Fermi Level	to Vacuum Level (ϕ = 4.5eV)
$N_{4,5}$	3.3	7.8
N_3	55.9	60.4
N_2	62.6	65.1
N_1	95.2	99.7

Calculated Energy Losses for silver

Fig. 5.6

In Chapter 4 we noted that the contaminants observed on the silver after exposure to air were sulphur, carbon and oxygen. If these have bonded to the surface via the 5s electrons of silver, then they will no longer be available separately to enter into a plasma oscillation. It should be pointed out that the above interpretation of the energy losses has not taken into account possible interband transitions involving final states above the vacuum level.

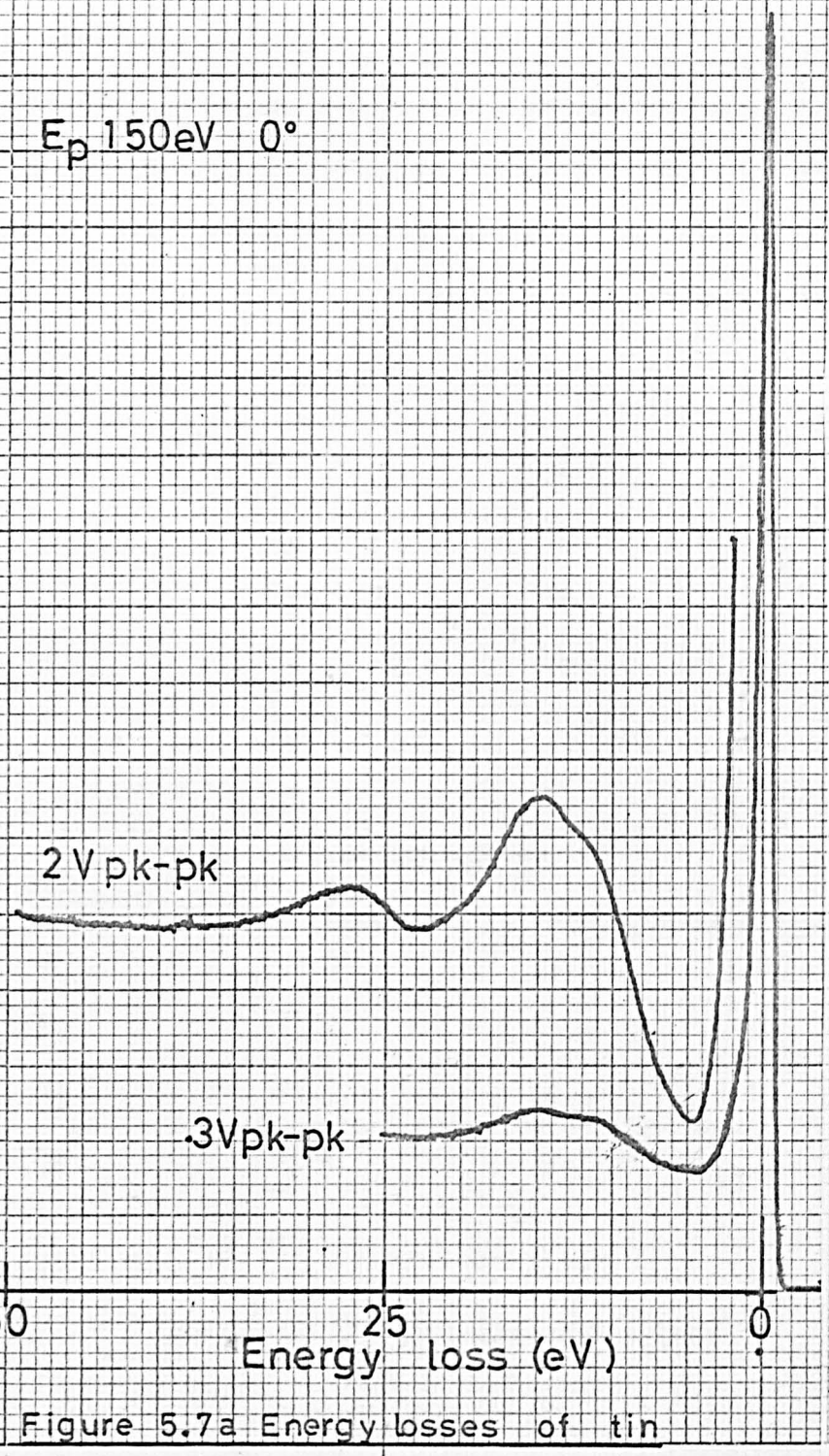

Figure 5.7a Energy losses of tin

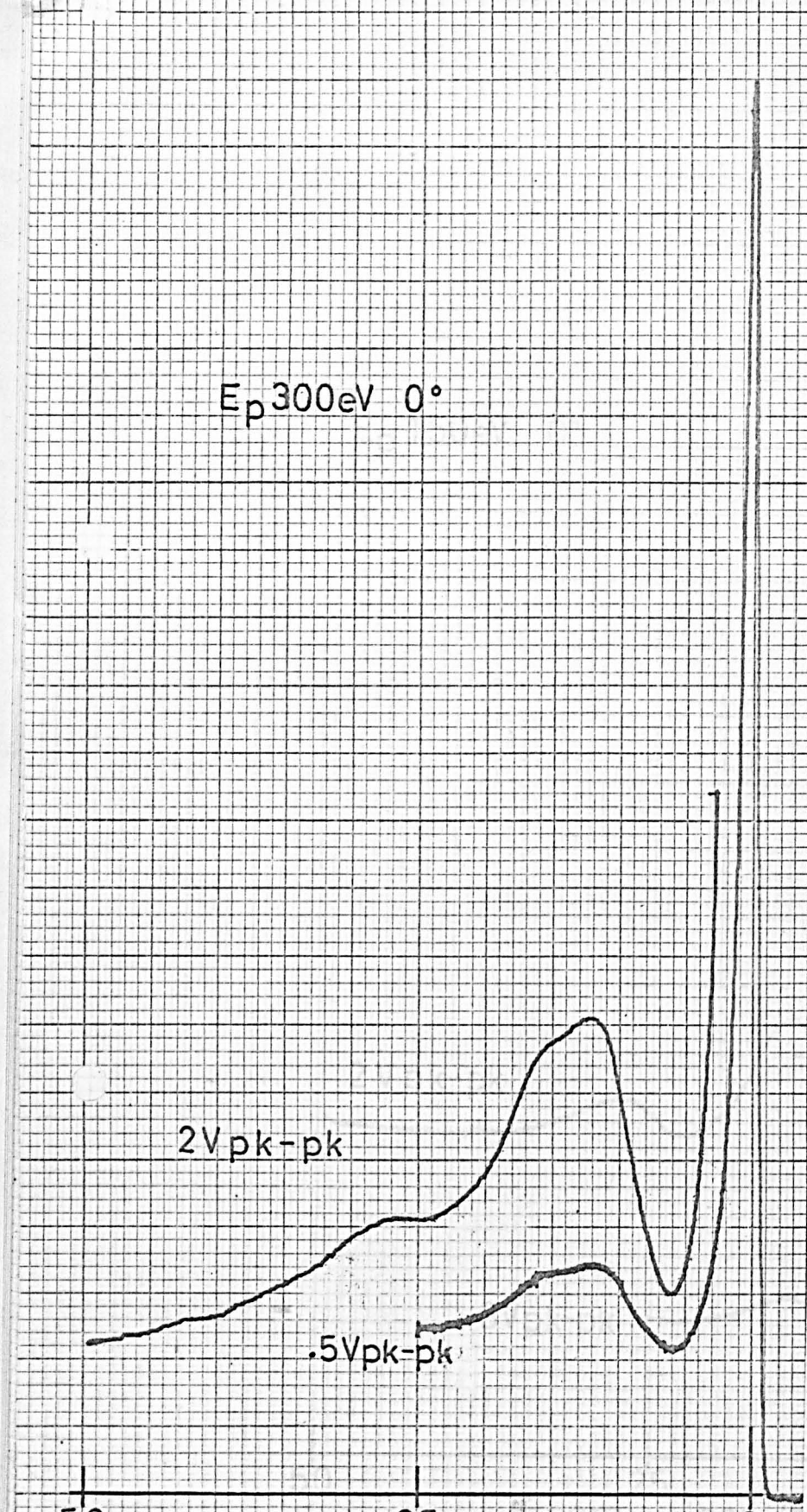

Figure 5.7b Energy losses of tin

Figure 5.7c Energy losses of tin

5.4 Tin

5.4.1 Results

Figure 5.7a-c shows the energy losses observed for tin at varying primary energies of from 150eV to 500eV. The losses occur at 11, 15 and 27eV, and in Figure 5.8 further losses of about 60, 75 and 88eV can be seen. Figure 5.9, taken with a primary energy of 1keV, shows the effect on the 11eV loss of changing the angle of incidence to 60° to normal. There is also slight evidence of a loss at about 5eV, which only appears with a primary energy of 1keV, at normal incidence, when the resolution was 0.2%.

A summary of the results obtained under various incident conditions is given in Table 5-IV below, together with the relevant figures for reference.

Table 5-IV

E_p	θ	Losses	Figure
150	0	11 15 27	5.7a
300	0	12 16 27	5.7b
500	0	11 15 27	5.7c
500	0	11 15	-
500	0	12. 15.5	-
600	0	12 16 28 60 75 88	5.8
1000	0	5? 11 16 28	5.9a
1000	60	11 15 27	5.9b
300	60	11 15	-

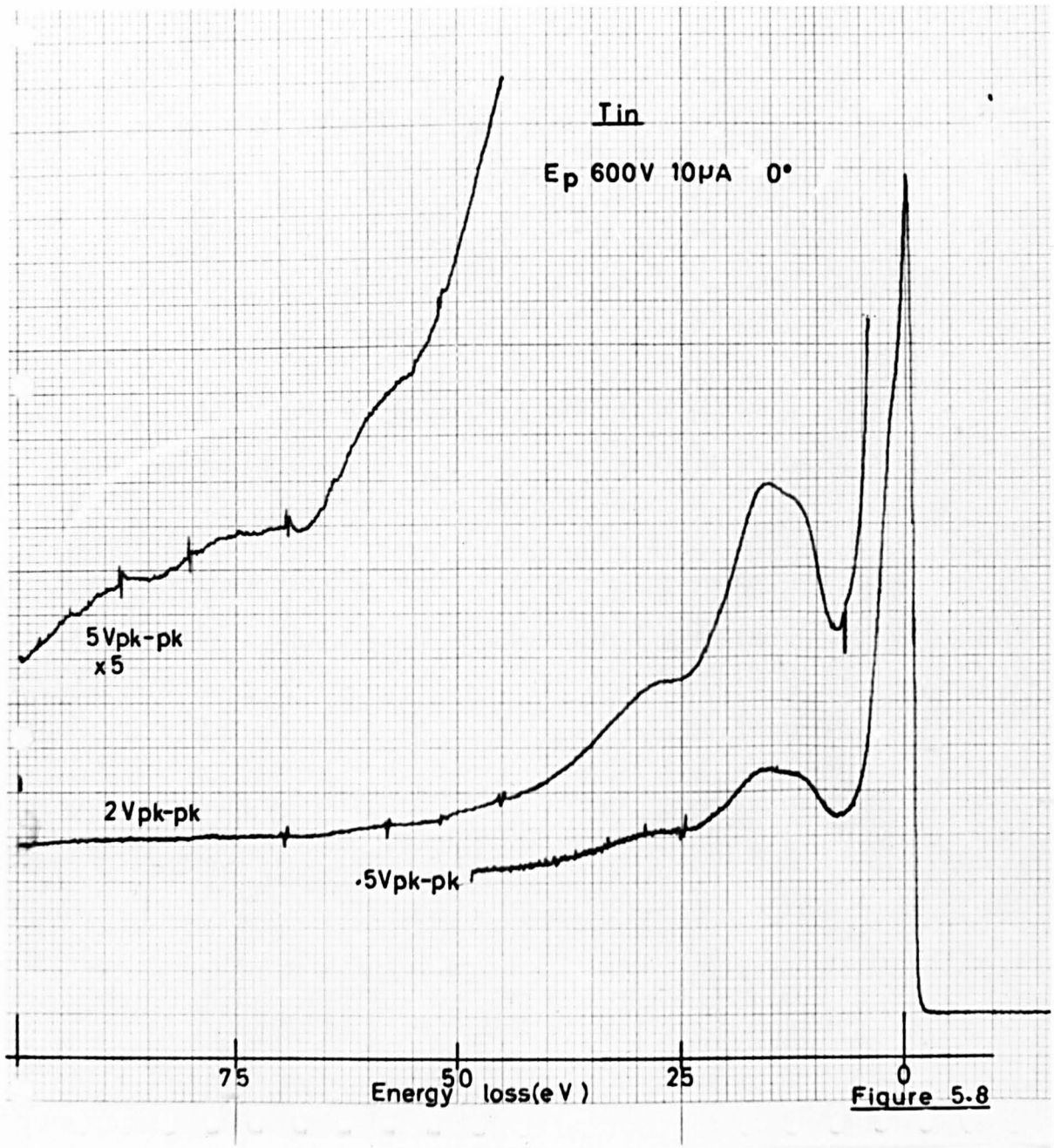
Tin
Ep 600V 10μA 0°
5Vpk-pk
x5
2Vpk-pk
.5Vpk-pk
75
50
25
0
Energy loss(eV)

Figure 5.8

5.4.2 Discussion

The present results for tin are compared with the other published work, obtained by transmission and reflection, in Table 5-V below.

Table 5-V

Present Work	5?	11	15.5		27			60	75	88	R
Powell (1960)		10.4	14.1	24.7	27.8	38.6	41.9	56.7			E
Marton (1954)	4.5	12.4	18.0	23.9							T
Watanabe (1954)	6.3	13	19.5								T

The calculated free electron value for the surface and bulk plasma losses in tin, assuming four free electrons per atom, are 10 and 14.4eV; they agree well with our observed values of 11 and 15.5eV. The loss seen at 27eV is thus attributed to a bulk plus surface loss (experimental 26.5, theoretical 24.4eV), though there could be a contribution from an ionisation loss of the $N_{4,5}$ level (23.9eV + ϕ). The loss at 60eV could be an $N_{2,3}$-$N_{4,5}$ interband transition of calculated energy 64.7eV (See Figure 4.14) and that at 88eV an ionisation loss of the $N_{2,3}$ level (88.6eV + ϕ). The loss at 75eV is unassigned, and its origin unknown.

An alternative explanation for the higher losses is that they are all multiples of the 11 and 15.5eV loss, and that for some reason the

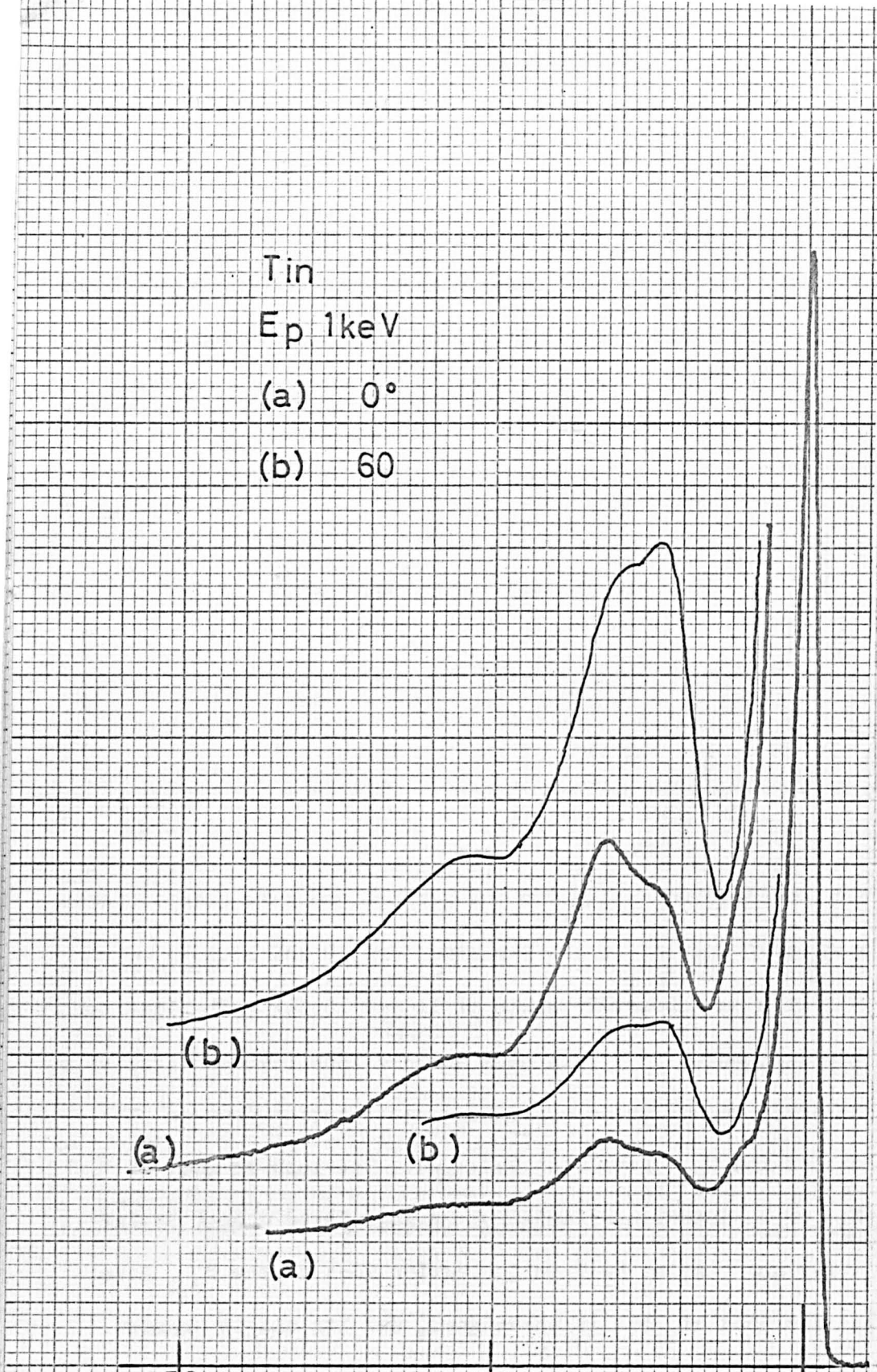

Figure 5.9 Effect of incident angle

2B (31), 2B+S (42) and 3B (46.5) were not seen. Possible assignments would then be: 60eV peak - 3B+S (57.5) and 4B (62); 75eV peak - 4B+S (73) and 5B (77.5); and 88eV peak - 5B+S (88.5) and 6B (93). It seems most ulikely that this explanation is justified in view of the lack of the other multiple loss peaks.

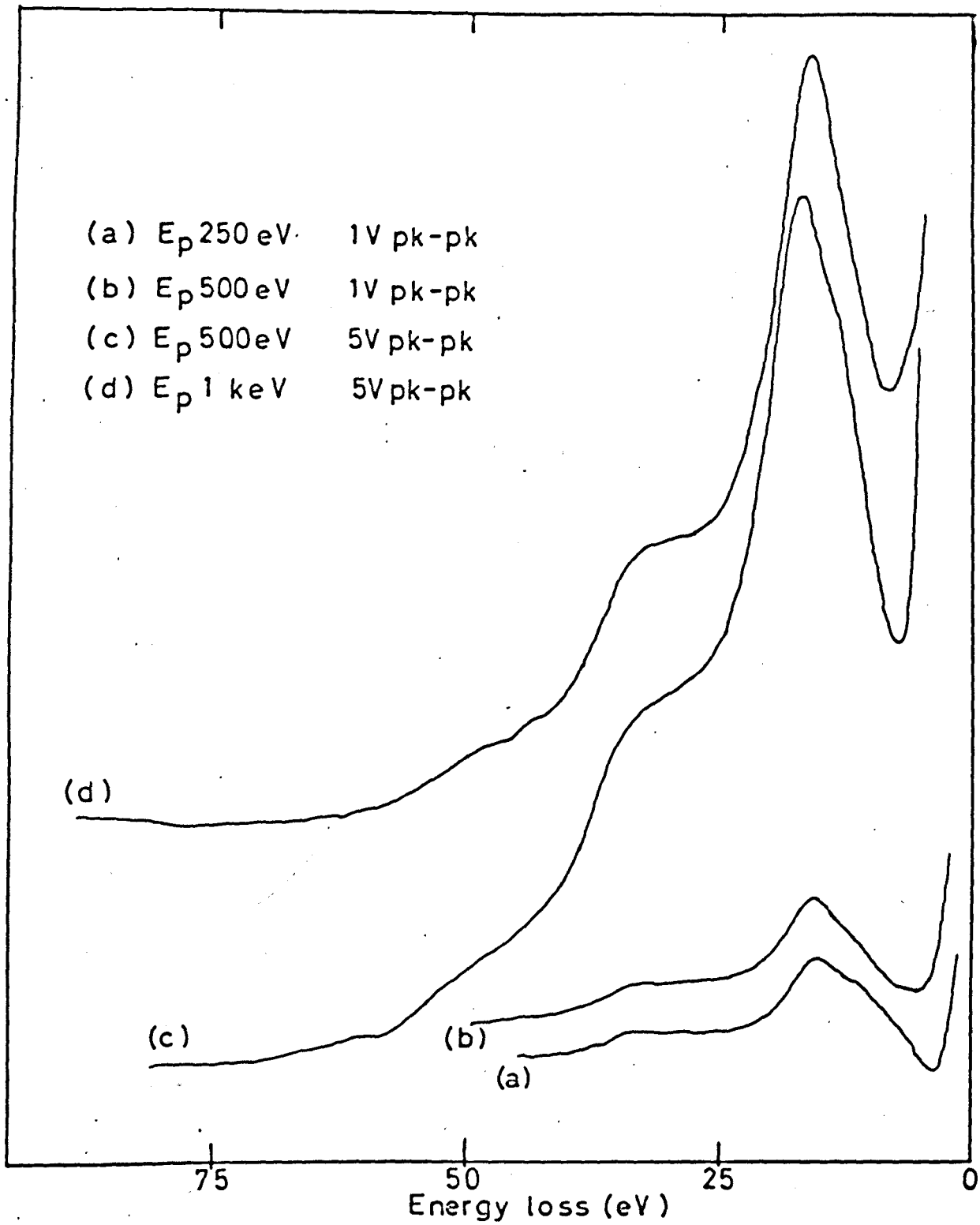

Energy loss spectra of antimony normal incidence

Figure 5.10

5.5 Antimony

5.5.1 Results

Energy loss spectra obtained for antimony at normal incidence for primary energies of 250, 500 and 1000eV are shown in Figure 5.10. The major losses can be seen to occur at 11.5eV, 16eV and 34eV. Small losses at 43, 50 and about 61eV can also be seen on two of the plots. In Figure 5.11 we show the spectrum for a primary energy of 1keV and 60°, showing the larger loss at 11.5eV and also small losses at around 50 and 64eV. Spectra plotted on an expanded scale for incident energies of 100-500eV are shown in Figure 5.12. A summary of the measured energy losses under the various conditions is given in Table 5-VI below.

Table 5-VI

E_p	θ	Losses						Figure
250	0		11	16	34			5.10a
500	0			16	34			5.10b
500	0		11	16	33	50	61	5.10c
1000	0	6	11	16	33	43 49	80?	5.10d
250	60		12	16	35			-
500	60		12	16	35			-
1000	60		12	16	34	50	65 82?	5.11
100	0	7		16	34			5.12a
200	0		12	15.6 28	34			5.12b
500	60		11	15.6	33			5.12c

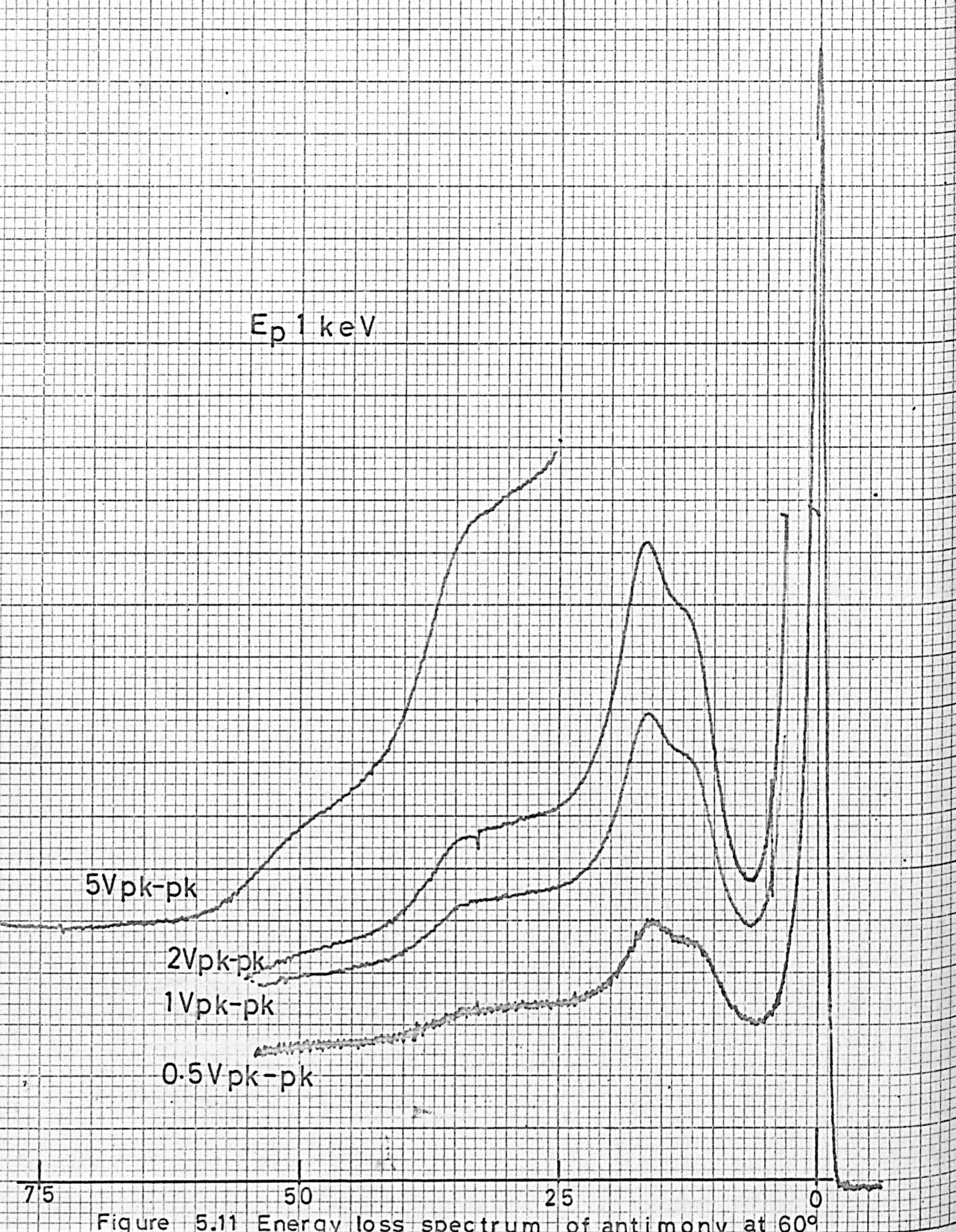

Figure 5.11 Energy loss spectrum of antimony at 60°

5.5.2 Discussion

The observed energy losses for antimony are compared with the results of other workers in Table 5-VII below.

Table 5-VII

Present work	6?	11.5	16	28	34	43	49	63	81	R
Powell (1960)		11.3	15.9	26.5	32.3	48.8				E
Mollenstedt (1949)			15	20	31					T
Marton & Leder (1954)			14.2	24.3						T
Leder & Marton (1964)	4.3		14.9		30.6					T
Watanabe (1954)	6.5		18	24.5						T
Leder (1956)	5.3		15.6	30.2						T
Gauthé (1959)			15.0	29.8						T

From their behaviour with energy and incident angle, the 11.5 and 16eV losses are assigned to surface and bulk plasma losses. The calculated values, assuming five free electrons per atom are 11 and 15.4eV respectively, again in fairly good agreement with the observed values. The 28eV loss can then be attributed to a bulk plus surface loss (free electron value 26.4, experimentally calculated 27.5eV), the 34eV loss to two bulk plasmons, the 43eV to two bulk plus one surface, the 49 to three bulk and the 63 to four bulk losses.

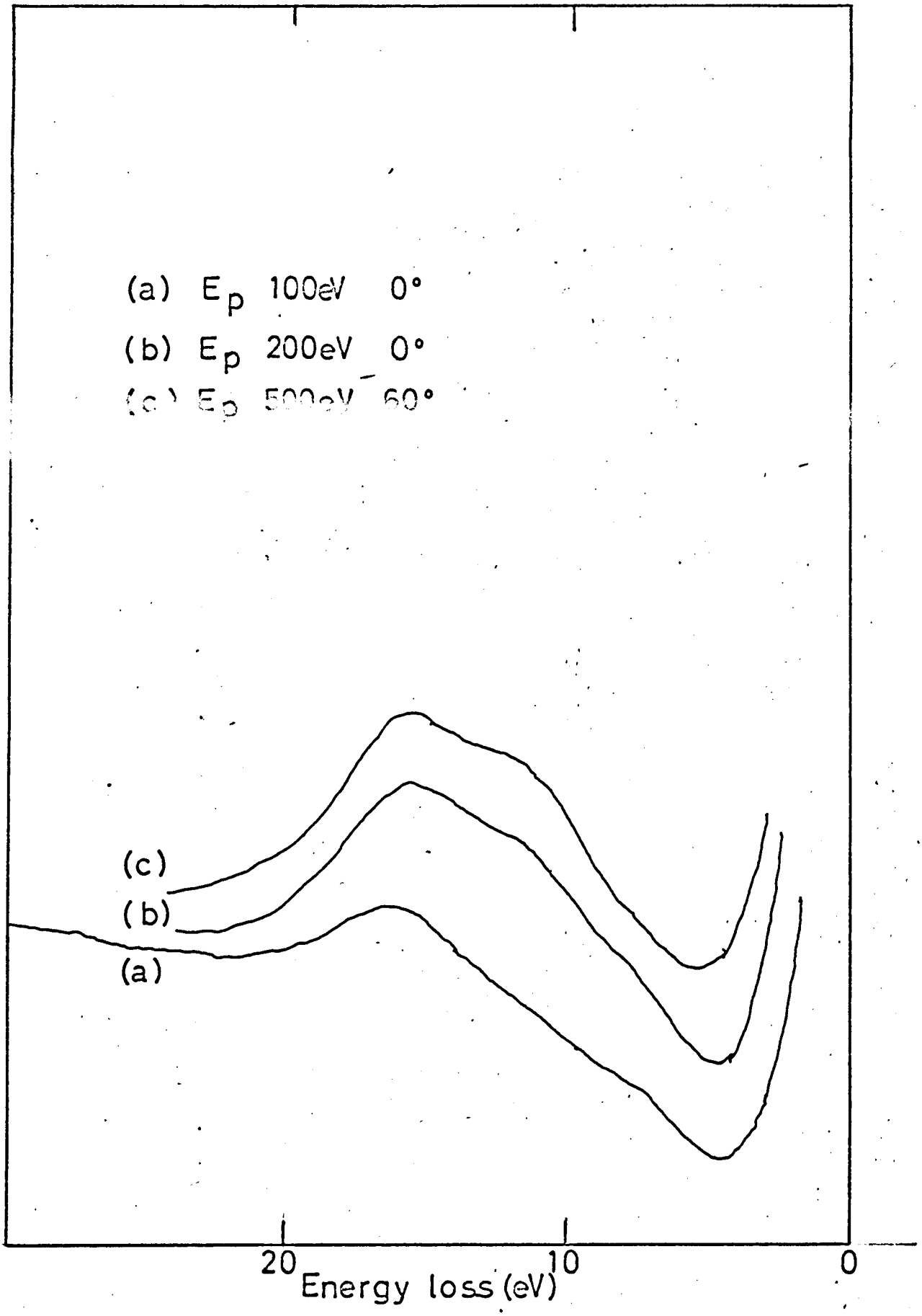

Figure 5.12 Low energy losses of antimony

The predicted interband transitions and ionisation losses, using the energy level diagram of Figure 4.18 occur at 27eV ($N_{4,5}$-O), 31.4 + ϕ ($N_{4,5}$), and 67eV ($N_{2,3}$-$N_{4,5}$); hence a contribution from these to the losses cannot be ruled out. The small peak at ~81eV occasionally seen could be an $N_{2,3}$-O interband transition, or five bulk losses.

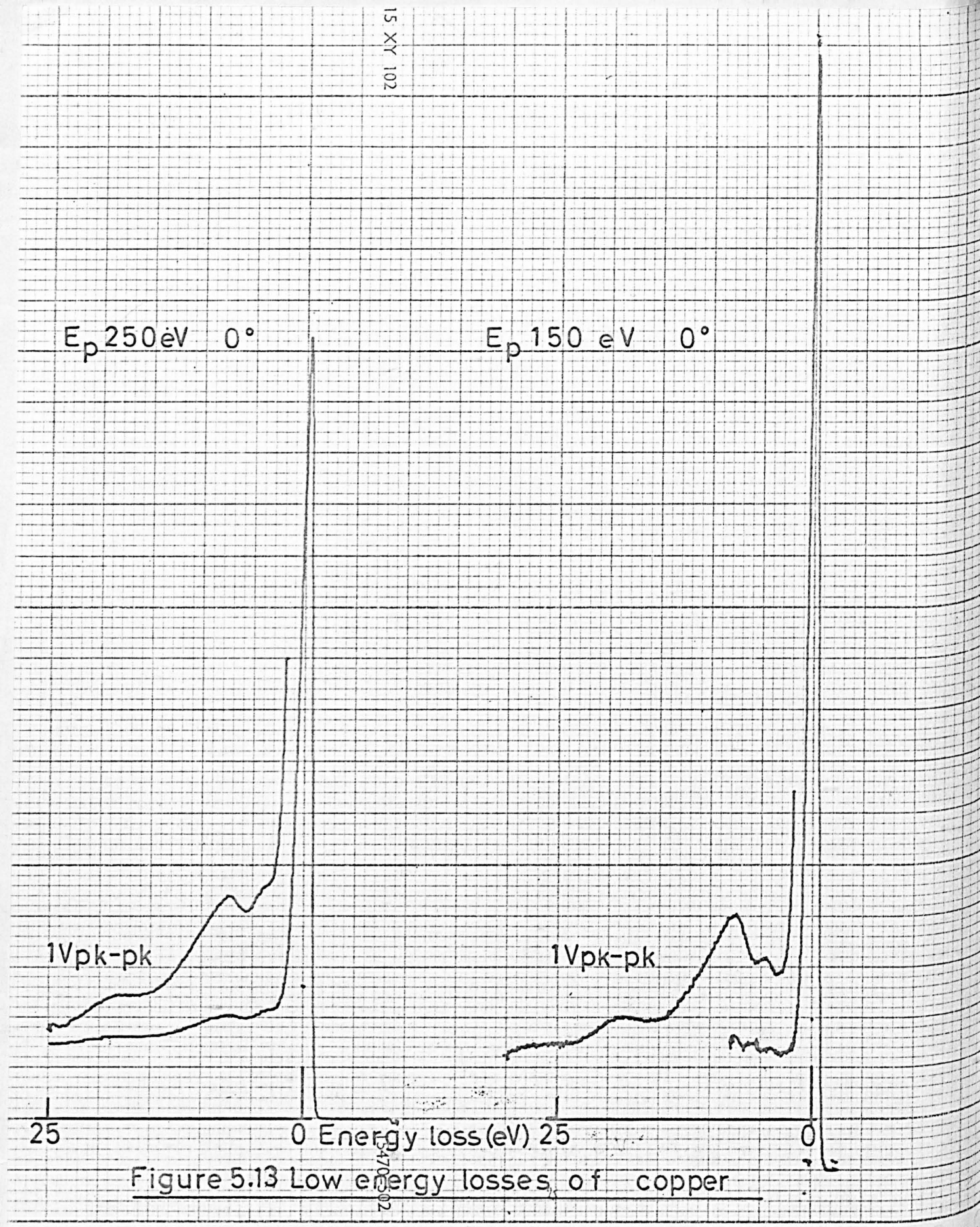

Figure 5.13 Low energy losses of copper

5.6 Copper

5.6.1 Results

Figure 5.13 shows two plots of the characteristic energy losses of copper, taken at normal incidence with primary energies of 150 and 250eV. A small loss at 4.5eV and a larger one at 7.5eV are visible, together with broad peaks at 19 and 27.5eV. At the higher primary energy of 500eV, Figure 5.1 reveals extra losses at energies of 19, 28, 37.5 and 80eV; very small bumps can also be seen at 49, 54, 63 and 71eV (approximately). The 4.5eV loss has merged into the tail of the primary peak, and the 7.5eV loss apparently moved to 8eV, because of the background slope.

5.6.2 Discussion

Comparisons of the present work with other published characteristic loss values are given in the Table 5-VIII below.

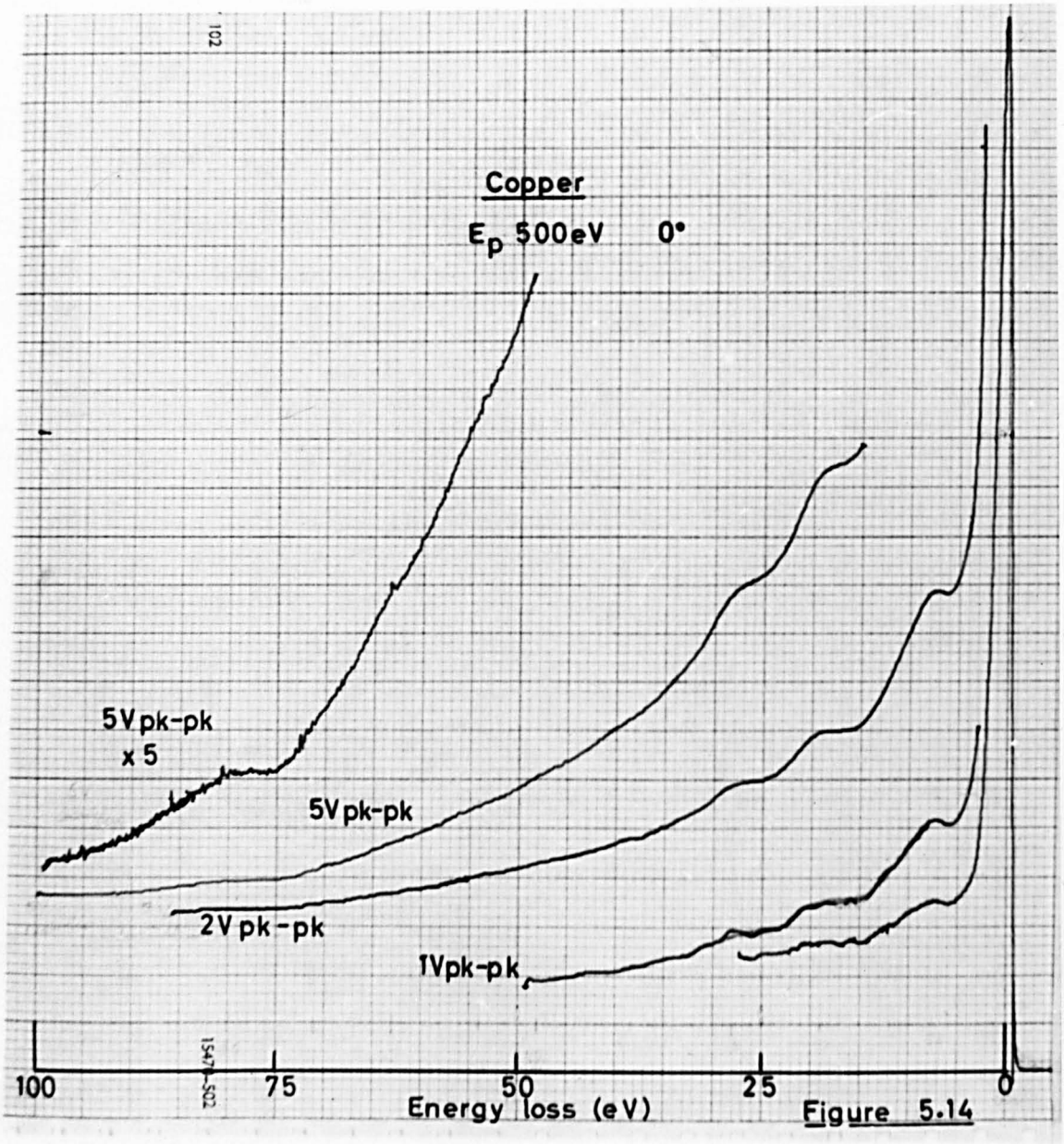
102
Copper
E_p 500eV 0°
5V pk-pk
x 5
5V pk-pk
2V pk-pk
1Vpk-pk
1547-502
100
75
50
25
0
Energy loss (eV)

Figure 5.14

Table 5-VIII

Present work	4.5	7.5	19	27.5	37.5	weak (49	54	63	71)	80	R
Robins & Swan (1962)	4.5	7.6	19.1	27.3						77.4	E
Powell (1960)	4.4	7.2	19.9	27.1							E
Suleman (1971)											R
Jordan & Scheibner (1968)	4.5	7.5	19.5	27.5	39.0						R
Marton, Leder & Mendowlitz (1955)	3.5	7.5	14.0	23.0	34.0						T
Jenkins & Chung (1971b)	4.0	7.4	11.8 17.0 19.0	26.6	37.0	46.8	58				R

It can be seen that there is quite good agreement in this case between the results obtained by different methods and with various instruments. Optical data (e.g. Ehrenreich and Philipp 1962) also predict a loss at around 2.5eV, but this would be lost in the elastic peak, except at very low primary energies. It seems generally accepted that the loss at 4.5eV is an interband transition of the d electrons of copper to vacant states above the Fermi level. Despite the fact that the work of Jenkins and Chung on oxygen exposure negated the results of Jordan and Scheibner in that no rapid decrease of the 7.5eV loss was found, it is still considered that this is probably a surface plasma loss of one free electron per atom.

The theoretical value is 7.6eV, and the associated bulk value is expected at 10.8eV. It is strange that only a few workers have seen a peak at about this value. The peaks at 27.5 and 37.5eV can be explained as surface and bulk plasma losses associated with 11 electrons per atom, the theoretical values being 25.5 and 36eV.

The 19eV loss is presumably a combination of surface plus (unseen) bulk, which would be expected at 18.4eV. A recalculation of the plasmon energy for copper by Joshi (1960) including the differing effective masses of the s and d electrons involved in the oscillation, places the bulk plasmon energy at 20.8eV, i.e. where we have assumed the surface loss to be. It is evident that the theoretical background to the energy losses of the transmtion metals still has a long way to go before a generally accepted explanation can be obtained.

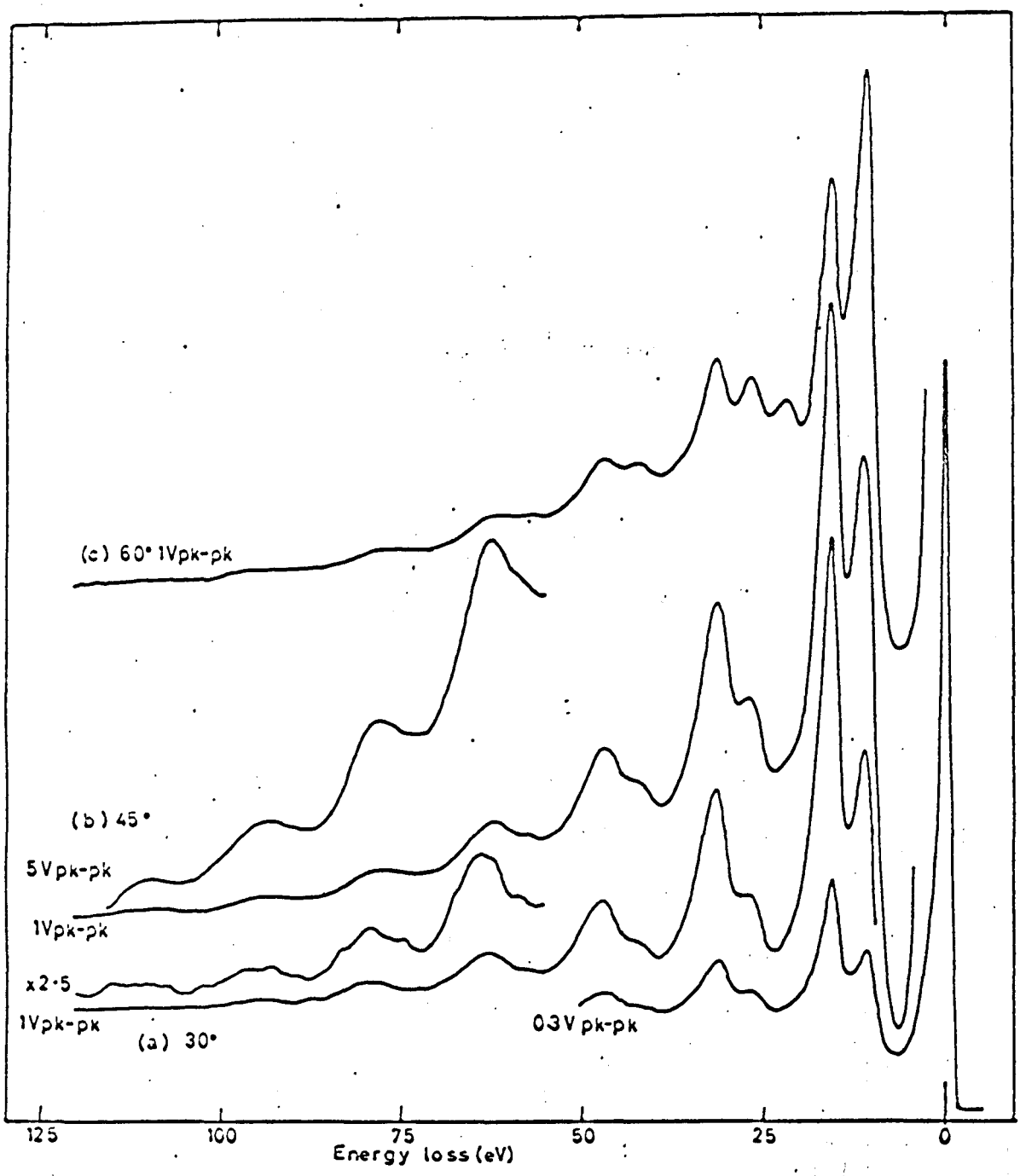

Figure 5.15 Characteristic loss spectrum of aluminium

5.7 Aluminium

5.7.1 Results

The valence electrons of aluminium form a free electron gas, and as a result, the energy loss spectrum is very strong. In Figure 5.15a-c, we see the loss spectrum for a primary energy of 1keV and angles of incidence of 30°, 45° and 60° to normal; unfortunately we were not able to plot the spectrum at normal incidence as the equipment developed a 'gremlin' at the crucial time, and there was breakdown somewhere in the retarding grid circuit. Nevertheless, multiple and combination losses up to 110eV were found at this energy.

The energy loss spectra with a primary energy of 500eV are shown in Figure 5.16; in curve (a) we tried to overcome the breakdown problem that developed by simulating a high primary energy using target bias (Chapter 2.3.4). This plot used a bias of +300eV, giving an effective primary energy of 800eV, but the amplitude of the elastic peak and energy losses was attenuated by a factor of three, compared to the case without bias. Further increase in bias only worsened the attenuation, so the idea was abandoned. Plots (b) to (e) show the dramatic effect on the relative amplitudes of the losses with changes in incident angle from 0° to 60°.

Figure 5.17, taken with an expanded scale consists of five plots ((c) - (g)) with a primary energy of 250eV and incident angles of from 0° to 75°, and two plots ((a) and (b)) with 125eV primary energy at 0° and 45°.

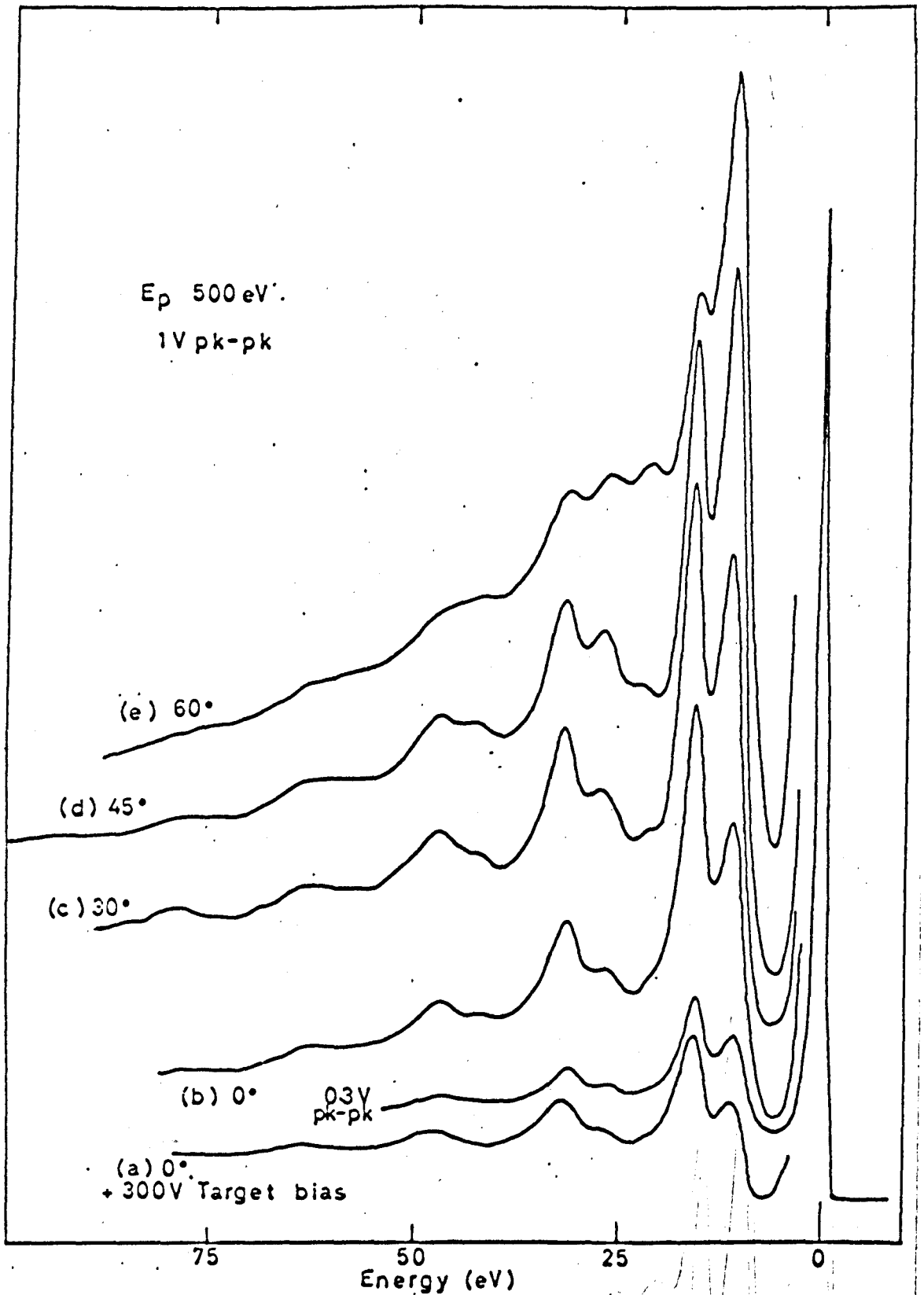

Figure 5.16 Energy losses of aluminium

5.7.2 Deconvolution

The loss spectra obtained under the various conditions consist of the superimposition of a large number of multiple and combination losses, whose widths are much greater than their separation. Consequently, if we wish to examine, for example, the variation of peak heights with the variation of the different parameters, it is necessary to find some means of deconvoluting the individual contributions of the constituent peaks to the observed spectrum. Probably the best way of doing this is numerically; if it is possible to predict the mathematical form of each constituent peak, then a least squares fit to the observed spectrum can be made by suitable adjustment of the component amplitudes. Recent work of this nature on aluminium has been reported by Burge and Misell (1969), who have also (1968) criticised previous analyses of the Aluminium spectrum. Their work was done on a transmission spectrum of Aluminium, where the contribution from surface and surface-volume combination losses were small and the contribution from surface multiple losses assumed negligible. They stated that in the case where there are multiple surface losses and bulk losses (as in reflection measurements) "the computing problems involved are formidable" for the application of their method.

The method we used was rather simpler (in that it was not necessary to write an enormous computer program) but probably not very accurate, and was similar to that used by Allen (1969) in the analysis of his energy loss data. By courtesy of the Physics Department of the University of Birmingham, we were able to use a Dupont Curve resolver

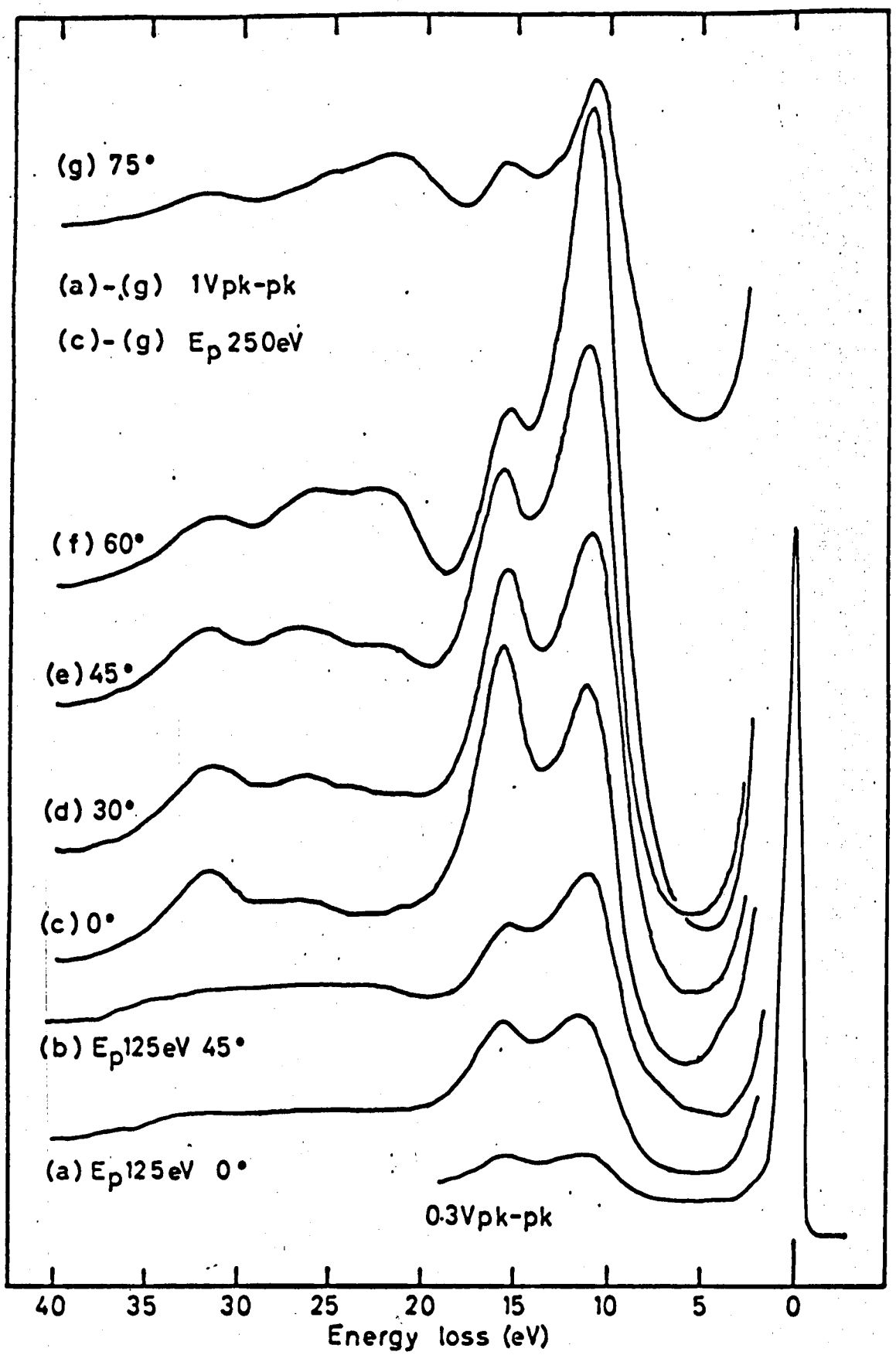

Figure 5.17 Low energy losses of aluminium

for a day; the instrument contains ten function generator channels, which were set up to reproduce gaussian curves of a variable amplitude width and 'position' i.e. median energy in our case. The curve to be analysed was superimposed by projection on to the output corresponding to the sum of the channels, and the variable parameters were adjusted until a good fit to the experimental data was obtained. By displaying each individual channel in turn, the constituent peaks could be plotted. Unfortunately, at the time of the measurements, the machine was badly in need of a service, and there was a slight jitter on the output trace when more than one channel was on; also the pen recorder was not working properly. Consequently the results described are at best very approximate, but serve to illustrate the applicability of the technique.

Figures 5.18 and 19 illustrate the deconvolution of the spectra shown in Figure 5.16 (b) and (e) respectively, i.e. for a primary energy of 500eV and incident angles of 0° and 60°. The baseline chosen was fairly arbitrary, but consistent throughout the spectra. The main point demonstrated is how large the multiple losses are, compared with the small 'bumps' on the original trace. It was found, not surprisingly, that once the machine was set up it was not necessary to make alterations in the position or width of the peaks; alteration of relative amplitude in general being sufficient to fit the plotted curves.

If more time had been available on the machine (and it had been working properly), it should have been possible to set up the analogues of the calculated line-shapes corresponding to the combination and

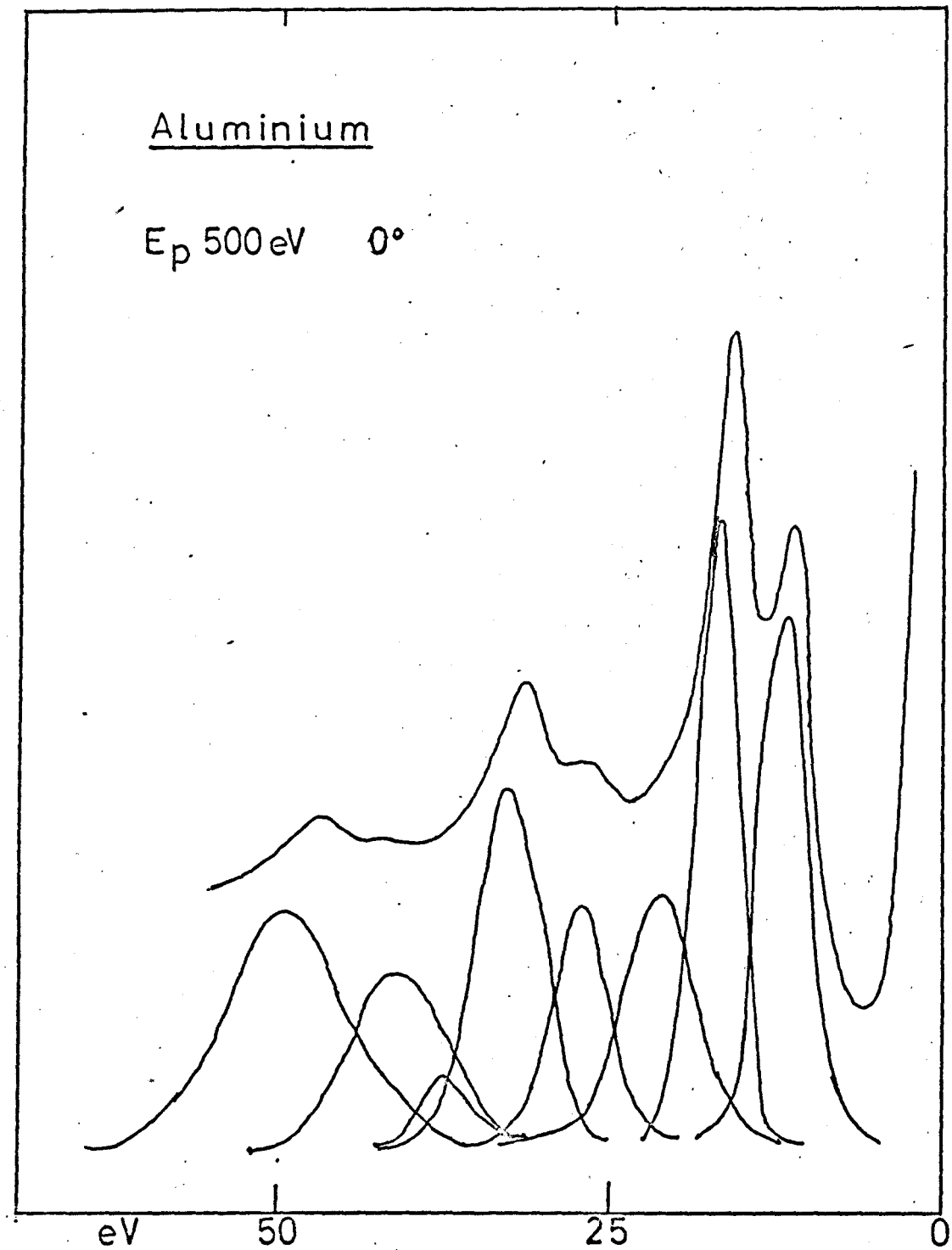

Figure 5.18 Deconvoluted energy loss spectrum

multiple losses. This may have resulted in a more accurate estimate of the component amplitudes.

The limitation on the number of channels available means that it was only possible to fit the first 50eV of each spectrum; the amplitude and position of the last two channels was not recorded, since they were used to build up the 'tail' of the distribution to make the preceding channels more accurate. As mentioned previously, the plotter attachment was not working properly, so it was necessary to sketch out each channel manually; this contributed more to the errors.

Figure 5.20 shows a plot of the ratio of the amplitudes of the first bulk to surface loss for the range of primary energies and angles that we had time to analyse. Unfortunately, the errors on this plot are not too easy to determine, since we were able only to do an analysis for one trace of each type in the time available. It is evident that the plots taken at 60° show a larger error, presumably because at this angle the ratio is becoming a rapid function of angle.

In other respects the figure shows the qualitative features that one would expect for the behaviour of surface and bulk losses. At low primary energies the surface loss predominates, even at normal incidence, and at 60° to normal incidence it predominates even at a primary energy of 1keV. It was thought appropriate to plot the ratio in this case, since it avoided introducing additional errors that would have arisen had we attempted to normalise each plot.

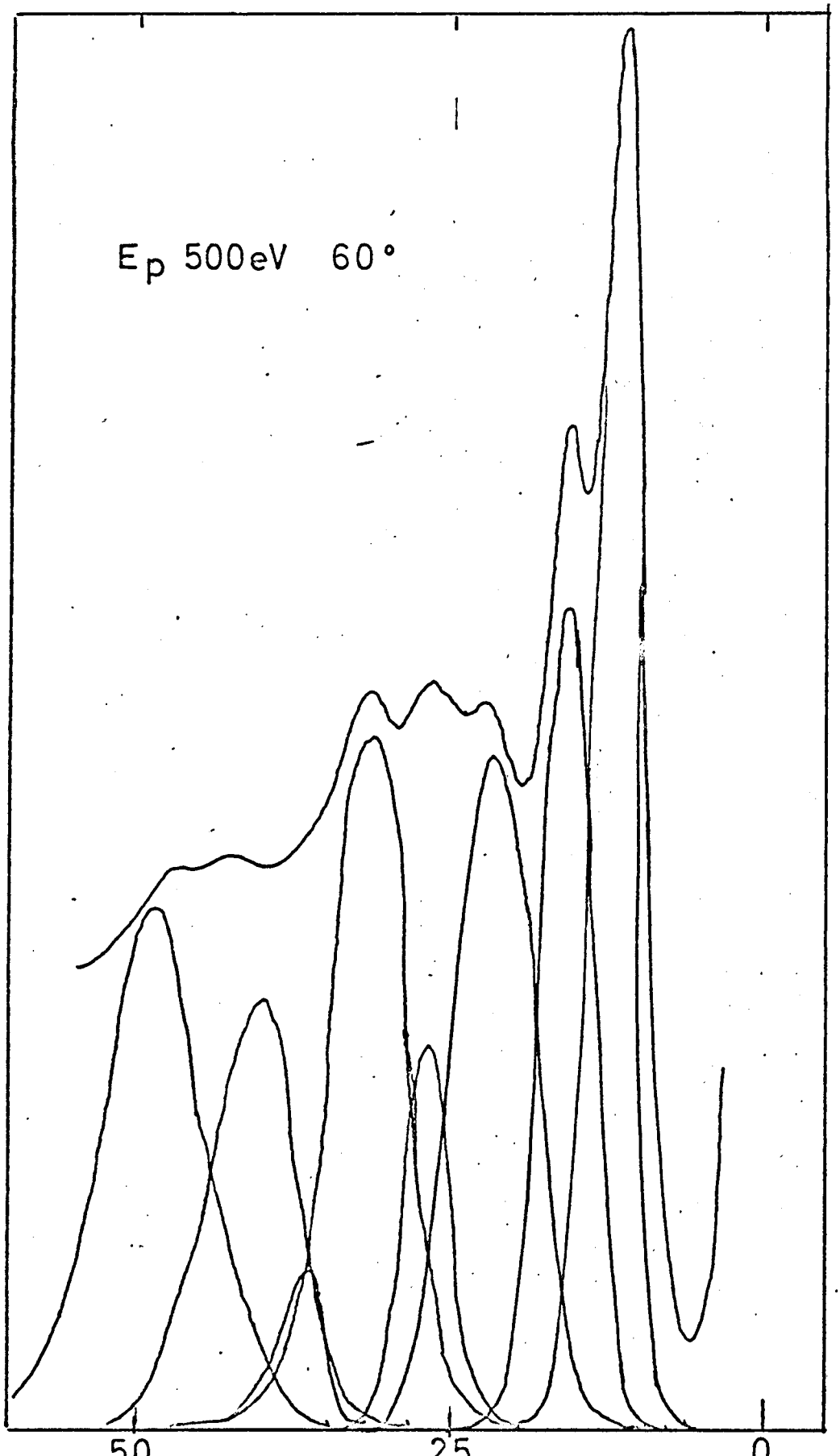

Figure 5.19 Deconvoluted aluminium loss spectrum

The other advantage of the deconvolution was that it made possible the identification of multiples and combination losses that were difficult to resolve on the original traces.

5.7.5 Discussion

A summary of the observed losses under the various incident conditions is given in Table 5-IX, together with the calculated values of plasmon energies based on three free electrons per atom. The observed peaks show remarkable agreement with the calculated free electron values, confirming that the free electron treatment is ideally suited to aluminium.

The results of Suleman (1971) and Powell and Swan (1959) are given in Table 5-X below. Suleman used a primary energy of 800eV and normal incidence, and Powell and Swan used primary energies from 760 to 2020eV at 45°. Much of the other published work on aluminium, relates to partially oxidised films, and as these two authors have shown, oxidation has a drastic effect on the observed loss spectrum.

Table 5-X

Characteristic energy losses found for aluminium by Suleman and Powell and Swan

	(S)	(B)	(2S)	(S+B)	(2B)	(1S2B)	(3B)
Suleman	11	15.6		26.4	31.4		46.5
Powell and Swan	10.3	15.3	20.5	25.6	30.5	41.1	46.1

	(1S3B)	(4B)	(5B)	(6B)	(7B)
Suleman		62	77.9		
Powell and Swan	56	61.4	77	91.8	108.6

Table 5-1X Observed energy losses for aluminium

Assigned / Calculated E_p	θ	1S 11.2	1B 15.8	2S 22.4	S+B 27	2B 31.6	3S 33.6	2S1B 38.2	1S2B 42.8	4S 44.8	3B 47.4	2S2B 54	1S3B 58.6	4B 63.2	1S4B 74.4	5B 79	1S5B 90.2	6B 94.8	7B 110.6
125	0	11.2	15.5																
250	0	11.2	15.7																
500	0	11	15.5		26.2	31.2			42		47			62.5					
500	0	11	15.6		26.5	31.2			42		46.6			63					
125	30	11	15.5																
250	30	11	15.6		26.5	31.5													
500	30	11	15.6	21.5	26.8	31.5			42		46.5			63	78.5				
1000	30	11	15.6		26.5	31.6			42		47		57	62.5	73.5	79		95	110
125	45	11.2	15.5																
250	45	11.2	15.5	22	26.5	31.2													
500	45	11	15.6	22	26.5	31.2		37?	42		46.8		57	63		78			
1000	45	11	15.5	22?	27	31.5			42		47		57	62.5	72.5	78		93.5	110
250	60	11	15.5	22.5	26.5	31.5			42.5										
250	60	11	15.6	22.5	26	31.5			42.5										
500	60	11	15.5	22	26.5	31.2			42.2		47.2			63					
500	60	11	15.5	22	26.5	31.5		37	42.5		47			62	(76)	(76)			
500	60	11	15.6	22	26.5	31.5													
1000	60	11	15.6	21.6	26.6	31.5			42.5		47		57.5	62.5	74.5	78.5	90	95	
250	75	11	15.6	22			32.5												
Average		11	15.6	22	26.5	31.4	32.5	37	42.2		46.9		57.1	62.7	73.5	78.5	90	94.5	110

It would appear that perhaps the film in the measurements of Powell and Swan was very slightly oxidised, since their values for the surface and surface-bulk combination losses are about 0.7eV lower than those of Suleman and the present work. In his work on liquid aluminium, Powell (1968) also reports the surface loss as occurring at about 10.3eV, but his background pressure was of the order of 10^{-6}torr.

In the work reported here, we have been able to identify far more surface-bulk combination losses than previously reported, and in the deconvoluted curves identify a 34eV peak as due to 3 surface plasma losses and a 37eV peak as two surface losses plus a bulk loss.

A summary of the peaks located with the curve resolver is given in Table 5-XI. The half-widths of the peaks was generally 4-5eV, but the 22eV, 31.5eV and 33eV peaks were found to be about 7eV wide, perhaps because on occasions with the last two peaks we were trying to fit one peak where there should have been two. Jenkins and Chung (1971c) also measured the characteristic losses of a clean aluminium crystal, but their results were plotted in the second differential mode, so it is not appropriate to make comparison in detail with the present work.

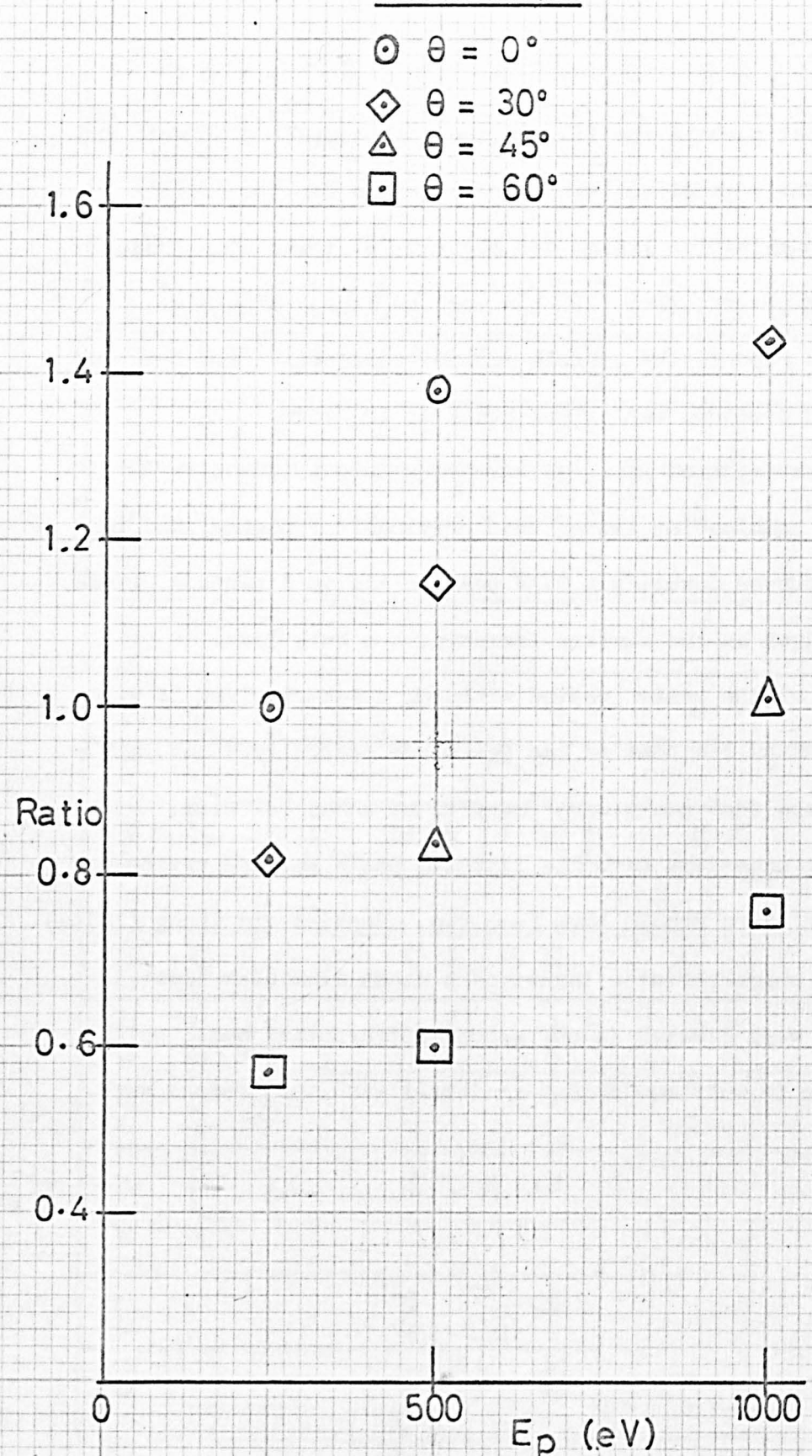

Figure 5.20 Ratio of bulk to surface amplitude

Table 5-XI

Deconvoluted results for Aluminium

Ep	θ	1S	1B	2S	S+B	2B	3S	2S1B	1S2B	4S	3B
Calculated		11.2	15.8	22.4	27	31.6	33.6	38.2	42.8	44.8	47.4
250	0	11	15.7	21.5	26.5	31	33.5	38			
250	30	11	15.7	21.7	26.3	30.5	34				
250	60	11	16	22	26.8	31	34				
500	0	11	16	20.5	26.5	32		37	41.5		
500	30	11	15.7	21.5	26.7	31.7	36.5		40.5		
500	45	11	16.5	22.2	27.2	32.5		37	41		
500	60	10.5	16	21.5	27	31.5		36.5	40		
1000	30	11	16	21.5	26.7	32		37.5	41		
1000	45	11	16	22	27	32		37.5	41		
1000	60	10.5	15.5	22	26	31.5		36	40		
Average		10,9	15.8	21.7	26.7	31.5	33.8	36.8	40.7		

5.8 General Discussion and Conclusions

In the preceding pages we have reported the characteristic energy loss spectra observed for a number of metals. Since this analyser integrates over all scattering angles, the widths of the loss peaks are measured as quite broad, on account of dispersion. The spectra for palladium, silver and copper are quite difficult to interpret, since there are so many processes which could give rise to loss peaks; these processes tend to interact to displace the observed peaks from their calculated position. It is also not clear how many electrons are taking part in the plasma oscillation, or their effective mass. In the case of tin and antimony, the losses can be fairly well understood on the basis of the free electron theory with four and five electrons per atom, respectively.

The loss spectrum of aluminium is the most impressive; all the peaks observed can be interpreted on the basis of the plasma oscillation theory. The crude attempts at deconvolution of the spectrum have produced some interesting results for the variation of the relative amplitude of the surface and bulk loss with incident conditions, though further work in this direction is called for; it has also made possible the identification of some multiple and combination losses hidden in the experimental curve.

The resolution of the analyser, as measured by the width of the elastic peak, has been demonstrated as about 0.2% at 1keV primary energy, falling to about 0.7% at 100eV. This is perhaps more due to the difficulties of deflecting the primary beam onto the optimum position at low energies, and the energy spread of the primary beam than an actual degradation of resolution. These figures are approximately an order of magnitude better than the quoted figures for commercial instruments. The great advantage of the present instrument over other analysers has proved to be the ease with which it is possible to take measurements over a variety of incident angles, and still collect all the secondary electrons. To this end we have been able to extend measurements from normal incidence to about 75^{o} in certain cases, when it was possible to hit the target. This facility assists in the identification of surface plasma losses, and also increases the amplitude of the observed multiple and combination losses. Many more combination losses were found in the present study of aluminium than have been previously reported.

CHAPTER 6

CHARACTERISTIC ENERGY GAINS FROM Pd, Ag, Cu and Al

6.1 Introduction

This chapter concerns perhaps the most interesting but baffling portion of the secondary electron spectrum, the region of the slow peak. It is suggested that the 360° design of the analyser makes significant improvements to the operation in the lower energy range, enabling the detection of many small peaks superimposed on the 'slow' electron peak, in the region 0 - 25eV. Obviously these slow electrons are very sensitive to extermal magnetic field, but the screening employed (Chapter 2) has proved to have been adequate.

Results are presented in 6.2 for the palladium, silver, copper and aluminium surfaces, which have also been studied (Chapters 4 and 5) by characteristic energy loss and Auger electron spectroscopy. Time limitations prevented a thorough investigation of the tin and antimony surfaces, so the results have not been included. Measurements were made using the second differential mode (Figure 2.14) of the analyser, and peak positions are tabulated as the points of maximum negative excusion, as this is the most readily identifiable feature of the spectrum.

For technical reasons, it was not found possible to use the first differential detection circuit, except at very low primary currents. The design of the circuit (Figure 2.8) incorporates a series resistor between the grid and power supply in order to enable the a.c. modulation to be applied; when a large grid current was drawn at low values of

retarding voltage, the voltage drop across this resistor became appreciable, so that the measured voltage did not correspond to the actual voltage on the grid.

Fortunately, an input transformer is used in the second differential circuit so the problem did not arise. The work function of the analyser grid was not measured, so that we have had to assume a value of 5eV when calculating the electron energies relative to the Fermi level of the target.

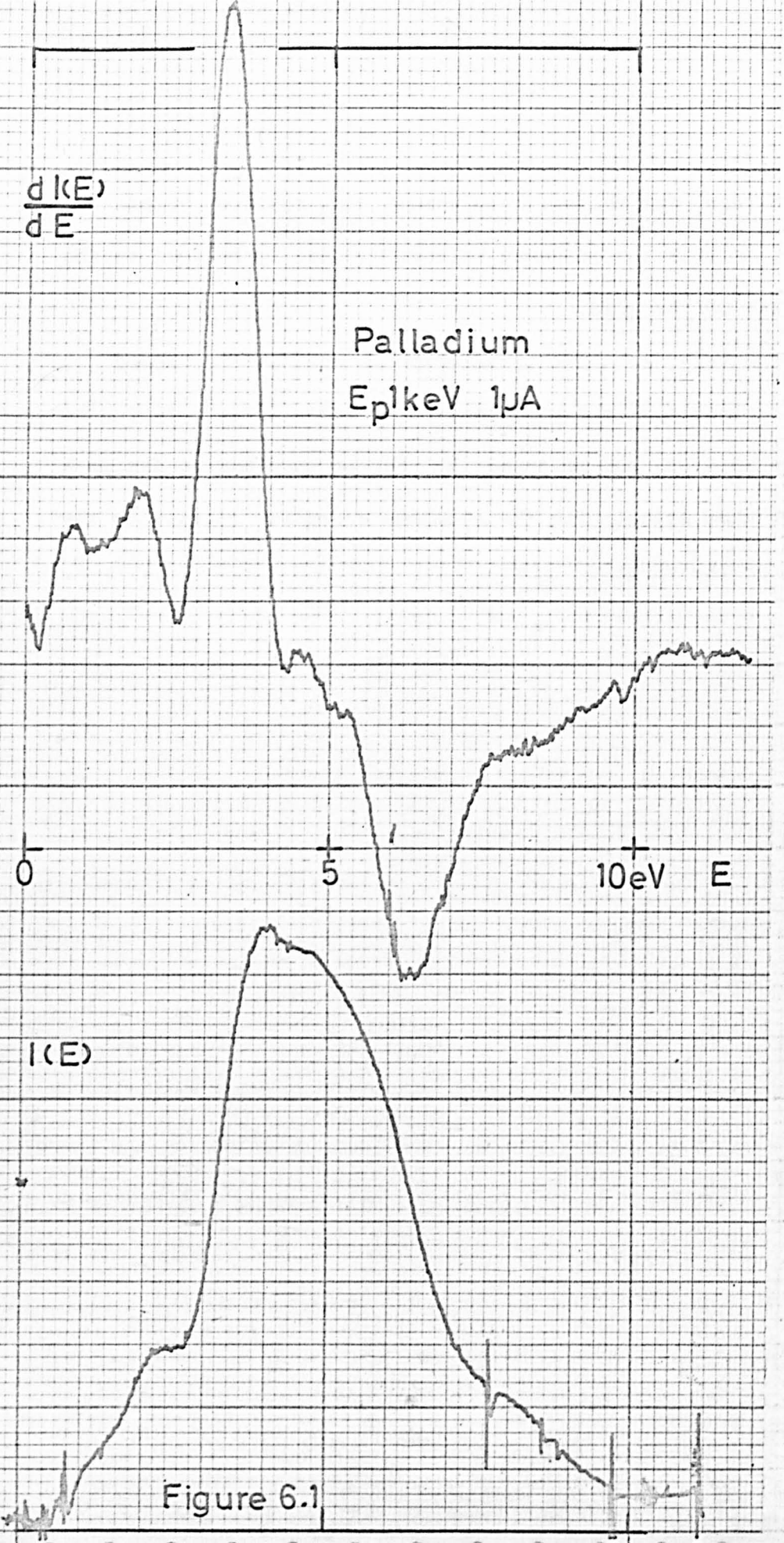

Figure 6.1

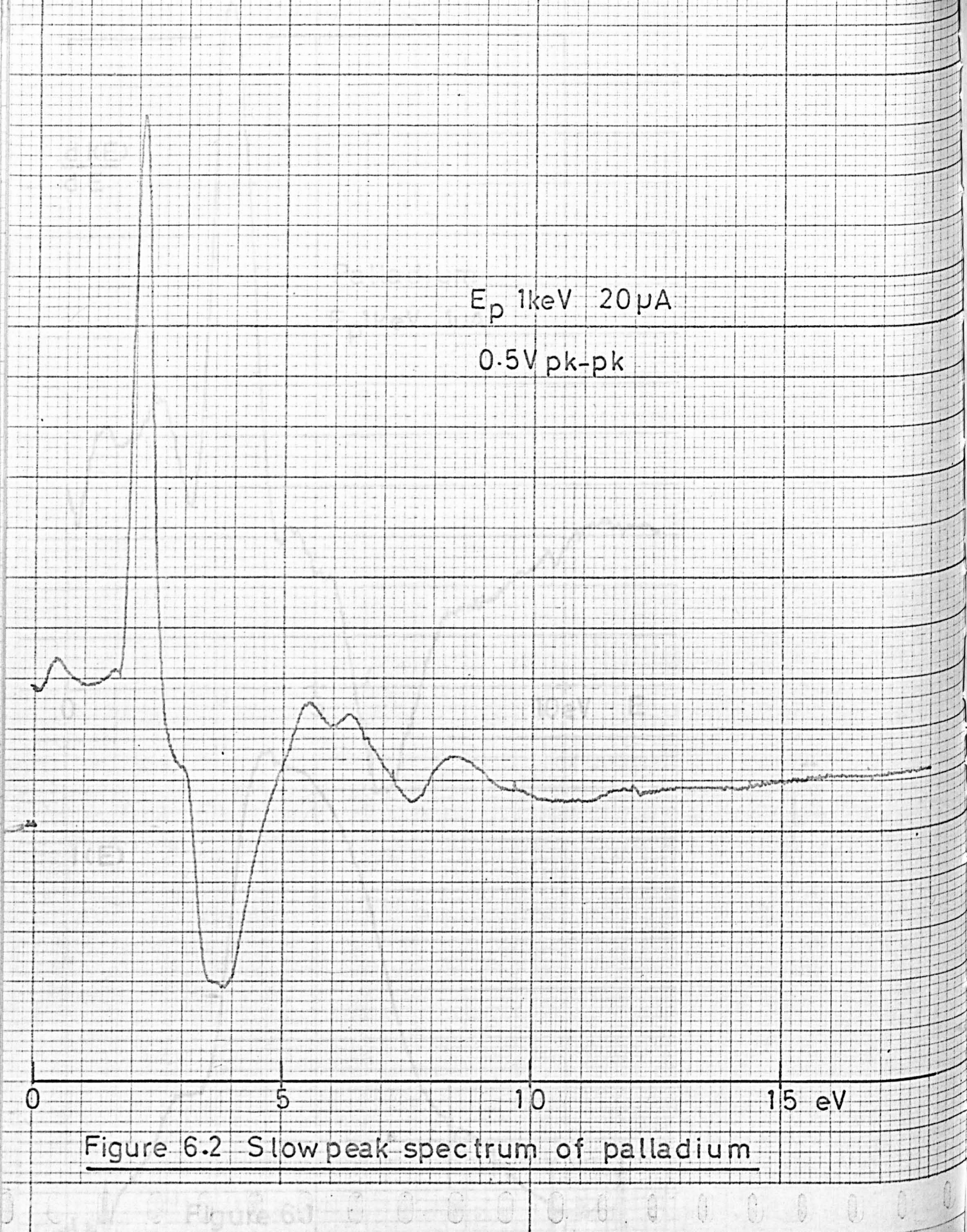

Figure 6.2 Slow peak spectrum of palladium

6.2 Results

Figure 6.1 shows comparison spectra taken using the first and second differential modes. Even with the low value of 1μA primary current, it was found necessary to shift the lower trace by 0.3eV to correct for the (average) potential drop across the resistor. It is also evident from the figure that the small peaks are greatly accentuated by using the second differential.

Increased sensitivity was achieved when the primary current was increased to 20μA, as is shown in Figure 6.2; peaks are visible at 1.2, 3, 3.7, 6 and 7.5eV.

The spectrum of silver contained far more structure, as can be seen in Figure 6.3, where some fourteen peaks may be noticed. The peaks were seen at 1.2, 2.2, 3.0, 3.2, 4.1, 4.8, 5.2, 6.2, 7.0, 7.5, 8.8, 9.8, 12.4 and 16.2eV.

Increasing the modulation amplitude to just 1v p-p, however, sufficiently degraded the resolution for the number of peaks observed to drop to 9, as is shown in Figure 6.4.

The spectrum of copper is similar to that of silver. In Figure 6.5 can be discerned some eleven peaks at 1.1, 2.0, 2.4, 3.2, 4.1, 4.8, 5.7, 6.4, 7.1, 8.6 and 9.8eV, with two small peaks at about 12 and 13eV.

Fewer peaks are evident in the aluminium spectrum shown in Figure 6.6, where we can see peaks at 1.2, 2.8, 4.0, 5.7, 6.8, 10.3 and 11.5eV.

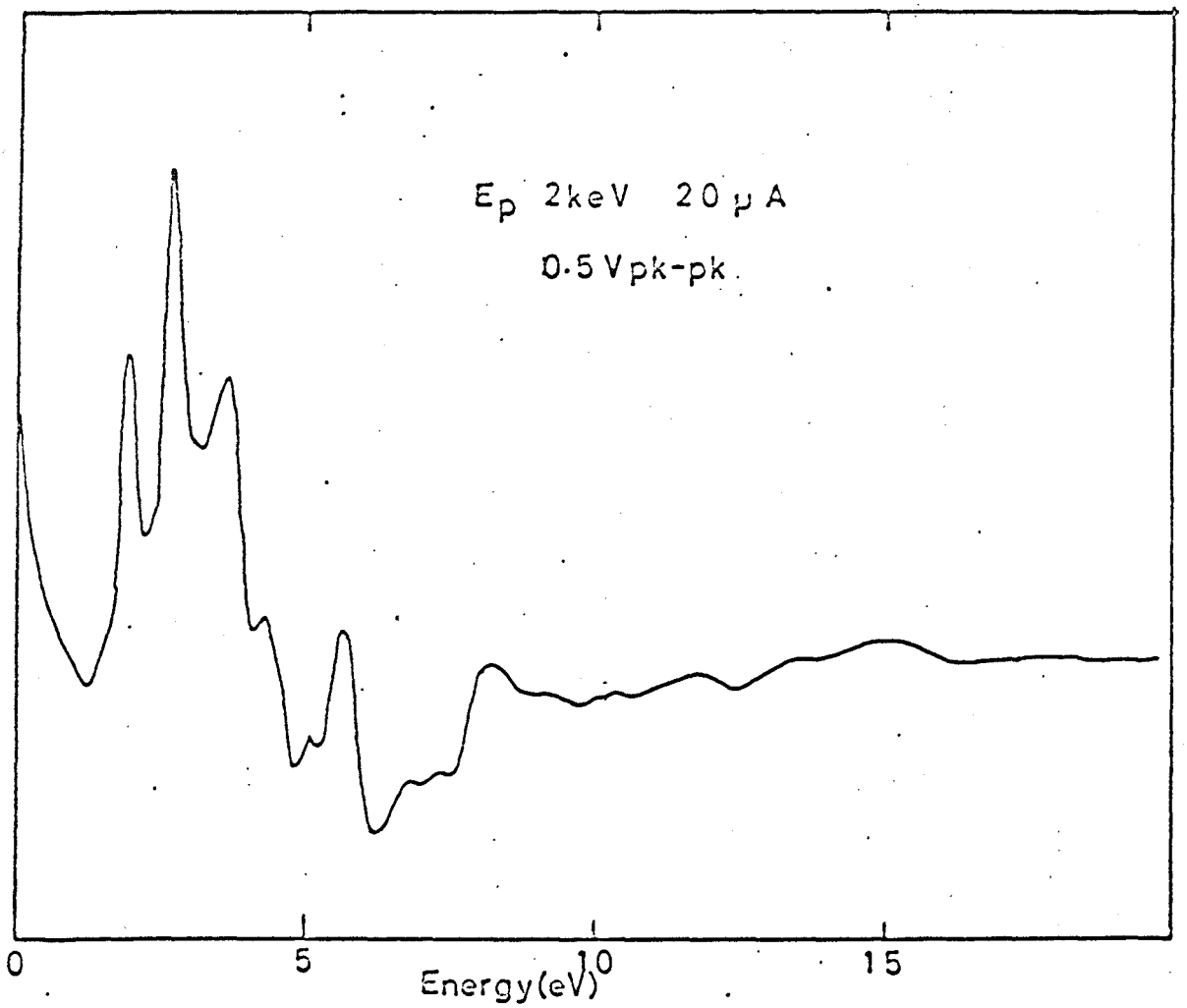

Characteristic Energy gains for silver

Figure 6.3

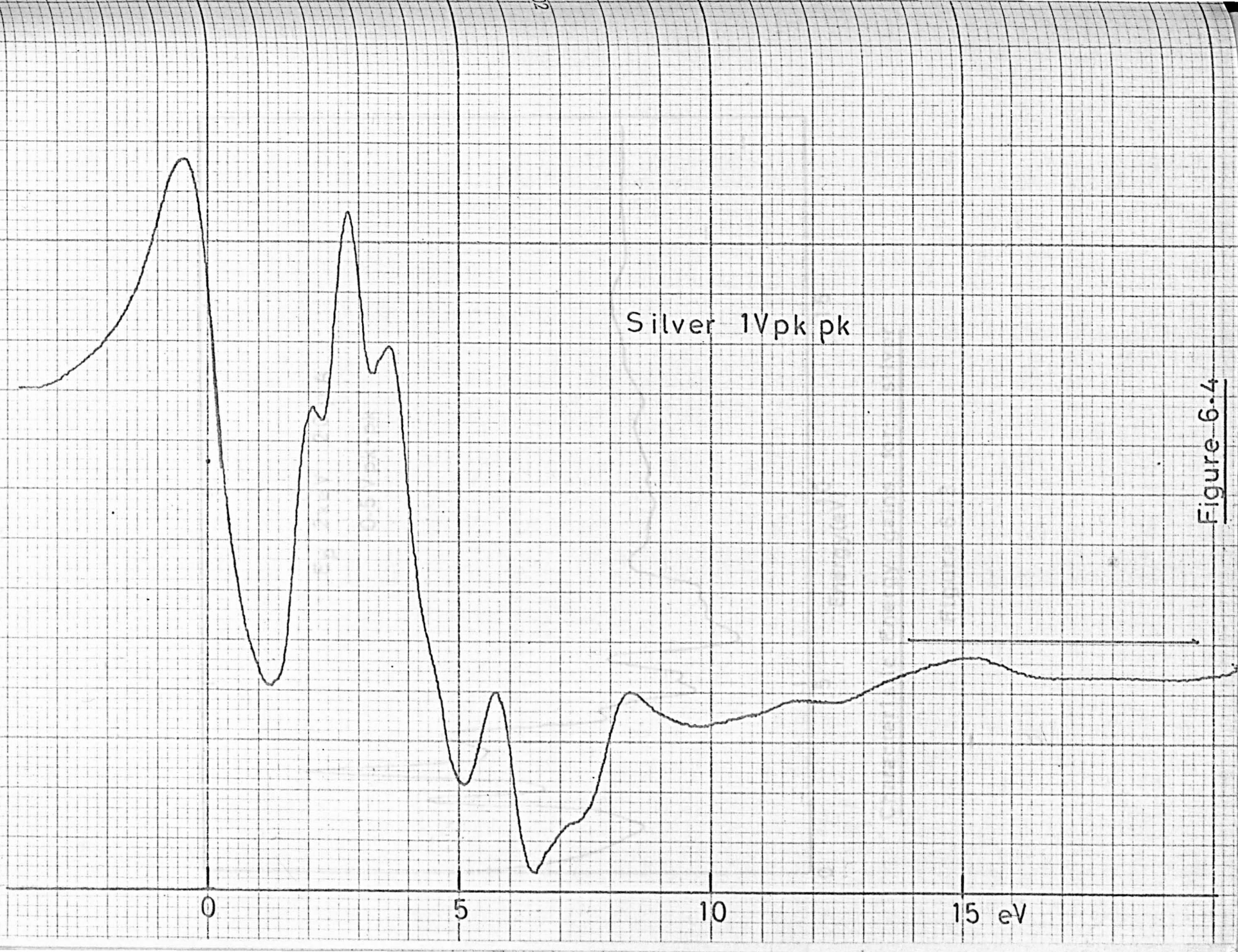

Figure 6-4

Similar results have been reported by Jenkins and Chung for copper (1971b) and aluminium (1971c) and these results are compared with their values in Table 6-I below.

Table 6-I

Silver	Copper		Aluminium	
Fig. 6.3	Fig. 6.5	J & C	Fig. 6.6	J & C
1.2	1.1		1.2	
2.2	2.0	1.9	2.8	2.5
3.0	2.4		4.0	
3.2	3.2	3.3	5.7	6.0
4.1	4.1		6.8	
4.8	4.8	5.0	10.3	10.5
5.2	5.7		11.5	
6.2	6.4	6.6		
7.0	7.1			
7.5	8.6	8.0		
8.8	9.8	10.5		
9.8	12	12.5		
12.4	13			
16.4				
		19.5		
		21.5		
		25.5		

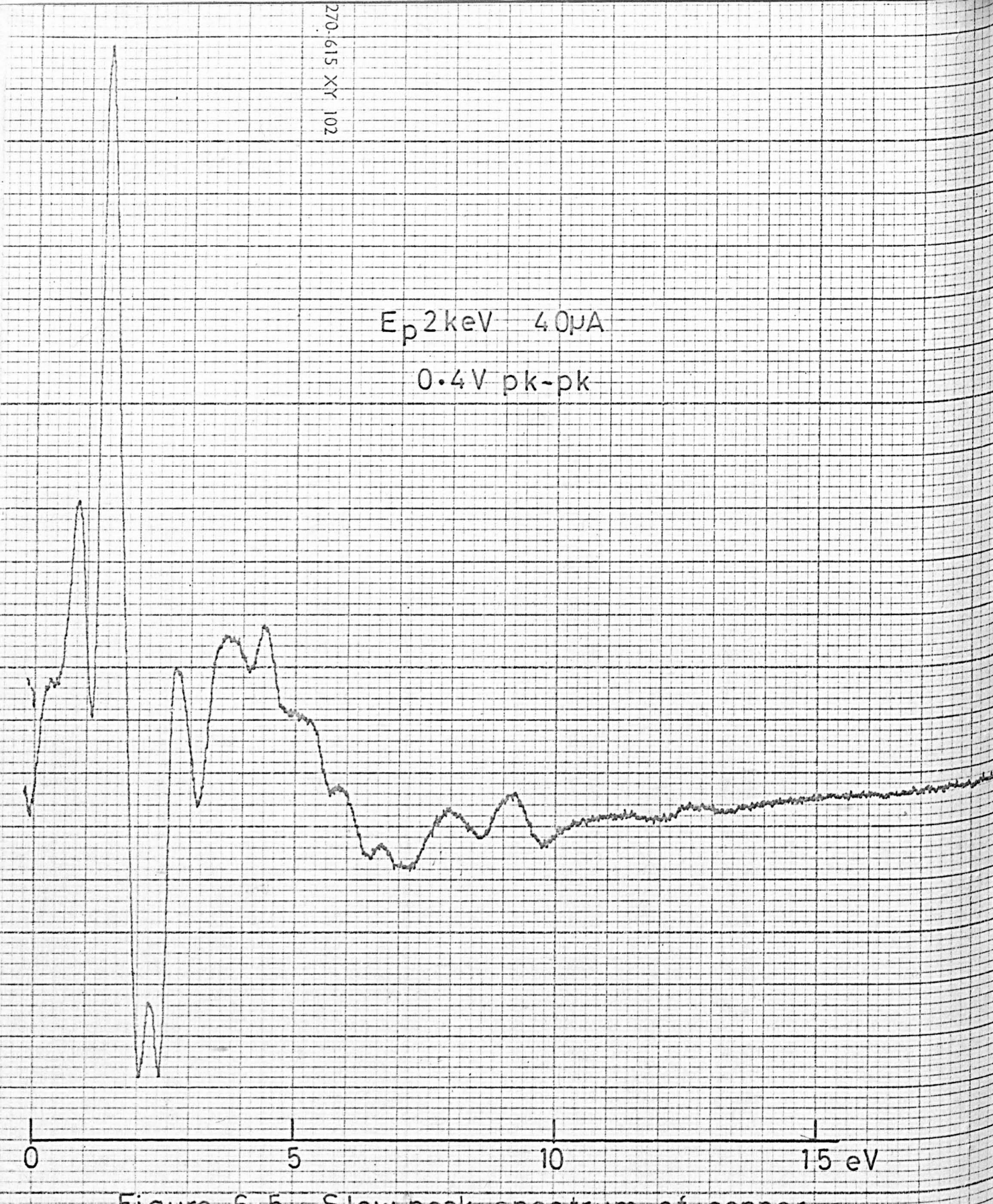

Figure 6·5 Slow peak spectrum of copper

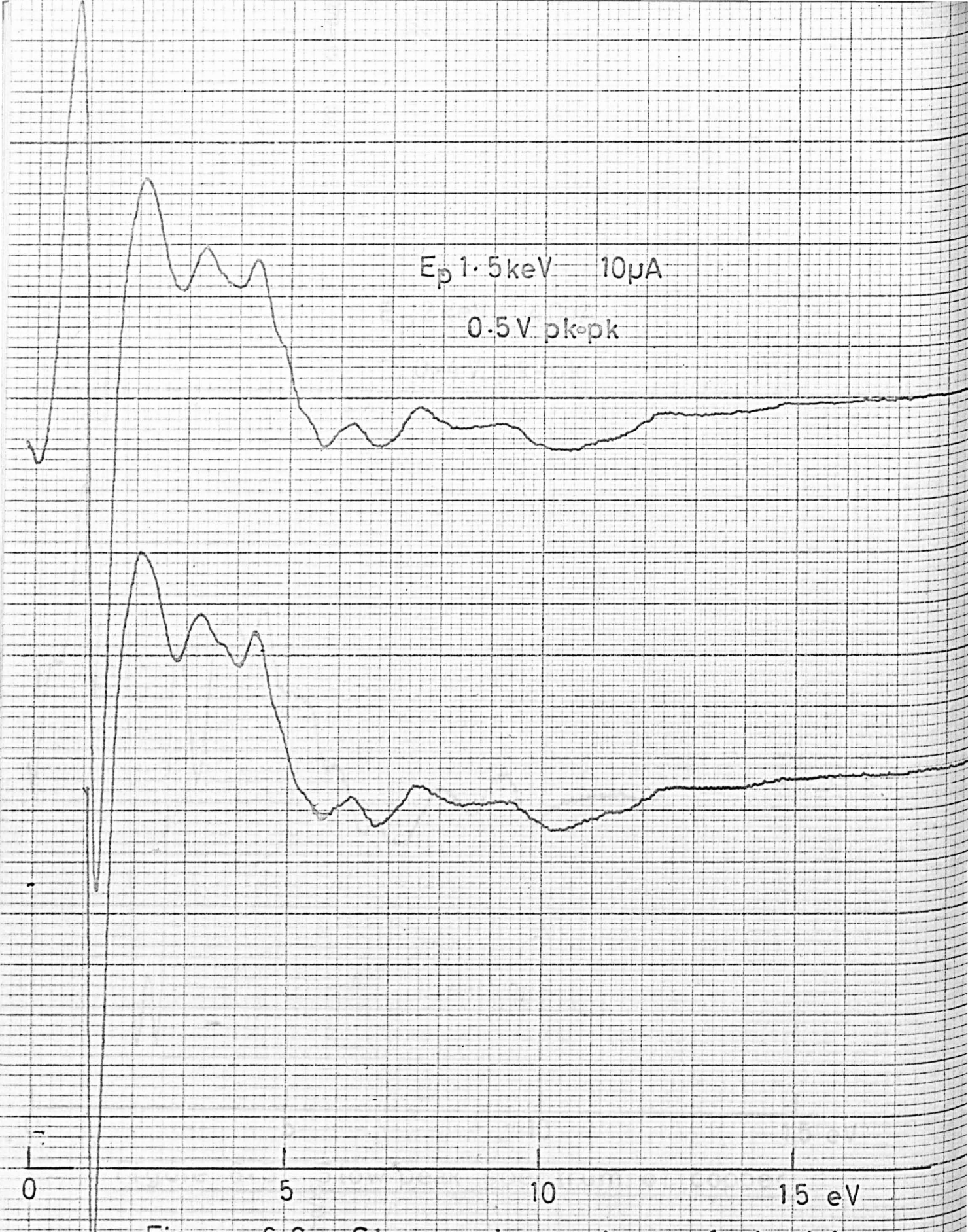

Figure 6.6 Slow peak spectrum of aluminium

Jenkins and Chung referred to their energies as 'gains' from the 0.5eV inelastic peak, so this quantity has been added to their tabulated values in each case for direct comparison with these results. Results have also been quoted by von Koch (1970) for the case of aluminium, but it is not clear what was the zero energy level for his observations, so that it is difficult to make meaningful comparisons. In general, more peaks were seen than reported by Jenkins and Chung, though the spectrum of copper was not continued beyond 15eV. This could be due in part fo the superior resolution of this analyser, but also to the fact that Jenkins and Chung were studying prepared crystal surfaces, whereas these results refer to a polycrystalline sample.

Results taken with varying incident angles are not given as time did not permit a thorough study, and it was not clear if slight shifts which were observed were due to changes in the background slope of the slow peak, or were in fact genuine.

6.3 Discussion

In Chapter 1 we discussed briefly the possible explanations for the origins of "characteristic energy gains" which could give rise to peaks in the low energy portion of the secondary electron spectrum. They involved similar basic principles as those concerned with "characteristic energy loss" phenomena, namely single and many electron excitations in the solid.

The single electron excitation theory involves the ejection of conduction band electrons, either directly by the incoming beam, or as a result of transitions between critical points in the Brillouin zone. If we assume that an incoming primary electron excites a valence band electron to a conduction band state above the vacuum level, then there are two possible decay mechanisms: (a) the electron can be ejected from the solid with an energy corresponding to its initial energy; (b) the electron may de-excite via a transition to another critical point state, the transition energy being transferred to a third electron, which will appear as a CVV Auger electron.

The many electron, or plasmon gain, theory assumes that, just as electrons may lose energy by the creation of plasmons, electrons may gain energy by the decay of plasmons. This theory was put forward by Jenkins and Chung (1971b) to explain their results on copper, and they claimed a certain degree of correlation between the energy losses,

energy 'gains' and satellite peaks they observed either side of Auger peaks. The correlation may have been rather fortuitous, particularly as they measured their 'gains' from the observed maximum in the slow peak. A simple calculation would show that there are many more electron states near a peak in the density of states in the valence band, so that this would be a more suitable initial energy to choose. In this case, it is necessary to add the work function of the energy analyser to the observed values, in order to relate them directly to the energy levels of the target.

If the plasmon gain theory is correct, then aluminium would be a very suitable subject for investigation, since it possesses strong losses compounded of the 1.1eV surface and 15.4eV bulk losses. The "characteristic gain" spectrum of aluminium, however, contains much weaker structure than that of copper and silver, and also it cannot be simply related to the known plasmon energies. It would thus appear that plasmon gain processes are not primarily responsible for the observed peaks.

In order to examine the single electron excitation theory, it is necessary to know something about the detailed band structure of the metals in the region of the vacuum level. Cooper et al. (1971) and Segall (1961, 1962) have published calculated band structures for silver, copper and aluminium and their energy band diagrams are shown in Figures 6.7 and 6.8(a),(b). The diagrams for silver and copper are very similar with the sp band crossing the vacuum level at certain points in the zone, and coming within the d band below the Fermi level at

other points. The band structure of aluminium is, however, much more akin to that of a nearly free electron gas, as would be expected.

Interband transitions can occur between the points of high symmetry marked as Γ X W L and K. Direct (constant k) transitions can occur between different levels at the same symmetry point, and indirect transitions between levels at different symmetry points. In Table 6-II are listed the calculated energies of the states of high symmetry for the three metals with reference to the Fermi Energy. Also included for aluminium are two levels, $X_{(est)}$, obtained by extrapolation of the upper Z_1 and Z_4 lines.

In order for these conduction band states to be detected as direct emissions, they must have sufficient energy to be above the vacuum level. If we assume a work function of about 5eV, then only four silver levels, five copper levels and no aluminium levels possess sufficient energy to escape the solid. Consequently, in attempting to explain the observed low energy peaks, we are dealing either with conduction band states of higher energy, or Auger-type transitions between the states of lower energy.

It seems reasonable that states of energy about 25eV above the Fermi level may have quite a low population, but it is quite feasible to generate energies of this order from Auger-type transitions involving lower energy states. For example, calculation of all the possible Auger transitions for aluminium, based on Γ ionization, yields energies of from 5eV to 19eV above the Fermi level, corresponding to emission energies

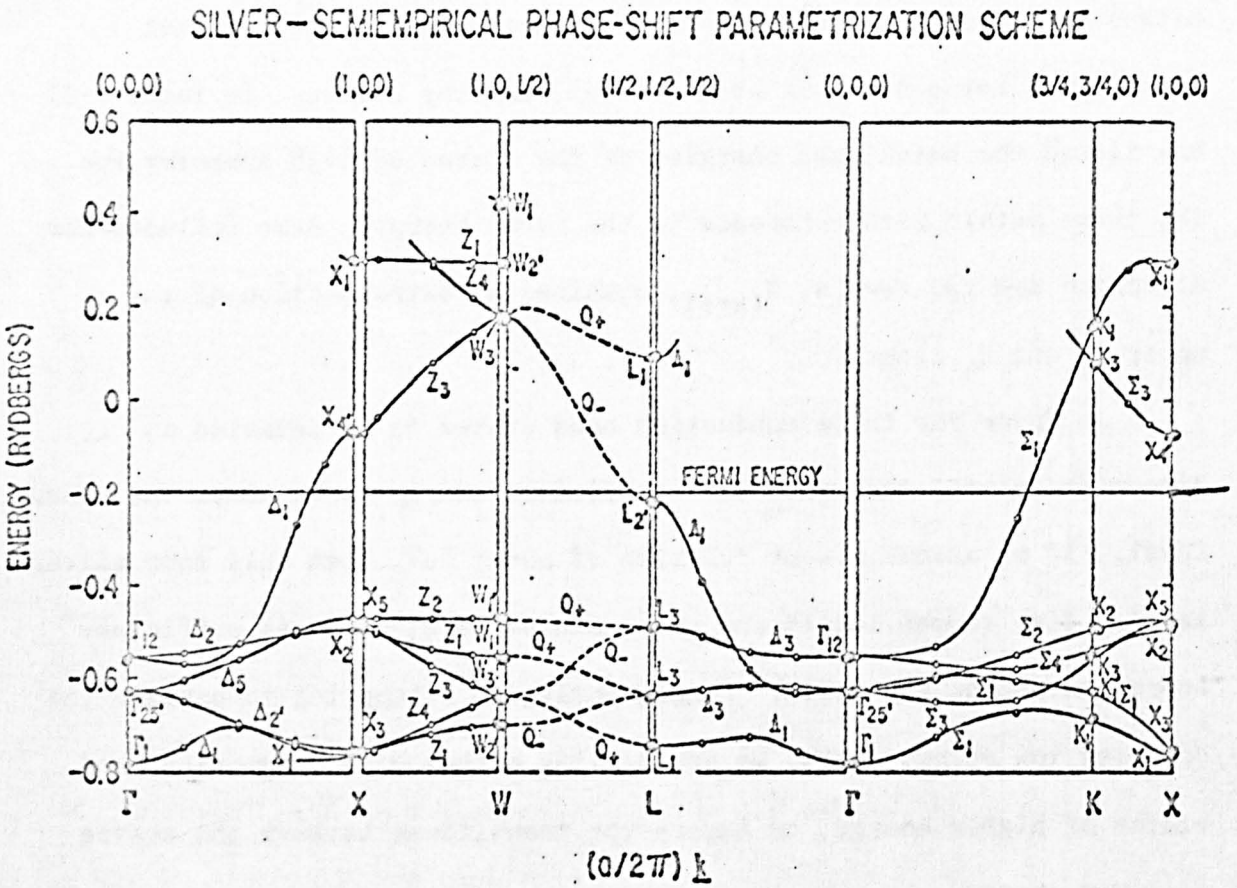

Energy bands of silver from Cooper et al. (1971)

Figure 6.7

of up to about 14eV taking into account the work function. The number of possible transitions for copper and silver is much greater, but it may be possible to eliminate those transitions which have a high photon yield.

It is not possible to say categorically at present that single electron excitations and conduction band Auger electrons are responsible for the observed phenomena but the theory seems more plausible than one based on plasmon gains. Greater confidence will result from a more thorough theoretical and experimental investigation. It does seem possible, however, that the examination of the true secondary peak will provide useful information on the band structure of solids.

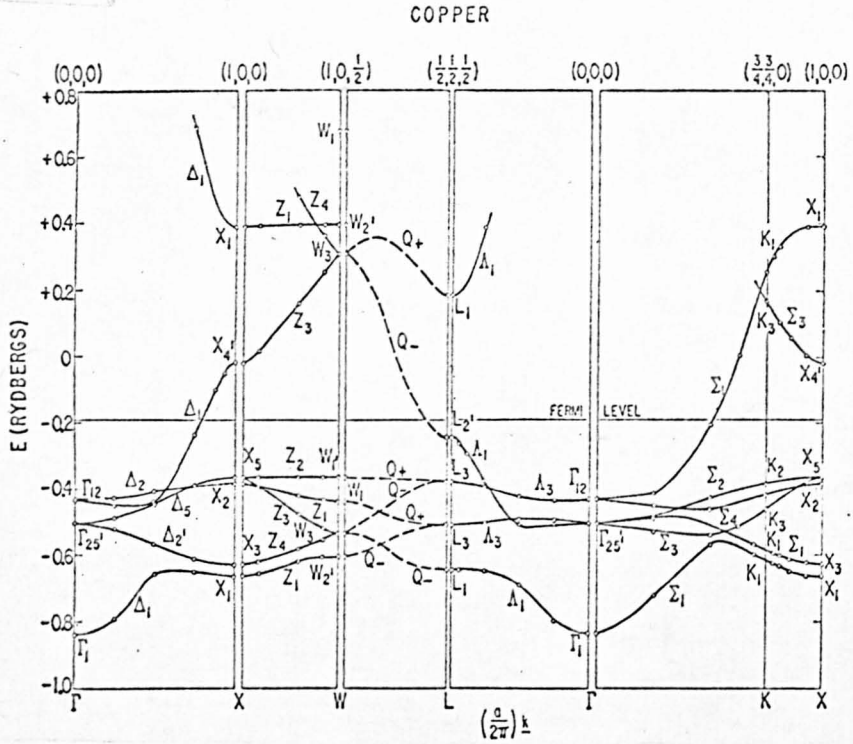

(a) . The calculated energy bands for Cu along the various symmetry axes in the Brillouin zone and on the zone surface for the *l*-dependent potential.

copper

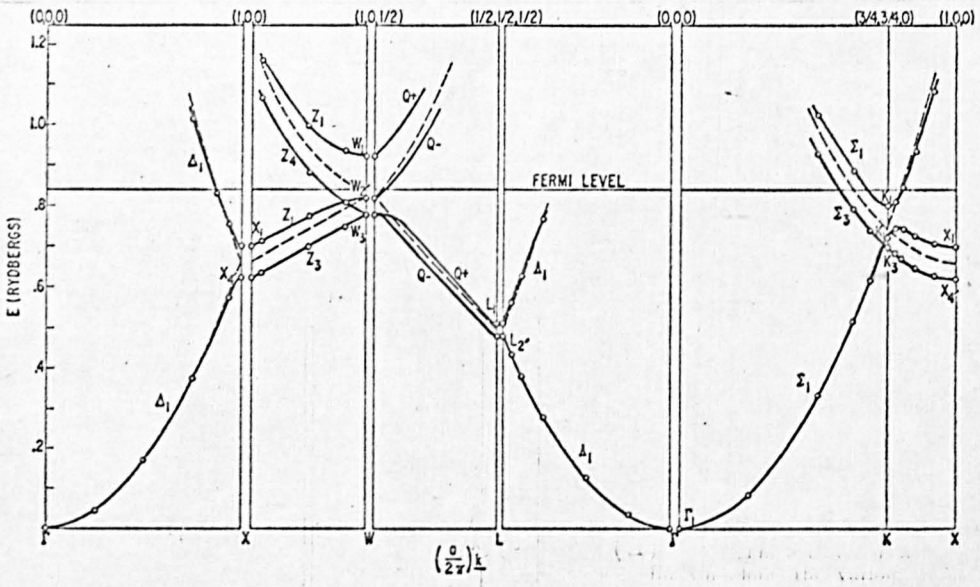

(b) . . . The energy bands for the various symmetry axes within the Brillouin zone and on the zone surface. The circles represent the calculated energies while the dashed curves indicate the free electron energy bands.

aluminium

Figure 6.8

Energy Bands of Cu and Al from Segall (1961, 1962)

TABLE 6-II Approximate energies of states at symmetry points (from Cooper 1971, Segall 1961/2)

Point	Level	Ag	Cu	Al
Γ (0,0,0)	$\Gamma 1$	-7.91	-8.89	-11.43
	$\Gamma 25'$	-5.80	-4.38	
	$\Gamma 12$	-4.85	-3.40	
X (1,0,0)	X1	-7.66	-6.57	
	X3	-7.46	-6.08	
	X2	-4.04	-2.72	
	X5	-3.72	-2.49	
	X4'	+1.70	+2.10	-2.97
	X1	+6.75	+7.78	-1.93
	X (est)			+3.67
	X (est)			+3.81
L ($\frac{1}{2},\frac{1}{2},\frac{1}{2}$)	L1	-7.39	-6.30	
	L3	-5.91	-4.46	
	L3	-3.97	-2.68	
	L2'	-0.30	-0.87	
	L1	+3.97	+5.06	
K ($\frac{3}{4},\frac{3}{4},0$)	K1	-6.64	-5.95	
	K1	-5.87	-5.50	
	K3	-4.90	-3.81	
	K4	-4.60	-3.21	
	K2	-4.04	-2.74	
	K3	+3.84	+4.78	-1.92
	K1	+4.89	+5.95	-0.52
	K1			-0.23
W (1,0,$\frac{1}{2}$)	W2'	-6.82	-5.77	
	W3	-5.94	-5.77	
	W1	-4.80	-3.47	
	W1'	-3.72	-2.48	
	W3	+5.17	+6.71	-0.87
	W2'	+6.70	+7.87	-0.29
	W1	+8.51	+11.69	+1.13

CHAPTER 7

CONCLUSIONS AND SUGGESTIONS FOR FURTHER STUDIES

In this thesis we have tried to give an account of the various processes involved and the phenomena observed in the study of secondary electron emission. In particular, the construction of an apparatus for measuring the secondary electron yield of materials, and the energy distribution of these secondary electrons has been described. We have explained the advantages of detection of the differential of the energy distribution, and detailed the electronic requirements of the problem.

The equipment has been shown to be a versatile tool for the study of surfaces. The flexibility of the design has enabled measurements of characteristic energy losses and Auger spectroscopy to be performed at at a variety of incident angles. Secondary electron yield measurements have also been made, and a future use for the apparatus is the examination of the effects of surface contaminants on the yield parameters. However, Auger spectroscopy only analyses the top few atomic layers, and the escape depth of secondary electrons can be of order 50Å, so that the scope of such investigations would be limited. A more suitable analytical tool in this case might well be photo-electron spectroscopy, where the depth of analysis more nearly corresponds to the surface region of interest from the secondary yield standpoint.

The measurements on the Zr/Al showed that it is a suitable material for use where a low secondary yield is important, but the Auger spectroscopy also revealed that there was no aluminium on the surface of the getter, despite its bulk concentration of 16%. Fine structure found in the $M_{4,5}\ N_{4,5}\ N_{4,5}$ Auger spectra of palladium, silver, tin and antimony was similar to that reported by Pessa et al. (1969, 1971) and interpreted as spin-orbit splitting of the final state configuration. Characteristic energy losses from the main Auger transition were also seen for some metals, and in the case of aluminium a peak which can be interpreted (Suleman and Pattinson 1971) as a plasmon gain was found.

The peaks discovered in the low energy region and termed characteristic energy gains do not seem to bear much relation to the characteristic energy losses and it is presumed that different mechanisms are involved in each case. There is a great scope for the further examination of the these peaks, particularly since the 360° analyser seems to detect them with such good resolution. At present it appears that the energy gains can be associated with preferential emission of conduction band electrons of energies corresponding to the symmetry points near the Fermi surface. Further work is needed to substantiate this, particularly since possible Auger decay processes complicate the identification.

During the period covered by this thesis, the study of the energy distribution of secondary electrons has grown from the rather narrow field of characteristic energy loss spectroscopy into the powerful tool of

Auger electron spectroscopy. In just a few years an exciting new analytical tool has emerged for the study of clean surfaces. Whereas it seems likely that the cylindrical mirror analyser or variants thereof will for the next few years be the instrument offering the greatest sensitivity and resolution for Auger electron spectroscopy, there will still be a place for instruments based on a retarding field analyser. The retarding field analyser is particularly suited where variations of incident angle are to be made or secondary electron yield or appearance potential spectroscopy undertaken in conjunction with the Auger spectroscopy.

The 360° retarding field analyser also appears to be the most effective analyser to date in the very low energy region 0-25eV.

REFERENCES

A

AKSELA, S. (1971) Z. Physik, 244, 268.

ALLEN, R.M. (1969) Ph.D. Thesis, University of Keele.

ASHCROFT, N.W. (1966) Optical properties and electronic structure of metals and alloys, North Holland, p.366.

AUGER, P. (1925) J. Phys. Radium, 6, 205.

B

BAROODY, E.M. (1950) Phys. Rev., 78, 750.

BASSETT, P.J., GALLON, T.E. and PRUTTON, M. (1972) Paper and demonstration given at 6th Thin Films Conference, York.

BEARDEN, J.A. and BURR, A.F. (1967) Rev. Mod. Phys., 39, 125.

BISHOP, H.E. and RIVIÈRE, J.C. (1969) J. App. Phys., 40, 1740.

(1970) App. Phys. Lett. 16, 21.

BISHOP, H.E., RIVIÈRE, J.C. and COAD, J.P. (1970) A.E.R.E. Report R6485, also published (1971) in Surf. Sci. 24, 1.

BRUINING, H. (1936) Physica, 3, 1046.

(1938) Physica, 5, 901.

(1954) The Physics and applications of secondary electron emission, Pergamon Press.

BURGE, R.E. and MISELL, D.L. (1968) Phil. Mag. 18, 251.

(1969) J. Phys. C., S2, 2, 1397.

BURHOP, E. (1952) The Auger effect and other radiationless transitions, C.U.P.

C

CHANG, C.C. (1971) Surf. Sci., 25, 53.

CHUNG, M.F. and JENKINS, L.H. (1970) Surf. Sci., 22, 479.

COAD, J.P. and RIVIERE, J.C. (1970) A.E.R.E. Report R6589 also published (1971) in Surf. Sci., 25, 609.

D

DAVISSON, C. and GERMER, L.H. (1927) Phys. Rev., 30, 707.

della PORTA, P., et al., (1962) 8th Nat. symp. A.V.S., London p.229.

E

EHRENREICH, H. and PHILIPP, H.R. (1962) Phys. Rev., 128, 1622.

EHRLICH, G. (1966) Ann. Rev. Phys. Chem., 17, 295.

F

FARNSWORTH, H.E. (1925) Phys. Rev., 25, 41.

G

GALLON, T.E., HIGGINBOTHAM, I.G. and PRUTTON, M. (1969) J. Phys. E., S2, 2, 284.

GAUTHE, B. (1959) Phys. Rev., 114, 1265.

GERLACH, R.L., HOUSTON, J.E. and PARK, R.L. (1970) App. Phys. Lett., 16, 179.

GIBBONS, D.J. (1966) Handbook of Vacuum Physics ed. A.H. Beck, Volume 3, Pergamon Press.

H

HAAS, T.W., GRANT, J.T. and DOOLEY, G.J. (1970) Phys. Rev. B., 1, 1449.

HAAS, T.W., GRANT, J.T. and DOOLEY, G.J. (1971) Proc. conf. on adsorption desorption phenomena, Florence, Academic Press.

HAAS, T.W., THOMAS, S. and DOOLEY, G.J. (1972) Private communication, in advance of publication.

HACHENBERG, O. and BRAUER, W. (1959) Advan. Elect. Phys., 11, 413.

HARRIS, L.A. (1968) J. App. Phys., 39, 1419.

HARROWER, G.A. (1956) Phys. Rev., 102, 340.

HAWORTH, L.J. (1935) Phys. Rev., 48, 88.

HODGSON, J.N. (1970) Optical absorption and dispersion in solids, Chapman and Hall, p.84

HOLLIDAY, J.E. (1968) Soft X-ray band spectra, Academic Press, p.101.

HOLLIDAY, J.E. and STERNGLASS, E.J. (1959) J. App. Phys., 30, 1428.

HOUSTON, J.E. and PARK, R.L. (1969) App. Phys. Lett., 14, 358.

(1970) App. Phys. Lett., 16, 179.

(1971) J. Vac. Sci. Tech., 8, 91.

HUGHES, A.L. and ROJANSKY, V. (1929) Phys. Rev., 34, 284.

J

JACKSON, A.G. and HOOKER, M.P. (1971) 27, 197.

JACOBS, H. and WOLK, B. (1949) Proc. I.R.E., 37, 1247.

JENKINS, L.H. and CHUNG, M.F. (1971a) Surf. Sci., 24, 125.

(1971b) Surf. Sci., 26, 151.

(1971c) Surf. Sci., 28, 409.

JORDAN, L.K. and SCHEIBNER, E.J. (1968) Surf. Sci., 10, 373.

JOSHI, N.V. (1969) Surf. Sci., 15, 175.

JULL, G.W. (1956) Proc. Phys. Soc., B, 69, 1237.

K

KINDL, B. (1963) Supp. Nuovo Cimento, I, 646.

KINDL, B. and RABUSIN, E. (1967) Supp. Nuovo Cimento, V, 36.

KOLLATH, R. (1937) Z. Phys., 38, 202.

KREUCHEN, K.H. and DISERENS, N.J. (1958) Proc. I.E.E., Pt. B,

Supp. 860.

L

LANDER, J. (1953) Phys. Rev., 91, 1382.

LEDER, L.B. (1956) Phys. Rev., 103, 1721.

LEDER, L.B. and MARTON, L. (1954) Phys. Rev., 95, 1345.

LEDER, L.B. and SIMPSON, J.A. (1958) Rev. Sci. Inst., 29, 571.

LIEBMANN, G. (1947) Phil. Mag., 39, 281.

M

MARTON, L. and LEDER, L.B. (1954) Phys. Rev., 94, 203.

MARTON, L., LEDER, L.B. and MENDOWLITZ, H. (1955) Adv. Elec. Electron Phys., 7, 183.

MOSS, A.R.L. and BLOTT, B.H. (1969) Surf. Sci., 17, 240.

MÖLLENSTEDT, G. (1949) Optik, 5, 499.

N

NOZIERES, P. and PINES, D. (1958) Phys. Rev., 109, 1062.

(1959) Phys. Rev., 113, 1254.

P

PALMBERG, P.W. (1968) App. Phys. Lett., 13, 183.

(1969) The structure and chemistry of solid surfaces ed. G.A. Somorjai, Wiley, N.Y.

PALMBERG, P.W., BOHN, G.K. and TRACY, J.C. (1969) App. Phys. Lett., 15, 254.

PALMBERG, P.W., JOHNSON, de W.C. and BOLL, H.J. (1964) Rev. Sci. Inst., 35, 244.

PALMBERG, P.W. and RHODIN, T.N. (1968) J. App. Phys., 39, 2425.

PARK, R.L., HOUSTON, J.E. (1971) Surf. Sci., 20, 664.

PARK, R.L., HOUSTON, J.E. and SCHREINER, D.G. (1970) Rev. Sci. Inst., 41, 1810.

PESSA, M., AKSELA, S. and KARRAS, M. (1969) Acta Polytechnica Scandinavica, Ph 65.

(1971) Phys. Lett., 31A, 382.

PINES, D. (1956) Rev. Mod. Phys., 28, 184.

PISANI, C. and della PORTA, P. (1967) Supp. Nuovo Cimento V, 261.

POWELL, C.J. (1960) Proc. Phys. Soc., 76, 593.

POWELL, C.J., ROBINS, J.L. and SWAN, J.B. (1958) Phys. Rev., 110, 3.

(1958) Phys. Rev., 110, 657

POWELL, C.J. and SWAN, J.B. (1959) Phys. Rev., 115, 869.

(1959) Phys. Rev., 116, 81.

(1960) Phys. Rev., 118, 640.

Q

QUINTO, D.T. and ROBERTSON, W.D. (1972) Private communication in advance of publication.

R

REDHEAD, P.A. (1970) J. Vac. Sci. Tech., 7, 182.

REDHEAD, P.A. and ARMSTRONG, R.A. (1970) Proc. NEVAC Symp. Ned. Tijdsch. voor Vac., 8, 145.

RITCHIE, R.H. (1957) Phys. Rev., 106, 174.

RIVIÈRE, J.C. (1968) A.E.R.E. Report M-2110.

ROBINS, J.L. (1961) Proc. Phys. Soc., 78, 1177.

ROBINS, J.L. and SWAN, J.B. (1962) Proc. Phys. Soc., 79, 857.

ROY, D. and CARRETTE, J.D. (1971) Can. Jour. Phys., 49, 2138.

RUDBERG, E. (1930) Proc. Roy. Soc., A127, 111.

RUDBERG, E. and SLATER, J.C. (1936) Phys. Rev., 50, 150.

RUTHEMANN, G. (1941) Naturwissenschaften, 29, 648.

S

SAR-EL, H.Z. (1967) Rev. Sci. Inst., 38, 1210.

SEAH, M.P. (1971) Surf. Sci., 26, 151.

SEGALL, B. (1961) Phys. Rev., 124, 1786.

(1961) Phys. Rev., 124, 1797.

(1962) Phys. Rev., 125, 109.

SEWELL, P.B., MITCHELL, D.F. and COHEN, M. (1969) Developments in App. Spectroscopy, 7A, 61.

SICKAFUS, E.N. and COLVIN, A.D. (1970) Rev. Sci. Inst., 41, 1349.

SIEGBAHN, K. et al (1967) ESCA, Atomic and molecular and solid state structure studied by means of electron spectroscopy, Almqvist and Wiksell, Uppsala.

SIEGBAHN, K. et al (1969) ESCA, applied to free molecules, North Holland.

STERN, E.A. and FERRELL, R.A. (1960) Phys. Rev., 120, 130.

STRAUSSER, Y.E. and UEBBING, J.G. (1970) Varian chart of Auger energies.

SULEMAN, M. (1969) Private communication.

(1972) Ph.D. Thesis, University of Keele.

SULEMAN, M. and PATTINSON, E.B. (1971) J. Phys. F., 1, L21.

(1972) Private communication.

T

TAYLOR, N.J. (1969) Rev. Sci. Inst., 40, 792.

(1969) Surf. Sci., 15, 169.

THARP, L.N. and SCHEIBNER, E.J. (1967) J. App. Phys., 38, 3320.

THOMAS, S. (1967) Ph.D. Thesis, University of Keele.

THOMAS, S. and PATTINSON, E.B. (1968) University of Keele C.V.D. Report RU20-5, p.4.

THOMAS, S. and PATTINSON, E.B. (1970) J. Phys. D., 3, 349.

TRACY, J.C. (1971) App. Phys. Lett., 19, 353.

TRACY, J.C. and PALMBERG, P.W. (1969) J. Chem. Phys., 51, 4852.

TUCK, R.A. (1972) Proc. 2nd UHV Conference, Swansea, to be published in Vacuum.

Von KOCH, C. (1970) Phys. Rev. Lett., 25, 792.

WAGENER, S. (1954) Proc. Phys. Soc., B7, 369.

WATANABE, H. (1954) J. Phys. Soc. Jap. 9, 1035.

(1956) J. Phys. Soc. Jap. 11, 112.

(1956) J. Electronmicroscopy 4, 24.

WATTS, C.M.K. and MATTHEW, J.A.D. (1972) Private communication in advance of publication.

WEBER, R.E. and PERIA, W.T. (1967) J. App. Phys. 38, 4355.

WILLIS, R.F. (1972) Paper given at 6th Thin Films Conference, York.

WILLIS, R.F., FEUERBACHER, B. and FITTON, B. (1971) Phys. Lett., 34A, 231.

WOLFF, P.A. (1954) Phys. Rev., 95, 56.

WORTHINGTON, C.R. and TOMLIN, S.G. (1956) Proc. Phys. Soc., A69, 401.

ZASHKVARA, V.V., KORSUNSKII, M.I. and KOSMACHEV, O.S. (1966) English translation Sov. Phys. Tech. Phys. 11, No. 1.

ELECTRON-INDUCED SECONDARY ELECTRON EMISSION SPECTROSCOPY OF SURFACES.

CORRIGENDA

Contents		
	114 w 5	discussion
Abstract		
	115 w 8	Sn,
	121 w 1	75°
p 4	116 w 3	η, E_p
	117 w 4	δ, E_p
p 5	122 w 8	surface
p 8	122 w 1	Möllenstedt
p 9	1 8 w 1	form
p 9	111 w 1	$\hbar\omega_p =$
p 12	1 1 w 1	insert for
	1 6 w 5	Nozières
	115 w 1	absorption
p 14	1 4 w 6	Rivière (* many occurences)
p 23	1 4 w10	beryllium
p 24	1 9 w10	sensitivity
p 28	1 2 w1-3	Watts and Matthew
	121 w 2	and
p 30	1 2 w10	connected
	1 8 w10	be
p 33	1 5 w 8	Bassett
	110 w 3	than
p 39	1 1 w12	delete (approach)
	119 w 1	suitably

p 40 l10 w 3 unity

l19 w 9 Cu

p 58 l19 w 4 2.13

p 65 l 2 w 6 Taylor's (delete '...')

p 72 Equation $B = \frac{2z}{L^2}\sqrt{\frac{2mV}{e}}$

p 73 Equation $r = \frac{1}{B}\sqrt{\frac{2mV}{e}}$

p 82 l 2 w 2 2.24

p 85 l 1 w14 were

p 87 l10 w 8 zirconium

p 94 l12 w 1 Haas

pp 96-97 Figure 4.5 not labelled

fp 104 "C&J"

fp 108 "C&J"

p108 l11 w 6 C & J

p110 l10 w10 Chapter

p122 l10 w 8 of

p141 l12 w 4 transition

p143 l12 w10 aluminium

l13 w11 aluminium

p152 l 7 w 3 external

l16 w 1 excursion

p158 l12 w 4 11eV

p163 l14 w14 delete (the)